Direct Observation of a Single Proton in a Penning Trap

Towards a Direct Measurement of the Proton g-Factor

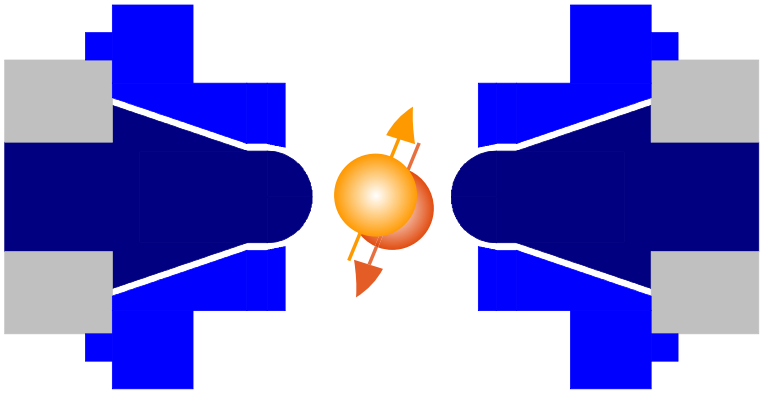

Dissertation zur Erlangung des Grades
Doktor der Naturwissenschaften
am Fachbereich 08 Physik, Mathematik und Informatik
der Johannes Gutenberg-Universität in Mainz

Susanne Waltraud Kreim
geb. in Leonberg
Mainz, den 19. Juni 2009

Für Kim und Magdalena

Zusammenfassung

In der vorgelegten Doktorarbeit werden Experimente vorgestellt, die an einem einzelnen Proton in einer Penningfalle durchgeführt worden sind. Die Eigenbewegung eines isoliert gespeicherten, freien Protons konnte elektronisch durch Kopplung an einen Resonanzschwingkreis nachgewiesen werden. Dies stellt eine nicht-destruktive Messung dar, d. h. das Teilchen geht während der Messung nicht verloren. Die freie Zyklotronfrequenz, die aus den drei gemessenen Eigenfrequenzen hervorgeht, ist eine von zwei zur Bestimmung des magnetischen Moments notwendigen Frequenzen. So wird im Gegensatz zu den existierenden Arbeiten eine direkte Bestimmung des g-Faktors ermöglicht. Planung, Entwicklung und Inbetriebnahme des experimentellen Aufbaus wurden im Rahmen dieser Arbeit durchgeführt, womit eine Messgenauigkeit von 10^{-7} erreicht wurde. Die dabei zu bewältigenden technischen Herausforderungen zur Bestimmung der zweiten Frequenz (der Larmorfrequenz) ergeben sich aus der Kleinheit des magnetischen Moments. Bei dem für diese Messung benötigten Spinzustand des Teilchens handelt es sich um einen internen Freiheitsgrad, der nur über eine Kopplung des magnetischen Moments an die Eigenbewegung bestimmt werden kann. Eine neuartige, hybride Penningfalle wird in dieser Arbeit vorgestellt, die als Quantensprung-Spektrometer die Spininformation auf die Eigenbewegung abbildet. Damit liegt der aus der magnetischen Kopplung resultierende Frequenzunterschied in den beiden Spinzuständen erstmalig in einem elektronisch detektierbaren Bereich.

Summary

This PhD thesis presents experiments performed on a single proton stored in a Penning trap. The eigenmotion of an isolated, free proton could be detected electronically via a coupling to a resonance circuit. This represents a non-destructive measurement, i. e. the particle is not lost during the measurement. The free cyclotron frequency emerging from the measured eigenfrequencies is one of the two frequencies required for the determination of the magnetic moment. This enables a direct determination of the g-factor contrary to already existing works. Design, developing, and commissioning of the experimental setup have been accomplished within the scope of this work leading to a measuring accuracy of 10^{-7}. The technical challenges for the determination of the second frequency (the Larmor frequency) arising from the smallness of the magnetic moment were mastered. Since the spin state required for this measurement is an internal degree of freedom, it can only be accessed through a coupling of the magnetic moment to the eigenmotion. A novel, hybrid penning trap is presented in this work, which imprints the spin information onto the eigenmotion, thus, realizing a quantum jump spectrometer. Therewith, the frequency shift of the two spin states resulting from the magnetic coupling reaches for the first time an electronically detectable range.

Contents

List of Figures

List of Tables

1 Introduction

Curiosity has ever been a main reason to augment knowledge. After having dwelt on the dimensions given by nature (unit of cubit, ounce or day), humankind commenced to reach out for the vast and for the tiny. Expanding knowledge towards the extremes, big (unit of light year or solar mass) and small (unit of femtometer or attosecond), generated the laws of physics describing nature beyond our everyday life experience. A hundred years ago, Einstein's theory of relativity, together with quantum mechanics, revolutionized our view of the world. Abstract symmetries became the new central principle raising once more the search for the one theory to explain all processes governing the universe. Today, the Standard Model of elementary particles already combines electromagnetism with weak and strong interactions, however, the link to gravitation still has to be established. High-precision measurements are essential for consolidating these theories and validating existing laws of physics. In particular, the determination of fundamental constants, which may yet drift in time, allows for gaining ground in return.

Any atomic system comprises fundamental properties, one of them being the magnetic moment whose direct determination represents such a high-precision measurement. Especially, the g-factor of the free electron has been measured by van Dyck and colleagues with a non-destructive detection technique using the continuous Stern-Gerlach effect in a Penning trap [1]. Based on these pioneering experiments, Gabrielse and co-workers succeeded in determining the g-factor with such an utmost accuracy, that a comparison with quantum electrodynamic calculations led to the hitherto most precise determination of the fine structure constant α [2,3]. Yet, if the electron is bound in a hydrogen-like system, the g-factor is changed by binding corrections, bound-state quantum electrodynamics, and nuclear structure effects. These contributions have been calculated and agree with the respective measurements within the uncertainty of $\approx 10^{-9}$ [4–7]. Then again, the contribution arising from nuclear structure effects can be partly eliminated if hydrogen-like systems are compared with lithium-like systems. To this end, experiments have been started at the University of Mainz aiming at the determination of the magnetic moment of the electron bound in Si^{13+} and Ca^{19+} as well as Si^{11+} and Ca^{17+} [8].

This work focuses on the measurement of the magnetic moment of a very simple charged system and at the same time a fundamental particle: the proton. It combines the successful measuring techniques of the experiments just mentioned with the idea of a direct determination of the proton g-factor and leads to captivating research. It is planned to measure the g-factor of a single, isolated proton stored in a cylindrical Penning trap with a relative uncertainty of 10^{-9} or better, thus establishing a counterpart to Dehmelt's famous g-2 experiment [1]. The proton (size of about 10^{-15} m) is a stable hadron and was discovered by Rutherford in 1919 [9]. It is part of the atomic nuclei being bound together by the strong nuclear interaction. Today, the proton's mass is

known to be 1 836 times the electron mass or $1.672\,621\,637(83) \cdot 10^{-27}$ kg.

Beginning in 1933, various experiments have been performed to determine the g-factor of the proton. However, none of them measured the magnetic moment of the free proton directly. Stern and colleagues conducted an experiment to determine the magnetic moment of the proton by deflecting a molecular hydrogen beam in an inhomogeneous magnetic field yielding $\mu_\mathrm{p} = 2.5\mu_\mathrm{N}$ with an accuracy of 10% and μ_N being the nuclear magneton [10,11]. A few years later, they were able to decrease the relative uncertainty to 3% by working with a beam of H_2 and HD, coming up with $\mu_\mathrm{p} = (2.46 \pm 3\%)\mu_\mathrm{N}$ [12]. With the method of molecular-beam magnetic-resonance [13], Rabi and co-workers succeeded in determining the magnetic moment to $\mu_\mathrm{p} = (2.785 \pm 0.02)\mu_\mathrm{N}$ [14,15]. A third way of conducting this experiment was realized by Bloch and colleagues after the development of the method of nuclear magnetic resonance (NMR) [16]. They performed the measurement in water extracting the magnetic moment of the proton to $\mu_\mathrm{p} = 2.792\mu_\mathrm{N}$ from the irradiated frequency. Although they were not able to reduce the uncertainty, the new experimental technique made the external magnetic field the limiting factor in determining the magnetic moment.

A great improvement was achieved when it became possible to combine two frequency measurements to obtain the magnetic moment in units of the nuclear magneton, and hence overcoming the limits of a conventional measurement of the magnetic field: In 1950, Bloch and Jeffries conducted a NMR experiment to extract the frequency of the nuclear resonance, which is equal to the Larmor frequency ω_L. They then combined it with a direct cyclotron measurement to determine the frequency of orbital rotation ω_c, both carried out in the same homogeneous magnetic field [17,18]. The determination of the magnetic moment thus reduced to a frequency ratio:

$$\frac{\mu_\mathrm{p}}{\mu_\mathrm{N}} = \frac{\omega_\mathrm{L}}{\omega_\mathrm{c}} = (2.792\,4 \pm 0.000\,2)\,. \tag{1.1}$$

A similar experiment was conducted by Hipple with the accelerating "omegatron", which resulted in good agreement with the stated value: $\mu_\mathrm{p} = (2.792\,68 \pm 0.000\,06)\mu_\mathrm{N}$ [19]. Collington and co-workers were able to improve the value of Jeffries to $\mu_\mathrm{p} = (2.792\,81 \pm 0.000\,04)\mu_\mathrm{N}$ by modifying the apparatus in such a way as to obtain narrower peak widths [20]. The best determination up to now was realized by Winkler and Kleppner in 1972 with a relative uncertainty of 10^{-8} [21]. They measured the electron-to-proton magnetic-moment ratio via spectroscopy of hyperfine states in a hydrogen maser located in a magnetic field. With that value, it became possible to likewise calculate the magnetic moment of the free proton with a relative uncertainty of 10^{-8} to $\mu_\mathrm{p} = 2.792\,847\,353(28)\mu_\mathrm{N}$ [22]. Karshenboim uses higher order corrections to parameters entering quantum electrodynamics calculations to extract the magnetic moment of the free proton from measurements with hydrogen atoms. Together with the proposed experiment on a single, free proton, this constitutes a stringent test of the underlying calculations.

The determination of the g-factor of a single proton reduces to non-destructively measuring the two frequencies ω_L and ω_c of a particle confined in a Penning trap with an electronic detection unit. In the case of the electron, this bound system of particle and

trapping potential has been called "geonium", where the binding potential is given by the quadrupole potential and magnetic field of the Penning trap. The direct determination of oscillation frequencies working with single trapped particles was already achieved in the group of Dehmelt in the 1970s when determining the g-factor of the free electron [1]. The free cyclotron frequency

$$\omega_\mathrm{c} = \frac{e}{m_\mathrm{p}} B \tag{1.2}$$

is deduced by measuring the independent eigenmotions of a particle in a Penning trap, see for example [23, 24]. A stored particle induced image currents in the trap electrodes which can be picked up by a resonance circuit without losing the particle from the trap. In this way, the particle's frequency is measured and it is resistively cooled into thermal equilibrium with the electronic detection unit. Extracting the Larmor frequency is somewhat more cumbersome. Looking at the spin motion, the g-factor relates the magnetic moment $|\vec{\mu}_\mathrm{s}|$ to the angular momentum $|\vec{s}|$, yielding in the case of an atomic nucleus:

$$|\vec{\mu}_\mathrm{s}| = \frac{g_\mathrm{s}\,\mu_\mathrm{N}}{\hbar}|\vec{s}|\,, \tag{1.3}$$

where $\mu_\mathrm{N} = e\hbar/(2m_\mathrm{p})$ is the nuclear magneton. Since this work deals solely with the spin motion, $g_\mathrm{s} \equiv g$. The energy eigenstates of a proton stored in a Penning trap, with charge e and mass m_p, are all Zeeman-split due to the presence of the external, homogeneous magnetic field $\vec{B}$. For a magnetic field in the axial direction $\hat{z}$, this energy shift is given in dependence of the spin state as:

$$\begin{aligned} \Delta E &= -\vec{\mu}\cdot\vec{B} \\ &= -g\,\mu_\mathrm{N}\,B\,\frac{\vec{s}}{\hbar}\cdot\hat{z} \;=\; m_\mathrm{s}\,g\,\mu_\mathrm{N}\,B\,, \end{aligned} \tag{1.4}$$

where $m_\mathrm{s} = \pm 1/2$ is the spin quantum number. The energy gap between the spin-up and the spin-down state is given by the Larmor precession frequency ω_L:

$$\hbar\,\omega_\mathrm{L} = g\frac{e\hbar}{2m_\mathrm{p}}B\,. \tag{1.5}$$

Inducing radio-frequency transitions between the two spin states and detecting the resulting spin state yields ω_L, which, together with the free cyclotron frequency, leads to the g-factor via the relation

$$g = 2\frac{\omega_\mathrm{L}}{\omega_\mathrm{c}}\,. \tag{1.6}$$

Measuring two frequencies down to a relative uncertainty of 10^{-9} bears challenges for experimental realization. Since the spin information is an internal degree of freedom for a particle confined in a Penning trap, it has to be coupled to an external degree of freedom, i. e. one of the eigenmotions. The so-called magnetic bottle field (a magnetic field inhomogeneity) introduced by Dehmelt in 1973, is exploited to imprint the spin state information onto the axial eigenmotion ω_z of the particle in the Penning trap [25]. Thus, the magnetic moment is coupled to ω_z shifting this frequency according to

the spin direction. This so-called continuous Stern-Gerlach effect is used to determine the spin state non-destructively [26]. The value of the frequency shift scales with the magnetic moment of the particle and the strength of the magnetic bottle. Conventional cylindrical Penning traps, like the one used for example in [27], cannot be employed, because a relative frequency shift on a 10^{-7} scale in the case of a proton is almost impossible to be detected efficiently. To this end, a novel Penning trap is introduced, which is called *the hybrid Penning trap* and which was developed in the context of this thesis [28]. In this trap the magnetic bottle field is greatly enhanced, thus, enabling the detection of the spin state of the proton. Unfortunately, the magnetic bottle field compromises a sensitive frequency measurement. Consequently, the double Penning trap technique will be employed to separate the frequency measurement from the spin-state analysis [29]. The former will be performed in the first, precision Penning trap located in the homogeneous region of the magnetic field. The latter will take place in the second, analysis trap which is located far enough away from the homogeneous region so as not to interfere.

To achieve a high-precision determination of the proton g-factor, long storage times are required. This is realized by performing the experiment in a closed setup at 4 K yielding extremely low background pressure ($p < 10^{-16}$ mbar). Contrary to conventional cooling methods with liquid helium cryostats, this experiment uses a pulse tube cooler to provide the cryogenic environment through gas expansion in a closed helium cycle. This environment places great requirements on the electronics needed to non-destructively detect the trapped proton, and it leads to low electronic noise. The use of superconducting resonant circuits increases the signal-to-noise ratio of the detection systems substantially. To this end, detection units have to be designed with a large inductance accompanied by a low parasitic capacitance in such a way as to yield optimal quality factors. Another challenge bears the in-trap creation of protons since the experiment takes place in a sealed chamber. The principle of an electron beam ion source can be used to implement a miniature device into the trap chamber permitting the production of protons in the magnetic field and at 4 K.

In the following chapters I will set the stage for the accomplishment of the experiment introduced above. Chapter 2 gives a theoretical view of storage and detection principles for charged particles. Cylindrical Penning traps are discussed in detail from the first efforts to today's electrostatically elaborate traps. In addition, the non-destructive detection of a single particle with an electronic detection unit is examined and different detection techniques are presented. Lastly, the continuous Stern-Gerlach effect is treated carefully by including a numerical example of the proton experiment. In chapter 3, the theoretical concepts for the hybrid Penning trap are developed and the design criteria for the toroidal hybrid Penning trap used in the proton experiment are discussed. As a result, the final toroidal hybrid Penning trap is presented. Chapter 4 focuses on the experimental setup including the cryogenic body and the double-trap tower. The electron beam ion source is characterized and discussed as well as the detection units for measuring the eigenfrequencies of the trapped particle. Inducing radio-frequency transitions for the spin-state analysis will also be studied. Moreover, commissioning measurements of the complete experimental setup are presented.

The procedure for detecting a single proton is tackled in chapter 5. Here, experimental data related to the creation, storage, and detection of various particles as well as pure proton ensembles are presented. Further, the sequence for isolating a single proton is presented and the results are discussed. Determining the free cyclotron frequency ν_c from the eigenmotions of the stored proton concludes this section. The following chapter deals with the characterization of the precision Penning trap in which the frequency measurements are performed. Electrostatic properties such as the optimal tuning ratio, orthogonality, and compensation are examined. Together with a conclusion, chapter 7 deals with further developments of the experimental setup which emerged while the first measurements were taken but go beyond the scope of this work. Further, different perspectives will be disclosed. For example, the envisaged measurement establishes the basis for testing fundamental principles of symmetry. With the g-factor of the proton determined, the experimental setup can likewise be used to perform the experiment with a single antiproton allowing in principle to reach the same relative uncertainty. Together, these measurements will provide a stringent test of the CPT-theorem on the baryonic sector [30, 31].

2 Storage and Detection of a Single Particle in a Penning Trap

Trapping of a charged particle in three dimensions can adroitly be realized by electromagnetic fields which are defined through the force $\vec{F}$ they exert on the particle:

$$\vec{F} = q\,\vec{E}(\vec{r},t) + q\,\frac{\vec{v}}{c} \times \vec{B}(\vec{r},t)\,, \tag{2.1}$$

where q and $\vec{v}$ are charge and velocity of the particle, respectively. At first, solely an electric field is considered for trapping, restricted to the time-independent case $\vec{E} \neq \vec{E}(t)$ with cylindrical symmetry $\vec{E} \neq \vec{E}(\theta)$ and reflection symmetry in the $z = 0$-plane. For stable trapping the electrostatic potential $\Phi(r,z)$ has to exhibit a minimum at the position of the particle. Furthermore, since the trapped charge is assumed to be the only free charge within the trapping volume, $\Phi(r,z)$ has to fulfill the Laplace equation

$$\Delta\Phi(r,z) = \frac{1}{r}\frac{\partial}{\partial r}\left(r\frac{\partial}{\partial r}\Phi(r,z)\right) + \frac{\partial^2}{\partial z^2}\Phi(r,z) \equiv 0\,. \tag{2.2}$$

The general solution of the Laplace equation can be expressed in terms of a Taylor expansion:

$$\Phi(r,z) = \Phi_0 + r\cdot\left.\frac{\partial\Phi}{\partial r}\right|_{(0,0)} + z\cdot\left.\frac{\partial\Phi}{\partial z}\right|_{(0,0)} + \frac{r^2}{2!}\cdot\left.\frac{\partial^2\Phi}{\partial r^2}\right|_{(0,0)} + \frac{z^2}{2!}\cdot\left.\frac{\partial^2\Phi}{\partial z^2}\right|_{(0,0)} + \ldots\,. \tag{2.3}$$

The simplest trapping potential is the ideal quadrupole potential which is obtained by plugging this form of the potential for orders $k < 3$ into the Laplace equation (2.2):

$$\Phi(r,z) = U_0\,C_2^{\mathrm{s}}\cdot\left(z^2 - \frac{r^2}{2}\right)\,, \tag{2.4}$$

where U_0 is the applied voltage and the coefficient C_2^{s} is here of dimension $1/\mathrm{m}^2$, the s denoting the fact that it is scaled to a unit of length. The force exerted on the particle can be determined with help of eq. (2.1):

$$\vec{F}_{\mathrm{el}} = -\nabla q\,\Phi(r,z) = -2\,q\,U_0\,C_2^{\mathrm{s}}\,z\,\hat{z} + q\,U_0\,C_2^{\mathrm{s}}\,r\,\hat{r}\,. \tag{2.5}$$

It is obvious from the above equation that neither pure minima nor maxima of the potential can exist in three dimensions, thus trapping has to be performed around an electrostatic saddle point where $q\,C_2^{\mathrm{s}} > 0$ holds. The potential is chosen such as to realize

trapping in the z direction enabling the introduction of expansion coefficients focusing on the potential in z:

$$C_k^{\mathrm{s}} = \frac{1}{k!}\frac{\partial^k \Phi}{\partial z^k}\bigg|_{(0,0)} . \tag{2.6}$$

Since the motion of a particle is restricted to a certain region in space only if the net force is zero, the temporal mean of the electric field has to vanish and $C_1^{\mathrm{s}} = 0$. The coefficient C_2^{s} denotes the strength of the quadrupole potential. The basic structure needed for creating an electric saddle point is a three-pole, cylindrically symmetric trap consisting of a center ring and two end caps (fig. 2.1). With a certain voltage applied to the ring while the end caps are kept at ground, a potential minimum or maximum (depending on the polarity of the applied voltage) appears at the center of the trapping volume along the symmetry axis $\hat{z}$. In combination with a homogeneous magnetic field $\vec{B} = B_0\hat{z}$ to trap the particle radially, trapping in three dimensions is achieved. First experiments were performed by Frans Michel Penning in the 1930's who used an axial magnetic field to force electrons onto cyclotron orbits [32]. Electrodes perpendicular to the magnetic field to achieve trapping in three dimensions were implemented by Pierce [33]. In 1959 Hans Dehmelt realized an electric quadrupole field by applying a voltage to hyperbolic electrodes, thus approximating the equipotential surfaces of a quadrupole potential.

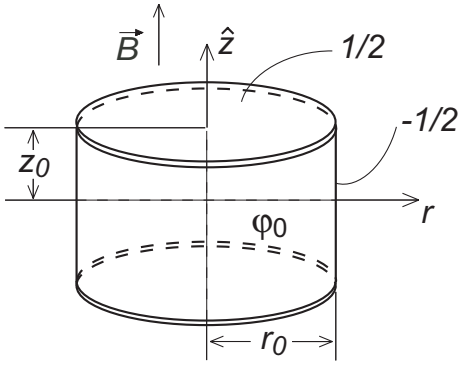

Figure 2.1: Simple cylindrical Penning trap consisting of a ring and two flat end caps and symmetry axis $\hat{z}$.

2.1 Particle Motion and Energy

A charged particle moving in a superposition of a homogeneous magnetic field $\vec{B} = B_0\hat{z}$ and an electrostatic field $\vec{E} = -\nabla\Phi$ with the potential presented in eq. (2.4) experiences the Lorentz force from eq. (2.1). The axial motion is decoupled from the others performing a harmonic oscillation about the origin with

$$\omega_{\mathrm{z}} = \sqrt{\frac{q}{m}\,\frac{U_0}{d^2}\,C_2}\,, \tag{2.7}$$

with $d^2 = \frac{1}{2}(z_0^2 + \frac{1}{2}r_0^2)$ being the characteristic trap dimension as defined by [34], where z_0 is half the length of the ring electrode and r_0 is the inner radius of the ring[1], as seen in fig. 2.1. The x- and y-component of the force are dominated by the magnetic field generating a cyclotron motion in absence of an electrostatic field with frequency

$$\omega_\mathrm{c} = \frac{q}{m}B\,. \tag{2.8}$$

The motion of the particle is fully described by the Newtonian equations

$$\begin{aligned} \ddot{x} &- \omega_\mathrm{c}\,\dot{y} - \frac{1}{2}\omega_\mathrm{z}^2\,x = 0 \\ \ddot{y} &+ \omega_\mathrm{c}\,\dot{x} - \frac{1}{2}\omega_\mathrm{z}^2\,y = 0 \\ \ddot{z} &+ \omega_\mathrm{z}^2\,z = 0\,. \end{aligned} \tag{2.9}$$

The equations of motion have been solved for example in [35, 36] with the well-known result:

$$\omega_\pm = \frac{\omega_\mathrm{c}}{2} \pm \sqrt{\left(\frac{\omega_\mathrm{c}}{2}\right)^2 - \frac{\omega_\mathrm{z}^2}{2}}\,, \tag{2.10}$$

the cyclotron frequency ω_+ and the magnetron frequency ω_- arising from the $\vec{E}\times\vec{B}$ drift. A particle moving in a Penning trap with these eigenfrequencies exhibits a hierarchical frequency structure:

$$\omega_+ \gg \omega_\mathrm{z} \gg \omega_-\,. \tag{2.11}$$

Since the classical equations of motions are linear, they essentially describe harmonic oscillator equations whose quantization is straightforward. An adequate solution of the appropriate Schrödinger equation has been presented among others in [37,38]. However, following Brown in [35], who includes raising and lowering operators, greatly simplifies the treatment and produces the energy eigenvalues of the respective Hamiltonian. Considering additionally the spin movement ω_L with magnetic quantum number m_L, allows for writing down the total energy E of the system:

$$\begin{aligned} E &= E_+ + E_\mathrm{L} + E_\mathrm{z} + E_- \\ &= \hbar\omega_+(n_+ + \frac{1}{2}) + \hbar m_\mathrm{L}\omega_\mathrm{L} + \hbar\omega_\mathrm{z}(n_\mathrm{z} + \frac{1}{2}) - \hbar\omega_-(n_- + \frac{1}{2})\,, \end{aligned} \tag{2.12}$$

with n_i being the quantum numbers of the three eigenfrequencies resulting from eq. (2.9). The energy level diagram is shown in fig. 2.2 where the splitting is greatly exaggerated for better visibility. The energy in the cyclotron motion is mostly kinetic energy whereas in the axial motion it alternates between kinetic and potential energy. These are stable motions, since reducing the energy in the mode reduces the amplitude. The magnetron degree of freedom, however, is almost exclusively potential energy meaning that the motion is an orbit around the top of a radial potential hill. The magnetron motion is unbound since any dissipative process increases the magnetron radius. Fortunately, the damping constant is large allowing for a metastable description of the motion since damping due to synchrotron radiation is infinitely long. The spin motion is an internal degree of freedom, which will be treated in detail in section 2.5.

[1] The difference in C_k^s and C_k will become apparent in section 2.2.

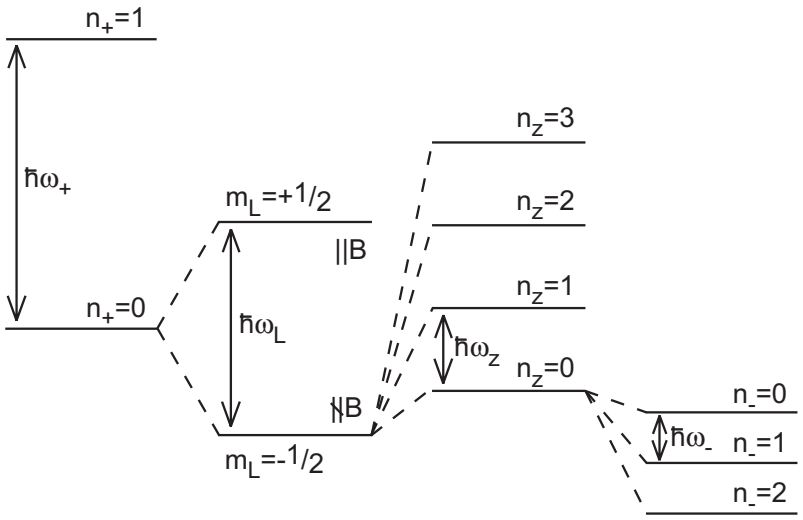

Figure 2.2: Energy level diagram of the eigenmotion of a particle in a Penning trap. It starts out with the cyclotron energy levels n_+ to the left. These levels are split first by the spin m_L, then by the axial n_z and magnetron motion n_-, respectively.

In the ideal case, the free cyclotron frequency ω_c is obtained via $\omega_c = \omega_+ + \omega_-$. However, real Penning traps have unavoidable imperfections which alter the ideal electrostatic potential, such as misalignment of the electrodes both internally and with respect to the magnetic field directions or deviation from the ideal geometry in the trap electrodes. This couples the three eigenmotions of the particle resulting in three coupled, linear second-order differential equations of motion for the case of second-order imperfections. Solving these equations as been performed in [23] yields the so-called invariance theorem, see also [39]. The invariance theorem is used for computing the free cyclotron frequency from the measurable eigenfrequencies of the imperfect trap:

$$\omega_c^2 = \bar{\omega}_+^2 + \bar{\omega}_z^2 + \bar{\omega}_-^2 \,. \tag{2.13}$$

2.2 Cylindrical Penning Trap

The potential field distribution inside a cylindrical Penning trap, shown in fig. 2.1, can be solved analytically using standard techniques for solving electrostatic boundary-value problems involving a series expansion in terms of orthogonal harmonic functions satisfying the boundary conditions as given for example in [40]. The traditional method as performed among others by Benilan and Audoin [41] and by Gabrielse and MacKintosh [42] exploits the fact, that complete knowledge of the potential is unnecessary since the particles are typically confined near the center of the trap. Thus, the potential can be expanded in spherical coordinates for $r \ll d$ in even powers of the small ratio r/d.

Following the multi-pole expansion from [42] yields the potential Φ_0:

$$\Phi_0(r,\theta) = \frac{1}{2}U_0 \sum_{k\ \text{even}} C_k \left(\frac{r}{d}\right)^k P_k(cos\theta) = U_0\,\varphi_0\,, \tag{2.14}$$

where k is even because of the assumed reflection symmetry with respect to the $z = 0$-plane. The boundary conditions are given by applying $-1/2\,U_0$ to the ring with inner radius $r = r_0$ and $+1/2\,U_0$ to the end plates at $z = \pm z_0$ yielding φ_0 as solution for the Laplace equation. The C_k-coefficients are the dimensionless expansion coefficients for the expansion of φ_0. To achieve the quadrupole field stated in eq. (2.4), anharmonicities quantifiable in terms of the next higher order terms in the above expansion have to be examined. The most important contribution arises from C_4. It can be tuned to zero mechanically by adjusting the ratio r_0/z_0, however, this also affects C_2. Another and much more sensitive possibility is the use of correction electrodes to precisely vary the resulting potential at the center of the trap, thus reducing or minimizing the anharmonicity of the trap. As a further development open-end-cap Penning traps have been designed suitable to introduce a beam into the trapping region [43]. Such a trap consists of a center ring, two identical correction electrodes, and two elongated, open-ended end caps comparable to fig. 2.3. A potential U_0 is applied between the end caps and the ring, and U_c to the correction electrodes. The potential inside the trap can be written as the superposition

$$\Phi = U_0\varphi_0 + U_\mathrm{c}\varphi_\mathrm{c}\,, \tag{2.15}$$

with φ_0 and φ_c being solutions to the Laplace equation satisfying the boundary conditions

$$\begin{aligned}
\varphi_0(r_0,z) &= \begin{cases} -\frac{1}{2} & 0 \le z \le z_1 \\ 0 & z_1 < z < z_0 \\ \frac{1}{2} & z_0 \le z \le z_\mathrm{e} \end{cases} \qquad \text{and} \quad \varphi_0(-z) = \varphi_0(z) \\
\varphi_\mathrm{c}(r_0,z) &= \begin{cases} 0 & 0 \le z \le z_1 \\ 1 & z_1 < z < z_0 \\ 0 & z_0 \le z \le z_\mathrm{e} \end{cases} \qquad \text{and} \quad \varphi_\mathrm{c}(-z) = \varphi_\mathrm{c}(z)\,.
\end{aligned} \tag{2.16}$$

Furthermore, rotational symmetry is still inferred as well as reflection symmetry in the $z = 0$-plane. The potentials can be solved using Bessel functions I_0 of first kind, zero order:

$$\Phi = \frac{U_0}{2}\sum_{n=0}^{\infty} A_n^{\mathrm{cyl}}\, I_0(k_n\,r)\,\cos(k_n\,z) + \frac{U_\mathrm{c}}{2}\sum_{n=0}^{\infty} B_n^{\mathrm{cyl}}\, I_0(k_n\,r)\,\cos(k_n\,z)\,. \tag{2.17}$$

The coefficients C_k are found by matching this analytical solution for the cylinder to the multi-polar form along the z-axis in the neighborhood of the origin, comparable to the above equation with coefficients A_n^{cyl}, B_n^{cyl}, and eq. (2.14). The evaluation performed in [43] presumed infinitely long end caps and negligible size of the gaps between the electrodes. For an exact solution, the effect of finite end caps and gaps have to be included with slight modifications as will be discussed in the following.

2.2.1 The five-pole Cylindrical Trap

The electrostatic potential $\Phi(r, z)$ for a cylindrical, five-pole Penning trap with open end caps and the boundary conditions shown in fig. 2.3 was calculated in [44]. This work aimed at a complete knowledge of the potential inside the trap, thus, the above ansatz of an expansion in r/d was discarded. A more general ansatz was chosen by comparing the series solution for the potential with the Taylor expansion from eq. (2.3). It yields coefficients C_k^{s} which are scaled to the characteristic length unit of a trap, i. e. mm, with the dimension of $1/\mathrm{mm}^k$. As such they are independent of specific trap lengths or geometries.

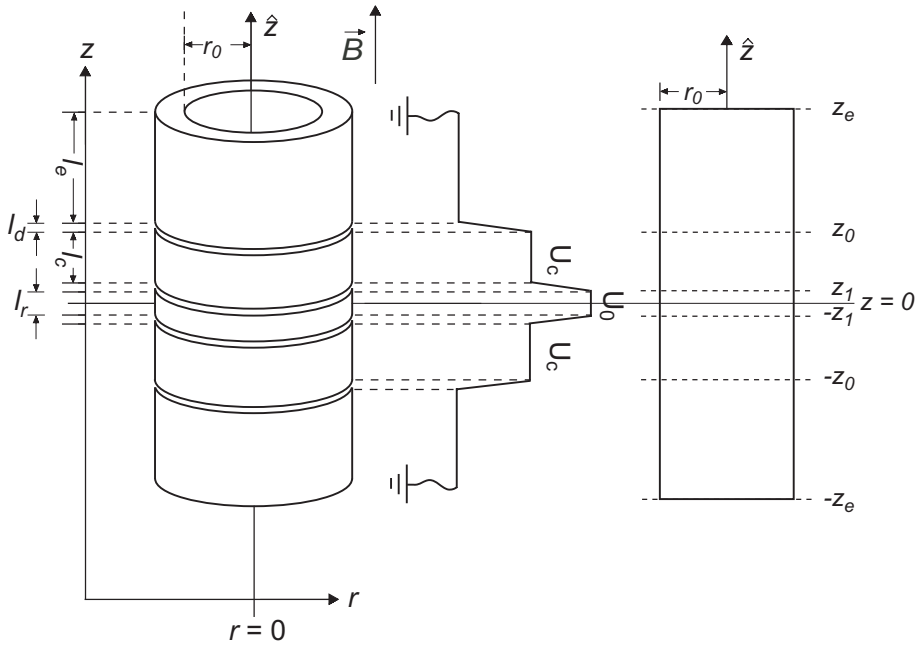

Figure 2.3: Open, five-pole cylindrical Penning trap with the symmetry axis $\hat{z}$. To the right, the potential distribution on the electrode surfaces is shown. The gaps between the electrodes are approximated by linear interpolation [45]. Thus, the required boundary values for determining $\Phi(r, z)$ are properly defined. On the far right, a cut through the inner surface of the trap is shown.

The calculation has been carried out assuming a trapping volume in which the requirement is fulfilled that $\Phi(r, z) = 0$ and $\Delta\Phi(r, z) = 0$. Furthermore, the domain of $\Phi(r, z)$ is given by $\Phi(r, z) = \{r\epsilon[0, r_0], \theta\epsilon[0, 2\pi], z\epsilon[-l/2, l/2]\}$. Here, only the solution is discussed:

$$\begin{aligned}\Phi(r,z) &= \sum_{n\ \mathrm{odd}} \left\{ \frac{8U_0}{L\, l_{\mathrm{d}}\, \kappa_n^2\, I_0(\kappa_n\, r_0)} \sin\left(\frac{\kappa_n\, l_{\mathrm{d}}}{2}\right) \left[\sin\left(\frac{\kappa_n (l_{\mathrm{d}} + l_{\mathrm{r}})}{2}\right) \right.\right. \\ &+ \left.\left. 2\,T \sin\left(\frac{\kappa_n (l_{\mathrm{d}} + l_{\mathrm{c}})}{2}\right) \cos\left(\frac{\kappa_n (2l_{\mathrm{d}} + l_{\mathrm{r}} + l_{\mathrm{c}})}{2}\right) \right] I_0(\kappa_n\, r) \cos(\kappa_n\, z) \right\}, \end{aligned} \tag{2.18}$$

where the different lengths in the equation correspond to the lengths of the different electrodes: l_e = end cap, l_c = correction electrode, l_r = ring, and l_d = distance between electrodes (see also fig. 2.3). The total length of the trap is given by $L = 4l_\mathrm{d}+2l_\mathrm{e}+2l_\mathrm{c}+l_\mathrm{r}$ and $\kappa_n = n\pi/L$. Furthermore, the tuning ratio T is given by $T = U_\mathrm{c}/U_0$. The modified Bessel function of first kind, zero order is denoted by $I_0(x) = 1+x^2/2^2+x^4/(2^2 4^2)+\ldots$. To simplify eq. (2.18), the coefficients A_n, B_n are introduced:

$$\begin{aligned} A_n^\mathrm{cyl} &= \frac{8}{L\, l_\mathrm{d}\, \kappa_n^2\, I_0(\kappa_n\, r_0)} \cdot \sin\left(\frac{\kappa_n\, l_\mathrm{d}}{2}\right) \cdot \sin\left(\frac{\kappa_n (l_\mathrm{d}+l_\mathrm{r})}{2}\right) \\ B_n^\mathrm{cyl} &= \frac{16}{L\, l_\mathrm{d}\, \kappa_n^2\, I_0(\kappa_n\, r_0)} \cdot \sin\left(\frac{\kappa_n\, l_\mathrm{d}}{2}\right) \cdot \sin\left(\frac{\kappa_n (l_\mathrm{d}+l_\mathrm{r})}{2}\right) \end{aligned} \tag{2.19}$$

with $n \,\epsilon\, \mathbb{N}$, odd. These coefficients depend only on the geometry of the trap. The coefficients C_k^s from eq. (2.6) can hence be identified:

$$C_k^\mathrm{s} = \frac{1}{U_0}\frac{1}{k!}\frac{\partial^k \Phi}{\partial z^k}\bigg|_{(0,0)} = \frac{1}{k!}\sum_{n\ \mathrm{odd}} \left[A_n^\mathrm{cyl} + T\, B_n^\mathrm{cyl}\right] \left[\frac{\partial^k}{\partial z^k}\cos(\kappa_n\, z)\right]_{z=0}, \tag{2.20}$$

where $I_0(0) = 1$ was used. The odd terms in k of the Taylor expansion vanish out of symmetry reasons yielding for even k:

$$C_k^\mathrm{s} = \frac{1}{U_0}\frac{1}{k!}\frac{\partial^k \Phi}{\partial z^k}\bigg|_{(0,0)} = \frac{1}{k!}\sum_{n\ \mathrm{odd}} \left[A_n^\mathrm{cyl} + T\, B_n^\mathrm{cyl}\right] (-1)^{\frac{k}{2}} \kappa_n^k\,. \tag{2.21}$$

Since only part of the potential depends on the correction voltage U_c, it is convenient to introduce D_k^s-coefficients for that part of the above expression [43]

$$D_k^\mathrm{s} = \frac{1}{k!}\sum_{n\ \mathrm{odd}} B_n^\mathrm{cyl} \cdot (-1)^{\frac{k}{2}} \kappa_n^k\,. \tag{2.22}$$

Normally, the expansion coefficients are split up as $C_k^\mathrm{s} = E_k^\mathrm{s} + D_k^\mathrm{s} \cdot T$, where E_k^s denotes the part dependent solely on the end caps. The coefficients C_k^s and D_k^s are functions of the relative trap radius r_0/z_0 and compensation electrode size l_c/z_0, which can be used for tuning (cf. fig. 2.3). The leading anharmonicity contribution C_4^s can be eliminated by the respective tuning ratio. However, this generally changes C_2^s and hence changes the axial frequency ω_z, thus the T-dependence of C_2^s has to be removed. This is achieved by orthogonalization (ibid.): for any l_c/z_0, there is a choice of r_0/z_0 such that D_2^s can be tuned to zero leading to a vanishing dependency of the axial frequency on the voltage applied to the correction electrodes, in other words $D_2^\mathrm{s} = \partial C_2^\mathrm{s}/\partial T = 0$ and $\omega_\mathrm{z} \neq \omega_\mathrm{z}(U_\mathrm{c})$. Furthermore, the next anharmonicity contribution, the C_6^s-coefficient, can be made zero by picking the corresponding value for z_c/z_0 such that $C_6^\mathrm{s} = 0$.

A conversion from the dimensionless coefficients C_k relating to a specific trap dimension as derived by Gabrielse and others to the coefficients C_k^s, which are scaled to $1/\mathrm{m}^k$, is possible but not exact. Since the calculation in [43] was performed assuming infinitely

long end caps and negligible gaps, the slight modifications arising from finite end caps and gaps are not accounted for in the conversion. The conversion reads for $k = 2$:

$$C_2 = 2\,d^2 \cdot C_2^{\mathrm{s}}\,, \tag{2.23}$$

where $d^2 = \frac{1}{2}(z_0^2 + \frac{1}{2}r_0^2)$ with z_0 being the axial distance from the center of the ring to the beginning of the end cap, in the case of the five-pole trap from fig. 2.3: $z_0 = z_1 + l_{\mathrm{c}} + 2l_{\mathrm{d}}$. Hence, the axial frequency in SI units is calculated via

$$\omega_{\mathrm{z}} = \sqrt{\frac{q}{m} U_0\, 2C_2^{\mathrm{s}}}\,. \tag{2.24}$$

For convenience, the C_k^2-coefficients are not given in $1/\mathrm{m}^k$ but scaled to $1/\mathrm{mm}^k$ since the dimension of mm is the characteristic length for Penning traps employed here. Expressing the potential with help of the C_k^{s}-coefficients is of great advantage when going to other trap geometries as will be seen in chapter 3. There, the coefficients of the toroidal hybrid trap are calculated from the potential in the same manner enabling a direct comparison of the traps' properties.

2.2.2 The Precision Trap of the Proton Experiment

The precision trap of the proton experiment is a five-pole cylindrical Penning trap. The precision trap is compensated and orthogonal following the routine outlined in section 2.2.1. For a fixed set of parameters $(z_1, r_0, l_{\mathrm{d}}, L)$, the D_2^{s}-coefficient can be tuned to zero by varying the length of the correction electrode l_{c}, cf. fig. 2.3. Figure 2.4a illustrates the result for such an analytical calculation. It can be seen that for $l_{\mathrm{c}} = 2.85\,\mathrm{mm}$ the trap is orthogonal and $D_2^{\mathrm{s}} = 0$. Subsequently, the trap was compensated for the fixed l_{c} by varying the tuning ratio T. The value of the coefficient C_4^{s} is shown as a function of T in fig. 2.4b yielding the ideal tuning ratio of $T_{\mathrm{id}}^{\mathrm{pt}} = 0.867049$. At this tuning ratio the next higher anharmonicity contribution is smaller than $C_6^{\mathrm{s}} < 10^{-6}$ and thus negligible. All parameters of the precision trap can be taken from tab. 2.1. Please note, that the lower end cap is 2 mm longer than the upper end cap ensuring a sufficient distance to target and holding plate not to perturb the harmonicity of the electrostatic potential.

Once the electrostatic parameters are computed, the effect of changes in the trap's electrostatic properties on the axial frequency of the trapped particle ν_{z} can be calculated. There are two major components, which later on facilitate the search for a detection signal: a change in frequency as a function of a voltage change close to ring voltage U_0 at which the particle is detected and a change in frequency as a function of a change in the tuning ratio close to $T_{\mathrm{id}}^{\mathrm{pt}}$. The former is referred to as sensitivity, the latter as non-orthogonality of the trap, both are listed in tab. 2.1. The non-orthogonality illustrates that particles in the trap can be detected even if the tuning ratio is only hit within a few percent.

The trapping potential of the precision trap with an inner diameter of 7 mm has been simulated with SIMION, a software for numerically simulating potential distributions

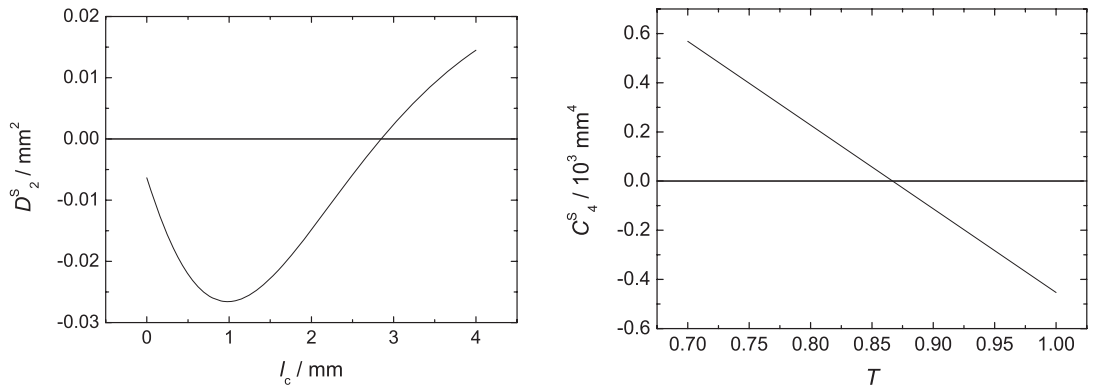

(a) Orthogonality tuning

(b) Anharmonicity tuning for a fixed l_c

Figure 2.4: Analytical calculation for orthogonality and anharmonicity tuning. (a) D_2^s as a function of the length of the correction electrode l_c, where the zero-crossing determines the ideal length for l_c. (b) C_4^s as a function of the tuning ratio T is plotted for $l_c = 2.85\,\text{mm}$ for which $D_2^s = 0$.

for geometries with axial symmetry. The trap electrodes are provided with potentials in such a way that the axial frequency of the proton ν_z coincides with that of the axial detection unit at $\nu_{LC} \approx 680\,\text{kHz}$. To this end, the voltage at the ring electrode is set to $U_0 = -3.3\,\text{V}$ and the correction electrodes are supplied with a voltage of $U_c = T_{id}^{pt} \cdot U_0$, where T_{id}^{pt} is the ideal tuning ratio presented above. The end caps are grounded. The effective potential in the center of the trap along the z-axis as shown in fig. 2.5a is slightly reduced as compared to the applied voltages resulting from the superposition of the different potentials. The data are compared to a harmonic potential (red curve) which was fitted within $\pm 2\,\text{mm}$ around the center. It can be seen, that the potential is to a very high degree harmonic.

The highly sensitive frequency measurement takes place in the precision trap at the very homogeneous region of the external magnetic field. Therefore, the magnetic inhomogeneity arising from the ferromagnetic ring of the analysis trap has to be negligibly small in order not to compromise the measurement. The upper limit for the position dependent component B_2 was set to $B_2 \leq 1\,\mu\text{T/mm}^2$ which results in a distance between the two traps of about 65 mm, see also fig. 2.5b. This B_2-term is on the same order of magnitude as the one arising from the parts of the trap itself and has been verified experimentally with a NMR-probe.

The effective electrode distance D needed to determine the resistive cooling time constant τ is calculated with a SIMION simulation for the respective detection - see section 2.3 for details. The pick-up configuration for the axial mode is a 01000-coupling yielding $D_{pt}^z = 7.37\,\text{mm}$ for the precision trap. For the detection of the cyclotron mode, the pick-up in the radial plane is needed. The simulations, however, delivered too large values and turned out to be unfeasible. First tests with detection unit and protons in the trap resulted in $D_{pt}^+ = 52.4\,\text{mm}$.

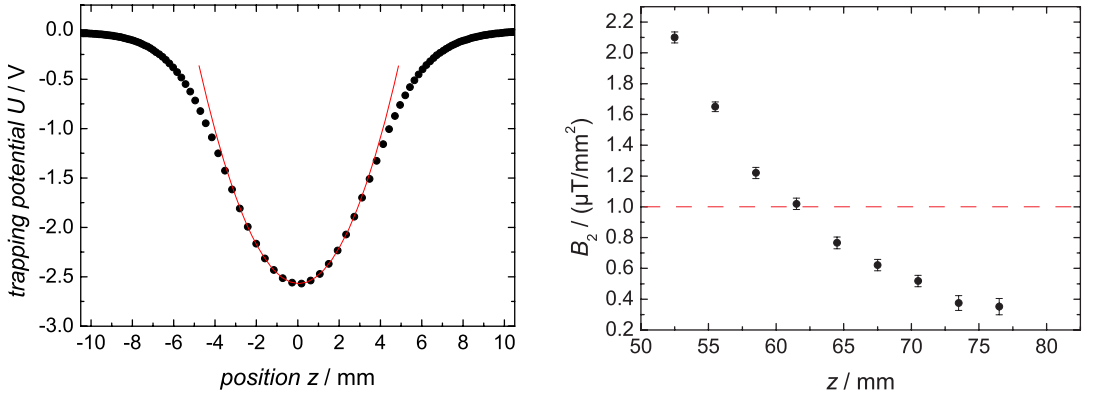

(a) Trapping potential of the precision trap

(b) Magnetic field inhomogeneity in the precision trap

Figure 2.5: (a) The trapping potential of the precision trap is shown as a result of a simulation with SIMION. At the ring electrode, a voltage of $U_0 = -3.3\,\mathrm{V}$ is applied, the correction electrodes are provided with a voltage of $T_{\mathrm{id}}^{\mathrm{pt}} \cdot U_0$, and the end caps are grounded. A harmonic potential (red curve) is fitted within $\pm 2\,\mathrm{mm}$ around the center, however, the curve is drawn for a wider interval. (b) The magnetic field inhomogeneity in the vicinity of the center of the precision trap introduced by the ferromagnetic ring of the analysis trap. The required distance between the two trap centers to meet the condition $B_2 \leq 1\,\mu\mathrm{T}\,/\,\mathrm{mm}^2$ is 72 mm.

Table 2.1: Optimized parameters of the precision trap: geometric and electrostatic properties.

r_0	$3.500\,\mathrm{mm}$	C_2^{s}	$-0.02895\,/\mathrm{mm}^2$
z_1	$0.460\,\mathrm{mm}$	D_2^{s}	$3.3863 \cdot 10^{-5}\,/\mathrm{mm}^2$
l_{c}	$2.848\,\mathrm{mm}$	C_4^{s}	$-5.3899 \cdot 10^{-7}\,/\mathrm{mm}^4$
l_{d}	$0.140\,\mathrm{mm}$	C_6^{s}	$-7.1179 \cdot 10^{-6}\,/\mathrm{mm}^6$
L	$23.000\,\mathrm{mm}$	$T_{\mathrm{id}}^{\mathrm{pt}}$	0.867049
$D_{\mathrm{pt}}^{\mathrm{z}}$	$7.37\,\mathrm{mm}$	$\frac{\Delta\nu_{\mathrm{z}}}{\Delta U_0}$	$-0.103\,\mathrm{Hz}\,/\,\mu\mathrm{V}$
		$\frac{\Delta\nu_{\mathrm{z}}}{\Delta T_{\mathrm{id}^{\mathrm{pt}}}}$	$-0.399\,\mathrm{Hz}\,/\,\mathrm{mUnit}$

2.3 Non-Destructive Detection of Particle Motion

The non-destructive frequency measurement of the particle's eigenmotion in the trap is based on an electronic detection method, the bolometric scheme [46]. Non-destructive in this context means that the particle is not lost after the measurement and that the measurement can be repeated many times with the same particle. Consider therefore a particle performing a harmonic oscillation between two parallel plates of a capacitor. The plates of the capacitor are separated by a distance D and assumed to be infinitely long and perpendicular to the particle motion along the z-axis; an impedance $Z(\omega)$ connects the two plates, as shown in fig. 2.6. The oscillating particle with $z(t) = \tilde{z}\cos\omega t$ induces a current depending on the charge q, the velocity of the particle $\dot{z}(t)$, and D [47]. The current flowing through the impedance is given by:

$$\begin{aligned} I_{\mathrm{ind}}(t) &= \frac{dQ}{dt} = \frac{q}{D}\,\dot{z}(t) \quad \text{and} \\ U_{\mathrm{ind}}(t) &= Z(\omega)\cdot I_{\mathrm{ind}}(t)\,, \end{aligned} \tag{2.25}$$

which is a valid description since the particle amplitude is small compared to the size of the trap. In the case of hyperbolic or cylindrical traps, a geometric correction factor is introduced which accounts for the differences arising from the trap shapes compared to a capacitor. A more general ansatz [48] delivers the "effective electrode distance" D which is determined by the actual configuration yielding the same electric field at the position of the particle as the two plates of the capacitor. It is defined via $D = U/\hat{\tilde{z}}\vec{E}$ for the axial motion, where U is the potential applied to the detection electrodes and $\vec{E}$ is the resulting electric field. In this context, it is convenient to identify the electrodes responsible for detection, by speaking for example of a 01000-coupling in the case of a five-pole trap if detecting only with one of the correction electrodes.

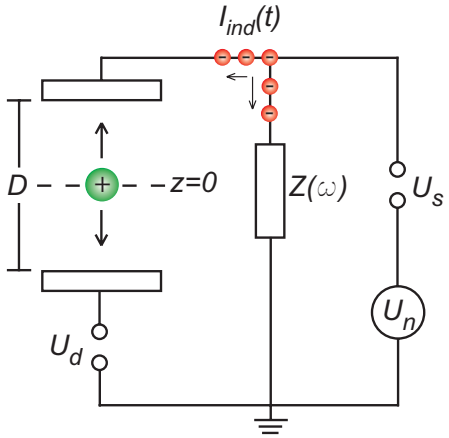

Figure 2.6: A particle oscillating between the two plates of a capacitor can be non-destructively detected with an impedance connecting the two plates.

The axial motion is monitored by amplifying and measuring $U_{\mathrm{s}}(t)$, which is composed of $U_{\mathrm{ind}}(t)$ and a noise voltage $U_{\mathrm{n}}(t)$. As long as the particle is not in thermal equilibrium

with the tank circuit, it is most likely needed to drive the oscillation with an external drive potential $U_\mathrm{d}(t)$ to be able to detect it above the noise which has to be included in the equation of motion. At the same time, the impedance exponentially damps the particle motion with a damping or resistive cooling time constant $\tau_\mathrm{z} = 1/\gamma_\mathrm{z}$:

$$\tau_\mathrm{z} = \frac{m}{q^2}\,\frac{D^2}{|Z(\omega)|}\,. \tag{2.26}$$

It is the characteristic time period for accomplishing a frequency measurement depending on particle, trap, and circuit properties. Furthermore, the resistive cooling time constant is the time constant with which the energy $E(t)$ of the particles decreases with time t as:

$$E(t) = E_0 \cdot e^{-\tau_\mathrm{z}\, t} \tag{2.27}$$

with E_0 being the initial energy of the particles. The equation of motion of the coupled system is consequently given by:

$$\begin{aligned} m\left(\frac{d^2}{dt^2} + \gamma_\mathrm{z}\frac{d}{dt} + \omega_\mathrm{z}^2\right) z(t) &= F(t) \\ \ddot{z}(t) + \frac{q^2}{m}\frac{|Z(\omega)|}{D^2}\,\dot{z}(t) + \frac{q\,U_0\,C_2}{m\,D^2} z(t) &= \frac{q}{m\,D}\left(U_\mathrm{d}(t) - U_\mathrm{n}(t)\right). \end{aligned} \tag{2.28}$$

A detailed discussion of the equation of motion and its solutions can be found in [35,49]. To increase the particle signal, it is convenient to increase the impedance by using an inductance in parallel to the trap. The resulting tank circuit yields a high parallel resistance in resonance R_p and compensates the capacitive reactance of the trap which is a major condition for the bolometric scheme. The considerations can be adequately undertaken for the detection of the cyclotron and magnetron motion.

2.3.1 Resonance Circuit

In a tank circuit, the impedance Z, which is a measure for the signal strength, consists of an inductance L and a capacity C as given in fig. 2.7. The losses within the components are denoted by R_L and R_C leading to an impedance of:

$$\begin{aligned} \frac{1}{Z} &= \frac{1}{i\omega L + R_\mathrm{L}} + \frac{1}{R_\mathrm{C}} + i\omega C \\ &\approx \frac{1}{R_\mathrm{C}} + \frac{R_\mathrm{L}}{\omega^2 L^2} + i\left(\omega C - \frac{1}{\omega L}\right), \end{aligned} \tag{2.29}$$

where the approximation is justified since under realistic conditions $R_\mathrm{L}/\omega^2 L^2 \ll 1$ holds.

The quality factor Q of a circuit is defined as

$$Q = \frac{1}{\tan\varphi}\,, \tag{2.30}$$

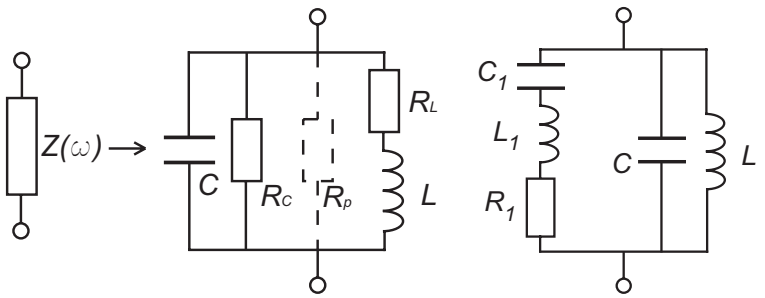

Figure 2.7: Tank circuit (left) and equivalent tank circuit (right) for the detection of the particle with inductance L, capacity C and ohmic resistor R. The parallel resistance in resonance is denoted by R_p.

where φ is the loss angle of the circuit defined as the ratio of effective resistance to reactance, see e. g. [50] for details. In resonance $\omega = \omega_\mathrm{LC} = 1/\sqrt{LC}$ with maximum impedance, the quality factor can be rewritten as

$$Q = \frac{R_\mathrm{p}}{\omega_\mathrm{LC} L} \tag{2.31}$$

$$= R_\mathrm{p}\,\omega_\mathrm{LC}\,C \tag{2.32}$$

with R_p being the parallel resistance in resonance. Since the induced voltage is given according to eq. (2.25), the absolute value of the impedance has to be calculated exploiting $|1/Z| = 1/|Z|$:

$$|Z(\omega)| = \frac{\omega/C}{\sqrt{(\omega^2 - \omega_\mathrm{LC}^2)^2 + \frac{\omega_\mathrm{LC}^2\,\omega^2}{Q^2}}}\,.$$

Plugging eq. (2.30) into the above equation leads to an experimentally useful relation for the quality factor:

$$Q = \frac{\omega_\mathrm{LC}}{\Delta\omega}\,, \tag{2.33}$$

where $\Delta\omega$ is the full-width-at-half-maximum. The expression for the impedance from eq. (2.33) makes it clear that for a given resonance frequency the capacity C should be small whereas the inductance L should be large. Moreover, the resonance becomes narrower the higher the quality factor Q.

2.3.2 Detection of an Excited or Cold Particle

With the detection system described above, the particle is always coupled to the tank circuit. Once the particle is excited at $\omega_\mathrm{LC} = \omega_\mathrm{z}$, the power P is dissipated in the resonance resistance R_LC according to $P = I_\mathrm{ind}^2 \cdot R_\mathrm{LC}$ and hence the particle is cooled yielding an exponential decay of the particle energy $E(t)$ according to eq. (2.27). During this time, the particle signal can be detected as a peak in the noise spectrum of the tank circuit as can be seen schematically in fig. 2.8. This method is used to quickly locate and detect the particle.

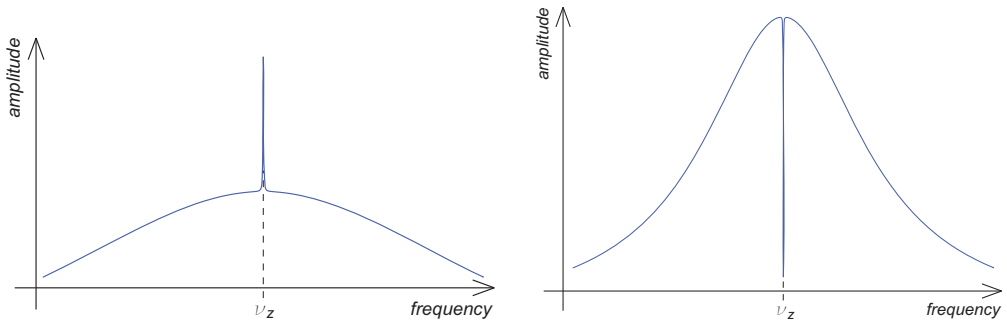

Figure 2.8: Spectra of an excited (left) and cold (right) particle within the noise spectrum of the detection circuit. Both curves are calculated with typical parameters for the planned experiment but drawn not to scale.

As the particle reaches thermal equilibrium with the tank circuit, it is more conveniently described via an equivalent circuit diagram. According to Wineland [49], eq. (2.28) can be expressed in terms of a series circuit (see fig. 2.7):

$$L_1 \frac{dI}{dt} + \frac{1}{C_1} \int dt I + R_1 I = 0 \,. \tag{2.34}$$

Thus, the harmonically bound particle can be described by an equivalent series circuit with the particle parameters $L_1 = mD^2/q^2$, $C_1 = q^2/m\omega_z^2 D^2$, and $R_1 = Z(\omega)$. On resonance, the particle shunts the detection system producing a minimum in the noise spectrum of the tank circuit as sketched in fig. 2.8, the so-called particle dip. Since the inductance of the particle is large compared to that of the detection unit $L_1 \approx 10^6\,\mathrm{H}$, it produces a very narrow dip with a line width

$$\Delta\nu = \frac{1}{2\pi\,\tau} \tag{2.35}$$

used for the high-precision measurement.

2.4 Sideband Cooling

The eigenfrequencies within the trap can be coupled in different ways when irradiating the sum or difference frequency. If, on the one hand, one motion is easily accessible for cooling with a resonance circuit at 4 K, it can be cooled until a thermal equilibrium is reached. If, on the other hand, a second motion is inept for this way of cooling, it can be coupled to the easily cooled eigenmode and cooled via energy transfer into this mode.

Since the magnetron motion is an unbound but metastable eigenmode with a large damping constant, it is crucial that an external mechanism be employed for cooling this mode. The method of motional sideband cooling was first introduced in a Penning trap by Wineland [51]. In this context "cooling" is used for reducing the motional amplitude and not necessarily for reducing the energy. To move the particle to the top of the radial

potential hill a quadrupole excitation at frequency $\omega_z + \omega_-$ is used enabling the cooling to the limit of [35]

$$T_- = \frac{\omega_-}{\omega_z} T_z \tag{2.36}$$

with $T_{z/-}$ being the temperature of the axial and magnetron motion, respectively.

2.5 Penning Trap Quantum Jump Spectrometer

The g-factor of a single particle as defined by eq. (1.6) results from a precise measurement of the particle's cyclotron and Larmor frequencies. As mentioned before, a magnetic bottle field is exploited to imprint the spin state information, which is an internal degree of freedom, onto the axial eigenmotion of the particle in the Penning trap. The observation of spatial quantization of the quantum-mechanical angular momentum was achieved by Stern and Gerlach [52]. The technique used in their experiment experienced a great development by Dehmelt who introduced the continuous Stern-Gerlach effect [26]. As in the classic Stern-Gerlach effect, changes in the spin state are detected via changes in the classical particle trajectories. However, what is observed is a change of the eigenfrequency of the particle in the potential well of the Penning trap.

In the homogeneous magnetic field $\vec{B} = B_0\hat{z}$ of the Penning trap, the energy eigenstates of a particle are Zeeman-split. For a magnetic field in the axial direction, this energy shift is given for a proton in dependence of the spin state as:

$$\begin{aligned} \Delta E &= -\vec{\mu} \cdot \vec{B} && (2.37) \\ &= -\frac{g\,\mu_N}{\hbar} B_0\, \vec{s} \cdot \hat{z} \\ &= g\frac{e\, m_s\, \hbar}{2\, m_p} B_0\,, && (2.38) \end{aligned}$$

where μ_N is the nuclear magnetic moment and m_p the proton mass. The energy gap $E = \hbar\omega_L$ between spin-up and spin-down state is given by the Larmor precession frequency ω_L:

$$\omega_L = g\frac{e}{2m_p} B_0\,. \tag{2.39}$$

The coupling between the internal and external degree of freedom is realized by the magnetic bottle field added to the homogeneous part B_0 resulting in an effective magnetic field of

$$\vec{B} = B_0 \cdot \hat{z} + B_2 \left(\frac{z^2 - r^2}{2} - z \cdot \vec{r} \right)\,. \tag{2.40}$$

In the presence of a quadratic magnetic field inhomogeneity B_2 symmetric around the z-axis the particle experiences the corresponding force F depending on the position z of the particle:

$$\begin{aligned} \vec{F} &= -\nabla(\vec{\mu} \cdot \vec{B}) \quad \text{and} && (2.41) \\ F_z &= -\mu_z\, B_2\, z\,. \end{aligned}$$

There are no odd terms present in eq. (2.40) because of the periodic motion of the trapped particle inside the Penning trap, and thus the cancellation of the linear contribution. The potential seen by the particle depends on its spin state as seen in fig. 2.9 since the magnetic moment is coupled to the axial eigenmotion shifting this frequency according to the spin direction. The potential shift has been calculated for a proton at 4 K with a motional amplitude of 40 μm. At a resulting trapping potential of a few hundred μV, the spin-up state sees a 0.1 neV shallower potential (blue curve), the spin-down state see a 0.1 neV steeper potential (red curve) as compared to the unperturbed potential (black curve).

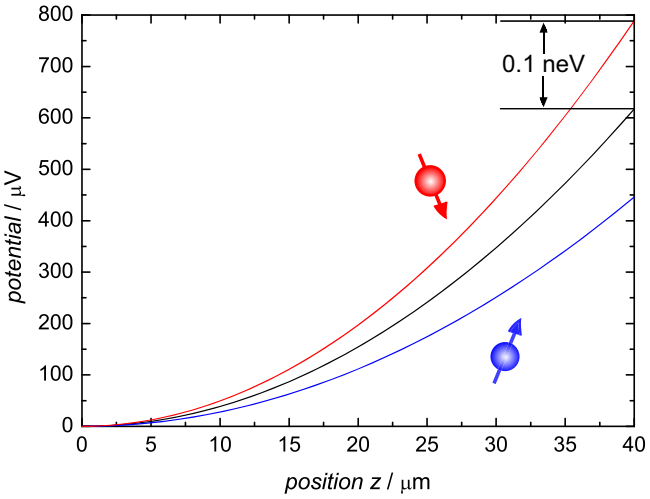

Figure 2.9: Potential in an inhomogeneous magnetic field calculated for the different spin states of a proton at 4 K and typical parameters of this experiment. The shift relative to the unperturbed potential (black curve) is greatly magnified.

An induced transition between spin up and spin down at the Larmor precession frequency can be detected by the observation of the corresponding frequency shift in the axial frequency $\Delta\omega_z$. This detection of a frequency shift is the direct observation of a quantum jump. The value of the frequency shift scales with the magnetic moment of the particle and the strength of the magnetic bottle:

$$\Delta\omega_z = \frac{\mu_z B_2}{m_p \omega_z} . \tag{2.42}$$

Inducing spin transitions for different radio-frequqency values ω_{rf} close to the theoretically calculated Larmor frequency ω_L results in a probability distribution, i. e. a resonance spectrum, yielding the actual Larmor frequency of the particle in the trap. In this way, a Penning trap quantum jump spectrometer is realized.

The inhomogeneous magnetic field interferes with the high-precision determination of the eigenfrequencies in the trap. To avoid this, a double Penning trap is used to separate frequency measurement and spin-state analysis [29]. Spin transitions are induced in the precision Penning trap, where the measurement of the eigenfrequencies is also

performed. Afterwards, the particle is transported into the analysis Penning trap with the inhomogeneous magnetic field region. To analyze whether a spin-flip has occurred in the precision trap, the corresponding frequency shift $\Delta\omega_z$ in the axial eigenmotion is now determined in the analysis trap. Since the transport is subject to fluctuations and heating, it is necessary to verify that the detected signal results from a spin-flip and is not caused by noise. Therefore, yet another spin-flip transition is induced to be able to differentiate between a spin-flip and a fake signal. The magnetic inhomogeneity, however, hinders driving the transition enforcing a detailed study of transition rates in the magnetic bottle field.

2.5.1 Transition Rates

In order to achieve a transition between the two spin states, an alternating magnetic field in the radio-frequency (rf) range $\vec{B}_1(t) = \hat{B}_1(\hat{x}\cos\omega_{\mathrm{rf}}t + \hat{y}\sin\omega_{\mathrm{rf}}t)$ has to be irradiated orthogonal to $\vec{B}_0$, where the frequency of $\vec{B}_1(t)$ has to match ω_{L}. Here, a purely co-rotating field is considered since the counter-rotating component is non-resonant and makes a negligible contribution [53]. The spin of the particle $1/2\hbar\vec{\sigma}$ is then governed by the homogeneous field $\vec{B}_0$ in the z-direction and the oscillating field $\vec{B}_1(t)$ in the xy-plane. In a quantum mechanical description, the Hamiltonian of the spin movement can be written as:

$$H = -g\frac{e\hbar}{2\,mc}\,\frac{1}{2}\,\vec{\sigma}\left(\vec{B}_0 + \vec{B}_1(t)\right)\,. \tag{2.43}$$

The Hamiltonian can be decomposed into the homogeneous part and the part caused by $\vec{B}_1(t)$: $H = H_0 + H_1$, where

$$H_0 = \hbar\omega_{\mathrm{rf}}\,\frac{1}{2}\,\sigma_{\mathrm{z}} \tag{2.44}$$

and

$$H_1 = \frac{1}{2}\hbar(\omega_{\mathrm{L}} - \omega_{\mathrm{rf}})\,\frac{1}{2}\,\sigma_{\mathrm{z}} + \frac{1}{2}\hbar\,\Omega\,(\sigma_{\mathrm{x}}\cos\omega_{\mathrm{rf}}t + \sigma_{\mathrm{y}}\sin\omega_{\mathrm{rf}}t)\,. \tag{2.45}$$

The Rabi frequency Ω is given by

$$\Omega = g\frac{e\hat{B}_1}{2\,mc}\,. \tag{2.46}$$

Further treatment of this problem is performed with the rotating wave approximation in the interaction picture. Moreover, small perturbations spreading the spin precession frequency over a range $\delta\omega_{\mathrm{L}}$ have to be considered for this kind of experiments since the relation holds that $\delta\omega_{\mathrm{L}} \gg \Omega$. To this end, the Rabi frequency has to be convolved with the inhomogeneities which has been done in [35] yielding for the transition probability P:

$$P = \frac{1}{2}\,\left[1 - \exp\left(-\pi\,\Omega^2\,(t_2 - t_1)\,\chi(\omega_{\mathrm{rf}})\right)\right]\,, \tag{2.47}$$

where $\chi(\omega_{\mathrm{rf}})$ denotes the line profile depending on the axial motion. The time during which the drive field is applied is given by $\delta = (t_2 - t_1)$.

The harmonic axial motion is coupled to an external circuit and thus kept in thermal equilibrium at temperature T. Fluctuations in the axial motion can be deduced from the equipartition of energy as

$$\frac{1}{2} m \omega_z^2 \langle z^2 \rangle = \frac{1}{2} k_B T \,, \tag{2.48}$$

with k_B being the Boltzmann constant. In addition, fluctuations arising from the magnetic bottle field are given by the line width parameter (ibid.)

$$\Delta(T) = \omega_L \frac{B_2}{B_0} \langle z^2(T) \rangle \,. \tag{2.49}$$

Since the thermal reservoir drives the oscillator with a force that is uniformly distributed in frequency ("white noise"), it is sufficient to consider two parameters: the axial damping constant γ_z cf. eq. (2.26) and the temperature T or equivalently the line width parameter $\Delta(T)$. The line profile $\chi(\omega)$ can be greatly simplified in the two limits $\gamma_z \ll \Delta(T)$ and $\gamma_z \gg \Delta(T)$. Since the weak coupling case applies for the analysis trap in which the magnetic bottle field is present, it will be treated in the following.

2.5.2 Numerical Example for the Case of Weak Coupling

Two typical trap parameters introduced above determine the damping constant γ_z and the line width parameter $\Delta(T)$: the effective electrode distance D and the magnetic inhomogeneity B_2, respectively. Assuming that the experiment is performed in a temperature range from 4 K to 30 K, a lower limit for $\Delta(T)$ can be delivered with the known inhomogeneity of the analysis trap of $B_2 = 4 \cdot 10^5\,\mathrm{T/m^2}$. For the evaluation of γ_z, the effective electrode distance D has to be calculated for the pick-up configuration used in the proton experiment. Since the axial signal will be detected using one correction electrode only, D has to be computed for the 01000-coupling yielding $D = 6.61\,\mathrm{mm}$. Moreover, the resonance resistance $R_{LC} = 2\pi\,\nu\,L\,Q = 25.71\,\mathrm{M\Omega}$ is needed resulting from the values for the axial detection system at the time of this measurement: $Q = 4000$, $L = 1.5\,\mathrm{mH}$, and $\nu = 682\,\mathrm{kHz}$. Finally, the lower limit amounts to

$$\frac{\gamma_z}{\Delta(T)} < 4.7 \cdot 10^{-5} \quad \text{at} \quad 4\,\mathrm{K} \le T \le 30\,\mathrm{K} \,, \tag{2.50}$$

corresponding to the case of weak coupling, thereby coupling the axial motion $z(t)$ loosely to the thermal reservoir. The line profile is given by (ibid.)

$$\chi(\omega) = \frac{\theta(\omega_{rf} - \omega_L)}{\Delta(T)} \exp\left(-\frac{\omega_{rf} - \omega_L}{\Delta(T)} \right) , \tag{2.51}$$

with $\theta(x)$ denoting the step function: $\theta(x) = 0$ for $x < 0$ and $\theta(x) = 1$ for $x > 0$.

A radial magnetic field strength of $\hat{B}_1 = 1.43\,\mu\mathrm{T}$ leads to a Rabi frequency of $\Omega = 382.56\,\mathrm{Hz}$ yielding a spin-flip rate of $60.89\,\mathrm{SF/s}$ (for further discussion see section 4.6). The transition probability P can thus be computed as a function of δ, which

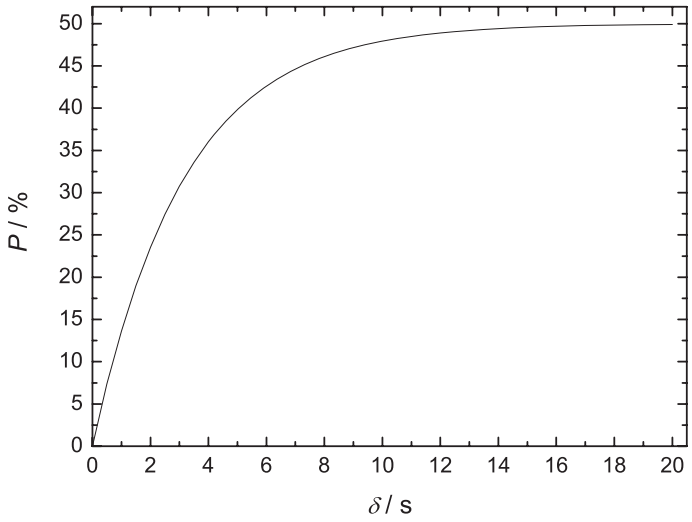

Figure 2.10: Spin-flip probability P in the analysis trap in the case of weak coupling as a function of δ, the time during which the drive field is applied. No Rabi oscillations are expected due to inhomogeneities leading to damping.

is shown in fig. 2.10 for $T = 30\,\mathrm{K}$. For $\delta = 5\,\mathrm{s}$ a transition probability of $P \approx 0.4$ is obtained which increases for $T = 4\,\mathrm{K}$ to $P \approx 0.5$. Reducing the driving time to $\delta = 500\,\mathrm{ms}$ yields $P \approx 0.35$ at $T = 4\,\mathrm{K}$. These numbers are much more favorable in the precision trap, since there the case of strong coupling holds.

3 The Toroidal Hybrid Penning Trap

The Larmor frequency, one of the two frequencies from which the g-factor is extracted, is determined by performing the continuous Stern-Gerlach effect in the magnetic bottle field of the analysis trap. This inhomogeneity has to be large enough to cause a detectable frequency shift for an unambiguous spin-state analysis. In the case of a single proton, conventional Penning traps (hyperbolic or cylindrical) are inapplicable since the frequency shift on a relative 10^{-7} scale is not efficiently detectable under experimental conditions. To this end, the *hybrid Penning trap* was introduced [28]: a combination of cylindrical electrodes and electrodes of non-cylindrical shape, e. g. toroidal or hyperbolic, as opposed to purely cylindrical traps consisting of cylindrical electrodes only. For this experiment, a hybrid trap was chosen with a toroidal ring and cylindrical correction electrodes and end caps: *the toroidal hybrid Penning trap*. As a result, the curved shape of the toroidal ferromagnetic ring enhances the curvature of the magnetic bottle hence enabling an efficient spin-state analysis.

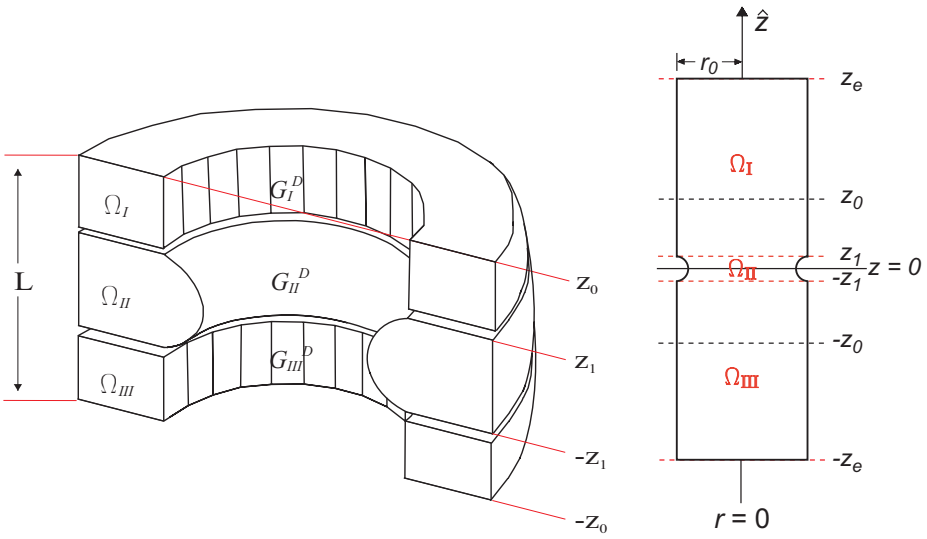

(a) 3D view of three-pole trap (b) 2D cut of five-pole trap

Figure 3.1: (a) Inner surface of a three-pole toroidal hybrid Penning trap. The trap is made out of axially symmetric electrodes, the ring being of toroidal shape. For simplicity, the upper and lower regions, Ω_{I} and Ω_{III}, are drawn to be cylindrical. (b) Extension to a five-pole toroidal hybrid trap. 2D cut through inner surface.

The electrostatic properties of the toroidal hybrid Penning trap can be calculated analytically with the "quasi"-Green's function method developed in [28]. The ansatz

features an extension of the Dirichlet problem to non-trivial geometries and leads to an analytical solution of the Laplace equation based on the Green's function approach. Optimization of the electrostatic properties such as anharmonicity compensation, orthogonality and optimum adjustment of frequency shifts is possible. The electrostatic potential $\Phi(\vec{x})$ has to be calculated within a closed volume defined by the trap electrodes to which arbitrary voltages are applied. This corresponds to solving the Laplace equation with Dirichlet boundary conditions for which the adequate Green's function has to be known. The toroidal hybrid trap outlined in fig. 3.1a does not exhibit a known analytical expression for the Green's function fulfilling Dirichlet boundary conditions on its entire surface as is the case with most hybrid traps. If, however, for each of its electrodes the corresponding Green's function is known, which does meet those conditions on the electrode's surface, then it is possible to construct a "quasi"-Green's function for the entire hybrid trap which delivers an analytical expression for $\Phi(\vec{x})$. In the following, the "quasi"-Green's function will be constructed for the trap sketched in fig. 3.1a with a rotationally invariant surface around the $\hat{z}$-axis. Generalization to the five-pole trap used in the actual experiment will become apparent.

3.1 Theoretical Concepts

In general, the electrostatic boundary-value problem is defined by the following integral equation [40]:

$$\begin{aligned} & \int_\Omega d^3x' \left[\Phi(\vec{x}\,')\nabla'^2 G(\vec{x} \mid \vec{x}\,') - G(\vec{x} \mid \vec{x}\,')\nabla'^2\Phi(\vec{x}\,')\right] \\ = & \oint_{\partial\Omega} dS' \left[\Phi(\vec{x}\,')\frac{\partial}{\partial n'} G(\vec{x} \mid \vec{x}\,') - G(\vec{x} \mid \vec{x}\,')\frac{\partial}{\partial n'}\Phi(\vec{x}\,')\right], \end{aligned} \tag{3.1}$$

where Ω is the trapping volume under consideration, $\partial\Omega$ the surface delimiting that volume, and $\Phi(\vec{x}\,')$ the electrostatic potential. $G(\vec{x} \mid \vec{x}\,')$ represents the Green's function for the Laplace equation. It is symmetric with respect to interchanging source coordinates, $\vec{x}\,'$, and field coordinates, $\vec{x}$: $G(\vec{x} \mid \vec{x}\,') = G(\vec{x}\,' \mid \vec{x})$. Further, it satisfies:

$$\begin{aligned} \nabla^2 G(\vec{x} \mid \vec{x}\,') &= \nabla'^2 G(\vec{x} \mid \vec{x}\,') = -4\pi\delta\left(\vec{x} - \vec{x}\,'\right) \\ G(\vec{x} \mid \vec{x}\,') &= \frac{1}{|\,\vec{x} - \vec{x}\,'|} + F(\vec{x} \mid \vec{x}\,')\,. \end{aligned} \tag{3.2}$$

$F(\vec{x}|\vec{x}\,')$ represents an arbitrary function satisfying

$$\nabla^2 F(\vec{x}|\vec{x}\,') = \nabla'^2 F(\vec{x}|\vec{x}\,') = 0 \,\forall\, \{\vec{x}, \vec{x}\,'\} \in \Omega\,.$$

In the case of Dirichlet boundary conditions, $F(\vec{x}\,|\vec{x}\,')$ is chosen such that the Green's function becomes equal to zero at the surface of the trap: $G^{\mathrm{D}}(\vec{x} \mid \vec{x}\,') = 0 \,\forall\, \vec{x}\,' \in \partial\Omega$. The function $F(\vec{x}|\vec{x}\,')$ is therefore a solution of the Laplace equation and represents the potential of a (mirror) charge distribution external to the volume Ω (ibid.). Assuming the absence of free charges within the region in which the potential is calculated,

$\nabla^2\Phi(\vec{x}\,') \propto \rho(\vec{x}\,') = 0 \,\forall\, \vec{x}\,' \in \Omega$, eq. (3.1) further simplifies to:

$$\int_\Omega d^3x' \left[\Phi(\vec{x}\,')\nabla'^2 G^{\mathrm{D}}(\vec{x} \mid \vec{x}\,')\right] = \oint_{\partial\Omega} dS' \left[\Phi(\vec{x}\,')\frac{\partial}{\partial n'} G^{\mathrm{D}}(\vec{x} \mid \vec{x}\,')\right]. \tag{3.3}$$

The validity of eq. (3.3) is not restricted to pure Green's functions satisfying eq. (3.2), but it applies whenever the volume Ω is free of charges, and for any function being equal to zero at its surface, $G^{\mathrm{D}}(\vec{x}|\vec{x}\,') = 0 \,\forall\, \vec{x}\,' \in \partial\Omega$. However, if the proper Green's function satisfying Dirichlet boundary conditions is known, eq. (3.3) simplifies to the conventional expression exploiting eq. (3.2):

$$\Phi(\vec{x}) = -\frac{1}{4\pi}\oint_{\partial\Omega} dS' \cdot \Phi(\vec{x}\,')\partial\, G^{\mathrm{D}}(\vec{x}|\vec{x}\,')\partial n' \,.$$

The boundary conditions, $\Phi(\vec{x}\,')$, are provided by voltages applied to the trap electrodes. Thus, the explicit knowledge of $G^{\mathrm{D}}(\vec{x}|\vec{x}\,')$ formally solves the potential problem, reducing it to a simple integral.

For the hybrid trap of fig. 3.1a, we introduce a "quasi"-Green's function, $\tilde{G}^{\mathrm{D}}(\vec{x}\,|\,\vec{x}\,')$, defined as:

$$\tilde{G}^{\mathrm{D}}(\vec{x} \mid \vec{x}\,') = \begin{cases} G^{\mathrm{D}}_{\mathrm{I}}(\vec{x} \mid \vec{x}\,') & \vec{x} \in \Omega \quad ; \quad \vec{x}\,' \in \Omega_{\mathrm{I}} \\ G^{\mathrm{D}}_{\mathrm{II}}(\vec{x} \mid \vec{x}\,') & \vec{x} \in \Omega \quad ; \quad \vec{x}\,' \in \Omega_{\mathrm{II}} \\ G^{\mathrm{D}}_{\mathrm{III}}(\vec{x} \mid \vec{x}\,') & \vec{x} \in \Omega \quad ; \quad \vec{x}\,' \in \Omega_{\mathrm{III}} \end{cases} \tag{3.4}$$

Each volume Ω_i denotes one of the i-regions into which the trapping volume of fig. 3.1a is divided. This partition of space is basically arbitrary but must fulfill the condition, that inside each Ω_i the Green's function satisfying Dirichlet boundary conditions on the physical part of that Ω_i-region (i. e. the metallic electrode) must be known. Thus, a set of functions $G^{\mathrm{D}}_i(\vec{x}|\vec{x}\,')$ must be provided satisfying

$$\nabla^2 G^{\mathrm{D}}_i(\vec{x}|\vec{x}\,') = \nabla'^{\,2} G^{\mathrm{D}}_i(\vec{x}|\vec{x}\,') = 4\pi\delta(\vec{x} - \vec{x}\,')$$

and $G^{\mathrm{D}}_i(\vec{x}\,|\,\vec{x}\,') = 0$ on the corresponding part of the trap's surface. In the example of fig. 3.1a, the partition is chosen such that there are three Ω_i-regions delimited by the "contact" planes $z' = \pm z_1$.

For the "quasi"-Green's function introduced the interchange symmetry of the arguments is broken: $\tilde{G}^{\mathrm{D}}(\vec{x}\,|\,\vec{x}\,') \neq \tilde{G}^{\mathrm{D}}(\vec{x}\,'\,|\,\vec{x})$; within this derivation the focus lies on the properties of $\tilde{G}^{\mathrm{D}}$ with respect to the source $\vec{x}\,'$. Furthermore, since the constituting functions $G^{\mathrm{D}}_i(\vec{x}\,|\,\vec{x}\,')$ are chosen such that each separately satisfies Dirichlet boundary conditions for the corresponding electrode, the "quasi"-Green's function satisfies Dirichlet boundary conditions on the entire surface of the trap: $\tilde{G}^{\mathrm{D}}(\vec{x}|\vec{x}\,') = 0 \,\forall\, \vec{x}\,' \in \partial\Omega$. As a consequence, eq. (3.3) still holds and is used to calculate the potential $\Phi(\vec{x})$.

3.1.1 Solution with the "Quasi"-Green's Function

In order to obtain $\Phi(\vec{x})$ from eq. (3.3), the Laplacian of the "quasi"-Green's function with respect to the source coordinates has to be evaluated. For source points within the

trap not lying on any of the contact planes separating the Ω_i-regions, this immediately yields: $\nabla'^2\tilde{G}^{\mathrm{D}}(\vec{x} \mid \vec{x}\,') = -4\pi\delta(\vec{x}-\vec{x}\,')\,\forall\, V x' = \{x', y', z' \neq \pm z_1\}$ due to the definition of the "quasi"-Green's function. Note that $\tilde{G}^{\mathrm{D}}(\vec{x}\,|\vec{x}\,')$ has a finite-step discontinuity at the planes separating the Ω_i-regions, $\vec{x}\,' = \{x', y', z' = \pm z_1\}$, which has to be taken into account when calculating the Laplacian $\nabla'^2\tilde{G}^{\mathrm{D}}(\vec{x} \mid \vec{x}\,')$. Since ∇'^2 represents a derivative operator and since the derivative of the Heaviside step-function results in the Dirac-delta, we assume the following ansatz for $\nabla'^2\tilde{G}^{\mathrm{D}}(\vec{x}|\vec{x}\,')$:

$$\nabla'^2\tilde{G}^{\mathrm{D}}(\vec{x} \mid \vec{x}\,') = -4\pi\delta(\vec{x}-\vec{x}\,') + \delta(z'-z_1)f_+(\vec{x} \mid \vec{x}\,') + \delta(z'+z_1)f_-(\vec{x} \mid \vec{x}\,')\,. \tag{3.5}$$

With this ansatz, the Laplacian of the "quasi"-Green's function for points not lying on the contact planes, $z' \neq \pm z_1$, is trivially recovered whereas the functions $f_\pm(\vec{x} \mid \vec{x}\,')$ have to be determined. It is obvious from eq. (3.5), that it suffices to evaluate $f_\pm$ for points

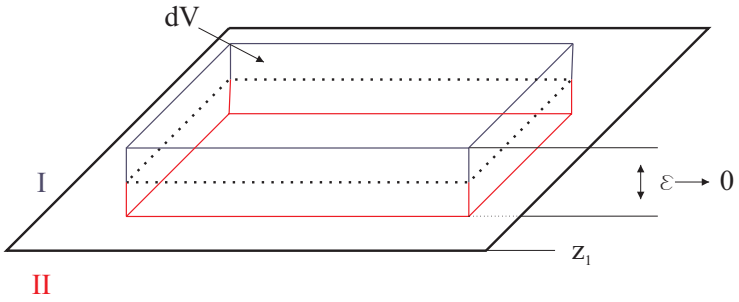

Figure 3.2: Illustration of the Gaussian box enclosing the point $\vec{x}\,' = \{r', \varphi', z' = +z_1\}$ which lies on the contact plane separating the regions Ω_{I} and Ω_{II}. $\tilde{G}^{\mathrm{D}}$ has a finite step discontinuity at any point on that contact plane.

lying on the contact planes: $\vec{x}\,' = \{r', \varphi', z' = \pm z_1\}$ for $f_\pm$ in cylindrical coordinates. On the one hand, consider an infinitesimal volume dV enclosing the point of interest $\{r', \varphi', z' = z_1\}$ as shown in fig. 3.2. The divergence theorem applied to $\tilde{G}^{\mathrm{D}}(\vec{x}|\vec{x}\,')$ at dV leads to:

$$\int_{dV} d^3x' \cdot \nabla'^2\tilde{G}^{\mathrm{D}}(\vec{x} \mid \vec{x}\,') = \oint_S d\vec{S}\,' \cdot \nabla'\tilde{G}^{\mathrm{D}}(\vec{x} \mid \vec{x}\,')\,. \tag{3.6}$$

In the limit $\varepsilon \to 0$, the lateral surface of the Gaussian box does not contribute to the surface integral in eq. (3.6), thus $\oint_S d\vec{S}\,' \cdot \nabla'\tilde{G}^{\mathrm{D}}(\vec{x}|\vec{x}\,') = \oint_{S_\perp} dS'_{\mathrm{z}}\, \frac{\partial}{\partial z'}\, \tilde{G}^{\mathrm{D}}(\vec{x}|\vec{x}\,')$. The top and bottom surfaces of the Gaussian box of fig. 3.2 are denoted by $S_\perp$; only these contribute to the surface integral. The integral on the top surface is performed while $z' = z_1 + \varepsilon \Rightarrow z' \in \Omega_{\mathrm{I}}$ and $\tilde{G}^{\mathrm{D}}(\vec{x} \mid \vec{x}\,') = G^{\mathrm{D}}_{\mathrm{I}}(\vec{x} \mid \vec{x}\,')$. For the bottom plane applies $z' = z_1 - \varepsilon$ and $\tilde{G}^{\mathrm{D}}(\vec{x}|\vec{x}\,') = G^{\mathrm{D}}_{\mathrm{II}}(\vec{x}|\vec{x}\,')$. Further, $dS_{z'}$ has the opposite orientation in the latter case as compared to the former, hence leading to:

$$\oint_S d\vec{S}\,' \cdot \nabla'\tilde{G}^{\mathrm{D}}(\vec{x} \mid \vec{x}\,') = \lim_{\varepsilon\to 0} \oint_{S_\perp} dS'_{\mathrm{z}}\, \frac{\partial}{\partial z'} \left[G^{\mathrm{D}}_{\mathrm{I}}(\vec{x} \mid r', \varphi', z_1+\varepsilon) - G^{\mathrm{D}}_{\mathrm{II}}(\vec{x} \mid r', \varphi', z_1-\varepsilon)\right]. \tag{3.7}$$

On the other hand, with the ansatz of eq. (3.5) and assuming that $\vec{x} \neq \vec{x}\,'$ (i. e. $\vec{x}$ is outside of dV), the volume integral in eq. (3.6) yields:

$$\int_{dV} d^3x' \cdot \nabla'^2 \tilde{G}^{\mathrm{D}}(\vec{x} \mid \vec{x}\,') = \int_{dV} dz' \cdot \, dS'_{\mathrm{z}} \, \delta(z - z_1) f_+(\vec{x} \mid r', \varphi', z') = \int_{S_\perp} dS'_{\mathrm{z}} \, f_+(\vec{x} \mid r', \varphi', z_1). \tag{3.8}$$

The explicit form of f_+ can now be derived by comparison of eq. (3.7) and eq. (3.8). Taking into account that $G_i^{\mathrm{D}}(\vec{x}|\vec{x}\,') = (1/|\vec{x} - \vec{x}\,'|) + F_i^{\mathrm{D}}(\vec{x}|\vec{x}\,')$ while taking the limit $\varepsilon \to 0$ in eq. (3.7), results in:

$$f_+(\vec{x} \mid r', \varphi', z_1) = \frac{\partial}{\partial z'} \left[F_{\mathrm{I}}^{\mathrm{D}}(\vec{x} \mid r', \varphi', z_1) - F_{\mathrm{II}}^{\mathrm{D}}(\vec{x} \mid r', \varphi', z_1) \right]. \tag{3.9}$$

The same considerations carried out for the contact plane between regions Ω_{II} and Ω_{III} deliver the function f_-:

$$f_-(\vec{x} \mid r', \varphi', -z_1) = \frac{\partial}{\partial z'} \left[F_{\mathrm{II}}^{\mathrm{D}}(\vec{x} \mid r', \varphi', -z_1) - F_{\mathrm{III}}^{\mathrm{D}}(\vec{x} \mid r', \varphi', -z_1) \right]. \tag{3.10}$$

Finally, computing the integral of eq. (3.3) and resolving for $\Phi(\vec{x})$ leads to the electrostatic potential inside the trap:

$$\begin{aligned} \Phi(\vec{x}) = & -\frac{1}{4\pi} \oint_{\partial\Omega} dS' \, \Phi(\vec{x}\,') \frac{\partial}{\partial n'} \tilde{G}^{\mathrm{D}}(\vec{x} \mid \vec{x}\,') \\ & + \frac{1}{2} \int_0^{r_0} dr' r' \, \Phi(r', z_1) \frac{\partial}{\partial z'} \left[F_{\mathrm{I}}^{\mathrm{D}}(\vec{x} \mid r', z_1) - F_{\mathrm{II}}^{\mathrm{D}}(\vec{x} \mid r', z_1) \right] \\ & + \frac{1}{2} \int_0^{r_0} dr' r' \, \Phi(r', -z_1) \frac{\partial}{\partial z'} \left[F_{\mathrm{II}}^{\mathrm{D}}(\vec{x} \mid r', -z_1) - F_{\mathrm{III}}^{\mathrm{D}}(\vec{x} \mid r', -z_1) \right]. \end{aligned} \tag{3.11}$$

In the above equation, r_0 represents the inner radius of the contact surface delimiting the different Ω_i-regions (see also fig. 3.1b). Note that the integral over φ' has been assumed to deliver the value 2π in the last two summands of eq. (3.11). This assumption is valid since the electrostatic potential is axially symmetric. In the usual case of the trap having point symmetry with respect to its central plane $z = 0$, the function f_- becomes identical to f_+ except for the negative sign. The opposite sign results from the opposite direction of the surface vector $d\vec{S}'$ when calculating the integral on the right side of eq. (3.6). Taking this symmetry into account, the calculation of the electrostatic potential simplifies to:

$$\begin{aligned} \Phi(\vec{x}) = & - \frac{1}{4\pi} \oint_{\partial\Omega} dS' \, \Phi(\vec{x}\,') \cdot \frac{\partial}{\partial n'} \tilde{G}^{\mathrm{D}}(\vec{x} \mid \vec{x}\,') \\ & + \int_0^{r_0} r' dr' \, \Phi(r', z_1) \cdot \frac{\partial}{\partial z'} \left[F_{\mathrm{I}}^{\mathrm{D}}(\vec{x} \mid r', z_1) - F_{\mathrm{II}}^{\mathrm{D}}(\vec{x} \mid r', z_1) \right]. \end{aligned} \tag{3.12}$$

Equation (3.12) constitutes an integral equation which will be solved for the toroidal hybrid trap in the following.

3.2 Application to the Toroidal Hybrid Trap

To calculate the electrostatic potential of the five-pole toroidal hybrid trap shown in fig. 3.1b, it is first mandatory to construct the appropriate "quasi"-Green's function. The basic Green's function solving the Laplace equation in cylindrical coordinates (see for example [40,54,55]) can be modified to yield the Green's function inside a cylindrical box satisfying Dirichlet boundary conditions:

$$G_{\mathrm{cyl}}(r,z \mid r',z') = \\ \frac{4}{L}\sum_{n=1,3..}^{\infty}\cos(\kappa_n z)\cos(\kappa_n z')\,\frac{I_0(\kappa_n r_<)}{I_0(\kappa_n r_0)}\Big[I_0(\kappa_n r_0)K_0(\kappa_n r_>) - I_0(\kappa_n r_>)K_0(\kappa_n r_0)\Big]. \quad (3.13)$$

Here, most parameters can be identified following the definitions from eq. (2.18) and fig. 2.3. The notation $r_{>(<)}$ means the bigger (smaller) of (r, r'). The symbols I_0 and K_0 represent the modified Bessel functions of zeroth order, first and second kind, respectively. Further, the electric potential is assumed to be point-symmetric with respect to the trap's center ($z = 0$), thus only $\cos(\kappa_n z)$-functions appear in the series. For eq. (3.13) to be strictly valid, the trap should be closed by a grounded disk on each side allowing for the basic Green's function in cylindrical coordinates to be simplified to a series with the summation index κ_n running over odd n as compared to an integral form with continuous summation index κ. Usually, the traps used in experiments are not closed by such grounded disks. This issue has been investigated mathematically in [43]: an end cap three times longer than the inner radius suffices for deviations below one per cent of the trap's electrical properties compared to those calculated with an infinitely long open end cap. In addition, experimental data [6,7] exhibit deviations as low as one part in a million from the theoretical predictions of eq. (3.13). There, the experiment was performed in a cylindrical trap with $l_{\mathrm{e}} \simeq 2r_0$. For the toroidal hybrid trap a similar or even better accuracy can be assumed due to the enhanced shielding of the trap's center from outside by the toroidal ring.

The basic Green's function in toroidal coordinates [54–57] is used to derive the Green's function satisfying Dirichlet boundary conditions on the surface of a torus with circular cross section:

$$G_{\mathrm{tor}}(u,v \mid u',v') = \frac{1}{a\,\pi}\sqrt{\cosh v - \cos u}\,\sqrt{\cosh v' - \cos u'}\cdot\sum_{m=0}^{\infty}\epsilon_m\,\cos(mu)\cos(mu') \\ \times\frac{P_{m-\frac{1}{2}}(\cos v_<)}{P_{m-\frac{1}{2}}(\cosh v_0)}\cdot\Big(P_{m-\frac{1}{2}}(\cosh v_0)\,Q_{m-\frac{1}{2}}(\cosh v_>) - P_{m-\frac{1}{2}}(\cosh v_>)\,Q_{m-\frac{1}{2}}(\cosh v_0)\Big)\,. \quad (3.14)$$

Again, axial symmetry is inferred, and the electric potential is assumed to be invariant across the equatorial plane of the torus, thus only $\cos(mu)$- but no $\sin(mu)$-functions appear. As before, the notation $v_{>(<)}$ means the bigger (smaller) of (v, v'). The Legendre

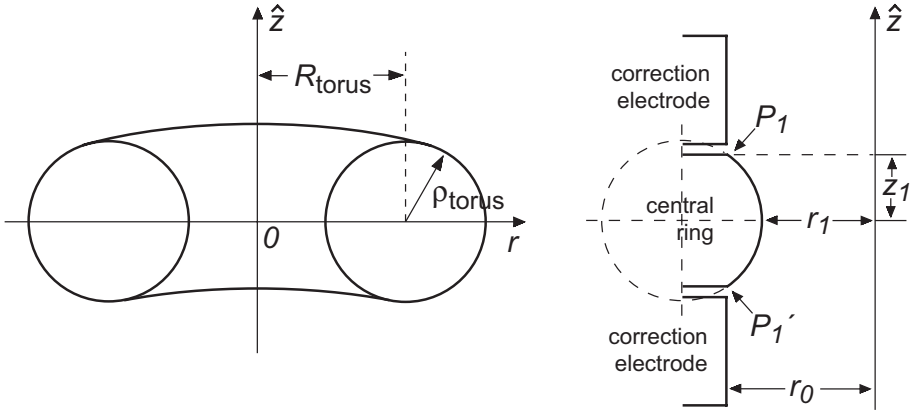

Figure 3.3: Parameters of the toroidal ring. The outer radius of the torus $R_{\rm tor}$ does not necessarily coincide with the inner radius of the cylindrical electrodes, r_0. This is reflected by the upper and lower cut-off planes of the torus at P_1 and P_1'.

functions of first and second kind are denoted by $P_{m-\frac{1}{2}}$ and $Q_{m-\frac{1}{2}}$, respectively. For the case discussed here with $m \in \mathbb{N}$, they are also known as *toroidal functions* (ibid.). The Neumann factor is given by $\epsilon_m = 2-\delta_{m,0}$. The toroidal coordinates $\{u, v, \varphi\}$ relate to the Cartesian coordinates via: $\{x, y, z\} = \frac{a}{\cosh v - \cos u}\{\cos\varphi \sinh v, \sin\varphi \sinh v, \sin u\}$ (ibid.). In this coordinate system, a toroidal ring is defined by $v = v_0$, with $v_0 = \text{constant} > 0$, $u \in [0, 2\pi]$ and $\varphi \in [0, 2\pi]$. For further calculation, the upper and lower points of the torus facing inside the trap are marked as P_1 and P_1', respectively (see fig. 3.3). In toroidal coordinates they are given by: $P_1 \equiv (u = \pi/2, v_0, \varphi)$ and $P_1' \equiv (u = 3\pi/2, v_0, \varphi)$. The choice of P_1 and P_1' is arbitrary, the choice made here has technical reasons: since the cut-off points are localized slightly below the ring's north and south pole, more of the correction electrodes is seen from the trap's center, and thus shielding due to the toroidal ring is reduced. An additional free parameter is the length of the ring seen from the inner side of the trap, $l_{\rm r} = 2 \cdot z_1$. Having specified z_1, P_1, P_1', and r_0, the toroidal ring is completely defined yielding the toroidal parameters: $a = \sqrt{r_0^2 + z_1^2}$ and $v_0 = \sinh^{-1}(r_0/z_1)$. With z_1 and r_0 chosen, the inner radius of the torus is given by $\rho_{tor} = \frac{z_1}{r_0}\sqrt{r_0^2 + z_1^2}$ and the distance from the $\hat{z}$-axis to the innermost point of the torus by $r_1 = \sqrt{r_0^2 + z_1^2}\,/\,(z_1 + \sqrt{r_0^2 + z_1^2})$.

3.2.1 Potential of the Toroidal Hybrid Trap

With the geometry of fig. 3.1b chosen, it is obvious that

$$G_{\rm I}^{\rm D}(\vec{x}|\vec{x}\,') = G_{\rm III}^{\rm D}(\vec{x}|\vec{x}\,') \equiv G_{\rm cyl}(\vec{x}|\vec{x}\,') \quad \text{and} \quad G_{\rm II}^{\rm D}(\vec{x}|\vec{x}\,') \equiv G_{\rm tor}(\vec{x}|\vec{x}\,')\,.$$

Using Abel's identity, the Wronskian of the Bessel functions of eq. (3.13) is evaluated to [56]: $I(x)\frac{dK(x)}{dx} - \frac{dI(x)}{dx}K(x) = \frac{1}{x}$ and similarly for the toroidal functions of eq. (3.14): $P(x)\frac{dQ(x)}{dx} - \frac{dP(x)}{dx}Q(x) = \frac{1}{x}$. With these Wronskian determinants, the derivative $\partial\tilde{G}^{\rm D}(\vec{x}, \vec{x}')/\partial n'$ on the trap's surface is greatly simplified. Using the boundary

conditions of fig. 3.1b, the electric potential $\Phi_0(\vec{x}) = \Phi_{\mathrm{cyl}}(\vec{x}) + \Phi_{\mathrm{tor}}(\vec{x})$ in zeroth-order is obtained:

$$\begin{aligned}
\Phi_{\mathrm{cyl}}(r,z) &= -\frac{1}{4\pi}\int_0^{2\pi} r_0\, d\varphi' \cdot 2\int_{z_1}^{L/2} dz'\, \Phi(r_0,z') \cdot \left.\frac{\partial\, G_{\mathrm{cyl}}(r,z \mid r',z')}{\partial\, r'}\right|_{r'=r_0} \\
&= \frac{2}{L}\sum_{n=1,3\cdots}^{\infty} \frac{1}{I_0(\kappa_n\, r_0)}\left[2\int_{z_1}^{\frac{L}{2}} dz'\, \Phi(r_0,z')\cos(\kappa_n\, z')\right] I_0(\kappa_n\, r)\cdot\cos(\kappa_n\, z) \\
\Phi_{\mathrm{tor}}(u,v) &= -\frac{1}{4\pi}\int_0^{2\pi} h_{\varphi'}\cdot d\varphi' \int_{\frac{\pi}{2}}^{\frac{3\pi}{2}} h_{u'}\cdot du'\, \Phi(v_0,u')\frac{1}{h_{v'}}\left.\frac{\partial\, G_{\mathrm{tor}}(u,v \mid u',v')}{\partial\, v'}\right|_{v'=v_0} \\
&= \frac{U_0}{2\pi}\sqrt{\cosh v - \cos u}\sum_{m=0,1\ldots}^{\infty} \epsilon_m \frac{\left[\int_{\pi/2}^{3\pi/2} du' \frac{\cos(mu')}{\sqrt{\cosh v_0 - \cos u'}}\right]}{P_{m-\frac{1}{2}}(\cosh v_0)} P_{m-\frac{1}{2}}(\cosh v)\cdot\cos(m\, u)\,.
\end{aligned} \tag{3.15}$$

The factor of 2 appearing in front of the integral $\int_{z_1}^{L/2} dz'$ arises from the symmetry of the trap around the $z = 0$-plane. Furthermore, it has been assumed that a constant voltage $U_0 \to \Phi(u', v_0) = U_0\, \forall\, u' \in [0, 2\pi]$ is applied to the ring. On the one hand, the scale factors of the toroidal coordinates, $h_{u'}$ and $h_{v'}$, are equal and cancel in the expression for calculating Φ_{tor} [57]. On the other hand, the scale factor $h_{\varphi'} = \frac{a\sinh v_0}{\cos u' - \cosh v_0}$ has to be included in the integral. Finally, the toroidal coordinates (u, v) can be transformed into the cylindrical ones (r, z) using the following transformation: $v = 2\,\mathrm{Re}\left[\coth^{-1}(\frac{r+i\,z}{a})\right]$ and $u = -2\,\mathrm{Im}\left[\coth^{-1}(\frac{r+i\,z}{a})\right]$ (ibid.). With the zeroth-order approximation $\Phi_0(r, z)$ it is now possible to solve the integral equation, cf. eq. (3.12):

$$\Phi(r,z) = \Phi_0(r,z) + \int_0^{r_0} dr'\, r'\, \Phi(r',z_1) \underbrace{\left[\frac{\partial F_{\mathrm{cyl}}(r,z \mid r',z_1)}{\partial z'} - \frac{\partial F_{\mathrm{tor}}(r,z \mid r',z_1)}{\partial z'}\right]}_{f_+(r,z|r',z_1)}\,. \tag{3.16}$$

The explicit form of the functions $F_{\mathrm{cyl}}(r, z \mid r', z')$ and $F_{\mathrm{tor}}(r, z \mid r', z')$ results from the corresponding Green's functions from eq. (3.13) and eq. (3.14), as defined in eq. (3.2):

$$\begin{aligned}
F_{\mathrm{cyl}}(r,z \mid r',z') &= -\frac{4}{L}\sum_{n=1,3..}^{\infty} \frac{K_0(\kappa_n r_0)}{I_0(\kappa_n r_0)}\cos(\kappa_n z)\cos(\kappa_n z')\, I_0(\kappa_n r) I_0(\kappa_n r') \\
F_{\mathrm{tor}}(u,v \mid u',v') &= -\frac{1}{a\,\pi}\sqrt{\cosh v - \cos u}\,\sqrt{\cosh v' - \cos u'}\cdot\sum_{m=0}^{\infty}\epsilon_m \frac{Q_{m-\frac{1}{2}}(\cosh v_0)}{P_{m-\frac{1}{2}}(\cosh v_0)}\cdot \\
&\qquad \cdot\cos(mu)\cos(mu')\cdot P_{m-\frac{1}{2}}(\cosh v)\, P_{m-\frac{1}{2}}(\cosh v')\,.
\end{aligned} \tag{3.17}$$

The structure of the integral equation (3.16) itself suggests already the solution: the zeroth-order approximation $\Phi_0(r, z)$ has to be substituted into the integral on the right

hand side of this equation to get the first-order correction:

$$\Delta\Phi_1(r,z) = \int_0^{r_0} dr'\, r'\, \Phi_0(r',z_1) f_+(r,z|r',z_1)\,,$$

which itself leads to the first-order approximation $\Phi_1(r,z) = \Phi_0(r,z) + \Delta\Phi_1(r,z)$. The solution of the integral equation is obtained by iteration: $\Phi(r,z) = \lim_{j\to\infty} \Phi_j(r,z)$, where $\Phi_j(r,z)$ denotes the jth-order approximation to the potential given by:

$$\Phi_j(r,z) = \Phi_0(r,z) + \underbrace{\int_0^{r_0} dr'\, r'\, \Phi_{j-1}(r',z_1)\, f_+(r,z \mid r',z_1)}_{\Delta\Phi_j(r,z)}\,. \tag{3.18}$$

The zeroth-order approximation of the potential $\Phi_0(r,z)$ as well as the propagator consist of linear combinations of the sets of functions $\{I_0(\kappa_n\, r)\cdot\cos(\kappa_n\, z)\}$ and $\{P_{m-\frac{1}{2}}(\cosh v)\cdot\cos(m\, u)\}$ as can be seen from eq. (3.15). These sets both form a basis of the linear space including the solutions of the Laplace equation in the appropriate coordinate systems. Hence, the corrections $\Delta\Phi_j(r,z)$ can be written as linear combinations of these sets, and the electric potential can be expanded with expansion coefficients A_n and B_m, respectively:

$$\begin{aligned}\Phi(r,z) = {} & U_0 \sum_{n=1,3\ldots}^{\infty} A_n\, I_0(\kappa_n\, r)\cdot\cos(\kappa_n\, z) \\ & + U_0\,\sqrt{\cosh v - \cos u} \sum_{m=0,1,2\ldots}^{\infty} B_m\, P_{m-\frac{1}{2}}(\cosh v)\cdot\cos(m\, u).\end{aligned} \tag{3.19}$$

These expansion coefficients are of the same nature as the one for the potential of the cylindrical trap defined earlier, cf. eq. (2.18). In order to obtain an explicit form of the potential $\Phi(r,z)$, the coefficients A_n and B_m have to be determined iteratively following the scheme presented above. Consequently, the expansion coefficients of the jth iteration of the potential $\Phi_j(r,z)$ are given by $A_n^{(j)}$ and $B_m^{(j)}$. Their value is related to the coefficients of the zeroth-order approximation through the correction terms $\Delta A_n^{(j)}$ and $\Delta B_m^{(j)}$ such that: $A_n^{(j)} = A_n^{(0)} + \Delta A_n^{(j)}$ and $B_m^{(j)} = B_m^{(0)} + \Delta B_m^{(j)}$. The zeroth-order approximation of the expansion coefficients can be taken from eq. (3.15), and the correction terms of the jth order are obtained by substituting $\Phi_{j-1}(r,z)$ in eq. (3.18). The correction terms $\Delta A_n^{(j)}, \Delta B_m^{(j)}$ are related to the expansion coefficients $A_n^{(j-1)}, B_m^{(j-1)}$ through a simple linear relation allowing for an expression in matrix notation:

$$\begin{pmatrix} A_n \\ B_m \end{pmatrix} = \sum_{j=0}^{\infty} \mathcal{U}^j \cdot \begin{pmatrix} A_n^{(0)} \\ B_m^{(0)} \end{pmatrix}\,. \tag{3.20}$$

The iteration coefficient j starts from $j = 0$ since the zeroth-order coefficients $A_n^{(0)}, B_m^{(0)}$ are included in the above summation. The square matrix $\mathcal{U}$ is of the dimension

$(N+M)\times(N+M)$ and depends only on the geometry of the trap: $\mathcal{U}=\mathcal{U}(L,R_0,z_1)$. In practice, $N=M=20$ suffices for calculating the potential close to the $\hat{z}$-axis, which is usually the region of interest. The explicit form of $\mathcal{U}$ and of the expansion coefficients can be taken from [28]. Technically, the matrix $\mathcal{U}$ together with the initial zeroth-order coefficients $A_n^{(0)}, B_m^{(0)}$ delivers the solution of the potential $\Phi(r,z)$ inside the toroidal hybrid trap.

3.2.2 Anharmonicity Compensation and Orthogonality

Following the derivation of the C_k^{s}- and D_k^{s}-coefficients from section 2.2.1, the determination of these coefficient for the toroidal hybrid trap is achieved through direct derivation from eq. (3.19). The first most relevant for anharmonicity compensation are given by:

$$\begin{aligned}
C_2^{\mathrm{tor}} &= -\tfrac{1}{2}\left(\sum_{n=1,3,\ldots}^{\infty} A_n\,\kappa_n^2 + \frac{\sqrt{2}}{a^2}\sum_{m=0,1\ldots}^{\infty} B_m(-1)^m(4m^2+1)\right)\\
C_4^{\mathrm{tor}} &= \tfrac{1}{24}\left(\sum_{n=1,3,\ldots}^{\infty} A_n\,\kappa_n^4 + \frac{\sqrt{2}}{a^4}\sum_{m=0,1\ldots}^{\infty} B_m(-1)^m(16m^4+56m^2+9)\right)\\
C_6^{\mathrm{tor}} &= \tfrac{1}{720}\left(\sum_{n=1,3,\ldots}^{\infty} A_n\,\kappa_n^6 + \frac{\sqrt{2}}{a^6}\sum_{m=0,1\ldots}^{\infty} B_m(-1)^m(64m^6+512m^4+1756m^2+225)\right).
\end{aligned} \tag{3.21}$$

Note that due to the symmetry of the potential across $z=0$ all odd coefficients vanish. Thus, with the coefficients A_n and B_m of eq. (3.20) already computed, the C_j^{tor}-coefficients can be found without loss of accuracy. Likewise, the D_2^{tor}-coefficient for orthogonality tuning is received:

$$D_2^{\mathrm{tor}} = -\frac{1}{2}\left(\sum_{n=1,3,\ldots}^{\infty}\frac{\partial A_n}{\partial T}\,\kappa_n^2 + \frac{\sqrt{2}}{a^2}\sum_{m=0,1\ldots}^{\infty}\frac{\partial B_m}{\partial T}(-1)^m(4m^2+1)\right). \tag{3.22}$$

Here, eq. (3.20) is used to achieve the desired level of precision when computing $\frac{\partial A_n}{\partial T}, \frac{\partial B_m}{\partial T}$.

3.3 The Toroidal Hybrid Trap of the Proton Experiment

When dealing with anharmonicity compensation in conventional Penning traps, the contribution of the C_6^{tor} is usually negligible with the optimal tuning ratio acquired which makes $C_4^{\mathrm{tor}}=0$. For the toroidal hybrid trap, however, this does not apply here. The contribution is no longer negligible. As in the case of the five-pole cylindrical trap (cf. section 2.2.1), different trap parameters can be used for anharmonicity tuning.

The toroidal hybrid trap of the proton experiment has been designed such, that it is fully compensated. Both coefficients, C_4^{tor} and C_6^{tor}, depend on the tuning ratio and

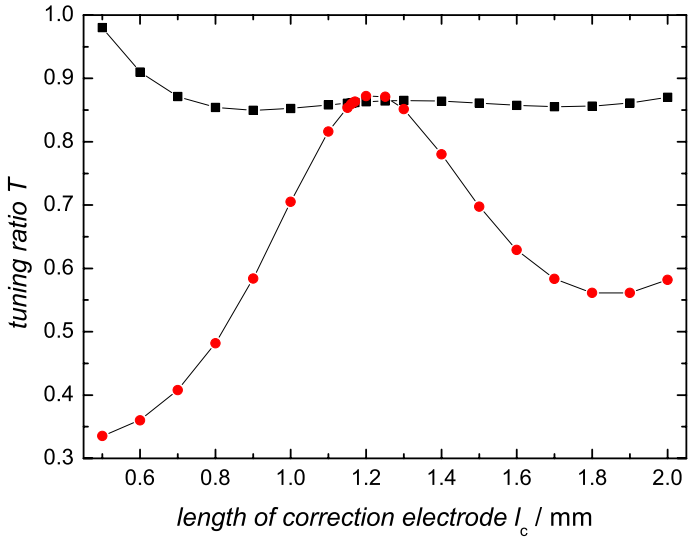

Figure 3.4: Compensation of the toroidal hybrid trap of the proton experiment. The ideal tuning ratio $T_{\mathrm{id}}^{\mathrm{at}}$ is given as a function of the length l_{c} of the correction electrode. The black squares show the tuning ratio $T(C_4^{\mathrm{tor}}, l_{\mathrm{c}})$ as a function of the length of the correction electrode l_{c} for $C_4^{\mathrm{tor}} = 0$. The red circles show $T(C_6^{\mathrm{tor}}, l_{\mathrm{c}})$ for $C_6^{\mathrm{tor}} = 0$. For different l_{c} there exists an ideal tuning ratio $T_{\mathrm{id}}^{\mathrm{at}}$ for which $C_4^{\mathrm{tor}} = C_6^{\mathrm{tor}} = 0$. In this example, there are two possible values of l_{c} within the region of interest plotted, lying between 1.0 and 1.5 mm.

their contribution to the electric potential can be made zero for the respective optimal tuning ratio. For every length of the correction electrode l_{c} there exists in each case a tuning ratio $T(C_i^{\mathrm{tor}})$ for which the coefficient is equal to zero. For one special length of the correction electrode l_{c} the two tuning ratios $T(C_4^{\mathrm{tor}}, l_{\mathrm{c}})$ and $T(C_6^{\mathrm{tor}}, l_{\mathrm{c}})$ are equal. This is the ideal tuning ratio T_{id} for which $C_4^{\mathrm{tor}} = C_6^{\mathrm{tor}} = 0$ holds as shown in fig. 3.4. To determine the ideal tuning ratio $T_{\mathrm{id}}^{\mathrm{at}}$, such a plot was created. For the hybrid trap $T_{\mathrm{id}}^{\mathrm{at}}$ has to be found by numerical calculations with arbitrary precision. Here, the black squares are numerical calculations of $T(C_4^{\mathrm{tor}}, l_{\mathrm{c}})$ for certain lengths of the correction electrode for which $C_4^{\mathrm{tor}} = 0$. The red circles denote $T(C_6^{\mathrm{tor}}, l_{\mathrm{c}})$ for different l_{c} for which $C_6^{\mathrm{tor}} = 0$. At the intersection of the two 'curves' lies the ideal tuning ratio $T_{\mathrm{id}}^{\mathrm{at}}$. For this trap, the length of the correction electrode was chosen to be $l_{\mathrm{c}} = 1.165\,\mathrm{mm}$ resulting in an ideal tuning ratio of $T_{\mathrm{id}}^{\mathrm{at}} = 0.8615$. Within this evaluation it proved to be sufficient to perform the expansion in Bessel functions etc. up to a summation index of $n = 45$ and the perturbation order up to an iteration index of $N, M = 10$. Convergence is not fully reached for $n = 45$, however, the difference in the results is below 1%. With the geometric constraints given, it is not possible to orthogonalize the trap.

The trapping potential of the analysis trap with an inner diameter of 3.6 mm has been simulated with SIMION. The trap electrodes are provided with potentials in such a way that the axial frequency of the proton ν_{z} coincides with that of the axial detection unit at $\nu_{\mathrm{LC}} \approx 680\,\mathrm{kHz}$. To this end, the voltage at the ring electrode is set to $U_0 = -1\,\mathrm{V}$ and the

correction electrodes are supplied with a voltage of $U_c = T_{id}^{at} \cdot U_0$, where T_{id}^{at} is the ideal tuning ratio presented above. The end caps are grounded. The effective potential in the center of the trap along the z-axis as shown in fig. 3.5a is slightly reduced as compared to the applied voltages resulting from the superposition of the different potentials. As a comparison, a harmonic potential is also plotted (red curve). It can be seen, that the potential is to a very high degree harmonic considering typical particle amplitudes of $\approx 100\,\mu$m.

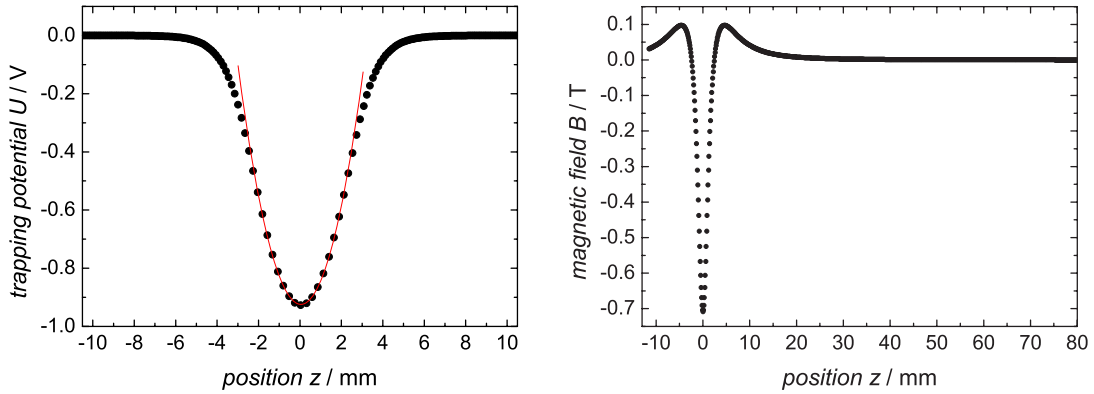

(a) Trapping potential of the analysis trap

(b) Magnetic field of the ferromagnetic ring

Figure 3.5: a) The trapping potential of the analysis trap is shown as a result of a simulation with SIMION together with a harmonic potential (red curve). At the ring electrode, a voltage of $U_0 = -1\,$V is applied, the correction electrodes are provided with a voltage of $T_{id}^{at} \cdot U_0$, and the end caps are grounded. b) The magnetic field introduced by the ferromagnetic ring shown was numerically calculated with the program SUSZI. The center of the analysis trap is at $z = 0$, the center of the precision trap is located at $z = 65\,$mm.

The toroidal hybrid trap functions as the analysis trap in which the spin state of a single proton will be detected. To this end, a magnetic bottle field B_2 is created which allows for this analysis according to eq. (2.42). Since the toroidal ring can be designed in such a way as to protrude far into the trap (cf. fig. 3.1b), the magnetic inhomogeneity at the center of the trap can be greatly enhanced. Please note, that the design of the toroidal ring is on the other side geometrically restricted since ferromagnetic material outside the Gabrielse angle reduces the B_2-term [35]. As ferromagnetic material a Cobalt-Iron compound (vacoflux 50 from the company *Vacuumschmelze*) was chosen with a saturation magnetization of $\mu_0 M = 2.35\,$T, where M is the magnetization of the material and μ_0 the permeability constant. This material has the highest saturation magnetization possible for a solid at room temperature. It introduces a negative magnetic component to the magnetic field of roughly 0.7 T per 1 T external field if saturated as shown in fig. 3.5b. As a comparison, the other machined parts of the trap (made out of copper or sapphire) influence the external magnetic field on a 10^{-6} scale; both values were numerically calculated with the program SUSZI and agree well with similar simu-

Table 3.1: Optimized parameters of the analysis trap: geometric, magnetic, and electrical properties.

r_0	1.800 mm	$T(C_4^{\mathrm{tor}})$	0.8616
r_1	1.292 mm	$T(C_6^{\mathrm{tor}})$	0.8614
z_1	0.770 mm	$T_{\mathrm{id}}^{\mathrm{at}}$	0.8615
l_{c}	1.165 mm	$C_4^{\mathrm{tor}}(T_{\mathrm{id}})$	$4.4908 \cdot 10^{-6}\,/\mathrm{mm}^4$
l_{e}	8.285 mm	$C_6^{\mathrm{tor}}(T_{\mathrm{id}})$	$3.0096 \cdot 10^{-7}\,/\mathrm{mm}^6$
l_{d}	0.140 mm	C_2^{tor}	$-0.09587\,/\mathrm{mm}^2$
L	21.0 mm	D_2^{tor}	$0.1411\,/\mathrm{mm}^2$
B_2	$400.3\,\mathrm{mT/mm}^2$	$\frac{\Delta\nu_{\mathrm{z}}}{\Delta U_0}$	$-0.341\,\mathrm{Hz}\,/\,\mu\mathrm{V}$
$D_{\mathrm{at}}^{\mathrm{z}}$	6.61 mm	$\frac{\Delta\nu_{\mathrm{z}}}{\Delta T_{\mathrm{id}}^{\mathrm{at}}}$	$-501.885\,\mathrm{Hz}\,/\,\mathrm{mUnit}$

lations performed within the diploma thesis of A. Mooser [58]. The resulting magnetic inhomogeneity is $B_2 = 400.3\,\mathrm{mT/mm}^2$. The precision trap is placed about 65 mm away from the center of the ferromagnetic ring resulting in a magnetic inhomogeneity below $B_2 \leq 1\,\mu\mathrm{T}\,/\,\mathrm{mm}^2$. Yet, the change in the magnetic field B_0 is on the order of $3 \cdot 10^{-4}$ T, which has to be included in the discussion of the magnetic field of the superconducting magnet.

Together with the requirements discussed above it was possible to construct a toroidal hybrid trap enabling the spin-state analysis of a single proton. Geometric, magnetic, and electrical parameters are given in tab. 3.1 and can be compared with figs. 2.3, 3.1b, and 3.3. For a voltage $U_0 = -1$ V applied to the ring an axial frequency of a single proton of 682 kHz in the analysis trap is received with a spin-flip jump of 251 mHz. The dependency of the axial frequency on the applied ring voltage is given by $\Delta\nu_{\mathrm{z}}/\Delta U_0 = -0.341\,\mathrm{Hz}/\mu\mathrm{V}$. Since the analysis trap is not orthogonal, ν_{z} becomes a function of the tuning ratio: with the calculated D_2^{tor}-coefficient of $D_2^{\mathrm{tor}} = 0.1411\,/\mathrm{mm}^2$, a milli-unit change in the tuning ratio shifts ν_{z} by 501.885 Hz, in other words $\Delta\nu_{\mathrm{z}}/\Delta T = -501.885\,\mathrm{Hz/mUnit}$. This is no longer a negligible effect and has to be dealt with when tuning the trap with the trapped proton inside. The detection of the axial mode is performed in the 01000-coupling yielding an effective electrode distance of $D_{\mathrm{at}}^{\mathrm{z}} = 6.61$ mm calculated with SIMION.

4 Experimental Setup and Commissioning

Attention is now turned to the features and commissioning of the experimental setup. As explained before, the g-factor of the proton is extracted from the precise determination of two variables, the free cyclotron frequency ν_c and the spin-precession frequency ν_L. Starting point for both measurements is a single, isolated proton stored in the Penning trap. To accomplish a high-precision measurement, long storage times are needed for which a good vacuum is mandatory. To minimize the background pressure, the double-trap tower is situated in a sealed, cryogenic ultra-high vacuum (UHV) trap chamber. Working at cryogenic temperatures provides practically infinitely long storage times and leads to an increase in the quality factor Q as well as a low noise level of the electronic detection units. In addition, the sealed UHV trap chamber requires an in-trap creation of protons, which is realized by implementing an electron beam ion source (EBIS). Finally, the magnetic field required to conduct the measurement is provided by a superconducting magnet in whose horizontal bore the experiment takes place. Thus, the mechanical setup has to be designed in such a way as to guarantee that the precision trap is located at the center of the magnetic field of the superconducting magnet. Furthermore, is has to meet the challenges arising from working in a horizontal bore at cryogenic temperatures and in vacuum.

Within this chapter, components needed to perform the proposed measurement are presented together with commissioning tests to check their technical reliability. First, the mechanical construction is tackled taking into account the constraints arising from the superconducting magnet. Second, the implementation of the trap tower is discussed: assembly, properties required for trapping and detecting particles, and functioning as an ion guide. Within this section, pressure and temperature of the insulating vacuum apparatus are presented. Additionally, the performance of the EBIS is examined followed by the generation and stability of the trapping potentials. Third, the detection units for electronically detecting the axial and cyclotron motion of the trapped particle are presented. They are comprised of a resonance circuit and an amplifier close to the trap as well as an amplifier at room temperature. It is followed by the section about cabling and electronic boards of the entire setup. Finally, a suitable method for inducing spin-flip transitions is described. As a summary, I will discuss the experimental sequence for the g-factor measurement to illustrate the usage of the different components of the experimental setup.

4.1 Mechanical Construction

Figure 4.1 shows a technical drawing of the experimental setup in a 2D-cut view. Since the superconducting magnet (shaded in the drawing) has a horizontal bore, the cryo-

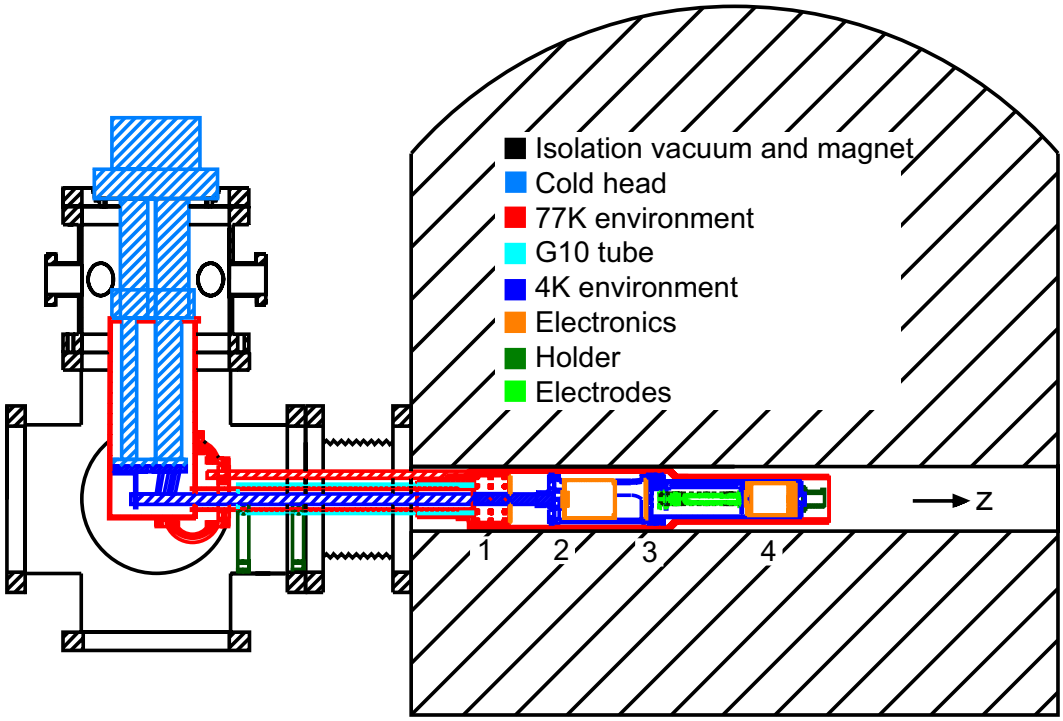

Figure 4.1: The experimental setup with double cross (left) and superconducting magnet (right, shaded). The z-axis of the magnet is indicated, which runs through the geometric center of the bore. Fore details, see text.

mechanical setup was designed such as to suffice this exceptional situation [59]. Optimum mechanical stability in the horizontal plane had to be realized while minimizing the parasitic heat load and bearing in mind thermal contraction effects. To this end, materials with a heat conductivity according to requirements (high or low heat transmission) and the proper elasticity have to be employed. Moreover, the used materials need to exhibit a low magnetic susceptibility not to interfere with the field of the superconducting magnet.

To realize the cryogenic vacuum within the trap chamber, three different temperature stages (liquid helium – 4 K, intermediate stage – 40 K to 80 K, and room temperature – 300 K) and two pressure stages (UHV and isolation vacuum) are required. The outermost "layer" is the bore with a length of 860 mm and a diameter of 88 mm which constitutes the isolation vacuum together with the double-cross construction made out of non-magnetic, 316LN stainless steel (black in the drawing). Inside of this room temperature environment an isolation vacuum pressure of a few 10^{-8} mbar is reached. The cryogenic environment is established by a low-vibrational Gifford MacMahon pulse tube cooler pumped by a closed helium circuit (light blue). It has two temperature stages, where 45 K and 4 K can be reached in the unloaded case within a few hours. The first stage (red) with heat shields made out of high-purity aluminum acts as buffer for the

second stage (blue). A G10 tube (cyan) with a high mechanical stiffness and a comparatively low thermal conductivity is mounted inside the double cross on stainless steel holders (dark green) to mechanically anchor the horizontally arranged heat shields of the first stage. It has been thermally cycled many times and does not exhibit any sign of mechanical abrasion or wear. Inside of it runs a high-purity copper rod connecting the UHV trap chamber (cf. fig. 4.3) with the second stage via a coupling flange (located inside the claw fastener, cipher 1) thus supplying the UHV trap chamber with liquid-helium temperature. The second and last fixing point for the UHV trap chamber is a spacer made out of polyetheretherketone (PEEK, dark green), which is fastened to the surrounding heat shield via Kevlar thread. The pivot for accessing the 4 K region is the aluminum claw fastener at the one end of the G10 tube (left of cipher 1) holding the heat shield and being thermally connected to the first stage by three high-purity copper rods running above the G10 tube.

4.2 Field of the Superconducting Magnet

One of the central prerequisites to realize a high-precision measurement is a very stable magnetic field known with a very low uncertainty. The magnetic field of a superconducting magnet provides the required magnitude and stability. The choice of the specific magnitude of the field is subject to different aspects: On the one hand, the accuracy of the measurement increases with increasing B_0 since relative fluctuations in ν_+ are lower. On the other hand, for a fast measurement and hence a small resistive cooling time constant τ it is convenient to have a small magnetic field since $\tau \propto 1/R_\mathrm{p}$ and $R_\mathrm{p} \propto 1/\nu_+(B_0)$, where R_p is the parallel resistance in resonance of the detection circuit. Additionally, the signal-to-noise ratio depends on the magnetic field as $S/N \propto 1/\sqrt{B_0}$ privileging a low magnetic field.

After due consideration the magnetic field has been set to $B_0 = 1.899\,831\,\mathrm{T}$ which is a suitable value for a first realization of the envisaged g-factor measurement. Furthermore, it was attempted to create a homogeneous region at the center of the bore of 0.1 ppm. To this end, the superconducting magnet has been shimmed to a proton Larmor frequency of 80.89 MHz using a NMR probe. The field distribution after shimming is shown in fig. 4.2a where the frequency of the NMR probe is plotted as a function of the position along the z-axis of the magnet, cf. fig. 4.1. There, the geometric center of the magnet coincides with $z = 0$. It was possible to achieve a peak-to-peak signal with the measuring device of 10 Hz which corresponds to homogeneity of 0.12 ppm within a cylindrical region of 7 mm diameter in the radial plane and 10 mm length along the z-axis. The data have been averaged with a bin size of 0.5 mm yielding the plot of the magnetic field. The data are plotted in such a way that the y-axis is scaled to the value of the magnetic field at $z = 0$ of $B_0 = 1.899\,831\,\mathrm{T}$ as seen from fig. 4.2b. The stability in time can be derived from first measurements performed with the experimental setup as seen from tab. 5.1 taking into account the shift arising from the ferromagnetic material of $\approx 3 \cdot 10^{-4}\,\mathrm{T}$, cf. section 3.3. Correcting the measured value of $B_0 = 1.899\,543\,\mathrm{T}$ (July 2008) and comparing it with the shimming data (December 2005) results in a stability in time

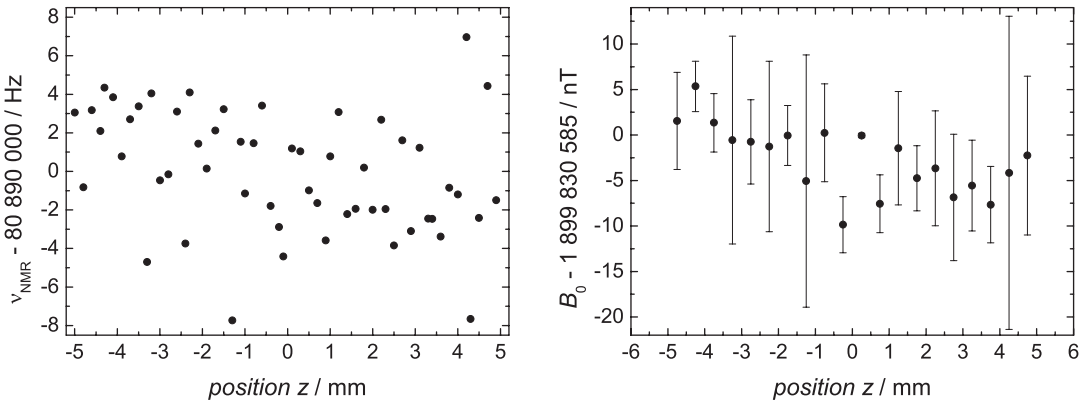

(a) Field distribution after shimming

(b) Magnetic field derived from shimming

Figure 4.2: (a) Shimming data taken with the NMR probe. The value for the proton Larmor frequency aimed at was 80.89 MHz. (b) The magnetic field close to the center of the superconducting magnet emerged from the left by averaging with a bin size of 0.5 mm. The data have been fitted with a linear regression (red line).

of the magnetic field of $(6.0 \pm 0.5) \cdot 10^{-7}$ / day. A further discussion is performed in section 5.5.2.

4.3 Trap Tower

A 3D-cut view of the UHV trap chamber and its contents is shown in fig. 4.3. The UHV trap chamber (blue) is made out of oxygen-free, high-conductivity (OFHC) copper, which has a high heat conductivity and is non-magnetic. The copper is gold-plated to prevent oxidation with a barrier layer of silver to hinder the gold from diffusing into the copper. At the upper end (left in the drawing), a mounting flange (UMF) with feedthroughs for cabling closes the UHV trap chamber using indium wire as a vacuum seal (cipher 3 in fig. 4.1). At the lower end, the UHV trap chamber can be pumped through a small tube before cooling it down. Inside the UHV trap chamber, the UMF holds the trap tower (different shades of green) consisting of the EBIS (green), the two Penning traps with the transport section (light green) isolated by sapphire rings (dark green), and the cyclotron detection unit (orange) comprising the resonator and the 4 K amplifier.

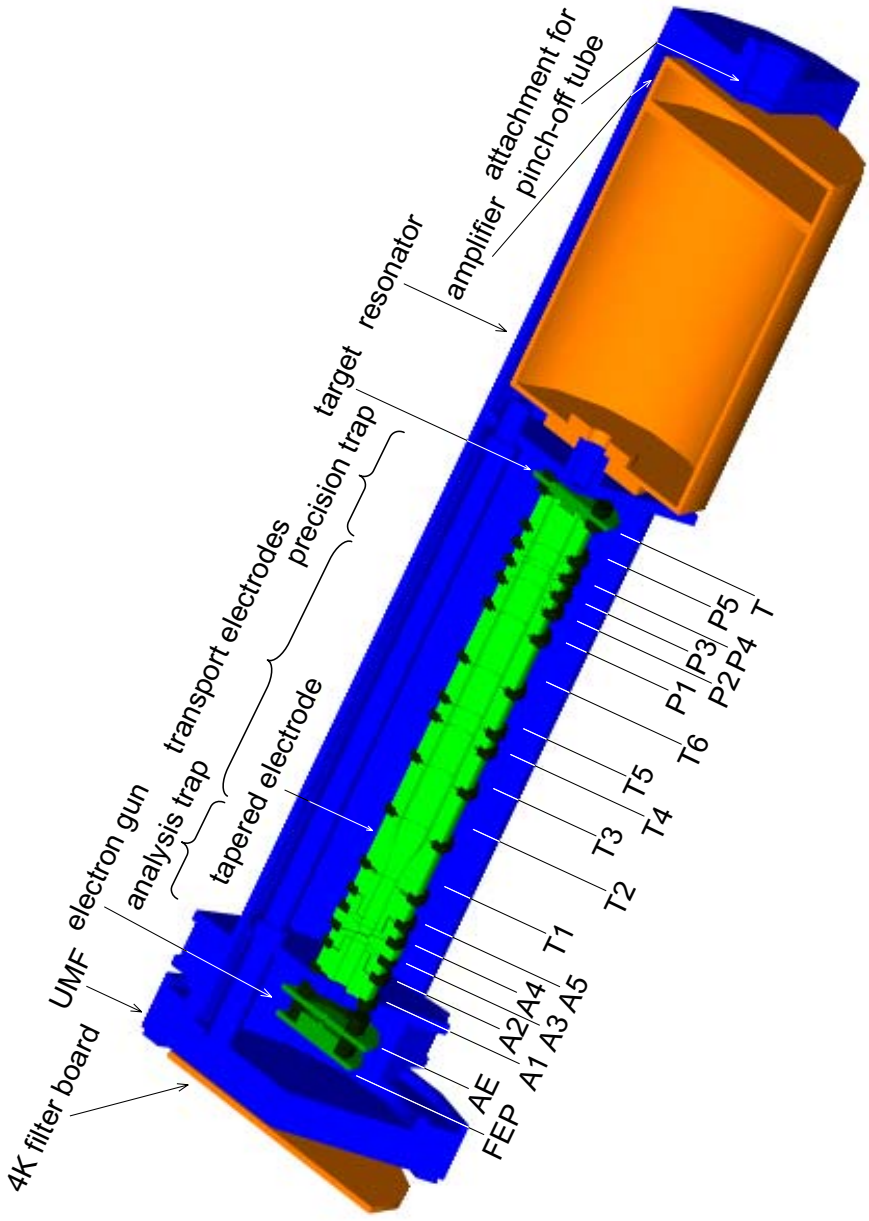

Figure 4.3: 3D-cut view of the UHV trap chamber (blue) with mounting flange on the lower end and a hole used for pumping on the upper end. The trap tower is mounted onto the mounting flange and is comprised of the electron beam ion source (green), the double Penning trap (light green) isolated by sapphire rings (dark green), and the cyclotron detection unit (orange). The 4 K filter board (orange) is also visible on the other side of the mounting flange.

The gold-plated electrodes and sapphire components are cleansed in an ultra-sonic bath with isopropanol before putting the trap tower together which is conducted in a clean room to minimize the risk of a short circuit due to contamination. The ohmic resistance between neighboring components and ground, respectively, are measured to be larger than 200 GΩ. The assembled electrode stack is thermally cycled between 300 K and 20 K repeatedly while controlling the resistances showing no discrepancy from former results nor problems with the mechanical fitting accuracy. The parasitic capacitances of both traps required for the exact dimensioning of the detection coils are measured using a coil wound out of 800 μm thick copper wire with a free resonance frequency of $\nu = (1310 \pm 3)$ kHz, an inductance of $L = (2.22 \pm 0.02)$ mH, and a self capacitance of $C_\mathrm{L} = (6.63 \pm 0.04)$ pF. The coil comparable in size to the axial detection coil is set up within a copper resonator and capacitively coupled to the respective trap while all other electrodes are grounded. The precision trap exhibits a parasitic capacitance of $C^\mathrm{z}_\mathrm{pt} = (13.0 \pm 0.5)$ pF, whereas the analysis trap has $C^\mathrm{z}_\mathrm{at} = (17.0 \pm 0.5)$ pF for the axial detection with 01000-coupling. In the case of the cyclotron detection, the precision trap features $C^+_\mathrm{pt} = (9.37 \pm 0.5)$ pF. The relatively large error in the parasitic capacitances arises from not being able to identically reproduce the experimental setup, e. g. exactly reproducible solder joints or the like.

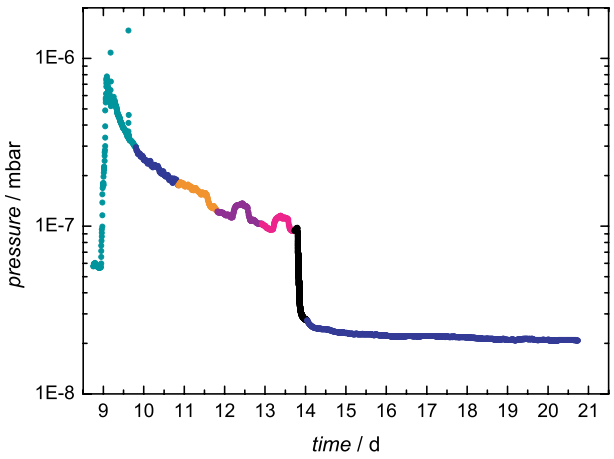

Figure 4.4: Pressure in the UHV trap chamber developing during the bake-out procedure at room temperature. The different colored data denote different measuring sequences.

Subsequently, the assembled trap tower is put in the UHV trap chamber and closed on one side with the indium sealed UMF and brass screws. On the other side, the soldered pinch-off tube (cf. fig. 4.3) is set up for pumping. At room temperature, the UHV trap chamber is pumped for several days and baked out from the ninth day on. The pressure is measured on the other side of the pinch-off tube allowing to estimate the pressure within the UHV trap chamber. The development of the pressure is as expected, part of the pressure curve is shown in fig. 4.4 where the start point of the baking is clearly visible on the ninth day because of an increase in pressure by about an order of

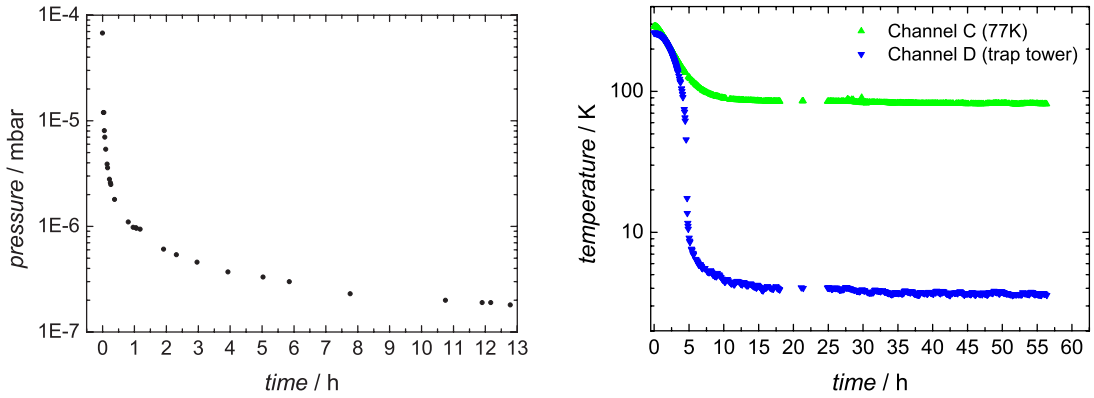

(a) Pressure inside the insulating vacuum apparatus

(b) Temperature inside the insulating vacuum apparatus

Figure 4.5: The pressure development inside the bore vacuum at room temperature is shown on the left and the temperature development of the two cooling stages inside the bore vacuum on the right.

magnitude. After two weeks of pumping, the bake-out procedure is stopped followed by a drop in the pressure. An asymptotic pressure value of $2.1 \cdot 10^{-8}$ mbar is reached at room temperature. After the pinch-off, the pressure slightly rose to $2.3 \cdot 10^{-8}$ mbar and stayed constant, ensuring a leak-proof cut (not shown in the figure).

Afterwards, the closed UHV trap chamber is fixed to the coupling flange of the copper rod at the position of the claw fastener, cipher 1 in fig. 4.1, and the heat shields are mounted. After closing the insulating vacuum apparatus, it is prepared for pumping and cooling down. At room temperature, it is possible to reach a pressure of $1.8 \cdot 10^{-7}$ mbar as seen in fig. 4.5a. The entire experimental setup is cooled down and reaches a stable value of a few Kelvin in less than a day, see fig. 4.5b. A limiting value of (3.5 ± 0.1) K is reached at the UHV trap chamber, ≈ 80 K at the first stage. The pressure of the isolation vacuum drops to $2.4 \cdot 10^{-8}$ mbar due to thermal freeze-out of residual gases. The pressure within the UHV trap chamber is expected to be better than 10^{-16} mbar, first measurements hereto will be presented in section 5.4.1.

Furthermore, the high-precision measurement requires a HF-proof apparatus. Several measurements have shown that it is absolutely necessary to ground all unused or temporarily unneeded connections since they function as HF antennas and collect TV, radio, and mobile phone signals at different frequencies throughout a spectrum from 200 kHz up to 2 GHz. Additionally, the to date unfiltered HV cables have to be equipped with appropriate filters in order not to disrupt the trapping potentials causing unwanted fluctuations in the particles' frequencies.

4.3.1 Electron Beam Ion Source

The EBIS consists of the electron gun and the target fixed to a holding plate (green in fig. 4.3). The electron gun is made up of a field emission point (FEP) fixed to a holding

plate and an acceleration electrode. The electrodes are made out of gold-plated OFHC copper, the electron gun is isolated with macor, since it possesses a higher dielectric strength than sapphire. Whenever an electric potential U_0 is applied between the holding plate and the acceleration electrode, electrons are emitted from the field emission point with an emission current $\propto E^2 \cdot e^{-1/E}$. The electric field strength E depends on the radius of curvature r of the surface at the tip and the length l of the field emission point:

$$E \propto \frac{l}{r} U_0 \,. \tag{4.1}$$

Thus, a small diameter ensures high currents at low voltages. The emitted electron beam travels through the trap tower following the magnetic field lines. Subsequently it hits the target ejecting atoms and molecules. The target is made out of black polyethylene which maintains its electric conductivity down to cryogenic temperatures, hence avoiding a modification of the trap potentials via electric charging. Furthermore, hydrogen atoms are bound only with a few eV enhancing the trapping rate for protons. The desorbed neutral particles with typical energies of some meV are ionized by collisions with the electron beam. The ones being located at the position of the trapping potential after ionization are consequently trapped in the potential created by the electrodes of the precision trap.

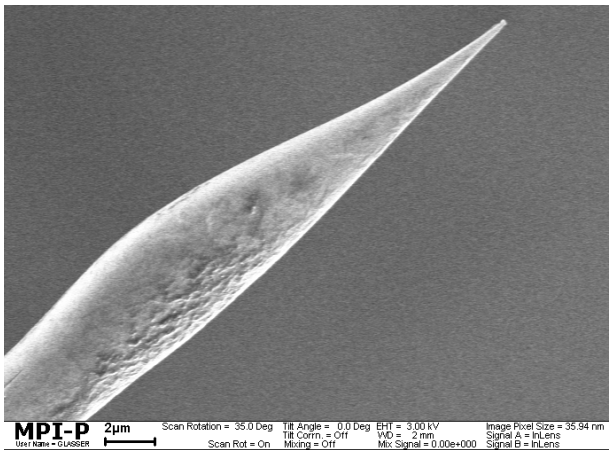

Figure 4.6: Picture of the field emission point with a measure of $2\,\mu$m.

A picture of the FEP with a measure of $2\,\mu$m is shown in fig. 4.6. It was taken with a scanning tunneling microscope at the Max-Planck-Institute for Polymer Research. The FEP is made out of tungsten wire with a diameter of $400\,\mu$m, the tip itself has a radius of curvature of 25 nm. Prior to implementing the EBIS into the final setup it is tested at room temperature to ensure its functionality in the high magnetic field of the superconducting magnet. Electron gun and target are fixed to the UMF and mounted into the insulating vacuum apparatus at the same position as later in the actual experiment. After five days of pumping and baking out at room temperature, a limiting pressure of $6 \cdot 10^{-8}$ mbar is reached in the insulating vacuum apparatus.

Subsequently, while the extraction voltage at the acceleration electrode is varied, the current flow is measured at the FEP, acceleration electrode, and target. During the measurement, the current at the acceleration electrode was negligible, thus fig. 4.7a solely shows the current at the FEP (black squares) and the target (red dots). Starting from an extraction voltage of 0.26 kV, electrons are emitted from the FEP but do not yet reach the target, which can be explained by the special geometry of the setup: the grounded trap holder is located between electron gun and remaining electrodes decelerating the emitted electrons. As soon as their energy is sufficient to overcome this potential barrier (in this measurement at 0.34 kV), the electrons hit the target and a current is measured. The error bars indicate the uncertainty in the read-out of the multimeter since there are large fluctuations in the electron current coming from the FEP. At 0.4 kV the FEP delivers already a few hundred fA in a stable way for a few minutes, which is enough for our purpose. During the measurement, a low negative voltage of −40 V is applied to the FEP resulting in an electron energy of 40 eV in the trapping volume. At this electron energy, the cross section for ionizing hydrogen atoms or molecules is maximum. Since the ionization probability has a maximum at about threefold of the ionization energy $\varphi_{\mathrm{H}} = 13.6\,\mathrm{eV}$, the kinetic energy of the electrons coming from the FEP it set to $\approx -40\,\mathrm{V}$. Finally, the FEP is ready to be implemented in the trap tower and put into operation in a high magnetic field at cryogenic temperatures.

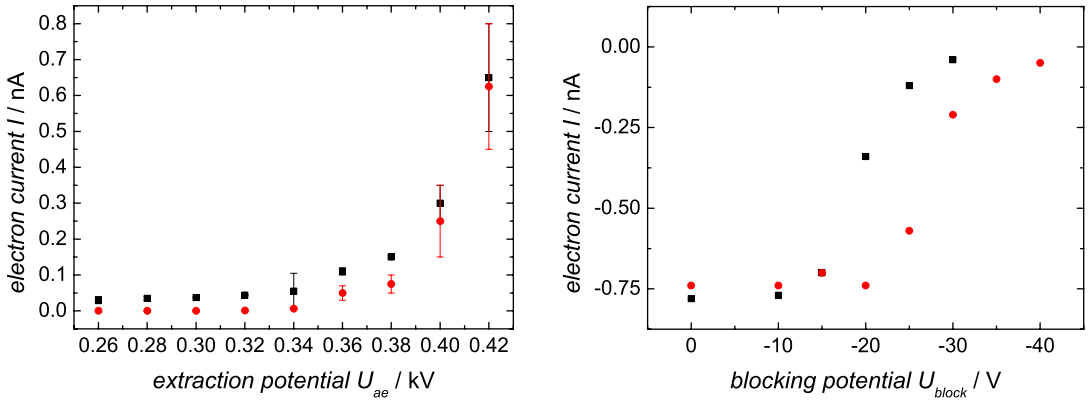

(a) Current-voltage characteristics of field emission point

(b) Electron current trapped by trap electrodes

Figure 4.7: (a) Current-voltage curve of field emission of the FEP implemented inside the bore vacuum in the magnetic field at room temperature. The high voltage U_{ae} is applied to the acceleration electrode. The black squares denote the current measured at the FEP, the red circles that measured at the target at the other side of the trap tower. (b) Electron current as a function of the blocking voltage U_{block} applied to two different transport electrodes (black squares and red circles).

As an alternative to the single FEP, an array of field emission points of copper nanowires has been investigated where the tips are grown as solid cylindrical sticks

with a diameter at the top of 150 nm [60]. The great advantages are the high density of emitters $N = 10^7/\mathrm{cm}^2$ and a high geometrical field enhancement factor $\beta = l/r = 150$ promising a high reliability since it yields high currents at comparatively low voltages. However, the tests performed at cryogenic temperatures in the bore of the superconducting magnet did not yield results beating the ones obtained with the FEP.

4.3.2 Trapping Potentials

The fully cabled trap tower is mounted to the coupling flange to test cabling and functionality of the electrodes as trapping devices. Within the insulating vacuum apparatus, a pressure of $5.6 \cdot 10^{-8}$ mbar is reached at a temperature of roughly 7 K at the position of the trap tower. By applying a positive high voltage to the acceleration electrode and a small negative voltage to the holding plate, electrons are emitted from the FEP and follow the magnetic field lines to hit the target on the other end of the trap tower. Subsequently, a negative voltage is applied to one of the electrodes to hinder the electron beam from hitting the target. The electron current is measured at the target as a function of the blocking voltage as shown in fig. 4.7b. It can be seen that the voltage needed to stop the electron beam lies above the kinetic energy of the electrons of 28.3 eV since the electrodes have at least a diameter of 3.6 mm giving rise to a potential screening effect. The blocking voltage is measured for all electrodes, the data of two of them is shown exemplarily. The black squares indicate a transport electrode of nearly 8 mm length with an inner diameter of 7 mm. The red circles represent another transport electrode with a length of only 3.5 mm and an inner diameter of 7 mm as well. Since the length along the path of the electron beam is smaller, the effective potential at the center of the trap is is also smaller, thus requiring a higher blocking voltage to stop the beam. As the case may be, compare with the potential simulations performed for the precision and analysis trap, figs. 2.5a and 3.5a, respectively.

All electrodes of the trap tower are supplied by the voltage source UM1-14 version DCK6-1 from the company *Stahl electronics*. It supplies 16 channels with voltage values between 0 and −14 V. The channels can be driven in the fast mode and in the ultra-high precision (UHP) mode. The fast mode comprises 16-bit channels and uses filters with a time constant of $\tau_{\mathrm{FM}} = 11$ ms, hence, delivering a stability of a few hundred μV. The UHP mode, on the other hand, uses 32-bit channels and filters with a time constant of $\tau_{\mathrm{UHP}} = 70$ ms yielding a two to three orders of magnitude better stability. The fast mode is used for example for preparing a single particle and is always employed unless stated otherwise. The UHP mode is required for the measurements on a single particle, e. g. investigation of the single particle dip.

The properties of the voltage source have been analyzed, inter alia the temperature stability is of great concern. Measurements performed for this purpose yielded a stability of 1 ppm/K. In addition, the stability of the voltage in time at a fixed temperature is investigated[1]. To this end, the voltage source itself and its supply unit are surrounded by copper blocks which are kept at 34 ° within a few ten mK using an optimized PID

[1] The detailed investigation of the stability of the voltage source is part of the PhD thesis of H. Kracke.

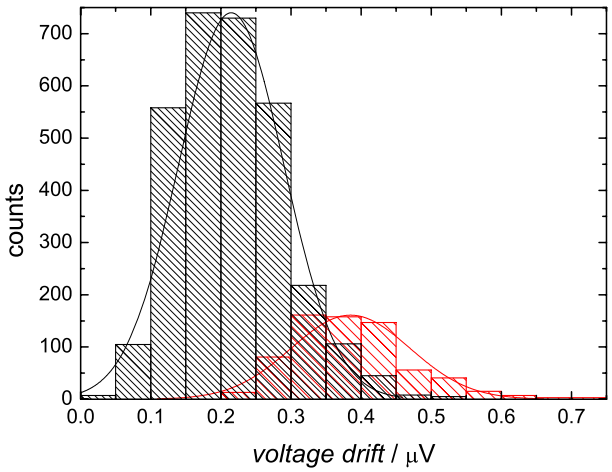

Figure 4.8: Stability in time of the DC voltage source UM1-14 version DCK6-1 taken with a temperature stabilization of the body of the voltage source. The black (red) data correspond to a bin size of one (five) minutes.

controller, i. e. proportional plus integral plus derivative controller. A single channel was kept at $-1\,\mathrm{V}$ for 63 hours taking data points every twelve seconds employing the reference multimeter 8508A from the company *Fluke* with an 8.5 digit resolution. These data were used to derive a histogram with a bin size of one minute and five minutes, plotted in black and red in fig. 4.8, respectively. The mean value of the black data set lies at $(2.15 \pm 0.75) \cdot 10^{-7}\,\mathrm{V}$, that of the red data set at $(3.85 \pm 0.85) \cdot 10^{-7}\,\mathrm{V}$. Since the typical time scale of the proposed measurements is on the order of minutes, these fluctuations are employed to derive a limiting accuracy. To decide whether it is sufficient for the envisaged high-precision measurements, the corresponding frequency shift in the axial frequency is calculated. As an example, a deviation of 300 nV corresponds to a shift in the axial frequency of $\delta_z = 100\,\mathrm{mHz}$, which relates to an uncertainty in the determination of ν_z of $1 \cdot 10^{-7}$ for the black data set. This is about a factor of two smaller than the expected frequency shift of a spin-flip transition, hence it can still be discriminated.

The fluctuations in the voltage are also caused by the temperature shifts of the copper block and ambiance. Figure 4.9 shows the temperature of the copper housing as well as that of the ambient air while the above data were taken. It shows very nicely how the absolute value of the controlled temperature drifts with that of the ambiance. Therefore, a more sophisticated temperature stabilization including the ambient air of the laboratory it is mandatory upon reaching down to uncertainties of 10^{-9}.

4.4 Proton Detection

The non-destructive frequency measurement via detection of image currents induced in the trap electrodes as outlined in sections 2.3.1 and 2.3.2 is in principle sensitive to a

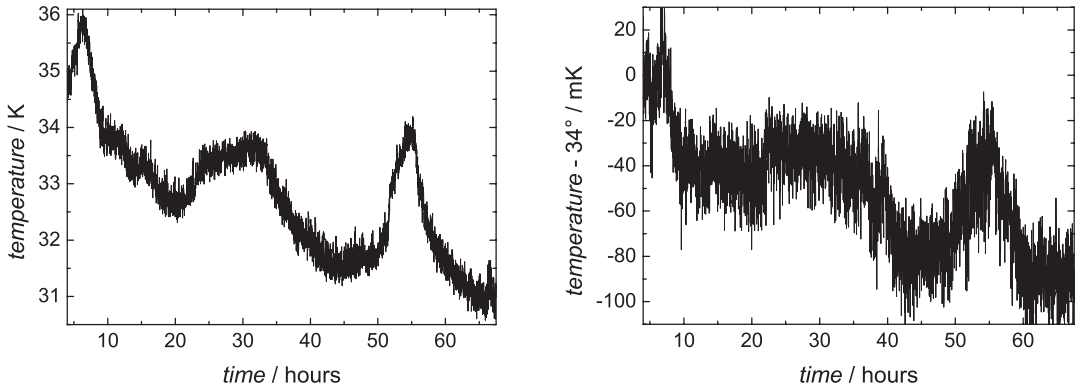

Figure 4.9: Temperature development during the measurement of the voltage stability. On the left, the development of the ambient laboratory air is plotted, on the right, the corresponding one of the copper housing of the voltage source.

single ion. At room temperature $T = 300\,\mathrm{K}$ with a characteristic trap dimension of $D \approx 1\,\mathrm{cm}$, the induced current is on the order of a few fA:

$$\langle I \rangle = \frac{1}{\sqrt{2}} \frac{q}{D}\, 2\pi\nu_\mathrm{z} \cdot z \approx 5\,\mathrm{fA} \tag{4.2}$$

for the axial motion with $\nu_\mathrm{z} \approx 680\,\mathrm{kHz}$. However, upon measuring the induced signal with high precision, not only the signal strength but also the noise background is crucial. Therefore, it is inevitable to tackle the signal-to-noise ratio S/N since a high S/N permits a fast measurement process which increases accuracy and shortens measurement time:

$$\frac{S}{N} = \frac{Z \cdot I}{\sqrt{4kT \cdot Z \cdot \Delta\nu}} = \frac{Q\omega L \cdot I}{\sqrt{4kT \cdot Q\omega L \cdot \Delta\nu}}\,, \tag{4.3}$$

where Z is the impedance of the detection unit, $\Delta\nu$ the bandwidth, and k the Boltzmann constant. It is obvious from eq. (4.3) that a reduction in temperature reduces thermal noise and thus facilitates the measurement. In addition, working with a narrow-band resonance circuit with a large parallel resistance in resonance $R_\mathrm{p} = Q\,\omega\,L = Q/(\omega\,C)$ including a high quality factor Q enhances the sensitivity. For this purpose, a highly sensitive, low-noise detection unit is realized by a system containing a helical resonator with inductance L, capacitance C, and resistance R as well as a field effect transistor (FET) amplifier [61]. A schematic drawing for the detection unit of the analysis trap is shown in fig. 4.10. A large inductance L increases the quality factor Q whereas it is favorable to minimize the capacitance C since it enters as $\omega = 1/\sqrt{LC}$. Parasitic capacitances are kept small by placing the detection units as close as possible to the trap. Furthermore, a high parallel resistance in resonance R_p diminishes the characteristic time scale for a measurement given by the resistive cooling time constant τ, eq. (2.26), thus leading to a fast measurement process. Working at cryogenic temperatures leads to a low electronic noise, i. e. Johnson noise, which further increases the signal-to-noise ratio (SNR). In this experimental setup, two detection units enable detecting two frequencies directly, the

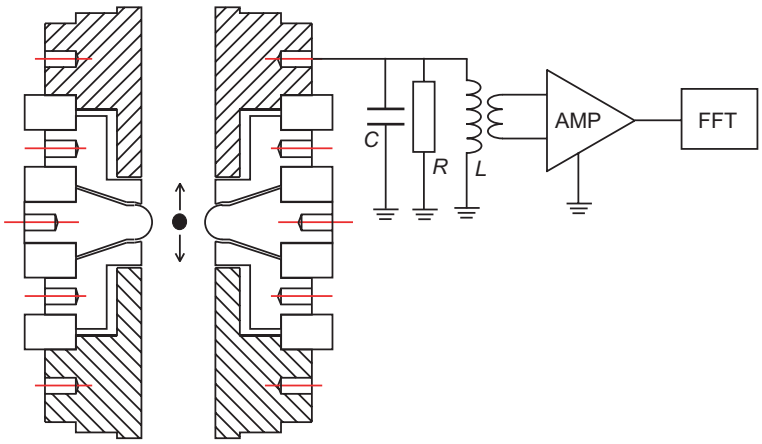

Figure 4.10: Schematic drawing of the electronic detection in the analysis trap with tank circuit (with inductance L, capacitance C, and resistance R) , inductive coupling, and amplifier. The signal is led to the FFT analyzer at room temperature.

cyclotron motion $\nu_+ \approx 29\,\mathrm{MHz}$ and the axial motion $\nu_z \approx 680\,\mathrm{kHz}$. The third frequency $\nu_- \approx 8\,\mathrm{kHz}$ is measured indirectly via a coupling to the axial motion. Each detection unit serves two different purposes: electronic detection and cooling. Moreover, the axial system not only addresses two frequencies but is also employed for detecting the spin orientation of the proton. In the following, design criteria are discussed exemplarily for the axial detection unit.

4.4.1 Tank Circuit for Detecting the Axial Motion

Electronic detection with a resonance circuit is realized by a helical resonator which consists of a cylindrical coil within a cylindrical housing acting as a HF shield [62]. The shield has to be designed such as not to negatively impact the coil's properties. The coil with inductance L exhibits a self capacitance C_L parallel to L and the trap. The number of windings of the coil is determined by the requirement that the frequency of the entire tank circuit has to match the trapped particle's oscillation frequency:

$$\nu_\mathrm{LC} = \frac{1}{2\pi\sqrt{L(C_\mathrm{L}+C_\mathrm{p})}}\,, \tag{4.4}$$

where the inductance is given by the helical resonator. The capacitance is made up of different contributions, one of them being the parasitic capacity of the coil itself, which has to be minimized to deliver a large parallel resistance in resonance R_p (cf. eq. 2.3.1). The total parasitic capacitance is given by C_p, comprising the entire trap tower (30 pF, measured with tank circuit), vacuum feedthroughs (2 pF per feedthrough, measured with tank circuit), cables (5 pF, estimated), other components of the detection unit ($\approx$ 15 pF, partly measured) and amounting to $C_\mathrm{p} \approx 55\,\mathrm{pF}$ for the axial detection circuit. Please keep in mind, that one detection system is used which is connected to both traps. For

an ideal dimensioning, the design follows Macalpine's $\lambda/4$-resonator which provides a rule of thumb for an optimal quality factor Q:

$$Q = 50\, D\, \sqrt{\nu}\,, \tag{4.5}$$

with resonance frequency ν of the free resonator and inner diameter D of the housing given in inch. The mechanics of the experimental setup limit the inner diameter to $D = 51\,\mathrm{mm}$ with a wall thickness of $0.5\,\mathrm{mm}$, with which the entire geometry of the helical resonator is fixed via the design instructions: Length of the housing $L = 1.325 \cdot D$, diameter of the coil body $d = 0.55 \cdot D$, and length of the coil body $l = 1.5 \cdot d$. The quality factor Q is influenced by different loss mechanisms which reduce the total energy stored in the resonator. Losses appear in all parts of the helical resonator and are usually split up as follows [63]: First, losses in the coil wire described by the ansatz $Q = \omega L / R_\mathrm{L}$ where the so-called skin and proximity effects have to be taken into account [64]. To reduce the loss resistance R_L, resonator and shield are machined out of type II superconducting NbTi which permits placing the detector in the high magnetic field near the trap, thus reducing parasitic capacitances and further increasing the SNR, cf. section 2.3. NbTi has a critical temperature of $9.5\,\mathrm{K}$ and is thus suitable for the cryogenic surroundings at $4\,\mathrm{K}$. Second, the ohmic resistance of the resonator R_R which arises from currents induced in the resonator leading to power dissipation. Last, those of dielectric sort R_D, for example in the wire insulation. One measure towards a reduction of dielectric losses is to machine the coil body out of polytetrafluorethylene (PTFE, also known as teflon) and to use as little material as possible.

The usage of superconducting material does not completely eliminate the ohmic losses in both, coil and resonator, since a finite residual resistivity remains. Two main causes give reasons therefore: On the one hand, in an external magnetic field above critical strength $H_{\mathrm{c}1}$, flux enters in type II superconductors via quantized flux lines or vortices, hence producing a mixed state which leads to a collapse of superconductivity above a critical value $H_{\mathrm{c}2}$. Due to the external magnetic field, the vortices begin to move in the mixed state causing the so-called flux-flow resistance, a macroscopically measurable resistivity [65]. On the other hand, the superconductor responses to an AC field which can be understood in the two-fluid model [66]. Within the superconductor, Cooper pairs constitute the superconducting component which carries the AC current. The normal component of unpaired electrons created by thermal breakup of Cooper pairs also carries the AC current resulting in a surface resistance. At low temperatures, however, this is dominated by a temperature-independent residual resistance which has merely been measured in the GHz range [67, 68]. Since it depends on the surface purity it can be reduced by preferably working with clean surfaces. These effects have to be considered when optimizing the design of the superconducting tank circuit in order to reach a maximum quality factor Q. In the case of the axial coil, this has been treated in [69].

The superconducting coil consists of formvar insulated NbTi wire with a core diameter of $50.8\,\mu\mathrm{m}$, $n_\mathrm{z} = 400$ windings are wound in a single layer around a PTFE body with a coil diameter of $d_\mathrm{z} = 31\,\mathrm{mm}$ and a length of $l_\mathrm{z} = 37.2\,\mathrm{mm}$. It exhibits an inductance of $L_\mathrm{z} = 1.45\,\mathrm{mH}$ and a self capacitance of $C_\mathrm{L}^\mathrm{z} = 4\,\mathrm{pF}$. Coupling to the amplifier is realized

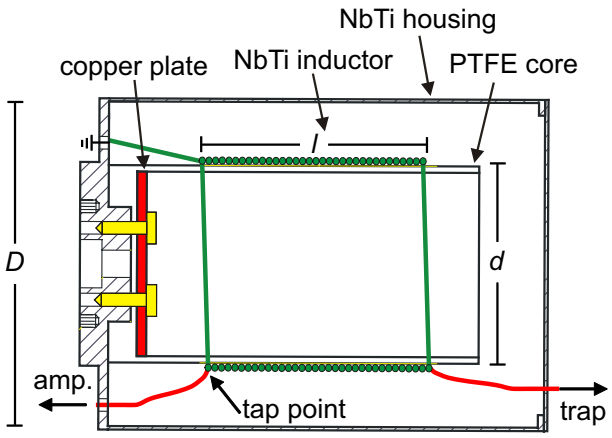

Figure 4.11: Drawing of the helical resonator. The NbTi wire (green) is coupled to copper wire (red) for further cabling. The copper plate (red) fixing the PTFE core to the NbTi shield is employed for sufficient thermalization.

by a tap point. Great care was taken to assemble the helical resonator as seen in fig. 4.11. The NbTi wire was coupled to thick copper wire (red) for further cabling. The copper plate (red) within the PTFE core was fixed with copper screws (yellow) to the NbTi housing to ensure good thermal contact.

The second component of the detection system is the cryogenic amplifier consisting of a source circuit with a source follower for impedance matching[2]. The amplifier is made up out of a field effect transistor NE25139 with a voltage noise of $\epsilon_{\mathrm{n}}^{\mathrm{z}} = (1.2 - 1.5)\,\mathrm{nV}/\sqrt{\mathrm{Hz}}$, a current noise of $\epsilon_{\mathrm{cn}}^{\mathrm{z}} = 5\,\mathrm{fA}/\sqrt{\mathrm{Hz}}$ at $\nu_{\mathrm{z}}^{\mathrm{LC}} = 680\,\mathrm{kHz}$, and delivers a gain of 4. The axial detection unit is located on the other side of the UMF beyond the 4 K filter board (cf. fig. 4.3). As such the parasitic capacitances arising from cabling are small, and the distortion of the magnetic field lines does not influence the magnetic field at the position of the traps. With the detection unit connected to the trap and completely wired, a quality factor of $Q_{\mathrm{z}} = 5300 \pm 50$ is reached at an axial frequency of $\nu_{\mathrm{z}}^{\mathrm{LC}} = 688.150\,\mathrm{kHz}$ resulting in a parallel resistance in resonance of $R_{\mathrm{p}}^{\mathrm{z}} = 33\,\mathrm{M}\Omega$ and a resistive cooling time constant of

$$\tau_{\mathrm{z}} = \frac{m}{q^2}\frac{(D_{\mathrm{pt}}^{\mathrm{z}})^2}{R_{\mathrm{p}}^{\mathrm{z}}} = 106\,\mathrm{ms} \tag{4.6}$$

with $D_{\mathrm{pt}}^{\mathrm{z}} = 7.37\,\mathrm{mm}$ from tab. 2.1 and using eq. (2.26). Finally, the axial detection unit is implemented in the isolating vacuum apparatus and is ready to be employed.

4.4.2 Tank Circuit for Detecting the Cyclotron Motion

The cyclotron frequency ν_+ has to be determined with the smallest error, since it contributes the most to the free cyclotron frequency ν_{c}. If applicable, consult tab. 5.1 for experimentally determined values of the three eigenmotions of a single proton in the

[2]Designing the cryogenic amplifiers is part of the PhD thesis of S. Ulmer.

precision trap. To enhance measuring sensitivity the cyclotron detection unit is placed inside the UHV trap chamber to minimize parasitic capacitances as seen in fig. 4.1 (cipher 4) and fig. 4.3 (orange). The geometric constraints, however, restrict the achievable inductance and hence limit the quality factor Q. Additionally, the HF losses in NbTi in that frequency range are so considerable, that the helical resonator is machined out of OFHC copper. Moreover, copper does not disturb the magnetic field of the superconducting magnet.

The helical resonator has an inner diameter of $D_+ = 42\,\mathrm{mm}$ resulting from the mechanical setup of the experiment. Hence, the coil with 13.1 windings has a length of $l_+ = 35\,\mathrm{mm}$ and a diameter of $d_+ = 23\,\mathrm{mm}$. It is wound on a PTFE core using copper wire with a diameter of 1 mm. The coil with $L_+ = 1.65\,\mu\mathrm{H}$ and $C_\mathrm{L}^+ = 2.5\,\mathrm{pF}$ exhibits a free resonance frequency of $\nu = 79\,\mathrm{MHz}$ and a quality factor at room temperature of $Q_+ = 800 \pm 10$ [59]. At cryogenic temperature with the entire setup connected as seen from fig. 4.12, a quality factor of $Q_+ = 950 \pm 10$ at $\nu_+^\mathrm{LC} = (28\,944\,749 \pm 50)\,\mathrm{Hz}$ with a width of $\Delta\nu_+^\mathrm{LC} = 30\,\mathrm{kHz}$ is achieved resulting in $R_\mathrm{p}^+ = 2.85\,\mathrm{M\Omega}$. In first experiments with a proton cloud, a resistive cooling time constant of $\tau_+ = 50\,\mathrm{s}$ to $60\,\mathrm{s}$ is measured. The second component is the cryogenic amplifier likewise located in the UHV trap chamber and included in the copper housing. The amplifier comprises a field effect transistor NE25139 as the main component, which exhibits a voltage noise of $\epsilon_\mathrm{n}^+ = 0.7\,\mathrm{nV}/\sqrt{\mathrm{Hz}}$ and a current noise of $\epsilon_\mathrm{cn}^+ = 5\,\mathrm{fA}/\sqrt{\mathrm{Hz}}$. Hence, a gain of 5 is reached with a SNR of about 50 for typical particle energies of $E_+ \approx 1\,\mathrm{eV}$. Furthermore, a varactor diode MA-46H-076 with a tunability of a few ten pF is implemented in the detection unit to be able to exactly tune the frequency of the resonance circuit to that of the particle. With the coupling chosen in the setup this correspond to a frequency tuning of $\pm 500\,\mathrm{kHz}$. The entire detection unit exhibits a parasitic capacity of 19 pF depending on the tuning of the varactor diode. At room temperature, a commercial, coaxial low-noise amplifier of the type ZFL-500LN from the company *mini circuits* is used before leading the signal to the FFT analyzer.

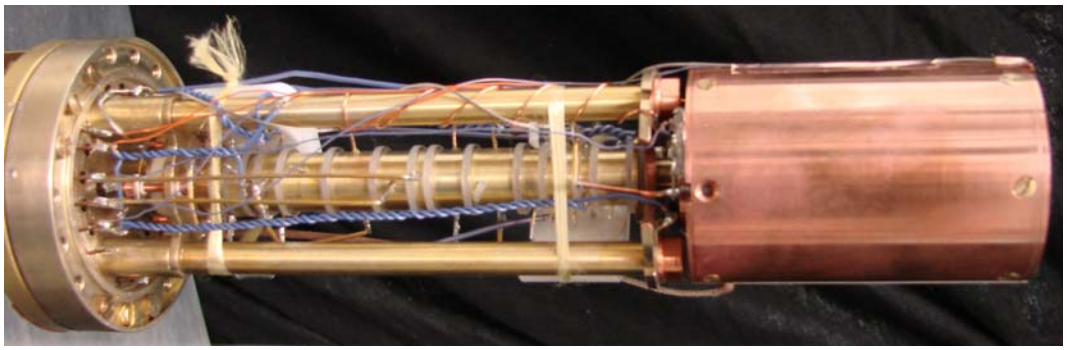

Figure 4.12: Completely assembled trap tower with the cyclotron resonator on the right.

4.5 Cabling and Electronic Boards

All electrodes within the UHV trap chamber as well as the detection systems have to be connected by cables to the electric devices at 300 K. To this end, the connection has to meet different requirements reaching in a high magnetic field from cryogenic to room temperature through different pressure zones. As an example, the DC line of the transport electrode T5 is shown in fig. 4.13. The electrode is located at the left, the electric device at the right side of the drawing. The connection starts in the UHV trap chamber which is located in the high magnetic field region and constitutes an ultra-high vacuum at a temperature of about 4 K. Inside, gold-plated, high-purity copper wire with a diameter below 1 mm is used. Alternatively, PTFE-insulated copper wire is used whenever the risk of an electric contact is given. The pins attached to the electrode itself are soldered with Sn90Ag10 solder prior to gold-plating in order not to contaminate the galvanic baths and to avoid thermal heating after completion. For all other soldering points conventional solder was used.

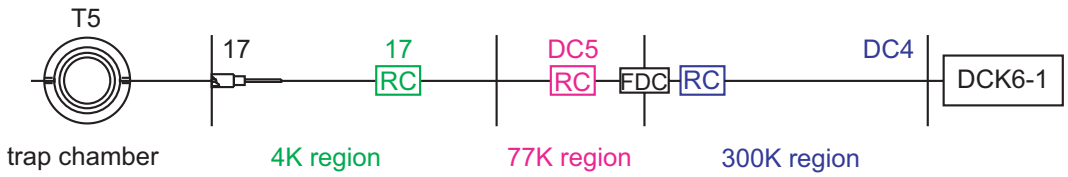

Figure 4.13: Exemplary connection of an electrode for applying a DC potential. For more details, see text.

Subsequently, the wire is attached to the feedthrough in the UMF. The UMF has space for 31 feedthroughs with a diameter of 3.91 mm and a dielectric strength of 1 kV as seen in fig. 4.14. Furthermore, it houses two feedthroughs with a diameter of 6.27 mm each and a dielectric strength of 2 kV. All feedthroughs with wire and mantel machined from copper were soft soldered into the UMF since there was not enough room for welding. In the example, the DC line is soldered to feedthrough number 17, as specified by the black cipher 17 in fig. 4.13. In the following, optionally varnish-insulated, 100 μm thick Cu84Ni4Mn12 wire or 200 μm thick Cu55Ni44Mn1 wire with a PTFE insulation of radially 200 μm was used for cabling. Both exhibit a low heat conductivity and are non-magnetic at low temperatures. Furthermore, constantan wire has a dielectric strength of $40 - 80$ kV/mm and is as such suitable for high-voltage (HV) lines. For the HV line of the acceleration electrode, a semi-rigid, cryogenic coaxial cable made out of stainless steel (SS-PTFE-SS) was used with an inner diameter of 2.2 mm and a nominal dielectric strength of 3 kV but tested higher.

All DC lines have to be filtered at the three temperature stages naturally given by the system in order not to transport perturbing AC signals into the UHV trap chamber. Thus, the connection goes from the feedthrough to the first RC-filter at 4 K, marked green in fig. 4.13. The cipher 17 above the filter indicates the filter number on the

Figure 4.14: Mounting flange of the UHV trap chamber. The machined piece is shown on the left, the gold-plated and with 33 electric feedthroughs equipped mounting flange with the adjacent workpiece on the right side.

electronic board[3]. The 4 K filter board is located above the UMF, represented in fig. 4.1 by cipher 3. At this temperature stage, filters for the HV lines were abandoned due to space reasons. Each RC-filter for a DC line has a cut-off voltage of $U_c = 50\,\mathrm{V}$, a cut-off frequency of $\nu_c = 143\,\mathrm{Hz}$, and a response time of $\tau = 1\,\mathrm{ms}$. The electronic board is manufactured out of PTFE to minimize rf losses and parasitic capacitances with the ground connection clamped to the adjacent workpiece as seen in fig. 4.15a.

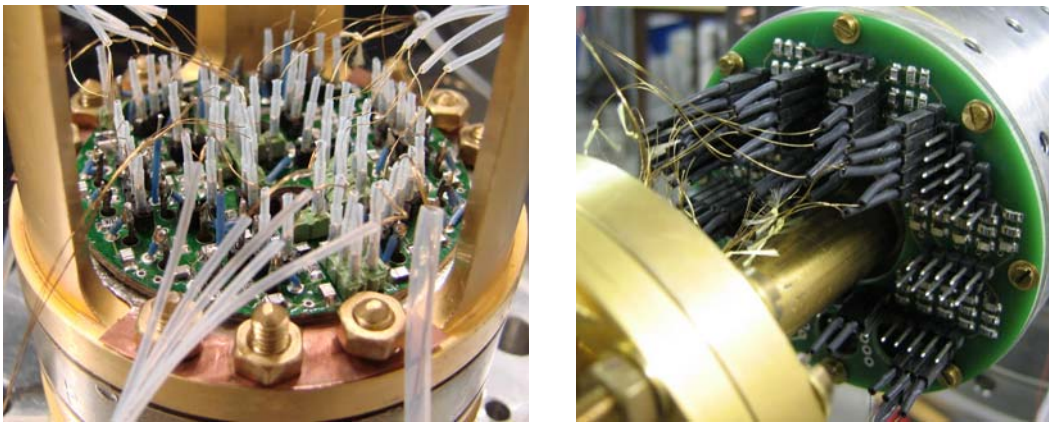

(a) Filter board at 4 K (b) Filter board at 77 K

Figure 4.15: Filter board at 4 K and at 77 K with outgoing connections. The soldered connections of the feedthroughs to the 4 K filter board are visible.

In the following, the connecting cable leads to the 77 K filter board, marked magenta in fig. 4.13. The cipher above the filter again indicates the filter number on the electronic

[3]The design of the filter boards is part of the PhD thesis of C. C. Rodegheri.

board. The filter here has the same properties as the one at 4 K. It is positioned at the end of the claw fastener (cipher 1 in fig. 4.1) and is shown in fig. 4.15b. Subsequently, the cable leads to the flange of the isolation vacuum at 300 K denoted in the drawing by the black box FDC (**f**lange for **DC** lines) through which it reaches the respective filter board (marked blue). Finally, it is guided to the DC voltage source UM1-14 version DCK6-1, indicated by the blue cipher. This voltage source with a stability of 1 ppm/K provides an accurate and stable voltage, one of the essential requirements for precision measurements.

4.5.1 Excitation and Detection

To conduct the measurement of the proton oscillation frequencies, different excitations for the individual eigenmotions of the stored proton are required. On the one hand, the axial motion of the particle has to be excited which is realized by a dipole excitation of the axial frequency ν_z. The setup allows for such an excitation in both traps through the trap electrodes $A4$ and $P5$ (for nomenclature of electrodes cf. fig. 4.3). On the other hand, a dipole excitation in the radial direction is needed for the cyclotron motion ν_+. To this end, a dipole excitation is directed at one half of a split electrode in each trap ($A5$ and $P4$), which is displaced from the center of the trap, is used for this excitation yielding a dipole component in the radial which accesses the cyclotron motion. The axial motion is not addressed by this excitation since the frequency lies a few orders of magnitude away. In principle, the radial quadrupole part could cause unwanted mode coupling, however, the cyclotron frequency does not comply with a sum frequency of the sort $\nu_+ = a\,\nu_z + b\,\nu_-$, where $a, b \in \mathbb{N}$. The magnetron motion is not directly excited but can be accessed via a quadrupole excitation at the sum frequency $\nu_z \pm \nu_-$ through the same split electrode.

For the excitation lines, manually built twisted-pair wire out of PTFE-insulated OFHC copper is employed in the UHV trap chamber, see therefor figs. 4.19 and 4.20. The connection is coupled to the DC line by a CC-filter, which comprises two capacitances in such a way that it constitutes a 1:3 voltage divider (10 dB). A 1 MΩ resistor is implemented in the DC line to keep the signal from traveling to the DC voltage supply, thus avoiding reflections. Concerning the split electrodes, a 1 MΩ resistor is put between the two halves to ensure that one half can still be used for excitation purposes while the DC potential is the same for both of them. On the other side of the UMF beyond the UHV of the trap chamber, cryogenic suitable coaxial cable with a PTFE-insulated, 100 μm thick brass conductor and a shield of braided CuNi is used to lead the excitation signals to the signal generator at atmospheric pressure and room temperature, disrupted at the exit of the double cross by yet another feedthrough. Several feedthroughs in the UMF as well as in the flanges of the isolation vacuum are used to transmit the UMF ("good") ground in order to eliminate offset potentials. This ground line is also connected to the 77 K stage to ensure thermal contact.

Three electrodes are employed for detection of the particle. In the precision trap, axial and cyclotron motion of the particle can be detected via trap electrode $P2$ and $P4$, respectively. In the analysis trap, however, only the axial motion can be monitored

via trap electrode $A2$. There are several reasons as to why the cyclotron motion cannot be measured: First, space reasons allow for just one cyclotron detection unit within the UHV trap chamber. Second, connecting both traps to one detection unit would introduce unwanted parasitic capacitances. And third, during the actual precision measurement, the detection of the cyclotron frequency ν_+ would destroy coherence with respect to the measurements performed in the precision trap, since monitoring the cyclotron motion with a resonance circuit would heat the cyclotron energy E_+, thus changing the quantum number. Moreover, since , solely the precision trap is attached in order not to perturb the detection signal more than explicitly needed. The detection line of the cyclotron motion goes from the electrode to the resonance circuit, the 4 K cyclotron amplifier (cipher 4 in fig. 4.1), and further to the feedthrough in the UMF. On the other side, it is guided with cryogenic coaxial cable in a CuNi tube through the feedthrough in the double cross to the room temperature amplifier and signal analyzer. As for the axial detection, the two detection lines are coupled capacitively inside the UHV trap chamber going to a single feedthrough in the UMF from where the line is guided to the resonance circuit and 4 K axial amplifier. The remaining connection compares to the one described above.

4.5.2 Wiring Diagram

Figures 4.19 and 4.20 show the wiring diagram of the experiment[4]. A connecting cable is drawn in black. Different colors indicate different applications at the three temperature stages. The most important ones are listed in the following: At 4 K, the filter board is depicted by the green color, the axial amplifier by yellow, and the cyclotron amplifier by orange. At 77 K, magenta pictures the respective filter board. The 300 K filter board is denoted by blue, the respective axial amplifier by dark yellow, and the cyclotron amplifier by red. All electronic devices needed for the experiment are shown in black at the top of the diagram. In conclusion, a distinct overview over the experimental setup is established. All devices are connected to a LABVIEW-based control system with which the experimental routines can be executed[5].

4.6 Induction of Spin-Flip Transitions

The Larmor frequency ν_L is accessed by driving a spin-flip transition and monitoring it in the axial motion of the particle stored in the trap. To be able to drive spin-flip transitions, an alternating magnetic field $\vec{B}_1(t) = \hat{B}_1(\hat{x}\cos\omega_\mathrm{rf}t + \hat{y}\sin\omega_\mathrm{rf}t)$ in the radio-frequency (rf) range with circular polarization and perpendicular to the $\hat{z}-$axis of the magnetic field B_0 has to be introduced at the center of both Penning traps. In the precision trap it is needed for the actual measurement, in the analysis trap it is needed to determine the spin state of the particle. A magnetic field amplitude of $\hat{B}_1 = 1\,\mu\mathrm{T}$ should be reached in order to achieve a reasonable spin-flip rate of about 60 spin-flips per second (for details see section 2.5.2). In general, there are two possibilities for generating

[4]The figures are moved to the end of this chapter for a better display alternative.
[5]Programming the control system is part of the PhD thesis of H. Kracke.

this field: using one of the trap electrodes or via a coil from outside the trap tower. The former choice was discarded, since coupling the signal directly to one half of a split trap electrode or even using it as part of a resonance circuit did not deliver a satisfying field strength B_1. The latter alternative, however, has to deal with the electromagnetic shielding of the copper electrodes.

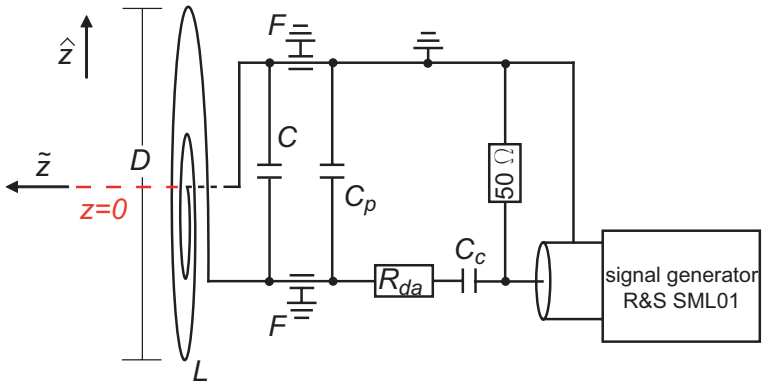

Figure 4.16: Resonance circuit for spin-flip excitation. Solely the coil with inductance L is implemented in the UHV trap chamber, the parallel capacitance C_p of the resonance circuit is located on the other side of the UHV trap chamber, beyond the UMF. The remaining components will be explained in the text.

A resonantly driven LC circuit positioned outside of the trap tower for external excitation is the most suitable configuration. Figure 4.16 shows the equivalent circuit diagram of the resonance circuit, where the rf signal provided by a Rhode&Schwarz SML01 signal generator is coupled capacitively via C_c to the resonance circuit and is terminated with a 50 Ohm resistor. Due to spatial constraints, a pancake coil (inductance L, self-capacitance C) with a diameter of $D = 20.0\,\mathrm{mm}$ and a radial distance to the trap center of $d = 14.5\,\mathrm{mm}$ is used. The coil center coincides with the trap center at $z = 0$, cf. fig. 4.17. The used material is a $510\,\mu\mathrm{m}$ thick copper wire with a PTFE insulation of $200\,\mu\mathrm{m}$ thickness, resulting in a distance of the wire centers of $910\,\mu\mathrm{m}$. The coil can be conceived as a concentric configuration of n windings yielding a n-times magnified current. To avoid unnecessary capacitive coupling, the one end of the coil lying inwards is connected to ground. The effective magnetic field could be further enhanced by a factor of two using a pair of coils in Helmholtz configuration. Furthermore, it would be less susceptible for spatial misalignment, however, the geometric constraints forbid it. Besides the coil – the only component of the resonance circuit placed inside the UHV trap chamber – the excitation unit consists of the parasitic capacitance of the two feedthroughs in the UMF (F) and a parallel capacitance C_p with a value well above the parasitic ones as such constituting a well-defined capacitance. An ohmic damping resistance R_da is introduced to limit the quality factor Q in such a way as to allow for a detuning of $\pm 500\,\mathrm{kHz}$ with a loss of no more than 3 dB. The resonance frequency of each coil and thus the number of windings has to match the Larmor frequency ν_L in the each trap. In the precision trap it amounts to $\nu_\mathrm{L}^\mathrm{pt} = 80.89\,\mathrm{MHz}$ whereas in the analysis trap

a frequency of $\nu_{\mathrm{L}}^{\mathrm{at}} \approx 40\,\mathrm{MHz}$ is required depending on the exact value of the magnetic field perturbation arising from the CoFe ring, which is not yet experimentally affirmed.

Since tuning of a resonance circuit is more difficult the higher the frequency, the following measurements focus on $\nu_{\mathrm{L}}^{\mathrm{pt}}$. In addition, they are conducted in the analysis trap since the magnetic inhomogeneity B_2 impedes the induction, hence "killing two birds with one stone". The power transfer is indeed similar for the two frequencies $\nu_{\mathrm{L}}^{\mathrm{pt}}$ and $\nu_{\mathrm{L}}^{\mathrm{at}}$, thus the experimental data can later on be transferred. To determine the number of required windings, two effects have to be considered which alter the frequency of the resonance circuit: since the experiment will be conducted at cryogenic temperature, a frequency shift of $\nu_{\mathrm{LC}}^{\mathrm{4K}} = 400\,\mathrm{kHz}$ going from a temperature of 300 K down to 4 K has to be factored in. Second, the shielding of the UHV trap chamber shifts the frequency by an additional $\Delta\nu_{\mathrm{shield}} = 2\,\mathrm{MHz}$:

$$\nu_{\mathrm{LC}}^{\mathrm{300K}} = \nu_{\mathrm{L}}^{\mathrm{pt}} + 2\,\mathrm{MHz} + 400\,\mathrm{kHz} = 83.292\,\mathrm{MHz}\,. \tag{4.7}$$

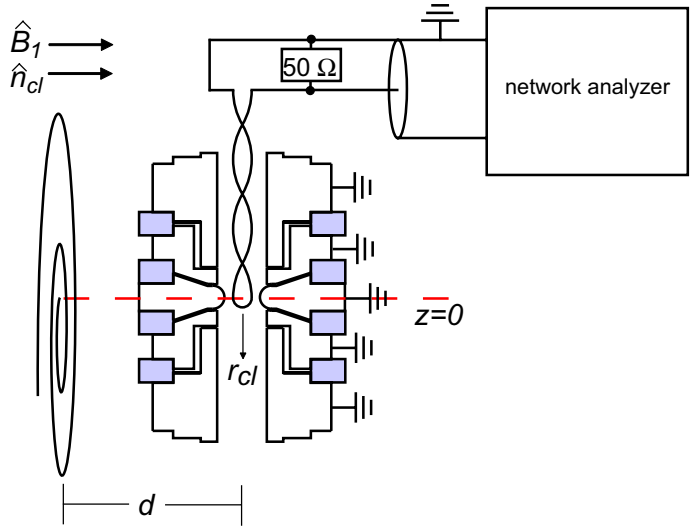

Figure 4.17: Experimental setup for detecting the magnetic field amplitude B_1 at the trap center. On the left, the coil as part of the resonance circuit is shown to which an alternating current is applied. A conductor loop picks up the induced signal at the center of the analysis trap, which is analyzed with a network analyzer. For explanation of the parameters see text.

Applying an alternating current to the resonance circuit establishes a radial magnetic field component at the trap center. The fraction reaching the position of the trapped particle is detected by a conductor loop with radius r_{cl} and surface $F = \pi\, r_{\mathrm{cl}}^2$, whose surface vector $\hat{n}_{\mathrm{cl}}$ is aligned with that of the coil. The voltage U_{ind} induced in the conductor loop is given by:

$$U_{\mathrm{ind}} = -\int \dot{\vec{B}}\, d\vec{F} = -\int \dot{B}\, dF \cos\varphi = -\int \dot{B}\, dF\,, \tag{4.8}$$

yielding with the expressions for F and B_1 from above:

$$U_{\mathrm{ind}} = -\frac{d}{dt}(\hat{B}_1 \sin\omega t) \cdot \pi\, r_{\mathrm{cl}}^2 = -\omega \hat{B}_1 \cos\omega t \cdot \pi\, r_{\mathrm{cl}}^2\,, \tag{4.9}$$

where B_1 is the magnetic field generated by the coil. The peak value of the magnetic field penetrating the conductor loop can be calculated from the induced voltage U_{ind}:

$$\hat{B}_1(\nu, P_{\mathrm{out}}) = \frac{\hat{U}(P_{\mathrm{out}})}{2\pi\,\nu \cdot \pi\, r_{\mathrm{cl}}^2} = \frac{\sqrt{2} \cdot \sqrt{10^{\frac{P_{\mathrm{out}}}{10}}}\, P_0\, R}{2\pi\,\nu \cdot \pi\, r_{\mathrm{cl}}^2}\,, \tag{4.10}$$

where the frequency measured with the conductor loop is equal to the drive frequency of the coil due to the small line width of the signal generator and is denoted by ν. The peak value of the induced voltage has to be calculated from the attenuation of the signal power P_{out} measured with a network analyzer, for which the general conversion from dBm to V or A holds. Since all values are measured in units of dBm, the reference value for the power is $P_0 = 1\,\mathrm{mW}$, and the voltage drop is measured at an ohmic resistance of $R = 50\,\mathrm{Ohm}$. Peak and mean values are related via $\hat{U} = \sqrt{2}\,U_{\mathrm{eff}}$. For comparison with the theoretical value, the magnetic field of the pancake coil is calculated via:

$$B_{\mathrm{eff}}^{\mathrm{in}}(P, \tilde{z}) = \sum_n \frac{\mu_0\, I_{\mathrm{eff}}(P)\, \pi r_n^2}{2\pi(\tilde{z}^2 + r_n^2)^{3/2}}\,, \tag{4.11}$$

where n is the number of windings and r_n is the radius of the nth winding presuming that the pancake coil is made up of n concentric loops. The magnetic field amplitude is calculated on the $\tilde{z}$-axis, which is perpendicular to the coil's surface and goes through its center (cf. fig. 4.16).

4.6.1 Determination of Coupling Capacitance and Damping Resistance

Different values for the coupling capacitance C_{c} are used to adjust the frequency of the coil to the Larmor frequency of the proton ν_{L} and to establish maximum power transfer. In addition, it reduces the capacitances from components beyond, yet, their parasitic influence lies below 0.5 % and is discarded in the following. The damping of the quality factor Q due to the coupling capacitance is neglected, since the damping resistance will later on anyhow limit the quality factor. A pancake coil as seen in fig. 4.16 with $n = 7$ windings, and inductance of $L = 0.5\,\mu\mathrm{H}$, and a self capacitance of $C = 5.2\,\mathrm{pF}$ exhibits an undamped frequency of $\nu = 105.3\,\mathrm{MHz}$ with a quality factor of $Q = 85$. It is employed to measure the power transfer of a 10 dBm input signal on and far-off resonance as a function of the coupling capacitance C_{c}. To make out the offset of power transfer, the hot end of the coil is excited via a shorted connection, hence $C_{\mathrm{c}} = 0$. This offset value is indicated by the blue line in the left graph of fig. 4.18 drawn parallel to the x-axis to be able to compare with the values attained far-off resonance. The magnetic field amplitude $\hat{B}_1$ induced in a conductor loop with a radius of $r_{\mathrm{cl}} = 1.5\,\mathrm{mm}$ is calculated from the measured attenuation via eq. (4.10). The highest magnetic field amplitude is reached for a coupling capacitance $C_{\mathrm{c}} = 1.5\,\mathrm{pF}$. For greater values of C_{c} it diminishes

as expected, for smaller values the setup limits the power transfer. The black squares denote the magnetic field amplitude $\hat{B}_1$ on resonance, the red circles the data far-off resonance. For a coupling capacitance of $C_c = 1.5\,\mathrm{pF}$ a magnetic field amplitude of $\hat{B}_1 = 46.5\,\mu\mathrm{T}$ is reached which corresponds to an enhancement of 30 dB taking into account the offset value of $1.5\,\mu\mathrm{T}$. Please note, that the conductor loop is placed directly in front of the coil leading to the higher values for the magnetic field amplitude than in the actual experiment, where the signal has to travel a certain distance until it reaches the position of the particle.

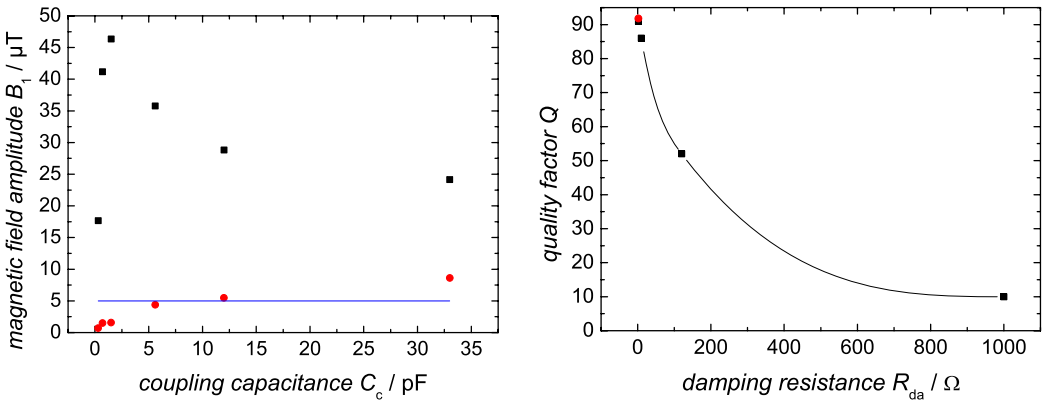

Figure 4.18: Adjustment of the coupling capacitance and the damping resistance of the resonance circuit. On the left, the enhancement of the magnetic field amplitude at the position of the conductor loop as a function of the coupling capacitance C_c is shown. The black squares denote the magnetic field on resonance, the red circles that far-off resonance. The blue line indicates the offset value. On the right, the quality factor Q of the resonance circuit as a function of the ohmic damping resistance R_{da} is shown. The black squares denote the measured data, the red circle an exemplarily calculated quality factor Q. The solid line is drawn to guide the eye.

The ohmic damping resistance is used to limit the quality factor Q in such a way as to allow for a reasonable detuning of about $\pm 500\,\mathrm{kHz}$ while remaining within the 3 dB width leading to a quality factor of approximately $Q \approx 80$. Without such a damping component, the quality factor would increase by about a factor of 10 when cooling the system to liquid helium temperature which would complicate the spin-flip excitation. Different values for the damping resistance R_{da} were implemented in the resonance circuit of fig. 4.16 to determine the impact on the quality factor Q. The results are shown on the right of fig. 4.18 (black squares), the solid line is drawn to guide the eye. The theoretical quality factor for a damping resistance of $R_{da} = 2.2\,\Omega$ was calculated to $Q = 92$ which is in good agreement with the measured data.

4.6.2 Shielding and Fine-Tuning of the Resonance Circuit

The copper electrodes constitute a rf shielding, yet the electromagnetic radiation travels through the gaps between the electrodes, since the sapphire isolation rings do not have a screening effect. Figure 4.17 shows a 2D-cut view of the analysis trap with the sapphire rings marked in gray and the isolating gaps shown. Moreover, also the slits of the split electrodes let the radiation pass. Different measurements have shown that the coil has to be placed in such a way that the magnetic field can travel through the slits and the gaps to enhance the field at the position of the trapped particle. The shielding effect of $\approx 5\,\mathrm{dB}$ – which corresponds to a reduction in the magnetic field of about 40 % in comparison to the value calculated with eq. (4.10) – is then partly compensated by the adapted orientation of the coil with respect to the trap electrodes[6].

Table 4.1: Results of the optimization of the resonance circuit for the spin-flip transition

parameter	symbol	value	reason
diameter	D	$20.0\,\mathrm{mm}$	geometric constraints
windings	n	≈ 6.5	undamped frequency
frequency	ν_{LC}	$83.3\,\mathrm{MHz}$	from eq. (4.7)
quality factor	Q	≈ 80	3 dB attenuation at $\pm 500\,\mathrm{kHz}$ detuning
coupling capacity	C_{c}	$(0.7 - 1.5)\,\mathrm{pF}$	maximum of power transfer
ohmic damping resistance	R_{da}	$(10 - 80)\,\Omega$	limiting the quality factor
parallel capacity	C_{p}	$\approx 2\,\mathrm{pF}$	well-defined tuning, negligible parasitic capacities

One of the tested resonance circuits is used to deduce an appropriate value for the parallel capacity C_{p}, see fig. 4.16. With $n = 6.25$ windings, a damping resistance of $R_{\mathrm{da}} = 10\,\Omega$, a coupling capacitance of $C_{\mathrm{c}} = 0.8\,\mathrm{pF}$, and a parallel capacitance of $C_{\mathrm{p}} = 2.2\,\mathrm{pF}$ a quality factor of $Q = 113$ is reached at a frequency of 83 MHz. Different measurements were performed to specify the exact dimensions of all components using a conductor loop to simulate the particle. Thus, with the appropriate components it is possible to tune the resonance circuit to the Larmor frequency of the proton ν_{L} except for a few kHz. A summary of the results for the different components is given in tab. 4.1 with a short explanation for each component. A proposed configuration is included in the wiring diagram, cf. figs. 4.19 and 4.20. With these design instructions at hand, the frequency of the resonance circuit can be tuned as needed also for the implementation in the analysis trap. With an input power of 10 dBm, the measured attenuation of $P_{\mathrm{out}} = 24\,\mathrm{dBm}$ yields a magnetic field amplitude of $\hat{B}_1^{\mathrm{LC}} = 1.43\,\mu\mathrm{T}$ which is sufficient to drive spin-flip transitions as calculated in section 2.5.2. a theoretical derivation was undertaken in [58] and agrees well with the presented results.

[6] The task of spin-flip excitation is investigated in great detail within the diploma thesis of A. Mooser.

4.7 Experimental Sequence

To conclude this chapter, I present the experimental sequence needed to determine the cyclotron and Larmor frequencies from which the g-factor can be extracted. The usage of all components introduced above will become apparent. In the following chapter, experimental results up to the determination of the free cyclotron frequency will be presented and discussed. The addressed measuring procedures will then be treated thoroughly and will become obvious.

- **Loading the trap:** After the setup is cooled down, thus having established a cryogenic UHV in the trap chamber, the EBIS is put into operation and provides different charged particles. While it is running, the electrodes of the precision trap are supplied with the voltages needed to trap the different species. To monitor the content of the trap the potential depth is varied such that the different species first undergo an axial dipole excitation at a frequency of $\nu_{\mathrm{LC}} + \delta$ and, secondly, are detected non-destructively by the axial detection unit upon coincidence of resonance frequency of the circuit and axial frequency of the particle $\nu_{\mathrm{LC}} \equiv \nu_{\mathrm{z}}$ by that generating a mass spectrum.

- **Preparing a pure proton cloud:** In a next step, the impurity ions are removed to obtain a pure proton cloud. To this end, the protons are kept in resonance with the tank circuit at $\nu_{\mathrm{LC}} \equiv \nu_{\mathrm{z}}(U)$ via the corresponding potential depth and are thus resistively cooled. At the same time, a strong excitation sweep directed at all axial frequencies below the axial frequency of the stored protons is applied to the end cap of the precision trap $P5$ and transfers enough energy to the other particles to be lost from the trap.

- **Isolation of a single proton:** The cyclotron motion of the proton cloud with frequency ν_+ can now be detected with the respective detection unit. With a slightly anharmonic trap – e. g. the tuning ratio not perfectly optimized – the frequencies of the particles becomes energy-dependent (for details see appendix A). Magnetic field inhomogeneities will amplify this effect. Therefore, a broadband dipole excitation in the radial direction will spread the ion cloud into distinguishable peaks. It is now possible to remove single particles with a well-directed excitation at a fixed frequency. Repeating this procedure successively removes all but one proton from the trap.

- **Determination of the free cyclotron frequency ν_{c}:** The single proton is cooled to cryogenic temperatures by keeping it in resonance with the axial and cyclotron detection units simultaneously. The magnetron motion is cooled by repeatedly applying a quadrupole excitation at the sum frequency $\nu_{\mathrm{z}} + \nu_-$ and thus transferring energy between the axial and the magnetron eigenmodes. Once the particle is in thermal equilibrium with the detection unit, it can be detected as a dip in the noise spectrum of the axial resonance circuit yielding the particle's frequency ν_{z}. The cyclotron frequency ν_+ is determined by first exciting this motion and

monitoring the subsequent cooling. While the particle is cooled, the cyclotron frequency changes and the amplitude of the signal decreases until the particle disappears in the noise spectrum of the cyclotron resonance circuit. When plotting the temporal frequency change, this end point corresponds to cyclotron frequency of the cooled particle in the trap. The magnetron frequency is determined via a coupling to the axial motion. The three measured variables supply the free cyclotron frequency ν_c via the invariance theorem given in eq. (2.13).

- **Determination of the Larmor frequency ν_L:** Since the energy eigenstates of the two spin states are not directly accessible in the precision trap, the proton is transported adiabatically to the analysis trap where the inhomogeneous magnetic field B_2 couples the magnetic moment to the axial eigenmotion of the particle. Consequently, a measurement of the axial frequency ν_z provides the spin state. With this information at hand, the particle is brought back to the precision trap where it is again resistively cooled. Subsequently, the Larmor frequency ν_L is irradiated to induce a spin-flip transition, and the particle is probed in the analysis trap yet another time. Fluctuations, however, affect the particle's motion and can mock a transition. Therefore, it is indispensable that a spin-flip transition is performed in the analysis trap to unambiguously determine the spin state and if so confirm a transition. Since the exact frequency of the particle in the precision trap ν_L^{exp} is unknown, the described sequence is conducted repeatedly for different excitation frequencies $\nu_L \pm \delta$ to yield the spin-flip transition probability as a function of the spin precession frequency from which ν_L^{exp} is deduced.

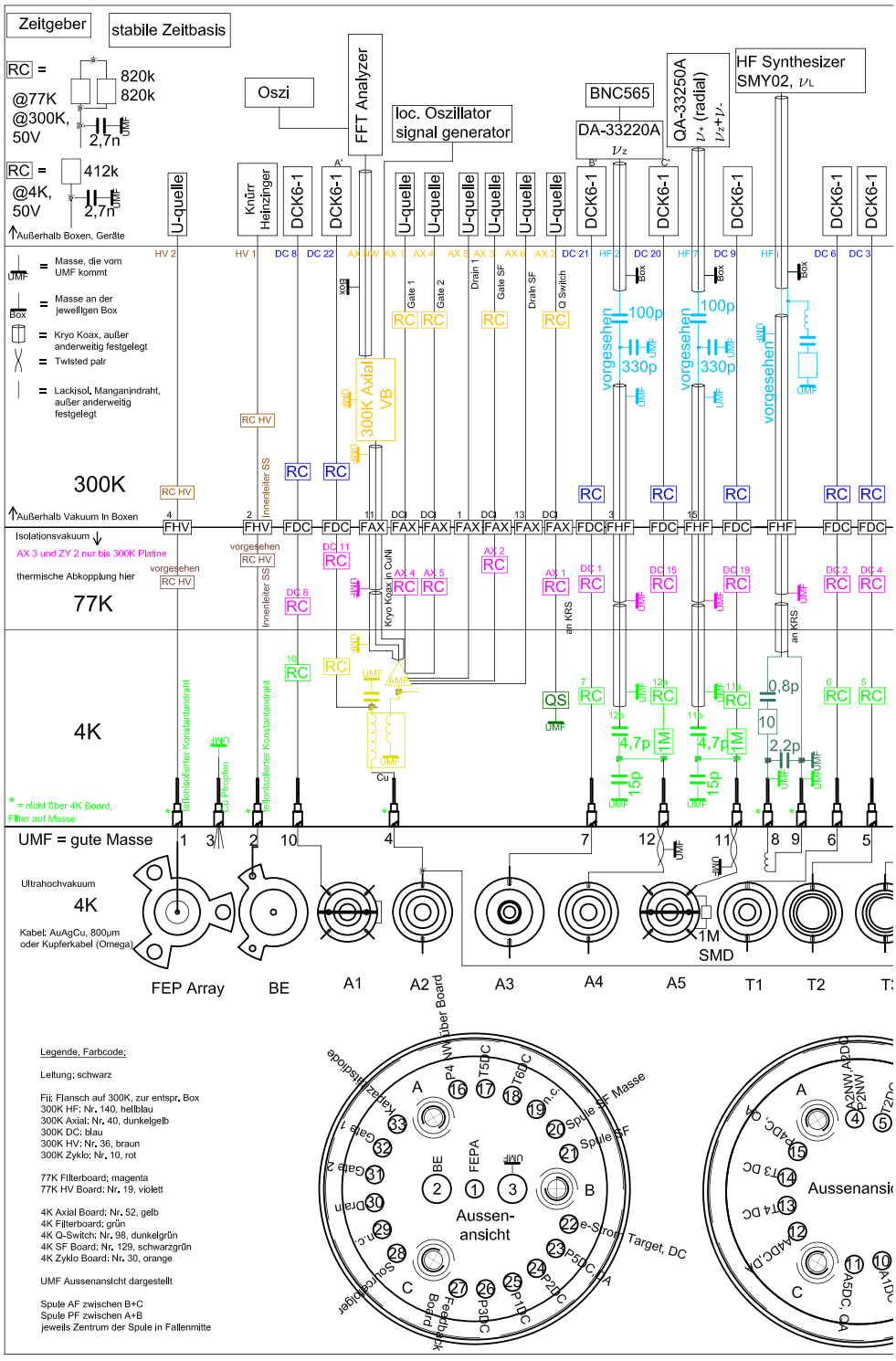

Figure 4.19: Connection diagram with color code for the different applications and temperature stages, left half of the diagram.

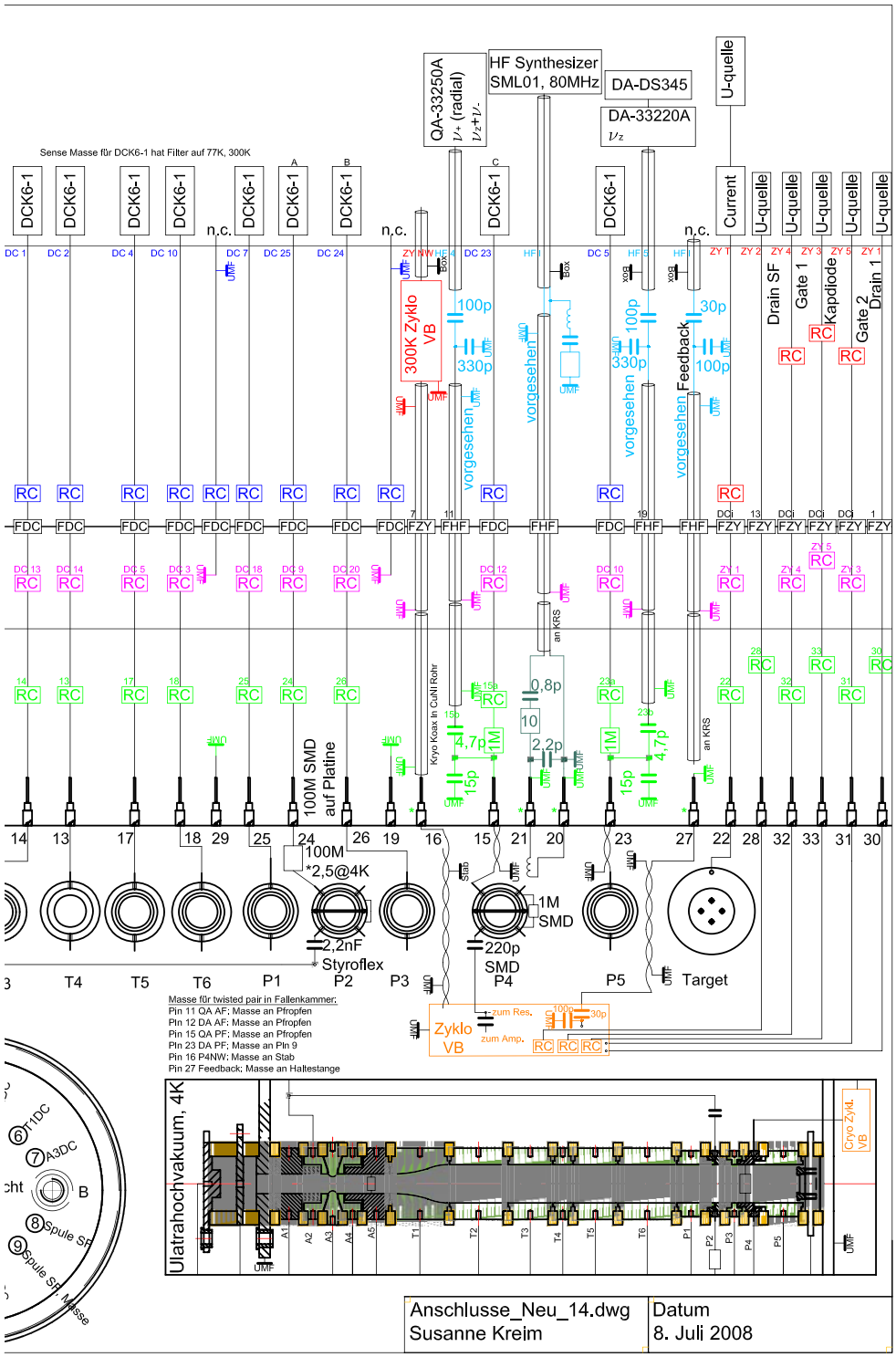

Figure 4.20: Connection diagram with color code for the different applications and temperature stages, right half of the diagram.

5 Detection of a Single Proton in the Precision Penning Trap

Up to now, all parts, which are needed to realize the measurement of the magnetic moment of a free proton, have been presented. The theoretical framework to create, trap, and detect protons has been reviewed, the hybrid trap required to perform and measure spin-flip transitions has been introduced, and the double Penning trap has been characterized. The essential components have been pieced together and various commissioning measurements assure the technical reliability of the experimental setup. It is now time to approach the experimental sequence discussed in the preceding chapter. According to section 4.7, I will present the first experimental data taken with the proton apparatus. The initial setting for the following measurements is a cryogenic ultra-high vacuum environment in the trap chamber with the system prepared as discussed in section 4.3.

5.1 Creation, Storage, and Detection of a Particle Ensemble

The electron beam ion source is put into operation to produce singly charged ions in the trapping potential of the precision trap. To this end, a five-pole cylindrical Penning trap is established by applying a voltage of $U_0 = -14\,\mathrm{V}$ to the ring electrode $P3$, a voltage of $U_\mathrm{c} = T_\mathrm{id}^\mathrm{pt} \cdot U_0 = -12.14\,\mathrm{V}$ to the correction electrodes $P2$ and $P4$, and by grounding the end caps $P1$ and $P5$ (for the tuning ratio cf. tab. 2.1, for nomenclature of electrodes cf. fig. 4.3). Here, the theoretically calculated, ideal tuning ratio for the precision trap is denoted by $T_\mathrm{id}^\mathrm{pt}$. Since all the presented measurements take place in the precision Penning trap the subscript pt is abandoned in the following. Subsequently, a high negative voltage of $U_\mathrm{AE} = -1.12\,\mathrm{kV}$ is applied to the acceleration electrode AE for 10 s yielding an electron current of about 200 nA. The emitted electrons are provided with a kinetic energy of 40 eV by applying $U_\mathrm{FEP} = -40\,\mathrm{V}$ to the field emission point FEP. After the electron gun is turned off, a mass spectrum in the axial mode is taken by varying the potential U_0 from $-14\,\mathrm{V}$ to $-2\,\mathrm{V}$ in 60 s while keeping the tuning ratio T_id constant. Whenever the axial frequency of an ensemble of particles reaches that of the axial detection system $\nu_\mathrm{z} \equiv \nu_\mathrm{z}^\mathrm{LC}$, they are detected as a peak in the spectrum of the circuit as their energy is much greater than the temperature of the cryogenic surrounding. Since the trapping potential $U_0 \propto m/q$ is proportional to the mass-to-charge ratio of the particles – see eq. (2.7) – the different trapped species can be identified.

Figure 5.1 shows such a mass spectrum of the axial mode taken in the precision Penning trap where protons (H^+) and molecular hydrogen ions (H_2^+) appear as expected at $U_0^\mathrm{cal} = -3.37\,\mathrm{V}$ and $U_0^\mathrm{cal} = -6.74\,\mathrm{V}$, respectively. Here, the superscript *cal* refers to

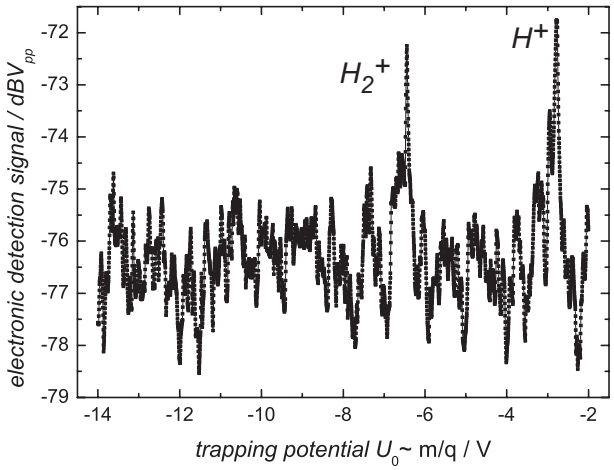

Figure 5.1: Mass spectrum of the axial mode in the precision Penning trap. According to the mass-to-charge ratio m/q, different species appear as peaks in the spectrum upon ramping the ring voltage U_0. In the spectrum presented, H^+- and H_2^+-ions are detected.

the theoretically calculated values for the trapping potential U_0. It is impossible that $^{12}C^{6+}$-, $^{16}O^{8+}$- or $^{12}C^{4+}$-ions are created and stored in the trap, which would appear at the same position as molecular hydrogen ions (H_2^+ or H_3^+). The third peak would appear at $U_0^{\mathrm{cal}} = -10.11\,\mathrm{V}$ showing all species with a mass-to-charge ratio of $m/q = 3$. The energy of the ionizing electrons is smaller than the electronic binding energies of the highly charged ions such that the ionization probability for preparing highly charged ions is negligible. The mass spectrum was taken without supplemental heating in terms of a dipole excitation in the axial mode.

5.2 Removing Impurity Ions

The particle ensemble shown in fig. 5.1 is subject to further investigation for obtaining a pure ensemble of protons. To this end, the proton ensemble is brought into resonance with the detection system, which has its frequency maximum at $\nu_{\mathrm{z}}^{\mathrm{LC}} = 688.15\,\mathrm{kHz}$ with a corresponding ring voltage of $U_0 = -3.35\,\mathrm{V}$ and a fixed tuning ratio of T_{id}. Since the anharmonicity contributions to the trapping potential can never be made zero, the particles' frequencies become a function of the eigenenergies, especially the axial frequency becomes a function of the cyclotron energy $\partial\nu_{\mathrm{z}}/\partial E_+ < 0$. Therefore, the ring voltage is set to $U_0 = -3.36\,\mathrm{V}$ yielding a deeper trapping potential, such that the frequency of the energetic protons moves towards the resonance frequency of the detection unit while being cooled. Subsequently, a dipole excitation is irradiated through the end cap $P5$ by sweeping the excitation frequency from 500 kHz to 1 kHz in 180 s with a power of 0 dBm. In this way, enough energy is transferred to all trapped species seeing the excitation in the axial motion such that they overcome the trapping potential and

leave the trap[1]. Later on, a mass spectrum is recorded by ramping the ring voltage U_0 from $-3.85\,\mathrm{V}$ to $-2.85\,\mathrm{V}$ within $10\,\mathrm{s}$ while irradiating an axial dipole excitation at $690\,\mathrm{kHz}$ with a power of $-40\,\mathrm{dBm}$. While the particles' frequency decreases, they first undergo the excitation which transfers sufficient energy in E_z to heat them such that the signal rises above the noise level. Second, the particles are detected by the resonance circuit while being resistively cooled, i. e. the energy in the corresponding motion is reduced. This happens with each particle at its respective frequency resulting in a peak in the mass spectrum, which is shown in fig. 5.2. The ensemble of energetic protons is clearly visible, the peak with a full-width-at-half-maximum (FWHM) of about $30\,\mathrm{mV}$ indicating a particle number of roughly 100. Moreover, a mass spectrum (not shown) was taken by ramping the ring voltage from $-14\,\mathrm{V}$ to $-2\,\mathrm{V}$ to ensure that other species are no longer present in the trap.

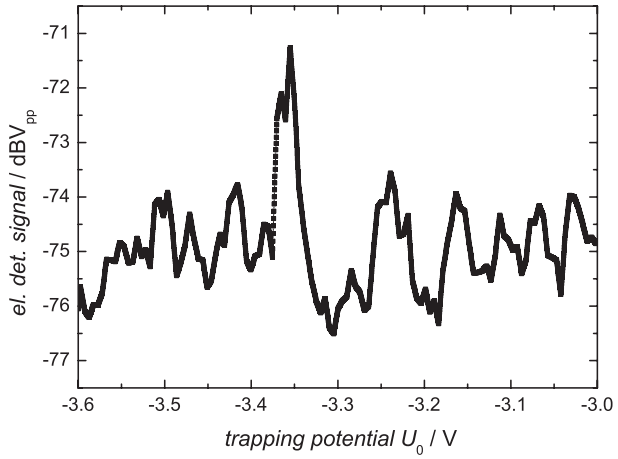

Figure 5.2: A mass spectrum of the axial motion in the precision Penning trap is shown where solely an ensemble of protons is present after removing impurity ions from the trap. The peak width of about $30\,\mathrm{mV}$ indicates a particle number of roughly 100.

The protons emitted from the target and stored in the precision trap are in the first instance very energetic particles. For further data acquisition and especially for an increase in measuring accuracy, the protons in the pure ensemble need to be resistively cooled in all eigenmotions. Figure 5.3 shows a proton ensemble before (red) and after (blue) resistively cooling of two of the three eigenmodes in the sense explained above. In this example, the FWHM of the red curve of $150\,\mathrm{mV}$ indicates more likely a particle number of 1000, considerably more than in the mass spectrum shown in fig. 5.2 and the spectra were taken with different initial conditions, thus the differing detection voltage. Furthermore, a different amplifier at room temperature was employed accounting for the differing background noise level.

[1]The power given in the text is the effective power applied to the electronic boxes. Further attenuation within the apparatus has to be considered additionally.

After having prepared a pure proton ensemble, the cyclotron motion is excited with a dipole excitation through the split correction electrode $P4$ with a span of 10 kHz and a power of -55 dBm, irradiated within 20 s. Subsequently, the particles are allowed to resistively cool into thermal equilibrium with the cyclotron resonance circuit with a cooling time of roughly 60 s. The magnetron motion is cooled via sideband cooling at a frequency of $\nu_z + \nu_- = 696$ kHz with a power of -45 dBm. After having excited the axial motion, the mass spectrum exhibits a FWHM of only 60 mV motivating the use of cooling prior to conducting other examinations. For further measurements, a notch filter was integrated in the routine. Since it attenuates only a small frequency range – in our case a few kHz around the proton frequency of 680 kHz – it is suitable for removing unwanted species.

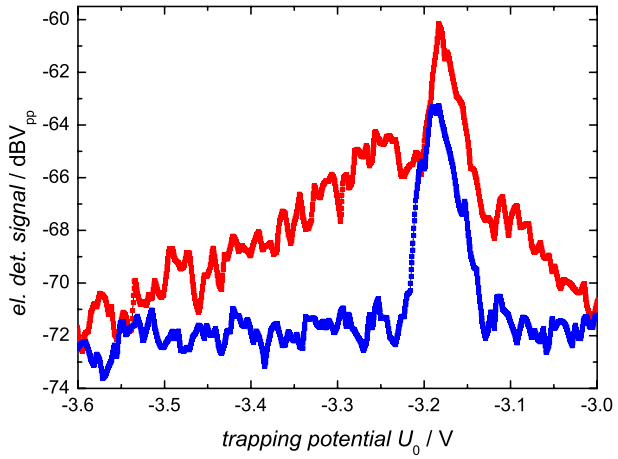

Figure 5.3: An ensemble of protons is shown before (red) and after (blue) resistive cooling of the three eigenmodes. For more details, see text.

5.3 Observation of Individual Protons

With a pure proton ensemble prepared in the trap, it is now feasible to determine their cyclotron frequency using a dipole excitation through the split correction electrode $P4$ which excites the energy and increases the cyclotron energy E_+. To this end, the trap depth is lowered by applying $U_0 = -14$ V to the ring electrode corresponding to a cyclotron frequency of $\nu_+ = 28.922$ MHz. Thus, it raises the margin for optimizing the experimental routine. In addition, it prolongates the cooling time since the particle peak is located on one shoulder of the resonance curve of the circuit. Consequently, a frequency sweep is employed around the cyclotron frequency ν_+ with a span of $10 - 20$ kHz for $10 - 20$ s and a power ranging from -55 dBm to -35 dBm to increase E_+. It is expected that a peak appears in the noise spectrum of the cyclotron detection unit which splits up into various peaks once the particle number has reached a sufficiently small number of a few tens of particles. During the irradiation each particle experiences the radial

excitation according to its relative phase. Hence, the particles within the ensemble are excited with varying efficiency and appear at different frequencies in the spectrum as seen from fig. 5.4a. The rising slope in the noise spectrum from left to right denotes the left shoulder of the resonance curve of the detection unit. Following figs. 5.4b and 5.4c, the peaks move closer together and towards higher frequencies while the particles are being resistively cooled by the cyclotron resonance circuit. After roughly ten minutes solely one peak is left which does not undergo further cooling but remains as such as seen from fig. 5.4d. Please note, that the area integral does not remain constant during data acquisition due to the cooling process. Usually, no particles are lost during the cooling of the cyclotron motion. Within the spectra of fig. 5.4 the peaks move towards higher frequency during cooling which indicates that a magnetic inhomogeneity is present, i. e. $B_2 < 0$. The relativistic effect leads into the same direction, however, it is calculated to be much smaller than the measured drift (cf. appendix A).

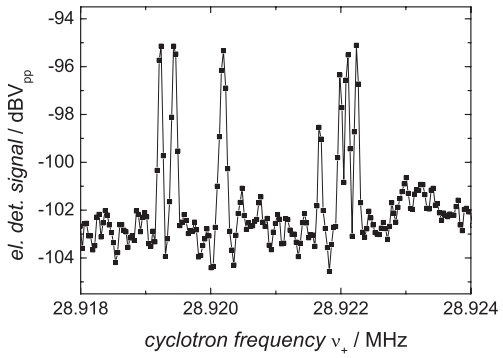

(a) Proton ensemble directly after dipole excitation, particles are split up into several peaks.

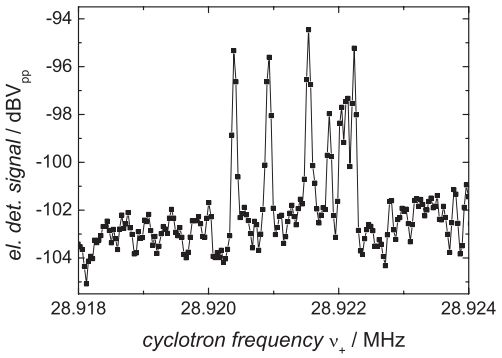

(b) Proton ensemble three minutes after excitation, particles are being cooled.

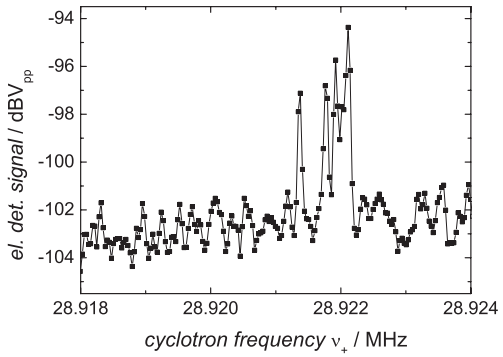

(c) Three more minutes later, peaks move together and towards higher frequency.

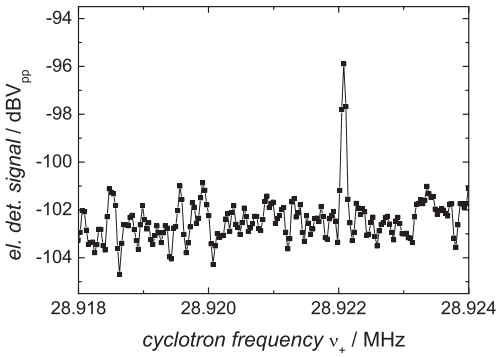

(d) Proton ensemble reunited and cooled, shot taken 15 minutes after excitation.

Figure 5.4: Dipole excitation of the cyclotron motion: the proton ensemble is split up into different peaks which reunite to one peak while experiencing cooling through the cyclotron detection unit.

In addition, a pure proton ensemble facilitates the search for a particle dip in the noise

spectrum of the axial detection unit (for a detailed explanation of the detection technique, turn to section 2.3.2). To detect a particle dip, the energy in all three eigenmodes has to be minimized. For this purpose, the cyclotron motion of the particle ensemble is cooled to reduce the cyclotron energy E_+. The cooling limit is reached when the peak disappears in the noise spectrum or the frequency drift ceases. Under the present experimental conditions, a particle dip in the noise spectrum of the cyclotron detection unit could not be achieved since the cooling time is about three orders of magnitude larger than the axial cooling time resulting in a significantly more narrow dip. At the same time, the ring voltage is set to U_0 to also cool the axial motion. The magnetron motion is cooled via sideband cooling by irradiating the sum frequency $\nu_z + \nu_-$ into the trap employing the split correction electrode $P4$. This produces a quadrupole field in the $(r-z)$-plane which is able to couple the two motions. It produces spikes in the axial detection signal whenever energy is transferred from the magnetron motion (E_-) into the axial motion (E_z), which in turn is cooled by the axial detection unit. Repeating this several times cools the magnetron motion into thermal equilibrium with the circuit.

To observe the single particle dip in the noise spectrum of the resonance circuit, ring voltage U_0 and tuning ratio T are now tuned until a dip emerges. The signal height of the particle dip in the noise spectrum increases the better the trap is optimized, which in turn is used to determine the optimal trap parameters at the maximum height corresponding to a ring voltage of $U_0 = -3.35455\,\mathrm{V}$ with a tuning ratio of $T = 0.851$. These experimental values are used later on for preparing a single proton. The optimization routine for the trap will be tackled in the next chapter.

5.4 Isolation of a Single Proton

Systematically removing protons from the trap is achieved by the following experimental sequence: The proton ensemble is cooled in the three eigenmodes so that the motional amplitudes of each particle are reduced, and coupling between the eigenmodes is minimized. Furthermore, the particle ensemble is less susceptible to perturbations which cause unwanted particle loss. For the purpose of cooling the axial motion, ring voltage and tuning ratio are set to the above determined parameters cooling the particle ensemble into thermal equilibrium with the detection unit. After the ensemble is cooled, it is radially excited with a dipole excitation at the cyclotron frequency ν_+ while residing in a trapping potential applied to the ring electrode of $U_0 = -10\,\mathrm{V}$. Consequently, the ensemble splits up into different peaks which are detected with the cyclotron circuit. While several particles can thus be identified, a well-directed, pulsed, strong excitation with a span of about 10 kHz is aimed at one of the peaks. The motional amplitudes are so strongly excited that the particles can then leave the trap. It is reasonable to assume that the excitation hits the so-called heating frequency $\nu_+ + \nu_-$ transferring enough energy into the magnetron motion such that these particles leave the trap. Subsequently, the trapping potential at the ring electrode is ramped back to U_0 to cool all eigenmodes and detect cyclotron and axial motion of the particle ensemble. The conventional method of evaporative cooling could also be employed, however, ramping the potential turned out

to be not as selective as the presented method.

Figure 5.5 shows such a sequence with the detected cyclotron motion on the left and the detected axial motion on the right side. Cyclotron and axial motion were monitored consecutively, not at the same time. The first two graphs (a, b) show an ensemble of a few tens of protons detected as a peak in the cyclotron motion and as a particle dip in the axial motion, respectively. They are followed by the spectra for three particles (c, d) and two particles (e, f). The sequence concludes with the spectra for one particle (g, h). The apparent broadening of the single particle peaks in the cyclotron mode arises from the fact that the spectrum is recorded while the particle is being cooled. The cyclotron frequency ν_+ is determined as the mean value of several single particle spectra as will be discussed in section 5.5. In the spectra on the right, the resonance structure of the detection circuit is shown in whose center the particle dip emerges. Please note, that the axial spectrum of two particles was taken with a different amplifier at room temperature, thus the higher signal. The axial frequency ν_z is determined from several single particle dip spectra.

5.4.1 Storage Time

It is routinely possible to repeatedly prepare a single proton in the precision Penning trap within a few hours. The storage time is usually on the order of days but not yet limited by the ultra-high vacuum, the particle is usually lost by attempts to optimize the experimental routine. From what has been measured so far, it is possible to give a first estimate on the pressure in the trap chamber. Following Diederich in "Observing a single hydrogen-like ion in a Penning trap" [70], an upper limit of $p < 10^{-14}$ mbar can be given. Accomplishing a similar measurement with a single proton stored in a Penning trap would require much longer measuring time since the charge exchange cross section is much smaller compared to $^{12}C^{5+}$. Gabrielse and co-workers reported an even lower value for the upper limit of $7 \cdot 10^{-17}$ mbar, which was determined during measurements concerning the antiproton mass [71]. Within the scope of this work a more detailed investigation of storage times was not pursued since in the context of the work presented here the storage time was never a limitation.

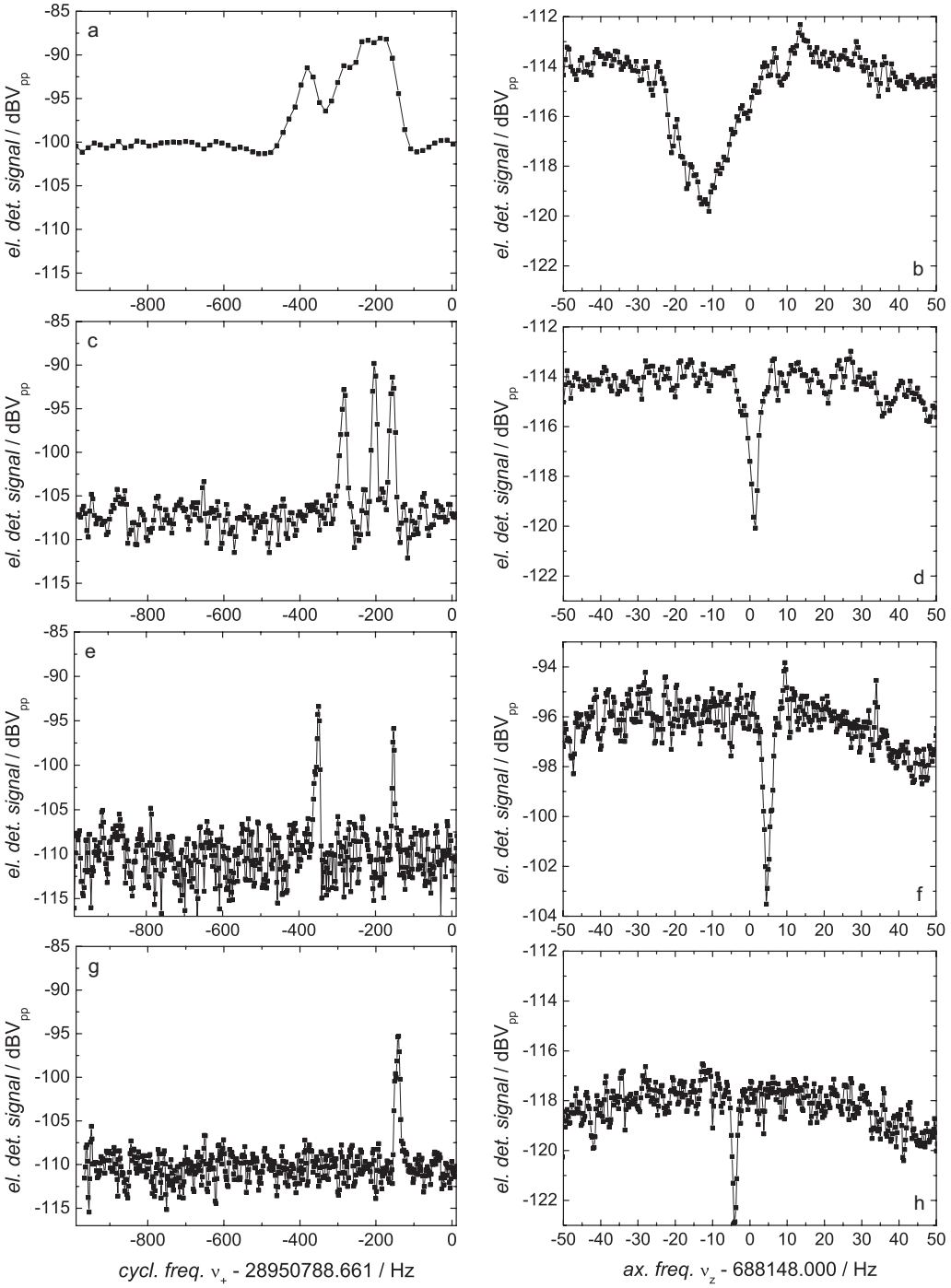

Figure 5.5: Successive reduction of the particle number from a proton ensemble of some ten particles to a single proton. On the left, the detection of the cyclotron motion as a peak in the noise spectrum is shown, on the right the detection of the axial motion as a particle dip in the noise spectrum. For further details, see text.

5.5 Eigenfrequencies of a Single Proton

A single, isolated proton prepared in the precision Penning trap allows for taking data towards the actual g-factor measurement and collecting statistics. Since the three eigenfrequencies of the particle in the trap provide us with the free cyclotron frequency ν_c needed to extract the g-factor – cf. eq. (1.6) – it is imperative to determine them with a very low uncertainty. The cyclotron frequency ν_+ has to be determined with the highest precision because it has the largest effect. After cooling of the three eigenmodes and subsequent excitation of the cyclotron motion, the particle signature appears as a peak in the noise spectrum of the cyclotron resonator and is cooled into thermal equilibrium with the circuit according to eq. (2.27). As long as the energy diminishes, the temporal cyclotron frequency change is recorded to determine the resistive cooling time constant τ_+ and the cyclotron frequency ν_+.

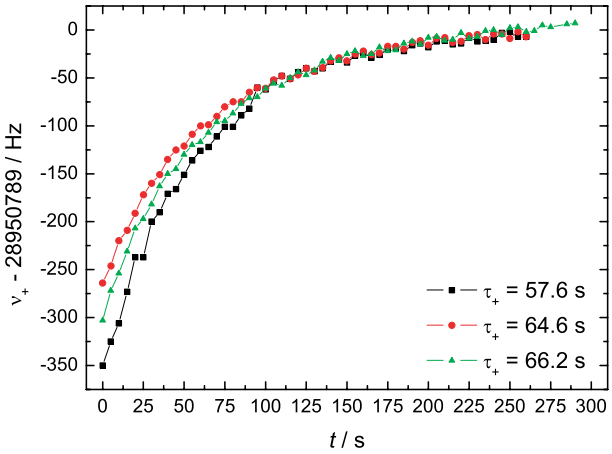

Figure 5.6: Temporal cyclotron frequency change while the single particle is cooled into thermal equilibrium with the resonance circuit. The three curves in red, black, and green denote three individual measurements carried out with the same single proton stored in the trap.

Figure 5.6 shows such curves of three consecutive measurements with a single particle trapped in the precision trap following the outlined routine. Although the starting energy is different for each measurement, after each excitation and cooling cycle the amplitudes approximate the same value of roughly $6\,\mu V_{pp}$ before disappearing in the noise spectrum. The requirement for a reliable data analysis of the same axial frequency is fulfilled within 3 Hz. Every data set is fitted with the function $\nu(t) = A{\cdot}e^{-t/\tau_+} + \nu_+$, where A corresponds to the initial amplitude. The value for ν_+ results from an extrapolation of time $t \to \infty$ and energy $E \to 0$. From these measurement, the mean value of the extrapolated values of the cyclotron frequency is determined to $\overline{\nu_+} = (28\,950\,788.7 \pm 4.3)$ Hz, which is chosen to be the zero on the y-axis of the plot. The resistive cooling time constant follows from the fits as $\overline{\tau_+} = (62.8 \pm 4.6)$ s, which is a reliable value in that sense that the determined cyclotron frequency lies well within the 3 dB-width of the detection circuit's

resonance. The cyclotron frequency is less than 3 kHz away from the resonance frequency of $\nu_+^{\mathrm{LC}} = 28.9475\,\mathrm{MHz}$, which is about 10% of the line width of the circuit resonance of $\Delta\nu_+^{\mathrm{LC}} = 30\,\mathrm{kHz}$.

The determination of the axial motion is achieved in a different way since the particle is detected as a dip in the noise spectrum of the detection unit. As described above, a particle cooled in all eigenmodes into thermal equilibrium with both detection units is the basis for detecting a particle dip. After the cyclotron motion has been cooled into thermal equilibrium and while the axial motion of the particle is resistively cooled, the single particle dip develops. Subsequently, the magnetron motion is cooled until the noise increase in the axial spectrum has disappeared and it can be assumed to be in thermal equilibrium with the axial detection unit. A single particle dip in the noise spectrum of the resonance circuit is recorded as seen in fig. 5.7a and fitted as a first ansatz with a simple inverted peak function

$$f(\nu) = U_0^{\mathrm{LC}} + 2\,A/\pi \cdot w/(4(\nu - \nu_{\mathrm{z}})^2 + \Delta\nu_{\mathrm{z}}^2)$$

taking ±50 data points around the center to determine the width of the particle dip. Here, U_0^{LC} denotes the baseline and A the amplitude. In this particular example, the center frequency is determined to be $\nu_{\mathrm{z}} = (688\,149.56 \pm 0.04)\,\mathrm{Hz}$ with a width of $\Delta\nu_{\mathrm{z}} = 0.99 \pm 0.13$. Figure 5.7b shows a zoom with only ±20 Hz around the center of the dip from which can be seen that a data point was taken every 250 mHz and that the fit follows nicely the dip signature. Considering several spectra for data analysis leads to an axial frequency of $\overline{\nu_{\mathrm{z}}} = (688\,149.5 \pm 0.1)\,\mathrm{Hz}$ and a width of $\overline{\Delta\nu_{\mathrm{z}}} = (1.0 \pm 0.1)\,\mathrm{Hz}$.

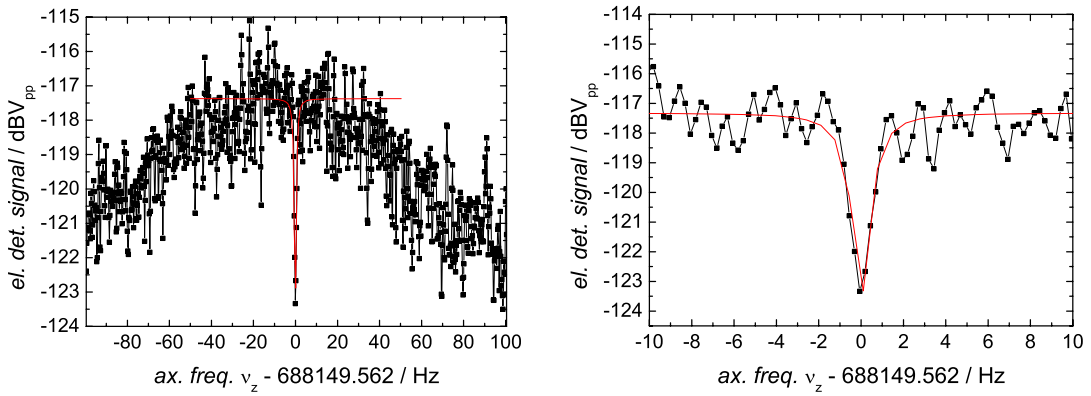

(a) Single particle dip in the noise spectrum of the axial detection circuit.

(b) Zoom into the noise spectrum with ±10 Hz around the dip center.

Figure 5.7: Detection of the axial motion of a single proton. (a) A single particle dip is shown with the respective Lorentzian fit. (b) A zoom with ±10 Hz around the dip center with the respective fit. A data point was taken every 250 mHz ensuring sufficient data points within the particle dip.

To decide whether the recorded spectrum is that of a single particle, the expected line width of the particle dip has to be considered which is calculated from eq. (2.35)

to $\Delta\nu_z = 1.5\,\mathrm{Hz}$ following eq. (4.6). To receive reliable evidence, different numbers of particles are prepared in the trap and a particle dip is recorded several times for each of them. Figure 5.8 shows the result of the respective Lorentzian fits for one, two, and three particles where the particle number was also determined by the number of cyclotron peaks as seen from fig. 5.5. The Lorentzian fit is a suitable lead since the extrapolation to zero particles yields a width of 0. It can be used to decide whether there is one proton present in the trap and to roughly discriminate between different particle numbers. Moreover, it is very unlikely that other particles are present in the trap. Singly charged impurity ions like $^{12}C^+$ or $^{16}O^+$, which cannot be detected with the implemented voltage source, would otherwise disturb the single proton causing frequency shifts due to Coulomb-Coulomb interaction and confounding a single particle dip measurement. However, for further data analysis, the Lorentzian fit does not deliver satisfying results which will be the topic of the following section.

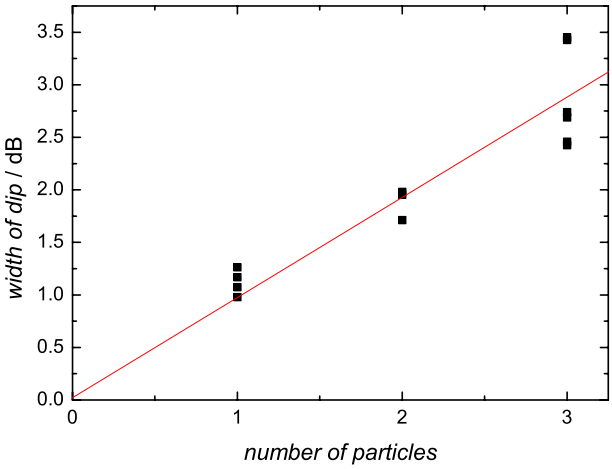

Figure 5.8: Performing a Lorentzian fit for several particle dips with different particle numbers results in the above graph, where the width of the particle dip $\Delta\nu$ is plotted as a function of the number of particles present in the trap together with a linear fit.

Please note, that the width of a single particle dip is on the order of $(1.0 \pm 0.1)\,\mathrm{Hz}$, which is considerably smaller than the calculated width of $\Delta\nu_z = 1.5\,\mathrm{Hz}$. This may be caused by the fact that the parallel resistance in resonance R_p^z is smaller than previously determined. The experimentally determined line width can be used to derive a more reasonable value for the parallel resistance in resonance. According to eq. (2.35), the resistive cooling time constant τ_z can be calculated from the measured line width yielding $\tau_z^{\mathrm{exp}} = 159\,\mathrm{ms}$. With an effective electrode distance of $D_{pt}^z = 7.37\,\mathrm{mm}$, the parallel resistance in resonance can hence be computed to $R_p^z = 22\,\mathrm{M\Omega}$,

As the last of the three eigenmodes, the magnetron frequency ν_- has to be considered, which is measured via a coupling to the axial motion at $\nu_z + \nu_-$ and $\nu_z - \nu_-$ enabling the detection as sidebands in the noise spectrum. Using the differential as well as the

summated result leads to a mean value of $\nu_- = (8\,679 \pm 202)\,\mathrm{Hz}$ for the magnetron motion. The apparently large error arises from the lack of cooling the eigenmotions, however, the effect on the free cyclotron frequency is negligibly small if the invariance theorem is employed as will become clear in section 5.5.2.

5.5.1 Investigation of the Single Particle Dip

A more sophisticated method for analyzing the data of the single particle dip is given by applying the tank circuit model to particles in a Penning trap [72]. It makes use of the fact that upon detection the particle is in thermal equilibrium with the axial detection unit. Hence, the impedance is made up not only of the parameters of the detection system, C_L^z and R_p^z from section 4.4.1, but also of those of the equivalent series circuit of the particle L_1, C_1, and R_1, cf. eq. (2.34). The single particle inductance is given by $L_1 = m_\mathrm{p}\,(D_\mathrm{pt}^\mathrm{z}/q)^2$, where m_p and q denote mass and charge of the proton, respectively. The effective electrode distance in axial direction for the precision trap is indicated by D_pt^z. The required single particle resistance can be computed via $R_1 = 2\pi\nu_\mathrm{z}\,L_1\,/\,Q_1$ if Q_1 were known. Yet, the resistive cooling time constant of both systems coincides allowing for putting $Q_1 = \nu_\mathrm{z}\,/\,\Delta\nu = 2\pi\tau_\mathrm{z}$ with τ_z from eq. (4.6) resulting in

$$R_1 = \frac{\nu_\mathrm{z}\,L_1}{\nu_\mathrm{z}}\,\frac{Z(\nu_\mathrm{z})\,q^2}{(D_\mathrm{pt}^\mathrm{z})^2\,m} = Z(\nu_\mathrm{z})\,. \tag{5.1}$$

Thus, the impedance of the detection unit can be used as the resistance of the particle at the respective axial frequency ν_z of the particle. Further parameters, which enter the consideration, are the particle number n yielding $R_n = R_1/n$ for more than one particle as well as the scaling factor A. The latter is necessary since the fitting data are recorded in units of voltage including according to $U = Z \cdot I$ not only the impedance but also the current I. It is therefore impossible to discriminate between particle current and any irregularities in the formula. Finally, the general fitting function for the impedance as a function of the frequency $Z(\nu)$ can be given with the fitting parameters n, A, and ν_z:

$$Z(\nu, \nu_\mathrm{z}, n, A) = \left| \frac{A}{\frac{n}{R_1(\nu_\mathrm{z}) + 2\pi\nu\,L_1\,I + \frac{1}{2\pi\nu\,C_1(\nu_\mathrm{z})\,I}} + \frac{1}{R_\mathrm{p}^\mathrm{z}} + \frac{1}{2\pi\nu\,L_\mathrm{z}\,I} + 2\pi\nu\,C_\mathrm{L}^\mathrm{z}} \right| . \tag{5.2}$$

The fitting function from eq. (5.2) can be used to fit not only symmetric but also dispersive line profiles. The results for a single particle are shown in fig. 5.9. In the case of the symmetric fit, the particle number yields $n = 0.97$. Several spectra have been treated that way resulting in a mean width of the single particle dip of $\overline{\Delta\nu} = (0.94 \pm 0.10)\,\mathrm{Hz}$. The measurements render possible a reliable method for determining the detected particle number which constitutes a good basis for gaining in precision and is subject to further investigation. The dispersive line profile shown in fig. 5.9b emerges whenever the frequency of the particle is detuned with respect to the resonance circuit's and nicely demonstrates a first attempt to tackle dispersive line profiles. It can be used to adjust the trap since a frequency shift arising from a tilt or the like can be easily identified.

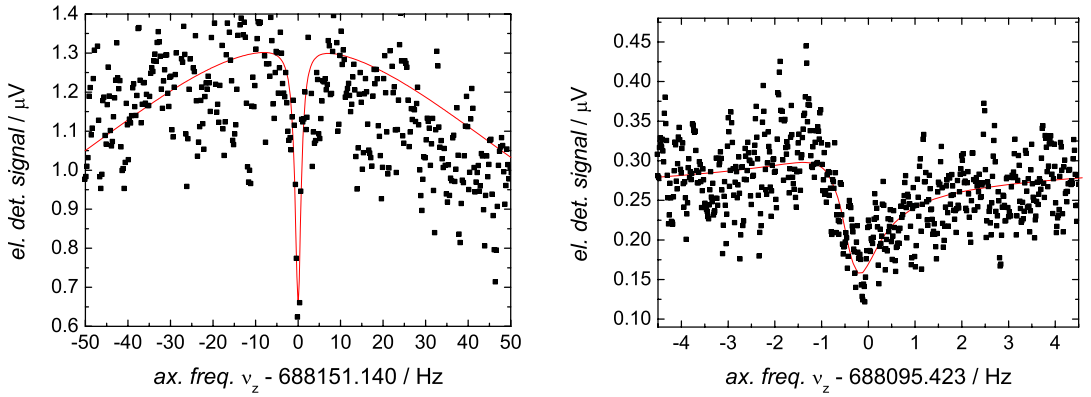

(a) Single particle dip at $U_0 = -3.35464\,\mathrm{V}$ with the fitting function $Z(\nu)$.

(b) Dispersive line profile at $U_0 = -3.35415\,\mathrm{V}$ with the fitting function $Z(\nu)$.

Figure 5.9: Detection of a single particle in the axial noise spectrum as a particle dip and a dispersive line profile with a tuning ratio of $T = 0.8515$. The data have been fitted with the fitting function $Z(\nu)$ of eq. (5.2).

For a high-precision measurement the particle signal not only has to be of good quality but also has to exhibit a high stability in time. To test the time stability, multiple single particle dip spectra have been recorded during a night for almost seven hours. For each recorded spectrum the center frequency of the single particle dip in the noise spectrum of the resonance circuit is determined. The measurement has been conducted in the ultra-high precision mode of the temperature stabilized voltage source. For a typical time scale of one minute, the center frequency exhibits a stability of $5 \cdot 10^{-3}\,\mathrm{Hz}$. This relates to a relative uncertainty in the determination of the axial frequency of $7 \cdot 10^{-9}$ which is not a limiting factor in the axial frequency determination.

5.5.2 Determination of the Free Cyclotron Frequency

After having measured the three eigenfrequencies of a single proton in the precision trap, the free cyclotron frequency ν_c can be calculated using the invariance theorem from eq. (2.13). The eigenfrequencies do not each have to be known with the same uncertainty since their contribution to the free cyclotron frequency is different. This becomes apparent upon looking at the relative error of the free cyclotron frequency determined using conventional error calculation

$$\frac{\Delta\nu_\mathrm{c}}{\nu_\mathrm{c}} = \underbrace{\left(\frac{\nu_+}{\nu_\mathrm{c}}\right)^2}_{\approx 1} \frac{\Delta\nu_+}{\nu_+} + \underbrace{\left(\frac{\nu_\mathrm{z}}{\nu_\mathrm{c}}\right)^2}_{\approx 10^{-4}} \frac{\Delta\nu_\mathrm{z}}{\nu_\mathrm{z}} + \underbrace{\left(\frac{\nu_-}{\nu_\mathrm{c}}\right)^2}_{\approx 10^{-8}} \frac{\Delta\nu_-}{\nu_-}\,. \tag{5.3}$$

Looking at the relative error in the free cyclotron frequency provides a first valuation of the uncertainty that can be reached with this experimental setup in the precision trap. Table 5.1 shows frequency measurements from three different days which allow for the derivation of the free cyclotron frequency. Each frequency determination arises from

taking the mean value of several individual measurements, performed consecutively at a single proton. As the eigenmodes have been measured at different trapping voltages U_0 they have to be scaled to the same ring voltage U_0 before calculating the free cyclotron frequency ν_c. Since the calculation depends most sensitively on the cyclotron frequency ν_+, the other eigenfrequencies are scaled to that respective trapping potential $U_0(\nu_+)$. In the case of the magnetron frequency, it is scaled by the measured frequency shift per voltage of 2.4 Hz/mV since scaling is tedious without knowledge of the magnetic field. The error arising from the shift of $\Delta\nu_- \,/\, \Delta U_0$ upon going to a different voltage is negligible compared to the error in the magnetron frequency itself. Please note, that the magnetron frequency was measured prior to cooling the different eigenmotions resulting in such a high error. Its effect on the free cyclotron frequency, however, is negligible due to eq. (5.3). The results from calculating the free cyclotron frequency ν_c with the invariance theorem are listed in tab. 5.1 together with the relative error $\Delta\nu_c$. Moreover, the magnetic field of the superconducting magnet B_0 can be deduced from ν_c using eq. (1.2) with the same uncertainty. The performed measurements demonstrate nicely how the uncertainty of the measured eigenfrequencies decreases with increasing expertise and knowledge of the experiment.

The results just discussed are based on data with little statistical information collected. During each measurement, the experimental conditions were very stable, however, the errors given in tab. 5.1 rather represent the fitting errors arising from the determination of the different frequencies than reliable standard deviations. In the near future, the experiment will be run over a long time span to produce better statistics. Systematic errors have not yet been taken into account. Comparing the two values of the free cyclotron frequency derived from measurements under similar experimental conditions, the relative error increases to low 10^{-6}. Although the two measurements cannot be used to derive a relative uncertainty, a more realistic error estimates leads to the supposition that the actual error of eq. (5.3) lies rather in the range of low 10^{-7}. A few examples of how to improve the measuring routine and the experimental setup will be given in chapter 7.

Nevertheless, it has been demonstrated that the free cyclotron frequency ν_c – one of the two ingredients needed to extract the g-factor – can generally be derived from the eigenfrequencies of the trapped proton with an uncertainty in the range of low 10^{-7}. The determination of the free cyclotron frequency can in turn be used to derive a drift in time of the magnetic field B_0. Comparing the data measured on July 15th with that measured on July 24th yields a drift in time of $(7.0 \pm 0.5) \cdot 10^{-7}\,/\,\mathrm{day}$, which agrees within 15% with the comparison done in section 4.2 with the shimming data. Albeit the experiment stands at the very beginning of data acquisition, already now it is possible to measure with a quite low uncertainty. The above presented evaluation sheds light on the envisaged high-precision measurement once systematics are under control and statistics are collected.

Table 5.1: Eigenfrequencies of a single proton in the precision trap with $T = 0.851$.

06/30/08	ν_i / Hz	U_0 / V	B_0 / μT
ν_-	$8\,679 \pm 202$	-3.349	
07/15/08			
ν_+	$28\,950\,788.7 \pm 4.3$	-3.35455	
ν_z	$688\,148 \pm 2$	-3.35455	
ν_c	$28\,958\,967 \pm 15$		$1\,899\,549.8 \pm 1.5$
07/24/08			
ν_+	$28\,950\,724.6 \pm 1.6$	-3.354845	
ν_z	$688\,180.1 \pm 0.1$	-3.354845	
ν_c	$28\,958\,902 \pm 6$		$1\,899\,543.0 \pm 0.6$

5.5.3 The Free Cyclotron Frequency as a Lead to Contact Potentials

In principle, there are two different ways of determining the free cyclotron frequency ν_c. Up to now, the three eigenfrequencies of the proton in the trap have been measured at a certain voltage U_0 applied to the ring electrode, and the experimental values have been used to compute the free cyclotron frequency ν_c according to the invariance theorem from eq. (2.13). It is also possible to measure the cyclotron frequency ν_+ for different values of the ring voltage U_0 and extrapolate to $U_0 = 0\,\mathrm{V}$ thus attaining the free cyclotron frequency ν_c. Comparing the two methods hints at possible contact potentials at the trapping electrodes. Figure 5.10 shows the cyclotron frequency ν_+ as a function of the voltage applied to the ring electrode U_0 measured within a few hours to the last measurement of tab. 5.1. A linear extrapolation (red curve) provides the free cyclotron frequency $\nu_c^{\mathrm{extr}} = (28\,959\,025 \pm 1)\,\mathrm{Hz}$ for $U_0 = 0\,\mathrm{V}$. This reveals a contact potential since it differs by 123 Hz from the calculated value of $\nu_c = 28\,958\,902\,\mathrm{Hz}$, corresponding to a contact potential of 50 mV. This measuring technique provides the resulting contact potential as the effective sum of possible contact potentials applied to the five trap electrodes. Further measurements indicate that not only a contact potential but also the proximity of the target gave rise to this discrepancy, which could be resolved in later measurements going beyond the scope of this work.

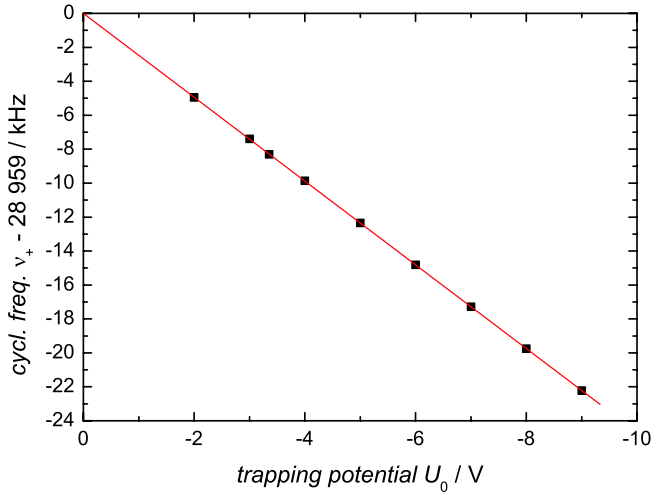

Figure 5.10: Cyclotron frequency ν_+ as a function of the voltage applied to the ring electrode U_0. The red curve denotes a linear extrapolation fitted to the data, where the intercept at the y-axis defines the zero in frequency.

6 Characterization of the Precision Penning Trap

The precision Penning trap was designed according to certain criteria explained thoroughly in section 2.2.2. For the envisaged high-precision measurement it is essential that the trap implemented into the experimental setup is optimized, the electrostatic properties are determined and under control. Once the axial motion of a single trapped particle has been detected, it is possible to use this detection signal for characterizing and tuning the trap. As a first step, the curvature of the potential – expressed by the C_2^{s}-coefficient – is determined. To this end, the axial frequency is measured for different values of the ring voltage U_0 with the tuning ratio fixed to $T = 0.851$. Subsequently, the C_2^{s}-coefficient is extracted with eqs. (2.7) and (2.23) to $C_2^{\mathrm{s}} = -(0.02747 \pm 0.0036)\,/\mathrm{mm}^2$. Within the error, the experimentally determined value coincides with the theoretically predicted one from tab. 2.1. All experimentally determined properties of the precision trap are listed in tab. 6.1.

6.1 Optimization of the Precision Penning Trap

An optimized Penning trap is the foundation for a high-precision measurement of a trapped particle because the potential is harmonic to a very high degree and the frequency dependence on motional amplitudes is minimized. Since the precision trap was designed as orthogonal and compensated, there exists a tuning ratio for which the trapping potential is maximally harmonic ($C_4^{\mathrm{s}} = C_6^{\mathrm{s}} = 0$) and the axial frequency neither depends on the voltage applied to the correction electrodes $\nu_{\mathrm{z}} \neq \nu_{\mathrm{z}}(U_{\mathrm{c}})$ nor on the cyclotron energy $\nu_{\mathrm{z}} \neq \nu_{\mathrm{z}}(E_+)$, cf. section 2.2.1. This tuning ratio has to be specified experimentally whereto the single particle dip in the noise spectrum of the axial detection unit is a very suitable basis: the more harmonic the trapping potential is, the deeper and narrower the single particle dip gets. In order to determine the optimal tuning ratio,

Table 6.1: Experimentally determined parameters of the precision trap

T	0.8510±0.0005	$D_{\mathrm{pt}}^{\mathrm{z}}$	8.99 mm
C_2^{s}	$-(0.02747\pm0.0036)\,/\mathrm{mm}^2$	$\frac{\Delta\nu_{\mathrm{z}}}{\Delta U_0}$	$-0.1\,\mathrm{Hz}/\mu\mathrm{V}$
D_2^{s}	$-(3.37\pm0.98)\cdot10^{-4}\,/\mathrm{mm}^2$	$\frac{\Delta\nu_{\mathrm{z}}}{\Delta T_{\mathrm{id}}^{\mathrm{pt}}}$	$-3.98\,\mathrm{Hz/mUnit}$
C_4^{s}	$-(5.41\pm0.17)\cdot10^{-5}\,/\mathrm{mm}^4$		

different tuning ratios are applied to the trap. Subsequently, the ring voltage U_0 is used to center the single particle dip in the noise spectrum of the resonance circuit, since the dip signature broadens if it is not properly centered. Then, the depth d as well as the width $\Delta\nu$ of the single particle dip are measured for the corresponding ring voltage U_0. Once the optimal tuning ratio is found, it can in turn be used to derive the expansion coefficient D_2^{s}. The following measurements were conducted in the UHP mode of the voltage source UM1-14 version DCK6-1.

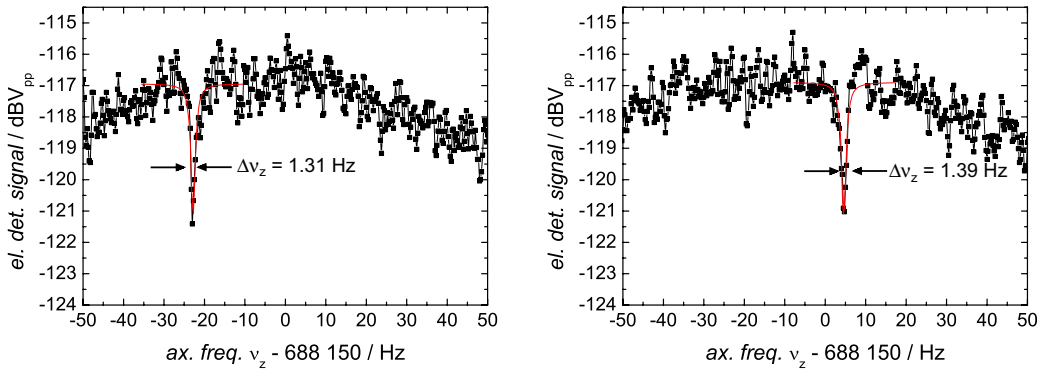

(a) $U_0 = -3.35455\,\mathrm{V}$, $d = 4.5\,\mathrm{dB}$

(b) $U_0 = -3.35478\,\mathrm{V}$, $d = 4.1\,\mathrm{dB}$

(c) $U_0 = -3.35473\,\mathrm{V}$, $d = 6.0\,\mathrm{dB}$

(d) $U_0 = -3.35463\,\mathrm{V}$, $d = 3.3\,\mathrm{dB}$

Figure 6.1: Single particle dips for different settings of the precision trap as part of an optimization measurement of the trap's electrostatic properties. The first three single particle dips were recorded for a tuning ratio of $T = 0.851$, the fourth one for $T = 0.850$. The red curves show the respective Lorentzian fit of the single particle dip. For more details, see text.

The first three graphs in fig. 6.1 show parts of the experimental sequence just outlined for a tuning ratio of $T = 0.851$. The ring voltage U_0 is tuned to center the single particle dip at $\nu_{\mathrm{z}}^{\mathrm{LC}} = 688\,150\,\mathrm{Hz}$, the center frequency of the axial resonator. In fig. 6.1a the ring voltage U_0 is set to a value for which the corresponding axial frequency of the particle ν_{z} is lower than $\nu_{\mathrm{z}}^{\mathrm{LC}}$ leading to a smeared particle signature. The same holds for fig. 6.1b where the axial frequency ν_{z} is higher than the resonance frequency of the

axial detection unit ν_z^{LC}. Both dip signatures are broader and flatter than the single particle dip of fig. 6.1c where the ring voltage is tuned in such a way that the particle's frequency coincides with the resonance circuit's. In this example, the center frequency ν_z^{LC} was hit by a few hundred mHz at $\nu_z = 688\,149.3\,\text{Hz}$ producing a single particle dip with a width of $\Delta\nu_z = 0.87\,\text{Hz}$ and a depth of $d = 6.03\,\text{dB}$ determined by a Lorentzian fit (red curve) which was performed for ± 50 data points around the center frequency. As a comparison, the fourth graph shows the centered single particle dip for a tuning ratio of $T = 0.850$. The single particle dip is located at $\nu_z = 688\,150\,\text{Hz}$ with a width of $\Delta\nu_z = 1.5\,\text{Hz}$ and a depth of $d = 3.33\,\text{dB}$ which clearly indicates a less optimized trap.

The sequence discussed on the basis of fig. 6.1 is iterated for different tuning ratios T. For each tuning ratio, several spectra are recorded and depth d as well as width $\Delta\nu_z$ of the single particle dip are extracted. Since the quality of the single particle dip depends on how well the particle frequency is centered, i. e. coincides with frequency ν_z^{LC} of the resonance circuit, it is crucial that the single particle dip appears at the same frequency in all spectra which was achieved within 300 mHz for a fixed tuning ratio. During the measurement series, however it was not possible to reproduce the exact frequency centering resulting in an effective center frequency of $\overline{\nu_z} = (688\,150.4 \pm 0.9)\,\text{Hz}$ was realized, the error arising from thermal fluctuations at room temperature at the time of this measurement, since the voltage source was not operated in the temperature stabilized mode. The results for seven different values of the tuning ratio are shown in fig. 6.2. As expected, the maximum in the depth d coincides with the minimum in the width $\Delta\nu_z$ allowing for a determination of the tuning ratio between $T = 0.851$ and $T = 0.852$. Fitting both data sets with different peak functions (Gauss and Lorentz) yields an optimal tuning ratio of $T = 0.8516 \pm 0.0002$ for the trap conditions at that time. As it is quite probable that contact potentials are generated differently at the trap electrodes with each loading of the trap with the electron beam ion source and since the optimal tuning ratio depends on the actual voltage applied to ring and correction electrodes, it may vary with every new start of the experimental sequence, cf. section 4.7. Therefore, the tuning ratio has to be optimized with each new run and may differ for the measurements discussed within this work. In conclusion, it has been demonstrated that this method is suitable to optimize the trap and determine the optimal tuning ratio.

Finally, the experimentally determined optimal tuning ratio of $T = 0.8510 \pm 5 \cdot 10^{-4}$ can now be exploited to determine an upper limit to the leading anharmonicity contribution given by the C_4^s-coefficient. The coefficient is calculated using eq. (2.21) leading to $C_4^s = -(5.41 \pm 0.17) \cdot 10^{-5}\,/\text{mm}^4$.

6.2 Determination of the Orthogonality of the Trap

The orthogonality of the trap – in other words the dependence of the axial frequency on the tuning ratio – is a property which very much facilitates data acquisition. On the one hand, without precise knowledge of the optimal tuning ratio, detection and identification of particles in the mass spectrum are still feasible. On the other hand, it is of great advantage that the measured variables solely depend on fluctuations of

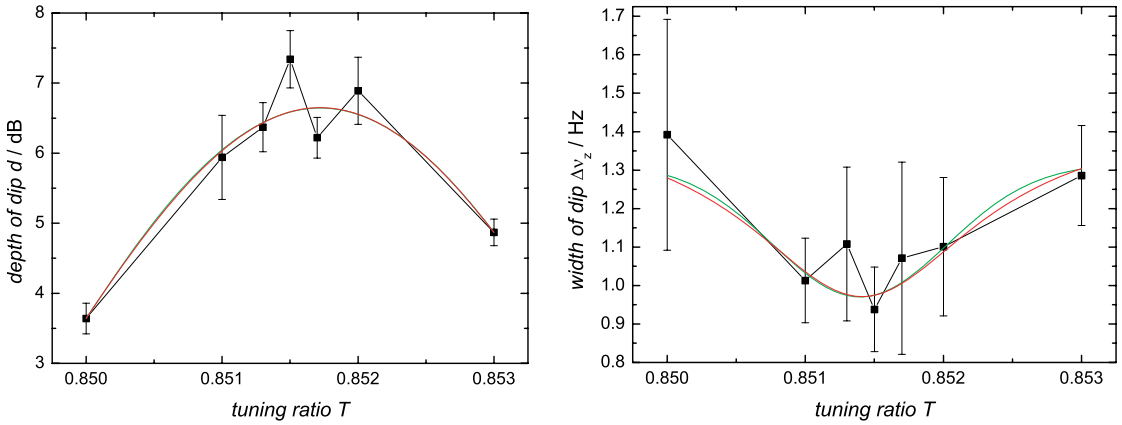

Figure 6.2: The two parameters depth d and the width $\Delta\nu_z$ of single particle dips are plotted for different tuning ratios T to determine the tuning ratio for which the trap is optimized.

one voltage applied, namely the ring voltage U_0. The leading expansion coefficient D_2^s from eq. (2.22) describing the degree of orthogonality enters in the calculation of the axial frequency ν_z since it is part of the expansion coefficient C_2^s from eq. (2.21). Again, eq. (2.7) is employed to express the voltage applied to the ring as a function of the tuning ratio where D_2^s enters as a parameter yet to be determined

$$U_0(T) = \frac{(2\pi\,\nu_z)^2\,m}{2\cdot 10^6\,q(E_2^s + D_2^s\cdot T)}\,. \tag{6.1}$$

To determine the orthogonality of the trap from the data of fig. 6.2, the ring voltage U_0 is extracted for each tuning ratio at which the single particle dip is centered in the noise spectrum of the circuit. The data points are plotted in fig. 6.3, where the error bars denote the uncertainty in the ring voltage U_0. The data are fitted with a rational fit function $U_0(T) = 1/(a + b\cdot T)$ (red curve). Through a comparison, the parameter b delivers the D_2^s-coefficient via

$$D_2^s = \frac{b\,m\,(2\pi\,\nu_z)^2}{2\cdot 10^6\,q} = -(3.37\pm 0.98)\cdot 10^{-4}/\mathrm{mm}^2\,. \tag{6.2}$$

From this, the orthogonality can be derived as $\Delta\nu_z\,/\,\Delta T = -3.98\,\mathrm{Hz/mUnit}$. This lies an order of magnitude above the theoretically predicted value of $\Delta\nu_z\,/\,\Delta T = -0.4\,\mathrm{Hz/mUnit}$, however, it shows nicely how an important trap property can be extracted from the optimization measurements performed. Certainly, there is room for improvements. For example, the frequency at which the particle has been detected varied from measurement to measurement leading to a mean value of $\overline{\nu_z} = (688\,150.4\pm 0.9)\,\mathrm{Hz}$ which inevitably led to a fake increase in the D_2^s-coefficient. Improvements towards a better temporal stability of the single particle dip concerning the voltage source have been discussed in section 4.3.2. Other improvements will be tackled in chapter 7.

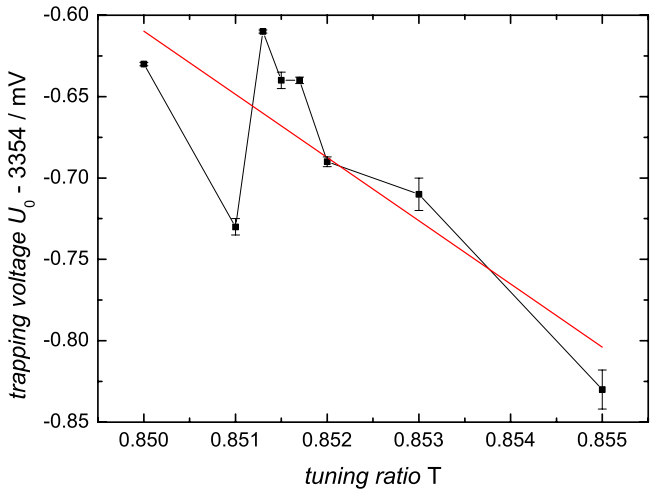

Figure 6.3: Voltage applied to the ring electrode U_0 for which the frequencies of single particle dip ν_z and resonance circuit ν_z^{LC} coincide as a function of the tuning ratio T. The red line is a rational fit function from which the expansion coefficient D_2^{s} is extracted.

6.3 Trap Imperfections

In a real trap, the electrostatic potential is never fully described by the expansion coefficients of eq. (2.21) of section 2.2.1, as machining errors, misalignment, voltage fluctuations or the like cause the experimentally determined coefficients to deviate from their calculated value. This constitutes a further reason as to why the experimentally determined coefficients presented above are different from the theoretical coefficients. The large discrepancy of the experimentally determined tuning ratio $T = 0.851$ from the theoretically calculated value of $T_{\mathrm{id}} = 0.867$ turns out to be caused by an incorrect positioning of the target too close to one of the end caps of the precision trap. Thus, the trap itself became asymmetric since one end was open, the other closed. With $T = 0.851$ it was possible to account for this asymmetry and detect the particle as a dip in the noise spectrum of the axial detection unit.

In general, an asymmetric potential can have various reasons which give rise to odd terms appearing in the expansion. If the end caps are affected, the shift is computed via c_k-coefficients, in the case of the correction electrodes via d_k-coefficients, following the calculations of Gabrielse in [43]. For $k = 1$, the axial equilibrium position of the particle will be shifted. Yet in this experiment, a large d_1-coefficient is favorable for electronic particle detection via a 01000-coupling in order to optimize detection sensitivity and resistive cooling of the axial motion, cf. section 2.3. The d_1-coefficient can be determined by employing the damping constant

$$\gamma_{\mathrm{z}}^{\mathrm{exp}} = \frac{q^2}{m}\,\frac{d_1^2}{4z_0^2}\,R_{\mathrm{p}}^{\mathrm{z}} = \frac{1}{\tau_{\mathrm{z}}^{\mathrm{exp}}}\,, \tag{6.3}$$

where the resistive cooling time constant $\tau_z^{exp} = 159\,\mathrm{ms}$ was experimentally determined from the single particle dip in the noise spectrum of the axial detection unit in the preceding chapter. It yields $d_1 = 0.8001$ which agrees with values measured in other cylindrical traps such as for example the one found ibid.

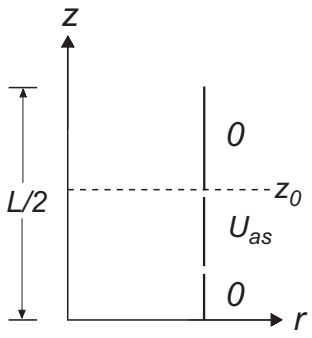

Figure 6.4: Asymmetric potential applied to the correction electrodes, symmetric under rotations about the z-axis and asymmetric under reflections across the $z = 0$ plane. Sketch of half the trap with length $L/2$.

The next contribution, $k = 3$, causes a shift in the axial frequency. If an asymmetric potential U_{as} is applied to the correction electrodes as seen in fig. 6.4 (cf. also fig. 2.3), it leads to a frequency shift in the axial motion of

$$\frac{\Delta\nu_z}{\nu_z} = -\frac{3}{4}\left(\frac{d}{z_0}\right)^4 d_1 d_3 \left(\frac{U_{as}}{U_0}\right)^2 , \tag{6.4}$$

from which the d_3-coefficient can be extracted. The measurement has been performed by applying different values of U_{as} to the correction electrodes and measuring the corresponding frequency shift $\Delta\nu_z$. However, these frequency shifts suggest an asymmetry which is unrealistic considering the trap geometry, the coefficient being more than an order of magnitude larger than in comparable traps. This is attributed to the proximity of the target and has to be remeasured once the trap tower is modified. Usually, the impact of a large d_3 (or c_3) is negligible since asymmetric potentials are not applied. However, since the two correction electrodes (and end caps) are supplied each by independent voltage channels, a systematic investigation of this effect is necessary to be able to identify an unwanted frequency shift arising from asymmetric voltage fluctuations to which only an upper limit can be given.

7 Conclusion and Perspective

Within this work, I have presented design, assembly, and commissioning of the experimental setup which is dedicated to the measurement of the proton g-factor. Feasibility studies and implementation of the required components have been completed, initial operation and first experimental results have been discussed. At present, the double Penning trap setup consisting of a conventional cylindrical trap and a novel hybrid trap has been successfully implemented into the cryogenic ultra-high vacuum chamber which in turn is surrounded by an elaborate insulating vacuum apparatus with an intermediate temperature stage. The electron beam ion source, which is integrated in the trap setup, allows for the creation of protons which can subsequently be stored in the precision trap. The production of a pure proton ensemble by removing impurity ions has been demonstrated and their eigenfrequencies have been detected with the respective non-destructive detection units.

It is now possible to isolate a single proton with a well-directed method and measure its eigenfrequencies in the precision Penning trap. These eigenfrequencies yield the free cyclotron frequency ν_c, one of the two frequencies needed to determine the g-factor. Although the experiment is in the fledgling stages, the first data I have taken with the experimental setup already allow for the determination of the eigenfrequencies in the precision trap down to a relative accuracy of 10^{-7} limited mainly by the few statistics collected. Extracting the free cyclotron frequency leads to the striking result of a relative uncertainty of only $2 \cdot 10^{-7}$. Gaining in experimental routine and realizing technical improvements will push this value towards the envisaged goal of 10^{-9}.

Monitoring the axial eigenfrequency enables the investigation of the trap's electrostatic properties. Important parameters of the precision trap have been specified such as the curvature of the potential, the orthogonality or the anharmonicity contribution. They allow for a comparison with the theoretically calculated values leading to an assessment of the geometric quality of the trap as well as the reliability of the theoretical derivation of chapter 2. Finally, trap imperfections have been analyzed yielding first estimates of the odd expansion coefficients of the potential, which in turn helps identifying possible frequency shifts.

The Larmor frequency ν_L – the other frequency entering eq. (1.6) to yield the g-factor – is determined by observing spin-flip transitions in the double Penning trap. The resonance circuit to drive the spin-flip transition is implemented, tested, and ready to be put into operation. The Larmor frequency has not been measured up to now since this step demands a fully characterized analysis trap and an adiabatically working single particle transport between the precision trap and the analysis trap.

The measurement sequence outlined in section 4.7 has been partly experimentally tested and established as became clear above. The next essential measure is the adiabatic

transport of a single proton. Transport simulation studies have been performed with SIMION and work is in progress towards an efficient transport of a particle ensemble, which can then be detected non-destructively in the analysis trap via the axial detection unit. An ensemble of protons has been transported from the precision trap towards the analysis trap, however, most of it is lost at the tapered electrode $T1$ (cf. fig. 4.3) due to a fast broadening of the magnetron motion. Detection of the proton ensemble as a peak in the noise spectrum of the axial detection unit has been achieved in the analysis trap with a copper ring instead of the ferromagnetic one. This drawback is being investigated. Meanwhile, it has been discovered that the ferromagnetic ring of the analysis trap is not the cause for the transport problems, since the same problems continue to exist after removal of the magnetic inhomogeneity. Attention is now turned to the tapered electrode which baffles the adiabatic transport in opposition to the simulations. At present, efforts are made towards a pulsed, non-adiabatic transport comparable with that at other Penning trap experiments. Once a particle ensemble is monitored in the analysis trap, the trap itself can be investigated. Characterization of the trap's properties and optimization of its parameters constitutes an obligatory test of the underlying theoretical derivation introduced in chapter 3 and comprises a feasibility study of the concept of hybrid Penning traps.

7.1 Further Developments at the Experimental Setup

In the following, I will discuss upcoming experimental measures and possible technical developments of the setup. During this first run of data acquisition, several ideas arose of how to improve the experimental setup, two of which I will elaborate on. As the measurements in chapters 4 and 5 have shown, the temperature stabilization of the voltage source is essential for reaching down to uncertainties better than 10^{-7}. A more sophisticated temperature stabilization including the ambient air of the laboratory is mandatory as has been discussed in section 4.3.2.

The cyclotron eigenmotion of the stored proton contributes dominantly to the determination of the free cyclotron frequency ν_c as became clear from eq. (5.3). It is measured by monitoring the temporal cyclotron frequency change while the single particle is resistively cooled into thermal equilibrium with the resonance circuit. A peculiar aspect is a periodic fluctuation of the frequency upon approaching the asymptotic limit. Figure 7.1 shows a single measurement of the temporal development of the cyclotron frequency of a single proton starting from $t = 100\,\mathrm{s}$ after excitation of the cyclotron frequency. The data have been split up in red and black data points to visualize a perturbation, which is transported to the trap via the mechanics of the heat conduction. The two curves correspond to vibrations of the pulse tube cooler arising from varying positioning of the piston during a cycle. Each data set has been fitted with an exponential decay denoted by the red and black curve, respectively, yielding a difference of 6 Hz in the determination of the cyclotron frequency: $\nu_+^{\mathrm{red}} = 28\,936\,824\,\mathrm{Hz}$ and $\nu_+^{\mathrm{black}} = 28\,936\,818\,\mathrm{Hz}$. Mechanical decoupling reduced the vibrations at the trap and enhanced the measurement accuracy leading to an uncertainty of only 2 Hz in the determination of the cyclotron frequency.

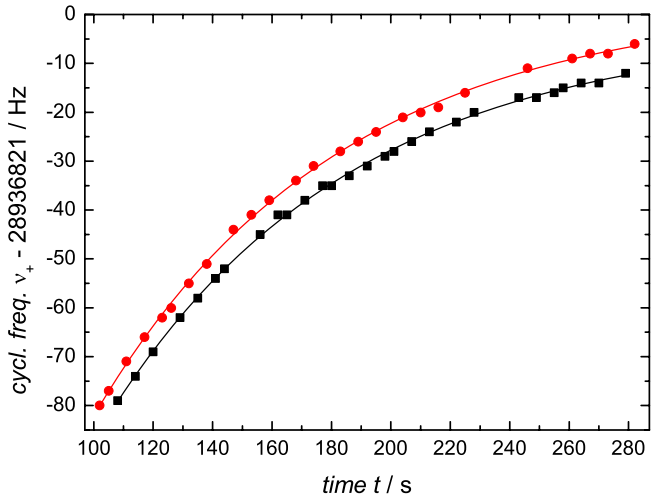

Figure 7.1: Temporal cyclotron frequency change while the single particle is cooled into thermal equilibrium with the resonance circuit. The curve of a single measurement is split up in red and black data sets to visualize the perturbation due to the vibration of the pulse tube cooler. The data are separately fitted with an exponential decay yielding a difference of 6 Hz in the cyclotron frequency.

Certainly, the further development of the computer control system is an issue. Data acquisition for frequency measurements is completed, the LABVIEW-based control system does not yet include all experimental sequences needed to perform the entire measurement. For example, the cyclotron excitation has been performed manually during the first run. Moreover, some electronic devices for the accomplishment of the continuous Stern-Gerlach effect are still missing.

Independent of the hitherto acquired data, the temperature of the stored particle – and hence that of the electronic detection units – is a parameter which quickly comes to mind when considering possible improvements. Performing the experiment at liquid helium temperature, fluctuations in the axial motion have to be taken into account arising from the considerably large amplitude of the particle of $z(4\,\mathrm{K}) \approx 40\,\mu\mathrm{m}$ according to eq. (2.48). Employing a He-3/He-4 mixing cryostat with a base temperature of a few tens of mK yields a particle amplitude of $\approx 4\,\mu\mathrm{m}$. In the precision trap, this gain of an order of magnitude is directly reflected in the influence of the B_2-term on the cyclotron frequency, a major contribution to the systematic error due to frequency shifts. Another possibility of reaching down to the mK-range is by the method of feedback cooling used in the experiments of Gabrielse [73].

Reaching down to even lower motional amplitudes can be achieved by means of sympathetic laser cooling using a single ion stored in a second Penning trap [74]. Heinzen and Wineland consider a source, i. e. in the case of this experiment the single proton, and a laser-cooled ion as a pair of coupled oscillators in the weak damping limit. The coupling can be switched on and off quickly compared with the exchange time t_{ex}. These conditions enable oscillatory exchange of energy between the two oscillators such that

the laser-cooled ion may be used to both cool and detect excitations in the source. The laser-cooled ion thus replaces the electronic detection unit. At first, the possibility of cooling alone is discussed where the ion is cooled to the zero-point state via sideband cooling while the oscillators are decoupled. The laser is then turned off and the coupling is switched on until the ion's zero-point state has been transferred to the source via image currents, i. e. until the exchange time has elapsed. Thus, the source resides in a well-defined quantum state. If, for example, the energy of the cyclotron eigenmotion of the stored proton is cooled into the zero-point state, the frequency shift of the axial motion due to a finite cyclotron energy is for all intents and purposes annihilated. Thus, it becomes possible to electronically detect the axial motion without this source of systematic error.

As a further step, detection is now included. To this end, both oscillators have to be prepared in the zero-point state and they have to be decoupled. Suppose now, that an external drive applied to the source puts at least one quantum of energy in its motion. This excitation can then be transferred to the ion by recoupling the two oscillators for a time t_{ex}. After the systems are again decoupled, the ion is probed using the sideband method. In the case of this experiment, a spin-flip is induced to the stored proton changing its quantum state. Thus, it becomes possible to map the internal degree of freedom onto another particle. The manipulated ion is then probed to read out the spin information.

For the detection of the axial eigenmotion, it is essential that the trapping potential is harmonic such that the frequency is not shifted even for large motional amplitudes z. However, an anharmonic contribution arising from finite values of the expansion coefficients C_4^{s} and C_6^{s} will always be present. If the trap is tuned in such a way, that the two coefficients have a different sign, their contribution to the frequency shift becomes a function of the motional amplitudes: Since the effect of the C_4^{s}-coefficient scales with z^4, it dominates the contribution to the frequency shift for small motional amplitudes, whereas for large motional amplitudes the contribution arising from the C_6^{s}-coefficient dominates. Consider a trapped particle which is cooled enough as to reside in a very harmonic trap leading to a negligibly small shift in the axial frequency. The particle's frequency is now shifted according to the sign of C_4^{s}. For a certain motional amplitude, the two contributions have the same magnitude but are of different sign, and hence the frequency shifts cancel each other out. It allows for detecting the axial eigenmotion with a large motional amplitude but without the frequency shift. One requirement is stabilizing the particle's motional amplitude which is realized in the group of Gabrielse by the single-particle self-excited oscillator [73]. This is accomplished by driving the trapped particle by an electric field, which is derived from the current that the particle motion induces in an electric circuit attached to the trap electrodes. This method allows for the detection of a five parts in 10^{10} frequency shift in a few seconds enabling the measurement of an electron spin-flip. Gabrielse and co-workers aim at utilizing this technique in their experiment for the determination of the g-factor of a free proton. Their setup comprises also a cylindrical Penning trap, however, the detection of a proton spin-flip is greatly handicapped due to a comparatively small magnetic bottle field and the three orders of magnitude smaller magnetic moment.

7.2 Advancement in the Detection of the Larmor Frequency

The determination of the Larmor frequency represents the most tricky part of the experimental sequence. In the case of a proton and with the parameters of this experiment, the frequency shift upon a spin-flip transition according to eq. (2.42) amounts to roughly 250 mHz at an axial frequency of ≈ 680 kHz, which corresponds to a 10^{-7} effect. This is a challenge to detect electronically since the axial frequency depends on the trapping voltages applied to ring and correction electrodes and thus on their fluctuations. Assuming a correlated fluctuation between ring and correction electrodes of 300 nV relates to a shift in the axial frequency of roughly 80 mHz complicating the unambiguous identification of a spin-flip. To evade these difficulties, the signal buried in noise can be recovered by a phase-sensitive measurement [75]. Application to the axial motion of a particle stored in a cylindrical Penning trap has been tackled in [76]. This method utilizes the fact that the temporal evolution of the phase depends on the spin state. The frequency shift is expressed in a phase difference, hence the full frequency information is not needed, and the signal-to-noise ratio increases. For this purpose, the phase of the trapped proton is allowed to evolve freely after having primarily excited its axial eigenmotion; freely in this context means undisturbed from the axial detection electronics. Since the phase of the spin-up state evolves more slowly than that of the spin-down state, a phase difference $\Delta\varphi$ can be detected after a waiting time t yielding a frequency resolution $\Delta\nu$ of

$$\Delta\nu = \frac{1}{t}\frac{\sigma(\Delta\varphi)}{2\pi}\,. \tag{7.1}$$

This way it is possible to beat the Fourier limit.

Another possibility to access the internal spin information is given by the method of Rabi oscillations. The trapped proton constitutes a two-level system with the two internal states $|0\rangle$ = spin up and $|1\rangle$ = spin down. Assuming that it resides in one of the states $\psi_1(0) = |0\rangle$, it can be transferred with a π-pulse into the second state $\psi(t) = |1\rangle$, where $\pi = \Omega\, t$, and Ω is the Rabi frequency from eq. (2.46). The excitation probability plotted as a function of the excitation time while keeping the excitation amplitude constant yields a Rabi profile. This method requires a temporal coherence of the spin eigenmotion and the drive signal. Looking at the temporal development, the Larmor frequency of the trapped particle is subject to three modifications: first, the influence of thermal fluctuations of the axial motion according to eq. (2.49) as $\Delta(T) \propto B_2\,\langle z^2(T)\rangle$; second, a modification due to the drift of the magnetic field of the superconducting magnet $\Delta(B_0) \propto \partial B_0/\partial t$; and third, a modulation arising from the asymmetric B_1-term of the magnetic field $\Delta(B_1) \propto B_1\, z\, \sin\omega_z\, t$. The thermal fluctuations of the axial energy can be prevented by changing the trapping potential U_0 in such a way that the axial frequency of the particle is far off the frequency of the resonance circuit and the coupling time between the circuit and the particle is much larger than the measurement time. Since the axial energy of the particle is thus constant, the Larmor frequency is shifted by a fixed value $\propto B_2$ which can be accounted for upon irradiating the transition signal. The temporal stability of the magnetic field B_0 was determined in section 4.2 and has to be compared with the characteristic time scale for the technique just introduced.

The numerics of section 2.5.2 deliver a Rabi frequency of $\Omega = 380\,\mathrm{Hz}$ yielding a Rabi period of $\tau_\mathrm{R} \approx 3\,\mathrm{ms}$. The magnetic field decays with a rate of $3.6 \cdot 10^{-15}/\mathrm{ms}$ which can be entirely neglected. Lastly, the B_1-term of the magnetic field has to be tackled. Since the period of the axial motion is $\tau_\mathrm{z} \approx 1\,\mu\mathrm{s}$, hence $\tau_\mathrm{R} \gg \tau_\mathrm{z}$, the modulation index leads to the development of strongly suppressed sidebands at discrete frequency values of $\nu_\mathrm{L} \pm \nu_\mathrm{z}$, which are negligibly far away for the arbitrarily narrow excitation signal at the Larmor frequency ν_L. Because of that, the Larmor frequency can be considered constant during the time scale of the measurement, e.g. about 8 ms for one spin-flip. Altogether, it should be possible to establish temporal coherence, the main requirement for the realization of Rabi oscillations.

In this context, the method of separated oscillatory fields introduced by Ramsey has to be considered as "icing on the cake" [77, 78]. Again, consider a particle in the initial state $\psi_1(0) = |0\rangle$ which is excited with a $\pi/2$-pulse into a superposition of the two internal states $\psi(t) = 1/\sqrt{2}\,(|0\rangle - i|1\rangle)$, where $\pi/2 = \Omega\, t$. Irradiating a second $\pi/2$-pulse after a waiting time t_w produces interference fringes depending on the phase α between first and second $\pi/2$-pulse. The final state is given by

$$\psi_1(2t + t_\mathrm{w}) = \frac{1}{2}\left((1 - ie^{-i\alpha})|0\rangle + (e^{i\alpha} - i)|1\rangle\right) . \tag{7.2}$$

Varying the phase α produces so-called Ramsey fringes from which the probability for finding the particle in one of the two states can be deduced.

7.3 Future Experiments

The hybrid trap design enables a variety of new experiments such as investigating the magnetic moments of bare light nuclei like deuteron, tritium or ^{3}He. The large magnetic bottle field allows for accessing the spin precession frequency directly. The determination of the magnetic moment of a ^{3}He nucleus (helion) in a helium atom is of special importance since it serves as a standard nuclear magnetic resonance technique [22].

The magnetic moment of the antiproton has recently been determined from the hyperfine structure of antiprotonic helium $\bar{\mathrm{p}}\mathrm{He}^+$ to $\mu_\mathrm{s} = -2.7862(83)\,\mu_\mathrm{N}$ which agrees with the proton magnetic moment within $2.9 \cdot 10^{-3}$ [79]. This newly determined value agrees within the error bars with the to date accepted value for the magnetic moment of the antiproton of $\mu_\mathrm{s} = -2.8005(90)\,\mu_\mathrm{N}$ achieved by Kreissl more than twenty years ago [80]. This constitutes an indirect determination of the magnetic moment of the antiproton bound in a three-body system by comparison with quantum electrodynamics calculations. With the experimental setup I have introduced, however, it will be possible to perform a direct measurement on a single, unbound antiproton. Just as in the case of the proton, its antiparticle can be stored in a Penning trap and be detected non-destructively with an electronic detection system [81]. The measurements to determine the free cyclotron and Larmor frequency are able to be conducted under the same experimental conditions. To perform this experiment, the experimental setup has to be taken either to AD at CERN, Geneva or to the planned FLAIR facility, Darmstadt. The only

modification arises from the external injection required to bring the antiproton into the trap tower. Within this restriction a similar accuracy should be reachable providing a stringent test of CPT symmetry.

A Perturbations Leading to Shifts in the Eigenfrequencies

The ideal trap model is not sufficient to extract the g-factor due to departures from an ideal electrostatic quadrupole potential, due to an inhomogeneous magnetic field, and due to relativistic corrections. Thus, the energy levels are shifted producing corresponding shifts in the measurable eigenfrequencies $\omega \to \omega + \Delta\omega$. These frequency shifts have been evaluated in matrix formulation in the classical limit with first order perturbation theory by Brown and Gabrielse [35]:

$$\begin{pmatrix} \Delta\omega_+/\omega_+ \\ \Delta\omega_\mathrm{z}/\omega_\mathrm{z} \\ \Delta\omega_-/\omega_- \\ \Delta\omega_\mathrm{L}/\omega_\mathrm{L} \end{pmatrix} = M \begin{pmatrix} \Delta E_+ \\ \Delta E_\mathrm{z} \\ \Delta E_- \end{pmatrix} . \tag{A.1}$$

Here, the matrix M stands for a general correction matrix having to be specified for one of the perturbations mentioned above. It is a 4×3 matrix since the spin energy is neglected in the classical limit. The energy of the three eigenmotions in the Penning trap denoted by E_+, E_z and E_- can be taken from eq. (2.12). The matrix formulation comprises nicely the different corrections: each of the three perturbations produces shifts in each of the four eigenfrequencies. Each of these shifts, in turn, is linear in the three classical excitation energies.

Now, consider as a first application the leading anharmonicity term in the quadrupole potential $\Delta U \propto C_4$. The response matrix M_V is calculated to (ibid.):

$$\begin{pmatrix} \Delta\omega_+/\omega_+ \\ \Delta\omega_\mathrm{z}/\omega_\mathrm{z} \\ \Delta\omega_-/\omega_- \\ \Delta\omega_\mathrm{L}/\omega_\mathrm{L} \end{pmatrix} = \frac{6\,C_4}{q\,U_0} \begin{pmatrix} \frac{1}{4}(\omega_\mathrm{z}/\omega_+)^4 & -\frac{1}{2}(\omega_\mathrm{z}/\omega_+)^2 & -(\omega_\mathrm{z}/\omega_+)^2 \\ -\frac{1}{2}(\omega_\mathrm{z}/\omega_+)^2 & \frac{1}{4} & 1 \\ -(\omega_\mathrm{z}/\omega_+)^2 & 1 & 1 \\ 0 & 0 & 0 \end{pmatrix} \cdot \begin{pmatrix} \Delta E_+ \\ \Delta E_\mathrm{z} \\ \Delta E_- \end{pmatrix} .$$

Since generally $\omega_- \ll \omega_+$ holds, factors of $\omega_+ - \omega_-$ have been approximated by ω_+ to simplify this matrix. As can be seen, the spin motion is not altered by an electrostatic potential. Looking at the shift in the axial frequency, the above equation yields:

$$\frac{\Delta\omega_\mathrm{z}}{\omega_\mathrm{z}} = \frac{6\,C_4}{q\,U_0} \left(-\frac{1}{2} \left(\frac{\omega_\mathrm{z}}{\omega_+} \right)^2 E_+ + \frac{1}{4}\,E_\mathrm{z} + E_- \right) . \tag{A.2}$$

Two characteristics should be mentioned: In the leading anharmonicity correction C_4 the axial frequency depends linearly on the cyclotron energy $\omega_\mathrm{z}^2 \propto E_+$. Furthermore, this term is used to monitor and minimize C_4 when compensating the anharmonicity.

The leading perturbation to the spatially homogeneous magnetic field $\vec{B}$ is that of a weak magnetic bottle: $\Delta\vec{B} = B_2\left[(z^2 - r^2/2)\hat{B} - (\hat{B}\cdot\vec{z})\,\vec{r}\right]$ yielding a correction matrix of the form (ibid.):

$$\begin{pmatrix} \Delta\omega_+/\omega_+ \\ \Delta\omega_\mathrm{z}/\omega_\mathrm{z} \\ \Delta\omega_-/\omega_- \\ \Delta\omega_\mathrm{L}/\omega_\mathrm{L} \end{pmatrix} = \frac{B_2}{B_0}\frac{1}{2m\,\omega_+\omega_-}\begin{pmatrix} -(\omega_\mathrm{z}/\omega_+)^2 & 1 & 2 \\ 1 & 0 & -1 \\ 2 & -1 & -2 \\ -(\omega_\mathrm{z}/\omega_+)^2 & 1 & 2 \end{pmatrix}\cdot\begin{pmatrix} \Delta E_+ \\ \Delta E_\mathrm{z} \\ \Delta E_- \end{pmatrix}.$$

The direction of the homogeneous magnetic field to which the bottle is added is denoted by $\hat{B}$. As long as the hierarchy of frequencies eq. (2.11) holds, the magnetic bottle produces identical shifts in the cyclotron and spin frequencies.

Finally, the relativistic corrections are being considered:

$$\begin{pmatrix} \Delta\omega_+/\omega_+ \\ \Delta\omega_\mathrm{z}/\omega_\mathrm{z} \\ \Delta\omega_-/\omega_- \\ \Delta\omega_\mathrm{L}/\omega_\mathrm{L} \end{pmatrix} = -\frac{1}{mc^2}\begin{pmatrix} 1 & \frac{1}{2} & -(\omega_\mathrm{z}/\omega_+)^2 \\ \frac{1}{2} & \frac{3}{8} & -\frac{1}{4}(\omega_\mathrm{z}/\omega_+)^2 \\ -(\omega_\mathrm{z}/\omega_+)^2 & -\frac{1}{4}(\omega_\mathrm{z}/\omega_+)^2 & \frac{1}{4}(\omega_\mathrm{z}/\omega_+)^4 \\ \frac{2}{9} & \frac{1}{2} & -(\omega_\mathrm{z}/\omega_+)^2 \end{pmatrix}\cdot\begin{pmatrix} \Delta E_+ \\ \Delta E_\mathrm{z} \\ \Delta E_- \end{pmatrix}.$$

Equation (2.11) has been used to simplify the matrix. The frequencies on the right side are the non-relativistic frequencies, the velocity of light is denoted by c. The effect arising from using relativistic frequencies instead, e. g. $\omega_\mathrm{z}(\gamma) = 1/\gamma\omega_\mathrm{z}(\gamma = 1)$, is negligible. To discuss the effect of relativistic corrections, the axial frequency is investigated:

$$\Delta\omega_\mathrm{z}^\mathrm{rel} == -\frac{\omega_\mathrm{z}}{mc^2}\left[\frac{1}{2}E_+ + \frac{3}{8}E_\mathrm{z} - \frac{\omega_+}{4}E_-\right], \tag{A.3}$$

where the leading correction acts as a mass shift. Since ω_z is inversely proportional to the square root of the mass of the particle, it is shifted down. Furthermore, the change in the kinetic energy of the magnetron motion can be neglected since $\omega_+ \gg \omega_-$ which is evident in the matrix element M_{31}. Finally, since the rest energy mc^2 sets the scale for these corrections, they will typically be very small. In the case of the proton, the effect of the other perturbations will dominate.

Furthermore, the temperature of the detection units serving as a thermal bath for resistively cooling the particle's eigenmotions leads to shifts which directly impact the g-factor resonance. Naturally, the detection units should be in thermal equilibrium with the second stage of the cold head, however, if the second stage is overloaded the temperature may rise. As an example, the shift of the actual value of the g-factor and broadening of the g-factor resonance curve, i. e. the increase in the full-width-at-half-maximum, are calculated for different values of the axial temperature T_z. Relativistic corrections are included and typical parameters of the proton experiment are used. Figure A.1 shows the results for both calculations which are both affecting the g-factor resonance on a 10^{-9} scale. Thus, for the envisaged high-precision measurement these shifts have to be taken into account.

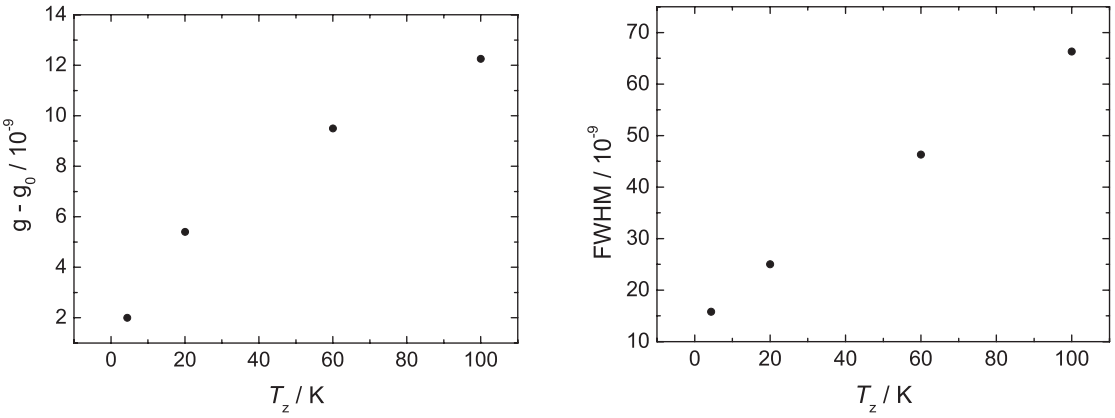

Figure A.1: On the left, the shift of the g-factor from g_0 as a function of the axial temperature T_z is shown. On the right, the broadening of the resonance curve is plotted, i. e. the increase in the full-width-at-half-maximum as a function of T_z. Both include relativistic corrections.

Bibliography

[1] R. S. Van Dyck, P. B. Schwinberg, H. G. Dehmelt, New high-precision comparison of electron and positron g-factors. *Phys. Rev. Lett.* **59**(1), 26 (1987).

[2] T. Aoyama, M. Hayakawa, T. Kinoshita, M. Nio, Revised value of the eight-order contribution to the electron g-2. *Phys. Rev. Lett.* **99**, 110406 (207).

[3] G. Gabrielse, D. Hannecke, T. Kinoshita, M. Nio, B. Odom, New Value of the Fine Structure Constant from the Electron g-Value and QED. *Phys. Rev. Lett.* **97**, 030802 (2006).

[4] K. Pachuki, A. Czarnecki, U. D. Jentschura, V. A. Yerokhin, Complete two-loop correction to the bound-electron g factor. *Phys. Rev. A* **72**, 022108 (2005).

[5] U. D. Jentschura, A. Czarnecki, K. Pachucki, V. A. Yerokhin, Mass measurements and the bound-electron g factor. *Int. J. Mass. Spectrom.* **251**, 102 (2006).

[6] H. Häffner, *et al.*, High-accuracy measurement of the magnetic moment anomaly of the electron bound in hydrogenlike carbon. *Phys. Rev. Lett.* **85**, 5308 (2000).

[7] J. L. Verdú, *et al.*, Electronic g Factor of Hydrogenlike Oxygen $^{16}O^{7+}$. *Phys. Rev. Lett.* **92**, 093002 (2004).

[8] B. Schabinger, *et al.*, Towards a g-factor determination of the electron bound in highly-charged calcium ions. *J. Phys. Conf. Ser.* **58**, 121 (2007).

[9] E. Rutherford, Collision of alpha particles with light atoms; an anomalous effect in nitrogen. *Phil. Mag.* **37**(222), 537 (1919).

[10] I. Estermann, O. Stern, Über die magnetische Ablenkung von Wasserstoffmolekülen und das magnetische Moment des Protons. II. *Z. f. Phys.* **85**, 17 (1933).

[11] R. Frisch, O. Stern, Über die magnetische Ablenkung von Wasserstoffmolekülen und das magnetische Moment des Protons. I. *Z. f. Phys.* **85**, 4 (1933).

[12] I. Estermann, E. C. Simpson, O. Stern, The magnetic moment of the proton. *Phys. Rev.* **52**, 535 (1937).

[13] I. I. Rabi, S. Millman, P. Kusch, J. R. Zacharias, The molecular beam resonance method for measuring nuclear magnetic moments. *Phys. Rev.* **55**, 157 (1939).

[14] J. M. B. Kellogg, I. I. Rabi, J. R. Zacharias, The gyromagnetic properties of the hydrogens. *Phys. Rev.* **50**, 472 (1936).

[15] J. M. B. Kellogg, I. I. Rabi, N. F. Ramsey, The magnetic moments of the proton and the deuteron. *Phys. Rev.* **56**, 728 (1939).

[16] F. Bloch, W. W. Hansen, M. Packard, The nuclear induction experiment. *Phys. Rev.* **70**(7), 474 (1946).

[17] F. Bloch, C. D. Jeffries, A direct determination of the magnetic moment of the proton in nuclear magnetons. *Phys. Rev.* **80**, 305 (1950).

[18] C. D. Jeffries, A direct determination of the magnetic moment of the protons in units of the nuclear magneton. *Phys. Rev.* **81**(6), 1040 (1951).

[19] H. Sommer, H. A. Thomas, J. A. Hipple, The measurement of e/M by cyclotron resonance. *Phys. Rev.* **82**(5), 697 (1951).

[20] D. J. Collington, A. N. Dellis, J. H. Sanders, K. C. Turberfield, Magnetic moment of the proton. *Phys. Rev.* **99**(5), 1622 (1955).

[21] P. F. Winkler, D. Kleppner, T. Myint, F. G. Walther, Magnetic Moment of the Proton in Bohr Magnetons. *Phys. Rev. A* **5**(1), 83 (1972).

[22] S. G. Karshenboim, V. G. Ivanov, The g-factor of the proton. *Phys. Lett. B* **566**, 27 (2003).

[23] L. S. Brown, G. Gabrielse, Precision pectroscopy of a charged particle in an imperfect Penning trap. *Phys. Rev. A* **25**(4), 2423 (1982).

[24] K. Blaum, High-accuracy mass spectrometry with stored ions. *Phys. Rep.* **425**, 1 (2006).

[25] H. G. Dehmelt, P. Ekstrom, Proposed $g-2/\delta\omega_z$ Experiment on Single Stored Electron or Positron. *Bull. Am. Phys. Soc.* **18**, 727 (1973).

[26] H. G. Dehmelt, Continuous Stern-Gerlach effect: Principle and idealized apparatus. *Proc. Natl. Acad. Sci. USA* **83**, 2291 (1986).

[27] N. Hermanspahn, *et al.*, Observation of the Continuous Stern-Gerlach Effect on an Electron Bound in an Atomic Ion. *Phys. Rev. Lett.* **84**, 427 (2000).

[28] L. Verdú, *et al.*, Calculation of electrostatic fields using quasi-Green's functions: application to the hybrid Penning trap. *New J. Phys.* **10**, 103009 (2008).

[29] H. Häffner, *et al.*, Double Penning trap technique for precise g-factor determinations in highly charged ions. *Eur. Phys. J. D* **22**, 163 (2003).

[30] R. Bluhm, V. A. Kostelecký, N. Russell, Testing CPT with anomalous magnetic moments. *Phys. Rev. Lett.* **79**(8), 1432 (1997).

[31] R. Bluhm, V. A. Kostelecký, N. Russell, CPT and Lorentz tests in Penning traps. *Phys. Rev. D* **57**(7), 3932 (1998).

[32] F. M. Penning. *Physica* **3**, 563 (1936).

[33] J. R. Pierce, *Theory and design of electron beams*. Van Nostrand (1949).

[34] G. Gabrielse, Relaxation calculation of the electrostatic properties of compensated Penning traps with hyperbolic electrodes. *Phys. Rev. A* **27**(5), 2277 (1983).

[35] L. S. Brown, G. Gabrielse, Geonium theory: Physics of a single electron or ion in a Penning trap. *Rev. Mod. Phys.* **58**(1), 233 (1986).

[36] M. Kretzschmar, Particle motion in a Penning trap. *Eur. J. Phys.* **12**, 240 (1991).

[37] G. Gräff, E. Klempt, Meesung der Zyklotronfrequenz freier Elektronen im Vierpolkäfig. *Zeitschrift f. Naturforsch.* **22a**, 1960 (1967).

[38] G. Gräff, E. Klempt, G. Werth, Method for measuring the anomalous magnetic moment of free electrons. *Zeitschrift f. Phys.* **222**, 201 (1969).

[39] G. Gabrielse, Why is sideband mass sprectrometry possible with ions in a Pennin trap. *Phys. Rev. Lett.* **102**, 172501 (2009).

[40] J. D. Jackson, *Classical Electrodynamics*. Wiley and Sons (2005).

[41] M.-N. Benilan, C. Audoin, Confinement d'ions par un champ électrique de radiofréquence dans une cage cylindrique. *Int. J. Mass Spectr. Ion Phys.* **11**, 421 (1973).

[42] G. Gabrielse, F. C. MacKintosh, Cylindrical Penning Traps with Orthogonalized Anharmonicity Compensation. *Int. J. Mass Spectr. Ion Proc.* **57**, 1 (1984).

[43] G. Gabrielse, L. Haarsma, R. S. L, Open-endcap Penning traps for high precision experiments. *Int. J. Mass Spectr. Ion Proc.* **88**, 319 (1989).

[44] J. L. Verdú, *Ultrapräzise Messung des elektronischen g-Faktors in wasserstoffähnlichem Sauerstoff*, Ph.D. thesis, Johannes Gutenberg-Universität Mainz (2003).

[45] N. H. Hermanspahn, *Das magnetische Moment des gebundenen Elektrons in wasserstoffartigem Kohlenstoff*, Ph.D. thesis, Johannes Gutenberg-Universität Mainz (2000).

[46] H. G. Dehmelt, F. L. Walls, "Bolometric" technique for the rf spectroscopy of stored ions. *Phys. Rev. Lett.* **21**, 127 (1968).

[47] W. Shockley, Currents to Conductors Induced by a Moving Point Charge. *J. Appl. Phys.* **9**, 635 (1938).

[48] S. Stahl, *Aufbau eines Experiments zur Bestimmung elektronischer g-Faktoren einzelner wasserstoffähnlicher Ionen*, Ph.D. thesis, Johannes Gutenberg-Universität Mainz (1998).

[49] D. J. Wineland, H. G. Dehmelt, Principles of the stored ion calorimeter. *J. Appl. Phys.* **46**, 919 (1975).

[50] R. Kories, H. Schmidt-Walter, *Taschenbuch der Elektrotechnik*. Harri Deutsch, Frankfurt Main (2004).

[51] D. J. Wineland, H. G. Dehmelt, Line shifts and widths of axial, cyclotron and G-2 resonances in tailorede, stored electron (ion) cloud. *Int. J. Mass Spectrom. Ion Phys.* **16**, 338 (1975).

[52] W. Gerlach, O. Stern, Der experimentelle Nachweis der Richtungsquantelung im Magnetfeld. *Zeitschrift f. Phys.* **9**, 349 (1922).

[53] F. Bloch, A. Siegert, Magnetic Resonance for Nonrotating Fields. *Phys. Rev.* **57**, 522 (1940).

[54] P. M. Morse, H. Feshbach, *Methods of theoretical physics*. New York: McGraw-Hill (1953).

[55] H. C. Cohl, J. E. Tohline, A. R. P. Rau, H. M. Srivastava, Developments in determining the gravitational potential using toroidal functions. *Astron. Nachr.* **321**, 363 (2000).

[56] M. Abramowitz, I. A. Stegun, *Handbook of mathematical functions with formulas, graphs, and mathematical tables*. Dover, New York (1965).

[57] G. B. Arfken, H. J. Weber, *Mathematical methods for physicists*. Academic Press, San Diego (2005).

[58] A. Mooser, *Untersuchung des Magnetfelds zur Spinflipanregung eines Protons in einer Penningfalle*, Master's thesis, Johannes Gutenberg-Universität Mainz (2009).

[59] S. Ulmer, *Entwicklung des experimentellen Aufbaus zur Messung des g-Faktors des Protons in einer Penning-Falle*, Master's thesis, Ruprecht Karls-Universität Heidelberg (2006).

[60] F. Maurer, *et al.*, Field emission of copper nanowires grown in polymer ion-track membranes. *Nucl. Instr. Meth. B* **245**, 337 (2006).

[61] S. R. Jefferts, T. Heavner, P. Hayes, G. H. Dunn, Superconducting resonator and a cryogenic GaAs field-effect transistor amplifier as a single-ion detection system. *Rev. Sci. Instr.* **64**, 737 (1993).

[62] W. W. Macalpine, R. O. Schildknecht, Coaxial resonators with helical inner conductor. *Proc. IRE* **47**, 2099 (1959).

[63] H. Meinke, F. W. Gundlach, *Taschenbuch der Hochfrequenztechnik*. Springer, Berlin (1968).

[64] R. Schiffel, A. Köhler, *Werkbuch Hochfrequenz-Technik*. Franzis, Poing (2003).

[65] J. Bardeen, M. J. Stephen, Theory of motion of vorices in superconductors. *Phys. Rev.* **140**, A1197 (1965).

[66] P. Schmüser, Superconductivity in high energy particle accelerators. *Prog. Part. Nucl. Phys* **49**, 155 (2002).

[67] P. Fabbricatore, *et al.*, First measurement of a NbTi rf cavitiy. *IEEE* **3**, 197 (1993).

[68] H. Padamsee, J. Knobloch, T. Hays, *Rf superconductivity for accelerators*. New York: John Wiley (1998).

[69] H. Kracke, *Entwicklung der kryogenen Nachweis-Elektronik zur Bestimmung der axialen Frequenz des Protons in einer Penning-Falle*, Master's thesis, Johannes Gutenber-Universität Mainz (2007).

[70] M. Diederich, *et al.*, Observing a single hydrogen-like ion in a Penning trap. *Hyp. Int.* **115**, 185 (1998).

[71] G. Gabrielse, *et al.*, Thousandfold improvement in the measured antiproton mass. *Phys. Rev. Lett.* **65**, 1317 (1990).

[72] X. Feng, M. Charlton, M. Holzscheiter, R. A. Lewis, Y. Yamazaki, Tank circuit model applied to particles in a Penning trap. *J. Appl. Phys.* **79**, 8 (1995).

[73] B. D'Urso, R. Van Handel, B. Odom, D. Hanneke, G. Gabrielse, Single-particle self-excited oscillator. *Phys. Rev. Lett.* **94**, 113002 (2005).

[74] D. J. Heinzen, D. J. Wineland, Quantum-limited cooling and detection of radio-frequency oscillations by laser-cooled ions. *Phys. Rev. A* **42**, 2977 (1990).

[75] D. P. Blair, P. H. Sydenham, Phase sensitive detection as a means to recover signal buried in noise. *J. Phys. E Sci. Instr.* **8**, 621 (1975).

[76] S. Stahl, *et al.*, Phase-sensitive measurement of trapped particle motions. *J. Phys. B: At. Mol. Opt. Phys.* **38**, 297 (2005).

[77] N. F. Ramsey, *Molecular beams*. Oxford University Press (1990).

[78] N. F. Ramsey, Experiments with separated oscillatory fields and hydrogen masers. *Rev. Mod. Phys.* **62**, 541 (1990).

[79] T. Pask, *et al.*, Antiproton magnetic moment determined from the HFS of $\bar{p}He^+$. *Phys. Lett. B* (2009), submitted.

[80] A. Kreissl, *et al.*, Remeasurement of the magnetic moment of the antiproton. *Z. Phys. C – Particles and Fields* **37**(4), 557 (1988).

[81] G. Gabrielse, *et al.*, Special relativity and the single antiproton: fortyfold improved comparison of $\bar{p}$ and p charge-to-mass ratios. *Phys. Rev. Lett.* **74**, 3544 (1995).

Danksagung

Mein ganz besonderer, herzlicher Dank gilt Prof. Dr. Klaus Blaum, der in mir die Begeisterung für das Protonexperiment geweckt hat, für die konstruktive Zusammenarbeit und großartige Unterstützung. Er schafft eine ideale Arbeitsatmosphäre und ist mir durch sein Engagement und seine Fairness ein Vorbild, auch für meine berufliche Zukunft.

Bedanken möchte ich mich bei Dr. Wolfgang Quint, mit dem ich mich über jeden noch so unscheinbar erscheinenden Teil des Experiments austauschen konnte und dessen Tipps im Anfangsstadium der Datennahme sehr hilfreich waren. Außerdem danke ich für die Durchsicht des Manuskripts.

Mein Dank geht auch an Prof. Dr. Jochen Walz, der durch seine eigene Herangehensweise oft neue Perspektiven eröffnete; ebenfalls an Prof. Dr. Hans-Jürgen Kluge und Prof. Dr. Günther Werth, die ihre langjährige Erfahrung eingebracht und dadurch das Experiment voran gebracht haben.

Ein Dankeschön geht an das bisherige Protonteam: Dr. José Verdú, Stefan Ulmer, Holger Kracke, Crícia de Carvalho Rodegheri, Andreas Mooser und Christian Mrozik. Insbesondere danke ich Stefan Ulmer für die kreative Zusammenarbeit, Holger Kracke für seinen scharfen Blick auf die Zusammenhänge und Crícia de Carvalho Rodegheri für die filigranen Hände beim Zusammenbau der Apparatur.

Mein Dank geht an die ehemaligen und derzeitigen Mitglieder der MATS Arbeitsgruppe, insbesondere an Dr. Rafael Ferrer für seine Freundschaft und an Dr. Szilard Nagy für seine Hilfsbereitschaft.

Bedanken möchte ich mich bei allen Mitarbeiterinnen und Mitarbeitern in den Werkstätten unter der Leitung von Siegbert Felzer, die mit ihrem Engagement effektiv zum Gelingen dieses Experiments beigetragen haben.

Ein Dankeschön geht an alle Mitarbeiterinnen und Mitarbeiter des wissenschaftsstützenden Bereichs am Lehrstuhl Bloch und am Institut. Speziell möchte ich Christine Best für ihre Unterstützung und den Hinweis auf die Nachwuchsgruppe von Klaus Blaum danken.

Mein tiefer Dank gilt meiner Familie für Anerkennung und Wertschätzung meiner Arbeit und meinem Mann Kim für seine Geduld und Liebe. Ein herzliches *Vergelts Gott* an die Mainzer Großeltern, deren Hilfsbereitschaft und Zeit in großem Maße zum Gelingen dieser Arbeit beigetragen haben. Zuletzt geht mein Dank an Magdalena: Du warst dabei, Du weißt warum.

Lebenslauf

Persönliche Daten

- Susanne Waltraud Kreim geboren am 10. Juni 1979 in Leonberg, Staatsangehörigkeit deutsch
- Eltern: Dipl.-Ing. (FH) Anne und Dipl.-Psych. Günter Kreim
- Geschwister: Martin (1971), Angela (1980), Reinhard (1983)
- Familienstand: verheiratet seit 22. September 2006 mit meinem Ehemann Kim Dieter Kreim
- Geburt der Tochter Magdalena am 19. September 2008

Berufliche Tätigkeit

	◦ Derzeit Abschluss der Promotion *Direct observation of a single proton in a Penning trap* (Doktorvater Prof. Blaum)
seit 12/2004	◦ Wissenschaftliche Mitarbeiterin in der Arbeitsgruppe MATS am Lehrstuhl Prof. Bloch
WS 05 - SS 07	◦ Betreuung des Fortgeschrittenenpraktikums *Zyklotronversuch*
WS 05	◦ Leitung der Übungsgruppe zur Spezialvorlesung im Hauptstudium *Laserspektroskopie, Fallen und ihre Anwendung*
SS 05	◦ Leitung der Übungsgruppe zur Vorlesung im Grundstudium *Elektrodynamik*

Ausbildung

24.06.04	◦ Verleihung von Diplomzeugnis und Diplomurkunde
12/2003 - 07/2004	◦ Wissenschaftliche Hilfskraft am Lehrstuhl Prof. Bloch, Johannes Gutenberg-Universität, Mainz
06/2003 - 06/2004	◦ Diplomarbeit *Präzisionsmessung von Wechselwirkungseigenschaften in optischen Gittern* am Lehrstuhl Prof. Hänsch, Ludwig Maximilians-Universität, München
07 - 09/2001	◦ Wissenschaftliche Hilfskraft am Lehrstuhl Prof. Zimmermann, Eberhard Karls-Universität, Tübingen
2000 - 2001	◦ Auslandsstudium an der University of Colorado, Boulder, USA und wissenschaftliche Hilfskraft am Lehrstuhl Prof. Cornell
14.08.00	◦ Vordiplom in Physik
1.04.00	◦ Aufnahme als Stipendiatin ins Cusanuswerk
WS 98/99	◦ Beginn des Studiums der Physik (Diplom)
19.06.98	◦ Abitur an der Geschwister-Scholl-Schule, Tübingen

Penning Trap Measurement of the Magnetic Moment of the Antiproton

José Verdú[1], Susanne Kreim[1], Joseba Alonso[1], Klaus Blaum[1,2], Slobodan Djekic[1,2], Wolfgang Quint[2,3], Stefan Stahl[4], Stefan Ulmer[1,3], Manuel Vogel[1], Jochen Walz[1], Günter Werth[1]

[1]*Institut für Physik, Universität Mainz, Staudingerweg 7, 55099 Mainz, Germany*
[2]*GSI, Planckstrasse 1, 64291 Darmstadt, Germany*
[3]*Fakultät für Physik und Astronomie, Albert-Ueberle-Str. 3-5, 69120 Heidelberg.Germany*
[4]*Dr. Stefan Stahl, Elektronik-Beratung, Kellerweg 23, 67582 Mettenheim, Germany*

Abstract. The measurement of the magnetic moment (or *g-factor*) of the antiproton and of the proton is a sensitive test of *CPT* invariance. In our experiment we will store and detect a single (anti)proton in a cryogenic Penning trap. The g-factor will be measured by detection of quantum jumps via the continuous Stern-Gerlach effect. Most of the experimental techniques to be used have been already successfully employed by our group for the measurement of the g-factor of the bound electron in hydrogen-like ions. However, the magnetic moment of the proton is smaller than that of the electron by a factor of 658. Our hybrid trap design combines cylindrical electrodes with a toroidal ferromagnetic ring electrode. With this novel trap, spin-flip transitions of the (anti)proton can be detected by observation of tiny differences in the axial frequency by a phase-sensitive method. With our apparatus, we envisage to determine the g-factor of the (anti)proton with an accuracy of 10^{-9} or better.

Keywords: Magnetic moment; Antiproton; CPT.
PACS: 11.30Cp, 11.30Er, 14.20Dh

INTRODUCTION

The comparison of the magnetic moments (or g-factors) of the antiproton and of the proton is a sensitive test of CPT invariance in the baryonic sector [1]. In our experiment a single (anti)proton in a Penning trap will be stored. The g-factor will be measured by detection of quantum jumps via the continuous Stern-Gerlach effect [2], which was applied for the first time by Dehmelt in the g-factor measurement of the free electron in a Penning trap [3]. Later on, this effect has also been utilized for electronic g-factor measurements on hydrogen-like ions [4, 5]. The principle of the continuous Stern-Gerlach effect is based on a coupling of the magnetic moment μ of a particle to its axial oscillation frequency ω_z in a Penning trap. This coupling is achieved by a quadratic magnetic field component ('magnetic bottle') superimposed on the homogeneous magnetic field B_0 of the Penning trap $B(z) = B_0 + B_2 z^2$. The axial frequency change $\Delta\omega_z$ due to a spin-flip transition is directly related to the coefficient B_2, which characterises the size of the quadratic field component.

CP796 Low Energy Antiproton Physics-LEAP '05
edited by Dieter Grzonka, Rafał Czyżykiewicz, Walter Oelert, Tomasz Rożek, and Peter Winter

$$\Delta\omega_z = \frac{B_2}{m_p \omega_z}\mu_p \qquad (1)$$

The measurement will be performed on a single antiproton in a cryogenic Penning trap [6]. With the trap and the vacuum enclosure of the apparatus kept at liquid-helium temperature, the background pressure is below 10^{-16} mbar and the storage time before antiproton annihilation is longer than several months [7]. The antiproton is resistively cooled close to the ambient temperature of 4 K by keeping its oscillation frequencies at the resonance frequencies of high-Q resonance circuits attached to the trap electrodes. The trapped antiproton is monitored via the currents which are induced in the trap electrodes by its oscillations. The g-factor of the antiproton is determined by measuring its cyclotron frequency and its spin precession frequency in the magnetic field of the trap.

$$g_p = 2\frac{\omega_L}{\omega_c} \qquad (2)$$

With the double Penning trap method [8] the g-factor of the antiproton can be determined with an accuracy of 1 ppb. Such a measurement would represent an improvement in accuracy by more than six orders of magnitude and is being prepared off-line with a single trapped proton.

HYBRID TRAP

Since the magnetic dipole moment of the proton is almost three orders of magnitude smaller than that of the electron, the axial frequency jump due to a spinflip becomes very small (Equ. 1). Using the same cylindrical trap geometry as for our previous heavy-ion experiments on hydrogen-like carbon $^{12}C^{5+}$ and oxygen $^{16}O^{7+}$ [5], the frequency change would be $\Delta\omega_z \approx 2\pi \times 20$ mHz, which is practically impossible to detect. In order to increase the frequency jump $\Delta\omega_z$, a novel trap design with a toroidal ring electrode made out of solid ferromagnetic material (nickel or cobalt-iron) will be used. A sketch of the hybrid trap is shown in Fig. 1, together with the 'Gabrielse-type' cylindrical trap.

The essential advantage of the hybrid trap – compared to the cylindrical trap – for the (anti)proton g-factor experiment is the bigger magnitude of the quadratic magnetic field component B_2, which is due to the smaller distance of the ferromagnetic material to the trapped particle. This stronger magnetic inhomogeneity will make it possible to detect spinflip transitions of a single trapped (anti)proton. For a given set of trap parameters, the axial frequency jump due to a spinflip transition increases from $\Delta\omega_z \approx 2\pi \times 100$ mHz in the case of the cylindrical trap to $\Delta\omega_z \approx 2\pi \times 300$ mHz, when the ring electrode is replaced by a toroidal electrode (*hybrid trap*), see Fig. 2.

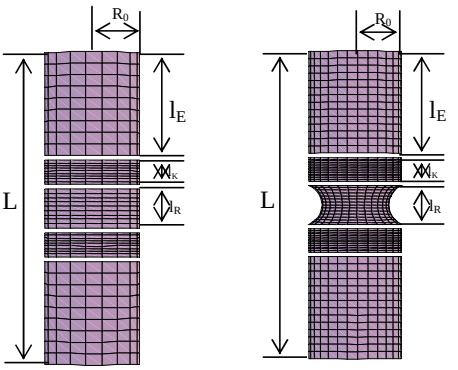

FIGURE 1. Sketch of the hybrid trap (right-hand side), together with the 'Gabrielse-type' cylindrical trap (left-hand side). Only the inner surfaces of the trap electrodes are shown. The lengths of the trap electrodes are l_R (ring electrode), l_K (correction electrodes for harmonicity tuning), and l_E (end electrodes). R_0 is the inner diameter of the cylindrical electrodes.

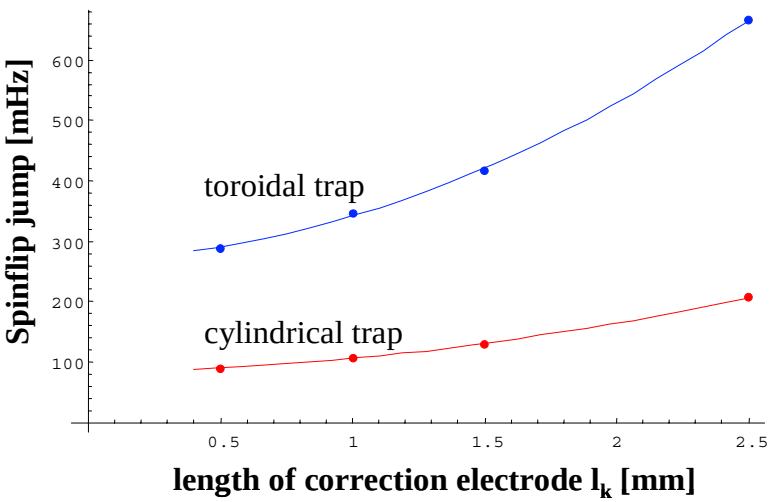

FIGURE 2. The axial frequency change of a single trapped (anti)proton due to a spinflip transition is plotted as a function of the length of the correction electrodes for the two cases of the cylindrical and of the novel hybrid trap.

The size of the frequency jump depends not only on the shape of the ring electrode, but also on other trap parameters, for example the length of the correction electrodes which are required for harmonicity tuning of the electrostatic trapping potential. With longer correction electrodes the axial frequency jump increases (Fig. 2), because the trapping potential becomes shallower (keeping fixed the voltages applied to the electrodes) and thus the axial frequency is reduced, which leads to a larger frequency change, see Equ. 1.

The influence of the inner radius of the trap electrodes on the strength of the 'magnetic bottle' B_2 - and thus on the (anti)proton's axial frequency jump - is shown in Fig. 3. A substantial increase can be achieved reducing the inner radius R_0 from 3.5 mm, as used in our heavy-ion experiments, to below 2 mm for the (anti)proton g-factor experiment.

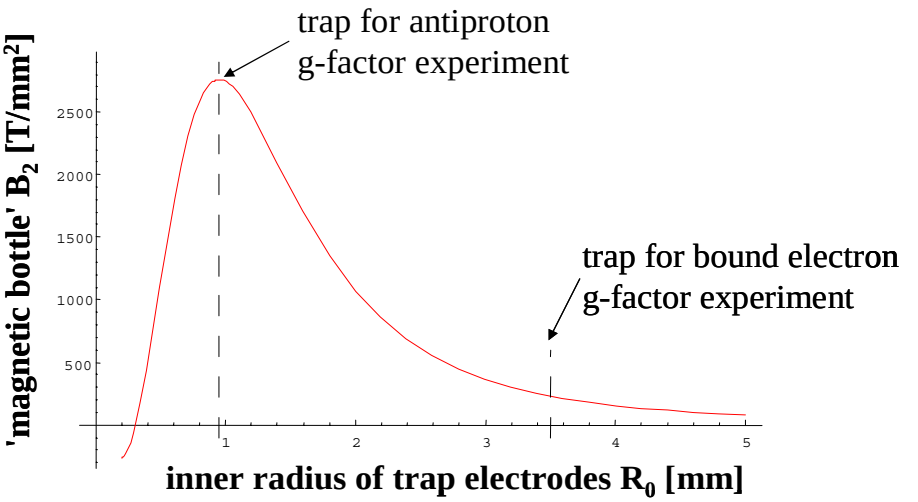

FIGURE 3. Dependence of the 'magnetic bottle' strength B_2 on the inner radius R_0 of the trap electrodes.

In a detailed study we have investigated all trap parameters to find the optimum trap geometry for the (anti)proton g-factor experiment. All trap parameters have been considered: the shape, inner radius, length and material of the trap electrodes, the dc voltages applied to electrodes, the strength of the magnetic field, etc., and have tried to optimize these parameters with respect to

- the size of the (anti)proton's axial frequency jump,
- the sensitivity of its axial frequency to external voltage fluctuations,
- the dependence of its axial frequency on the voltage at the correction electrodes ('orthogonality'),
- the electronic detection sensitivity,
- the time constants for resistive cooling,
- harmonicity range of the electrostatic trapping potential, and
- the stability of the magnetic field strength.

The results of our study are the topic of a forthcoming publication [9].

PHASE-SENSITIVE MEASUREMENT OF TRAPPED PARTICLE'S EIGENFREQUENCIES

We have developed and applied a novel method for the precise determination of small frequency differences of particle motions inside a Penning trap [10]. This phase-sensitive method plays an important role in our concept of the (anti)proton g-factor measurements. The integrated phase difference of the particle's motion relative to an excitation frequency with a well-defined phase is measured. Thereby, the Fourier-limit for frequency measurements based on Fourier-analyses of detection signals can be overcome. This method will allow us to significantly reduce the necessary measurement time and to increase the sensitivity to frequency differences. A related experiment which implicitly makes use of motional phase information has been described previously for free electrons by Gabrielse et al. [11].

The novel method is based on the fact that when the oscillation frequency of the trapped particle is different, so is the velocity of its phase evolution relative to a given initial phase. This is sketched in Fig. 4: the axial trapping frequency of the (anti)proton is lower in the case when its spin is parallel to the external magnetic field. Accordingly, the integrated phase of the (anti)proton's motion after a given time is different from the antiparallel case. Experimentally, a well-defined dipolar excitation of the particle motion with a fixed phase is performed by use of a burst generator. Then the particle is decoupled from the electronics and the phase evolves freely for a given waiting time. The phase information is subsequently acquired by re-coupling the detection electronics to the trapped particle. Finally, its motion is resistively cooled to the initial value for the next measurement to start. Note that it is not necessary to evaluate the full frequency information, since the frequency difference itself is expressed in terms of a phase difference. Thus, the novel scheme is not restricted by the Fourier limit.

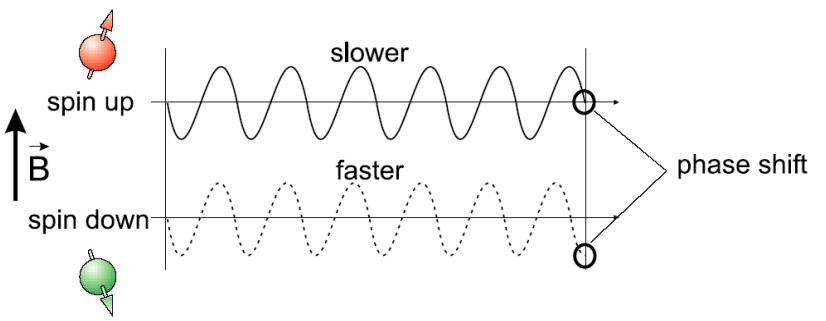

FIGURE 4. Schematic view of the frequency difference as expressed by the difference in the phase evolution.

OUTLOOK

Protons can be easily produced within a Penning trap, by bombarding a target with a low-energy electron beam. Our experiment starts therefore with the measurement of the proton's g-factor. Antiprotons, on the contrary, are very difficult to produce. Worldwide, only the AD facility at CERN and the future FLAIR facility at GSI/FAIR deliver low-energy antiprotons. For the measurement of the g-factor of the antiproton our experimental apparatus will move from Mainz to either CERN or GSI/FAIR.

ACKNOWLEDGMENTS

We acknowledge financial support from Deutsche Forschungsgemeinschaft (grant QU 122/3) and the Helmholtz Association of National Research Centers (HFG) under contract VH-NG-037.

REFERENCES

1. Robert Bluhm et al., *Phys. Rev. Lett.* **79**, 1432 (1997); R. Bluhm, V. A. Kostelecky and N. Russell, *Phys. Rev.* D 57, 3932 (1998).
2. W. Quint, J. Alonso, S. Djekic, H.-J. Kluge, S. Stahl, T. Valenzuela, J. Verdú, M. Vogel, and G. Werth, *Nucl. Instr. Meth.* **B 214**, 207 (2004).
3. R. S. Van Dyck, P. B. Schwinberg and G. Dehmelt, *Phys. Rev. Lett.* **59**, 26 (1987).
2. N. Hermanspahn, H. Häffner, H.-J. Kluge, W. Quint, S. Stahl, J. Verdú and G. Werth, *Phys. Rev. Lett.* **84**, 427 (2000);
5. H. Häffner, N. Hermanspahn, H.-J. Kluge, W. Quint, S. Stahl, J. Verdú and G. Werth, *Phys. Rev. Lett.* **85,** 5308 (2000); José Verdú *et al*., Phys. Rev. Lett. **92**, 093002 (2004).
6. G. Gabrielse, D. Phillips, W. Quint, H. Kalinowsky, G. Rouleau and W. Jhe, *Phys. Rev. Lett.* **74** (1995) 3544.
7. G. Gabrielse et al., *Phys. Rev. Lett*. **65,** 1317 (1990).
8. Lowell S. Brown and G. Gabrielse, Rev. Mod. Phys. **58**, 233 (1986).
9. J. Verdú, S. Kreim, et al., to be published.
10. S. Stahl, J. Alonso, S. Djekic, H.-J. Kluge, W. Quint, J. Verdú, M. Vogel, and G. Werth, *J. Phys.* **B 38**, 297–304 (2005).
11. B. D'Urso, B. Odom, and G. Gabrielse, *Phys. Rev. Lett.* **90,** 043001 (2003).

New Journal of Physics
The open-access journal for physics

Calculation of electrostatic fields using quasi-Green's functions: application to the hybrid Penning trap

J Verdú[1], S Kreim[2,5,6], K Blaum[3,4], H Kracke[2], W Quint[4], S Ulmer[2] and J Walz[2]

[1] Atominstitut der Österreichischen Universitäten, Stadionallee 2, A-1020 Vienna, Austria
[2] Institut für Physik, Johannes Gutenberg-Universität, D-55099 Mainz, Germany
[3] Max-Planck-Institut für Kernphysik, D-69117 Heidelberg, Germany
[4] Gesellschaft für Schwerionenforschung, D-64291 Darmstadt, Germany
E-mail: kreim@uni-mainz.de

New Journal of Physics **10** (2008) 103009 (23pp)
Received 18 June 2008
Published 8 October 2008
Online at http://www.njp.org/
doi:10.1088/1367-2630/10/10/103009

Abstract. Penning traps offer unique possibilities for storing, manipulating and investigating charged particles with high sensitivity and accuracy. The widespread applications of Penning traps in physics and chemistry comprise e.g. mass spectrometry, laser spectroscopy, measurements of electronic and nuclear magnetic moments, chemical sample analysis and reaction studies. We have developed a method, based on the Green's function approach, which allows for the analytical calculation of the electrostatic properties of a Penning trap with arbitrary electrodes. The ansatz features an extension of Dirichlet's problem to nontrivial geometries and leads to an analytical solution of the Laplace equation. As an example we discuss the toroidal hybrid Penning trap designed for our planned measurements of the magnetic moment of the (anti)proton. As in the case of cylindrical Penning traps, it is possible to optimize the properties of the electric trapping fields, which is mandatory for high-precision experiments with single charged particles. Of particular interest are the anharmonicity compensation, orthogonality and optimum adjustment of frequency shifts by the continuous Stern–Gerlach effect in a quantum jump

[5] Author to whom any correspondence should be addressed.
[6] This article comprises part of the PhD thesis of S Kreim.

spectrometer. The mathematical formalism developed goes beyond the mere design of novel Penning traps and has potential applications in other fields of physics and engineering.

Contents

1. Introduction

Penning traps are very suitable for precision experiments with charged particles since they provide long storage and observation times. Radial confinement is realized by a homogeneous magnetic field $\vec{B}$; axially the particles are trapped by an electrostatic field $\vec{E} \parallel \vec{B}$ in a harmonic trapping potential. Besides being able to confine a single charged particle, it is possible to detect it non-destructively with an electronic detection technique [1]. Currently, two types of Penning traps for measurements with relative uncertainties down to 10^{-13} [2] are being used: hyperbolic and cylindrical traps [3, 4]. The hyperbolic one has found a wide range of applications in mass spectrometry [5]. Cylindrical traps have been used for determining the g-factor of an electron bound in hydrogen-like carbon and oxygen [6, 7] as well as of the free electron [2, 8]. Moreover, Penning traps have been used to measure e.g. the antiproton's mass [9], masses of stable particles, atoms [10]–[12], and short-lived radioactive ions [13]–[16]. Furthermore, they

have been implemented in molecular electric dipole moment experiments [17], antihydrogen production [18, 19] or the most accurate test of the CPT symmetry in the lepton sector [20]. Such high-precision experiments depend critically on the correct design of the trap being used. Furthermore, novel kinds of Penning traps are coming into use: because of its scalability, for example, the planar Penning trap [21]–[23] offers possibilities for quantum computation with ions or electrons.

Our planned high-precision measurement of the magnetic moment of a single (anti)proton [24, 25] demands a Penning trap different from any existing one. The determination of the g-factor results from a precise measurement of the particle's cyclotron and Larmor frequencies [6, 7]. Since the latter is an internal degree of freedom, a magnetic bottle is exploited to imprint the spin state information onto an external degree of freedom, namely the axial eigenmotion of the particle. This so-called continuous Stern–Gerlach effect is used to detect the resulting frequency shift and thus the spin state non-destructively [26, 27]. Using a conventional cylindrical trap, like the one in [26], the continuous Stern–Gerlach effect would shift the axial frequency of a single (anti)proton on a relative 10^{-7} scale, making it almost impossible to detect efficiently. To this end, a novel Penning trap is introduced, which we call *the hybrid Penning trap*: a combination of electrodes of different shape, basically cylindrical end caps and correction electrodes and a toroidal or hyperbolic ring. In particular, the curved shape of a toroidal ferromagnetic ring enhances the curvature of the magnetic bottle by more than one order of magnitude compared with a cylindrical ring of similar dimensions and the same material, therefore making the resolution of the phase-sensitive Stern–Gerlach quantum jump spectrometer [28] big enough for the efficient determination of the spin state of a single (anti)proton.

In section 2, a 'quasi'-Green's function method is presented which will render the analytical calculation of a hybrid Penning trap (figure 1) possible. An analytical calculation of the entire electrostatic properties of a *toroidal hybrid Penning trap* consisting of two cylindrical end caps, two cylindrical correction electrodes and one toroidal ring (figure 3) will be presented in section 3. This trap is used to illustrate the 'quasi'-Green's function method developed in section 2. In section 4, detailed analytical expressions for the design of a toroidal hybrid Penning trap for high-precision experiments are given. Those formulae make the design of such traps considerably easier than any numerical approach. In section 5, further applications of the mathematical formalism developed to other fields of experimental physics are discussed focusing on ion-trapping technology and microwave engineering. Besides being our motivation for the measurement for the (anti)proton's g-factor, the power of this calculation technique goes beyond the design of the hybrid Penning trap and could be used in many other problems involving the Laplace equation.

2. The 'quasi'-Green's function solution to Dirichlet's problem

2.1. Definition of the hybrid Penning trap

The Green's function formalism is a well-known and powerful technique for calculating electrostatic potentials. In the case of ion traps, the electrostatic potential $\Phi(\vec{x})$ usually has to be calculated within a closed volume defined by some electrodes to which arbitrary voltages are applied. Mathematically, this problem simply corresponds to solving the Laplace equation with Dirichlet boundary conditions: if the adequate Green's function is available, the

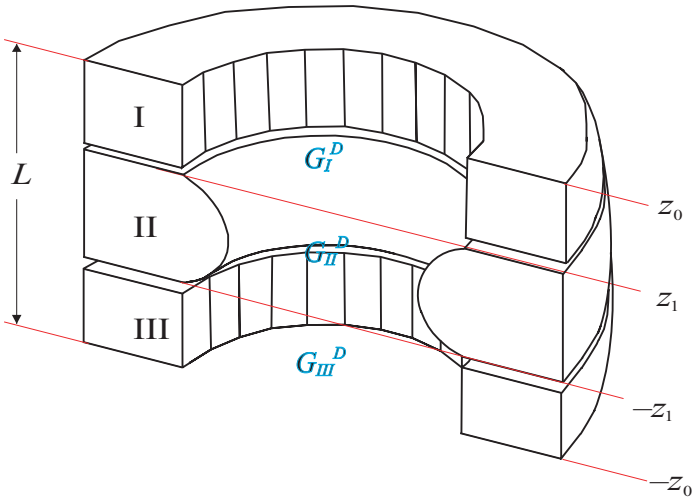

Figure 1. Inner surface of a three-pole hybrid Penning trap. The trap is made up of axially symmetric electrodes each with a different geometry. For simplicity of the figure, the upper and lower regions, Ω_{I} and Ω_{III}, respectively, are drawn to be cylindrical.

computation of $\Phi(\vec{x})$ becomes straightforward. Green's functions for electrodes with various shapes (hyperboloids, oblate and prolate spheroids, toroids, flat-ring cyclide discs, etc) are well known in the literature [29, 30]. These kinds of electrodes can be put together in many different ways, so that a vast class of well-defined trapping volumes can theoretically be envisaged with them. Any such combination of differently shaped electrodes defining a closed trapping region is what we call a *hybrid Penning trap*.

2.2. The potential problem in a hybrid Penning trap

Most hybrid traps, even if they are relatively simple like the one outlined in figure 1, do not have a known analytic expression for the Green's function fulfilling Dirichlet boundary conditions on their entire surface. If, however, for each electrode forming the trap, the corresponding Green's function, which does meet those conditions on the electrode's surface, is known, then it is possible to construct a 'quasi'-Green's function for the entire hybrid trap which delivers an analytic expression for $\Phi(\vec{x})$. The next paragraphs show formally how to construct such a 'quasi'-Green's function and how to calculate the electric potential with it. For simplicity, we will restrict the discussion to the trap sketched in figure 1, which is defined by two external cylindrical electrodes and one central ring with arbitrary but rotationally invariant surface around the $\vec{u}_z$-axis. Generalization of the presented formalism to other trapping geometries and/or to a higher number of electrodes will become apparent.

In general, the electrostatic boundary-value problem is defined by the following integral equation [31]:

$$\int_{\Omega} \mathrm{d}^3x' \left[\Phi(\vec{x}\,')\nabla'^2 G(\vec{x} \mid \vec{x}\,') - G(\vec{x} \mid \vec{x}\,')\nabla'^2\Phi(\vec{x}\,')\right] = \oint_{\partial\Omega} \mathrm{d}S' \left[\Phi(\vec{x}\,')\frac{\partial}{\partial n'} G(\vec{x} \mid \vec{x}\,') - G(\vec{x} \mid \vec{x}')\frac{\partial}{\partial n'}\Phi(\vec{x}')\right], \quad (1)$$

where Ω is the trapping volume under consideration, $\partial\Omega$ the surface delimiting that volume, and $\Phi(\vec{x}')$ the electrostatic potential. $G(\vec{x} \mid \vec{x}')$ represents the Green's function for the Laplace equation. It is symmetric with respect to interchanging the source, $\vec{x}\,'$, and field coordinates, $\vec{x}$: $G(\vec{x} \mid \vec{x}') = G(\vec{x}\,'|\vec{x})$. Further, it satisfies

$$\nabla^2 G(\vec{x} \mid \vec{x}') = \nabla'^2 G(\vec{x} \mid \vec{x}') = -4\pi\delta\left(\vec{x} - \vec{x}\,'\right); \qquad G(\vec{x} \mid \vec{x}') = \frac{1}{|\vec{x} - \vec{x}\,'|} + F(\vec{x} \mid \vec{x}'). \tag{2}$$

$F(\vec{x} \mid \vec{x}')$ represents any arbitrary function satisfying $\nabla^2 F(\vec{x} \mid \vec{x}') = \nabla'^2 F(\vec{x} \mid \vec{x}') = 0$, $\forall\{\vec{x}, \vec{x}\,'\} \in \Omega$. In the case of Dirichlet boundary conditions, $F(\vec{x} \mid \vec{x}')$ is chosen such that the Green's function becomes equal to zero at the surface of the trap: $G^{\mathrm{D}}(\vec{x} \mid \vec{x}') = 0 \ \forall \ \vec{x}\,' \in \partial\Omega$. The function $F(\vec{x} \mid \vec{x}')$ is thus a solution of the Laplace equation and it represents the potential of a (mirror) charge distribution external to the volume Ω [31]. Further, assuming the absence of free charges within the region where the potential is calculated, $\nabla^2\Phi(\vec{x}') \propto \rho(\vec{x}') = 0$, $\forall\,\vec{x}\,' \in \Omega$, equation (1) simplifies to

$$\int_\Omega \mathrm{d}^3x' \left[\Phi(\vec{x}')\nabla'^2 G^{\mathrm{D}}(\vec{x} \mid \vec{x}')\right] = \oint_{\partial\Omega} \mathrm{d}S' \left[\Phi(\vec{x}')\frac{\partial}{\partial n'} G^{\mathrm{D}}(\vec{x} \mid \vec{x}')\right]. \tag{3}$$

The validity of equation (3) is not restricted to pure Green's functions satisfying equation (2), but it applies whenever the volume Ω is free of charges and for any function being equal to zero at its surface, $G^{\mathrm{D}}(\vec{x} \mid \vec{x}') = 0\,\forall\,\vec{x}\,' \in \partial\Omega$. However, if the proper Green's function satisfying Dirichlet boundary conditions is known, then exploiting $\nabla^2 G^{\mathrm{D}}(\vec{x} \mid \vec{x}') = -4\pi\delta\,(\vec{x} - \vec{x}\,')$, equation (3) simplifies to the conventional expression $\Phi(\vec{x}) = -\frac{1}{4\pi}\oint_{\partial\Omega} \mathrm{d}S' \cdot \Phi(\vec{x}')\frac{\partial\, G^{\mathrm{D}}(\vec{x}|\vec{x}')}{\partial n'}$. The boundary conditions, $\Phi(\vec{x}')$, are provided by the applied voltages at the trap electrodes. Thus, the explicit knowledge of $G^{\mathrm{D}}(\vec{x} \mid \vec{x}')$ formally solves the potential problem, reducing it to a simple integral.

2.3. Definition of the 'quasi'-Green's function

For the hybrid trap of figure 1, we introduce a 'quasi'-Green's function, $\tilde{G}^{\mathrm{D}}(\vec{x} \mid \vec{x}')$, defined as

$$\tilde{G}^{\mathrm{D}}(\vec{x} \mid \vec{x}') = \begin{cases} G^{\mathrm{D}}_{\mathrm{I}}(\vec{x} \mid \vec{x}') & \vec{x} \in \Omega; \quad \vec{x}\,' \in \Omega_{\mathrm{I}}, \\ G^{\mathrm{D}}_{\mathrm{II}}(\vec{x} \mid \vec{x}') & \vec{x} \in \Omega; \quad \vec{x}\,' \in \Omega_{\mathrm{II}}, \\ G^{\mathrm{D}}_{\mathrm{III}}(\vec{x} \mid \vec{x}') & \vec{x} \in \Omega; \quad \vec{x}\,' \in \Omega_{\mathrm{III}}, \end{cases} \tag{4}$$

Each volume Ω_i denotes one of the i-regions into which the trapping volume of figure 1 is divided (see also figure 3). This partition of space is in principle arbitrary but must satisfy the condition that inside each Ω_i the Green's function satisfying Dirichlet boundary conditions on the physical part of that Ω_i-region (i.e. the metallic electrode) must be known. Thus, a set of functions $G^{\mathrm{D}}_i(\vec{x} \mid \vec{x}')$ must be provided satisfying $\nabla^2 G^{\mathrm{D}}_i(\vec{x} \mid \vec{x}') = \nabla'^2 G^{\mathrm{D}}_i(\vec{x} \mid \vec{x}') = 4\pi\delta(\vec{x} - \vec{x}')$ and $G^{\mathrm{D}}_i(\vec{x} \mid \vec{x}') = 0$ on the corresponding part of the trap's surface. In the example of figure 1, the partition is chosen such that there are three Ω_i-regions delimited by the 'contact' planes $z' = \pm z_1$. In principle, many different 'quasi'-Green's functions, $\tilde{G}^{\mathrm{D}}(\vec{x} \mid \vec{x}')$, can be constructed; the most convenient choice, however, depends on the actual geometry of the trap being considered.

For the 'quasi'-Green's function introduced, the interchange symmetry of the arguments is broken: $\tilde{G}^{\mathrm{D}}(\vec{x} \mid \vec{x}') \neq \tilde{G}^{\mathrm{D}}(\vec{x}\,'|\vec{x})$. Our focus is on the properties of $\tilde{G}^{\mathrm{D}}$ with respect to the source $\vec{x}\,'$. Since the constituting functions $G^{\mathrm{D}}_i(\vec{x} \mid \vec{x}')$ are chosen such that each separately

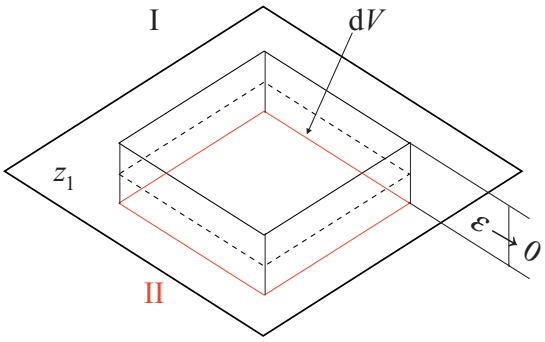

Figure 2. Illustration of the Gaussian box enclosing the point $\vec{x}\,' = \{r', \varphi', z' = +z_1\}$ which lies on the contact plane separating the regions Ω_{I} and Ω_{II}. $\tilde{G}^{\mathrm{D}}$ has a finite step discontinuity at any point on that contact plane.

satisfies Dirichlet boundary conditions for the corresponding electrode, the 'quasi'-Green's function satisfies Dirichlet boundary conditions on the entire surface of the trap: $\tilde{G}^{\mathrm{D}}(\vec{x} \mid \vec{x}') = 0$, $\forall\, \vec{x}\,' \in \partial\Omega$. As a consequence of this, equation (3) still holds and will be used in the following to calculate the potential $\Phi(\vec{x})$.

2.4. Solution with the 'quasi'-Green's function

In order to obtain $\Phi(\vec{x})$ from equation (3), the Laplacian of the 'quasi'-Green's function with respect to the source coordinates, $\nabla'^2 \tilde{G}^{\mathrm{D}}(\vec{x} \mid \vec{x}')$, has to be evaluated. For source points within the trap not lying on any of the contact planes separating the Ω_i-regions, this immediately yields: $\nabla'^2 \tilde{G}^{\mathrm{D}}(\vec{x} \mid \vec{x}') = -4\pi\delta(\vec{x} - \vec{x}')\, \forall \vec{x}\,' = \{x', y', z' \neq \pm z_1\}$, simply due to the definition of the 'quasi'-Green's function. The case of the contact surfaces has to be considered separately.

Note that $\tilde{G}^{\mathrm{D}}(\vec{x} \mid \vec{x}')$ has a finite-step discontinuity at the planes separating the Ω_i-regions, $\vec{x}\,' = \{x', y', z' = \pm z_1\}$. This discontinuity has to be taken into account when calculating the Laplacian $\nabla'^2 \tilde{G}^{\mathrm{D}}(\vec{x} \mid \vec{x}')$ at any of those points. Since ∇'^2 represents a derivative operator and since the derivative of the Heaviside step-function results in the Dirac-delta, we assume the following ansatz for $\nabla'^2 \tilde{G}^{\mathrm{D}}(\vec{x} \mid \vec{x}\,')$:

$$\nabla'^2 \tilde{G}^{\mathrm{D}}(\vec{x} \mid \vec{x}') = -4\pi\delta(\vec{x} - \vec{x}') + \delta(z' - z_1) f_+(\vec{x} \mid \vec{x}') + \delta(z' + z_1) f_-(\vec{x} \mid \vec{x}'). \quad (5)$$

With this ansatz, the Laplacian of the 'quasi'-Green's function for points not lying on the contact planes, $z' \neq \pm z_1$, is trivially recovered. The functions $f_\pm(\vec{x} \mid \vec{x}\,')$ still have to be determined.

It is obvious from equation (5) that it suffices to evaluate $f_\pm$ for points lying on the contact planes; in cylindrical coordinates: $\vec{x}\,' = \{r', \varphi', z' = \pm z_1\}$ for $f_\pm$, respectively. On the one hand, consider an infinitesimal volume $\mathrm{d}V$ enclosing the point of interest $\{r', \varphi', z' = z_1\}$ as shown in figure 2. The divergence theorem applied to $\tilde{G}^{\mathrm{D}}(\vec{x} \mid \vec{x}')$ at $\mathrm{d}V$ states that

$$\int_{\mathrm{d}V} \mathrm{d}^3x' \cdot \nabla'^2 \tilde{G}^{\mathrm{D}}(\vec{x} \mid \vec{x}') = \oint_S \mathrm{d}\vec{S}\,' \cdot \nabla' \tilde{G}^{\mathrm{D}}(\vec{x} \mid \vec{x}')\,. \quad (6)$$

In the limit $\epsilon \to 0$, the lateral surface of the Gaussian box does not contribute to the surface integral in equation (6), thus $\oint_S \mathrm{d}\vec{S}\,' \cdot \nabla' \tilde{G}^{\mathrm{D}}(\vec{x} \mid \vec{x}') = \oint_{S_\perp} \mathrm{d}S'_z \frac{\partial}{\partial z'} \tilde{G}^{\mathrm{D}}(\vec{x} \mid \vec{x}')$. The top and bottom surfaces of the Gaussian box of figure 2 are denoted by $S_\perp$; only these contribute to the

surface integral. The integral on the top surface is performed while $z' = z_1 + \epsilon \Rightarrow z' \in \Omega_{\mathrm{I}}$ and $\tilde{G}^{\mathrm{D}}(\vec{x} \mid \vec{x}') = G^{\mathrm{D}}_{\mathrm{I}}(\vec{x} \mid \vec{x}')$. For the bottom plane, $z' = z_1 - \epsilon$ and $\tilde{G}^{\mathrm{D}}(\vec{x} \mid \vec{x}') = G^{\mathrm{D}}_{\mathrm{II}}(\vec{x} \mid \vec{x}')$. Further, $\mathrm{d}S'_z$ has the opposite orientation in the latter case as compared with the former, hence leading to

$$\oint_S \mathrm{d}\vec{S}' \cdot \nabla' \tilde{G}^{\mathrm{D}}(\vec{x} \mid \vec{x}') = \lim_{\epsilon \to 0} \oint_{S_\perp} \mathrm{d}S'_z \frac{\partial}{\partial z'} \left[G^{\mathrm{D}}_{\mathrm{I}}(\vec{x} \mid r', \varphi', z_1 + \epsilon) - G^{\mathrm{D}}_{\mathrm{II}}(\vec{x} \mid r', \varphi', z_1 - \epsilon) \right]. \tag{7}$$

On the other hand, with the ansatz of equation (5) and assuming that $\vec{x} \neq \vec{x}\,'$ (thus $\vec{x}$ is outside of $\mathrm{d}V$), the volume integral in equation (6) yields

$$\int_{\mathrm{d}V} \mathrm{d}^3x' \cdot \nabla'^2 \tilde{G}^{\mathrm{D}}(\vec{x} \mid \vec{x}') = \int_{\mathrm{d}V} \mathrm{d}z' \cdot \mathrm{d}S'_z \, \delta(z - z_1) f_+(\vec{x} \mid r', \varphi', z') = \int_{S_\perp} \mathrm{d}S'_z \, f_+(\vec{x} \mid r', \varphi', z_1). \tag{8}$$

Now, we can obtain the explicit form of f_+ by comparing equation (7) with (8). Taking into account that $G^{\mathrm{D}}_i(\vec{x} \mid \vec{x}') = \frac{1}{|\vec{x} - \vec{x}\,'|} + F^{\mathrm{D}}_{\mathrm{i}}(\vec{x} \mid \vec{x}')$, while taking the limit $\epsilon \to 0$ in equation (7), results in:

$$f_+(\vec{x} \mid r', \varphi', z_1) = \frac{\partial}{\partial z'} \left[F^{\mathrm{D}}_{\mathrm{I}}(\vec{x} \mid r', \varphi', z_1) - F^{\mathrm{D}}_{\mathrm{II}}(\vec{x} \mid r', \varphi', z_1) \right]. \tag{9}$$

The same considerations carried out for the contact plane between regions Ω_{II} and Ω_{III} deliver the function f_-:

$$f_-(\vec{x} \mid r', \varphi', -z_1) = \frac{\partial}{\partial z'} \left[F^{\mathrm{D}}_{\mathrm{II}}(\vec{x} \mid r', \varphi', -z_1) - F^{\mathrm{D}}_{\mathrm{III}}(\vec{x} \mid r', \varphi', -z_1) \right]. \tag{10}$$

Finally, computing the integral of equation (3) and resolving for $\Phi(\vec{x})$, we obtain the electrostatic potential inside the trap:

$$\begin{aligned} \Phi(\vec{x}) = &-\frac{1}{4\pi} \oint_{\partial\Omega} \mathrm{d}S' \, \Phi(\vec{x}') \frac{\partial}{\partial n'} \tilde{G}^{\mathrm{D}}(\vec{x} \mid \vec{x}') \\ &+ \frac{1}{2} \int_0^{R_0} \mathrm{d}r' r' \, \Phi(r', z_1) \frac{\partial}{\partial z'} \left[F^{\mathrm{D}}_{\mathrm{I}}(\vec{x} \mid r', z_1) - F^{\mathrm{D}}_{\mathrm{II}}(\vec{x} \mid r', z_1) \right] \\ &+ \frac{1}{2} \int_0^{R_0} \mathrm{d}r' r' \, \Phi(r', -z_1) \frac{\partial}{\partial z'} \left[F^{\mathrm{D}}_{\mathrm{II}}(\vec{x} \mid r', -z_1) - F^{\mathrm{D}}_{\mathrm{III}}(\vec{x} \mid r', -z_1) \right]. \end{aligned} \tag{11}$$

In equation (11), R_0 represents the radius of the contact surface delimiting the different Ω_i-regions. Note that the integral over φ' has been assumed to deliver the value 2π in the last two summands of equation (11). This assumption is valid only if the electrostatic potential is axially symmetric. If this is not the case, those summands become surface integrals and the integration over $\varphi' \in [0, 2\pi]$ still has to be performed. In the usual case of the trap having point symmetry with respect to its central plane $z = 0$, the function f_- becomes identical to f_+ except for the negative sign. The opposite sign results from the opposite direction of the surface vector $\mathrm{d}\vec{S}'$ when calculating the integral on the right-hand side of equation (6). Taking this symmetry into account the calculation of the electrostatic potential simplifies to

$$\begin{aligned} \Phi(\vec{x}) = &-\frac{1}{4\pi} \oint_{\partial\Omega} \mathrm{d}S' \, \Phi(\vec{x}') \cdot \frac{\partial}{\partial n'} \tilde{G}^{\mathrm{D}}(\vec{x} \mid \vec{x}') \\ &+ \int_0^{R_0} r' \mathrm{d}r' \, \Phi(r', z_1) \cdot \frac{\partial}{\partial z'} \left[F^{\mathrm{D}}_{\mathrm{I}}(\vec{x} \mid r', z_1) - F^{\mathrm{D}}_{\mathrm{II}}(\vec{x} \mid r', z_1) \right]. \end{aligned} \tag{12}$$

2.5. Properties of the solution

Equation (12), or more generally equation (11), represents the formal solution of the boundary-value problem defined by the stack of electrodes of figure 1. With explicit knowledge of $F_i^{\mathrm{D}}(\vec{x} \mid \vec{x}')$, the electrostatic potential inside the trapping volume can be obtained by integration of equation (12). The main features of equation (12) are as follows.

1. It represents an integral equation: the potential $\Phi(\vec{x})$ appears not only as the pre-specified boundary conditions on the trap's surface but also in the second integral over the contact planes where $\Phi(\vec{x})$ is *a priori* unknown.
2. The first integral in equation (12) represents the zeroth-order approximation to the potential, $\Phi_0(\vec{x})$. It is the linear superposition of the potentials created individually by each electrode with the corresponding voltage. However, $\Phi_0(\vec{x})$ does not fulfill the boundary conditions on the surface of the entire trap. Upon putting the electrodes together to form the trap, the superficial charges induced by each electrode on all others arrange in such a way that the final electric potential, $\Phi(\vec{x})$, fulfills the boundary conditions on the entire trap's surface. The influence of these mutually induced charges on the final potential $\Phi(\vec{x})$ is given by the second integral in equation (12) denoted by $\Delta\Phi(\vec{x})$. The mathematical expression for the process described is an integral equation: $\Phi(\vec{x}) = \Phi_0(\vec{x}) + \Delta\Phi(\vec{x})$.
3. If all electrodes have the same shape, the functions F_i^D become the same $F_{\mathrm{I}}^{\mathrm{D}} = F_{\mathrm{II}}^{\mathrm{D}} = F_{\mathrm{III}}^{\mathrm{D}}$ and hence $\tilde{G}^{\mathrm{D}}$ simplifies to the usual Green's function. Furthermore, equation (12) reduces to the well-known expression of the electrostatic potential for the simple Dirichlet's problem.

In principle, equations (12) and (11) may be applied to many different problems. Their generalization to situations where axial symmetry is broken and/or where the shape of the electrodes is non-cylindrical is straightforward as long as a 'quasi'-Green's function as introduced in equation (4) can be constructed. In order to illustrate the power of the presented method, the complete calculation of the *toroidal hybrid trap* is performed with the help of equation (12) in the next section. The properties of such a trap will be discussed in detail in section 4. Other possible applications of equation (12) will be briefly presented in section 5.

3. Application of the method: the toroidal hybrid trap

As an example of the formalism presented, we calculate the electrostatic potential within a Penning trap formed by a toroidal ring of circular cross section and cylindrical correction electrodes and end caps, which fits exactly in the kind of hybrid trap considered in the previous section and outlined in figure 1. The toroidal hybrid trap is sketched in detail in figures 3 and 4. Applying equation (12) to the toroidal hybrid trap is straightforward; the first step consists of constructing the appropriate 'quasi'-Green's function.

3.1. Construction of an appropriate 'quasi'-Green's function

The basic Green's function for the Laplace equation, $\frac{1}{|\vec{x}-\vec{x}'|}$, has been calculated in cylindrical coordinates elsewhere [29, 31, 32]. A simple modification of that basic function leads to the Green's function inside a cylindrical box satisfying Dirichlet boundary conditions, employing

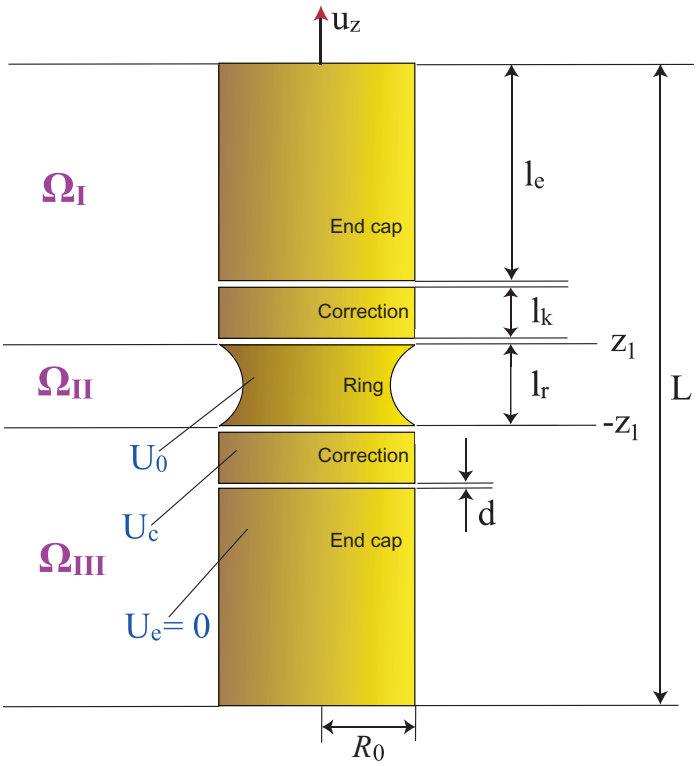

Figure 3. Inner surface of a hybrid Penning trap with toroidal ring electrode and cylindrical correction electrodes and end caps. Region I includes the upper correction electrode and end cap, region II includes the toroidal ring, and region III the lower correction and end cap electrode.

the coordinate system of figure 3:

$$G_{\mathrm{cyl}}(r, z \mid r', z') = \frac{4}{L} \sum_{n=1,3,\ldots}^{\infty} \cos(\kappa_n z) \cos(\kappa_n z') \frac{I_0(\kappa_n r_<)}{I_0(\kappa_n R_0)} \Big[I_0(\kappa_n R_0) K_0(\kappa_n r_>) - I_0(\kappa_n r_>) K_0(\kappa_n R_0) \Big]. \tag{13}$$

Here, $\kappa_n = n\pi/L$ with L being the total length of the trap given by $L = 4\,d + 2\,l_{\mathrm{e}} + 2\,l_{\mathrm{k}} + l_{\mathrm{r}}$. The notation $r_{>(<)}$ means the bigger (smaller) of (r, r'). The different letters denote the lengths of the different electrodes as shown in figure 3: l_{e} = length of the end cap, l_{k} = length of the correction electrode, l_{r} = length of the ring ($l_{\mathrm{r}} = 2z_1$), and d = the small gap between electrodes. The inner radius of the electrodes is given by R_0, which coincides with the parameter R_0 defined in section 2. The symbols I_0 and K_0 represent the modified Bessel functions of zeroth order, first and second kind, respectively. In equation (13) we have assumed axial symmetry (rotational invariance around $\vec{u}_z$); hence the azimuth angle φ does not appear. Further, we have assumed the electric potential to be point-symmetric with respect to the trap's center ($z = 0$); thus only $\cos(\kappa_n z)$-functions appear in the series.

For equation (13) to be strictly valid, the trap should be closed by a grounded disc on each side allowing for the basic Green's function in cylindrical coordinates to be simplified to a series with the summation index κ_n running over odd n only in contrast to an integral form with continuous summation index κ. Usually, the traps used in experiments are not closed

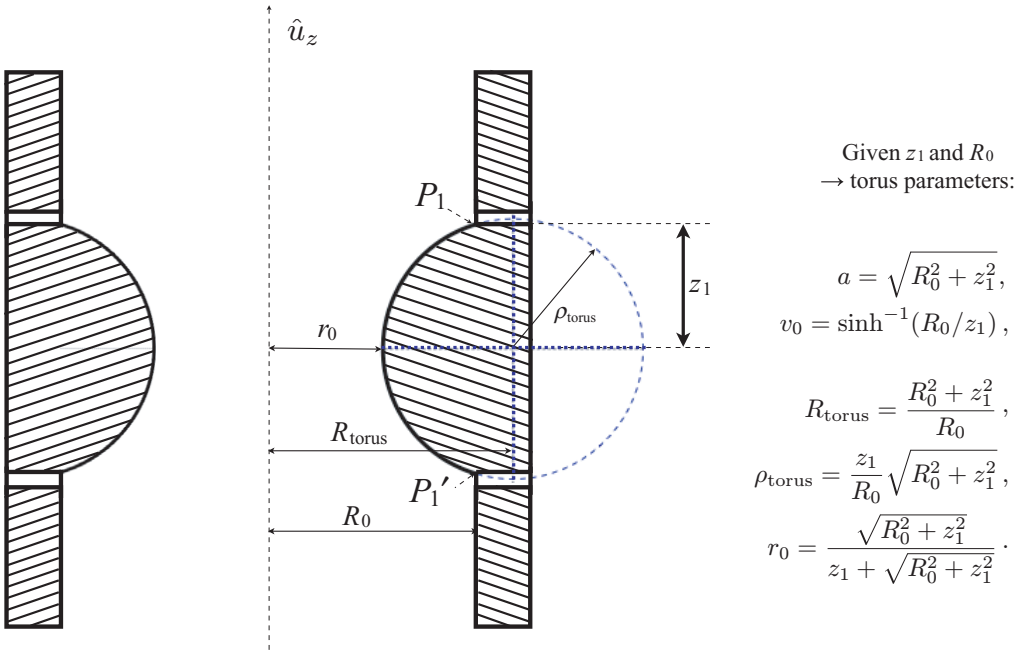

Figure 4. Parameters of the toroidal ring. The outer radius of the torus R_{torus} does not necessarily coincide with the inner radius of the cylindrical electrodes, R_0. This is reflected by the (arbitrarily chosen) upper and lower cut-off planes of the torus at P_1 and P_1', respectively: in this example, below the actual north and south poles of the torus.

by such grounded discs. This issue has been investigated mathematically in [33]: an end cap three times longer than the inner radius suffices for minimizing deviations (below 1%) of the trap's electrical properties calculated with equation (13) compared with those calculated with an infinitely long open end cap. In addition, the measurement of the electronic g-factor on carbon and oxygen [6, 7] has shown deviations as low as one part in a million in the experimental values of the coefficients c_2, c_4 and d_2 [34] from the theoretical predictions of equation (13) (see section 4). In this latter case, the measurements have been performed with a cylindrical trap with $l_e \simeq 2R_0$. For the toroidal hybrid trap a similar or even better accuracy can be assumed due to the enhanced shielding of the trap's center from outside by the toroidal ring.

The basic Green's function in toroidal coordinates has also been calculated elsewhere [29, 32, 35]. With it, the Green's function satisfying Dirichlet boundary conditions on the surface of a torus with circular cross section can be obtained employing standard techniques [31]; the result is:

$$G_{\text{tor}}(u, v \mid u', v') = \frac{1}{a\,\pi}\sqrt{\cosh v - \cos u}\,\sqrt{\cosh v' - \cos u'}\cdot\sum_{m=0}^{\infty}\epsilon_m\,\cos(mu)\cos(mu')$$
$$\times\frac{P_{m-(1/2)}(\cos v_<)}{P_{m-1/2}(\cosh v_0)}\cdot\big(P_{m-(1/2)}(\cosh v_0)\,Q_{m-(1/2)}(\cosh v_>)$$
$$-P_{m-(1/2)}(\cosh v_>)\,Q_{m-(1/2)}(\cosh v_0)\big)\,. \qquad (14)$$

$P_{m-(1/2)}$ and $Q_{m-(1/2)}$ denote the Legendre functions of first and second kind, respectively. For the case discussed here with $m \in \mathbb{N}$, they are also known as *toroidal functions* [29, 36]. The Neumann factor [29] is given by $\epsilon_m = 2 - \delta_{m,0}$. The toroidal coordinates $\{u, v, \varphi\}$ relate to the Cartesian coordinates via: $\{x, y, z\} = a/(\cosh v - \cos u)\,\{\cos\varphi \sinh v, \sin\varphi \sinh v, \sin u\}$ [29, 35]. In this coordinate system, a toroidal ring is defined by $v = v_0$, with $v_0 = \text{constant} > 0$, $u \in [0, 2\pi]$ and $\varphi \in [0, 2\pi]$. The notation $v_{>(<)}$ in equation (14) again means the bigger (smaller) of (v, v'). As before, axial symmetry is assumed and hence the azimuth φ does not appear in equation (14). Moreover, the electric potential is assumed to be invariant across the equatorial plane of the torus; thus only $\cos(mu)$—but no $\sin(mu)$—functions appear in equation (14).

For further calculation, we set the upper and lower points of the torus *looking into* the inner trap's surface as the points P_1 and P_1', respectively (see figure 4). In toroidal coordinates they are given by: $P_1 \equiv (u = \pi/2, v_0, \varphi)$ and $P_1' \equiv (u = 3\pi/2, v_0, \varphi)$. The choice of P_1 and P_1' is completely arbitrary; the reason for that specific choice is purely technical: since they are localized slightly below the ring's north and south poles, more of the correction electrodes is seen from the trap's center, and thus shielding due to the toroidal ring is reduced. An additional free parameter is the length of the ring seen from the inner side of the trap, $l_r = 2z_1$. Having specified z_1, P_1, P_1' and R_0, the toroidal ring is completely defined yielding the toroidal parameters: $a = \sqrt{R_0^2 + z_1^2}$ and $v_0 = \sinh^{-1}(R_0/z_1)$.

3.2. Potential of the toroidal hybrid trap in zeroth-order approximation

With the geometry of figure 3 chosen, it is obvious that $G_{\mathrm{I}}^{\mathrm{D}}(\vec{x} \mid \vec{x}') = G_{\mathrm{III}}^{D}(\vec{x} \mid \vec{x}') \equiv G_{\mathrm{cyl}}(\vec{x} \mid \vec{x}')$ and $G_{\mathrm{II}}^{\mathrm{D}}(\vec{x} \mid \vec{x}') \equiv G_{\mathrm{tor}}(\vec{x} \mid \vec{x}')$. Using Abel's identity, the Wronskian of the Bessel functions of equation (13) is evaluated to [36]: $I(x)\frac{\mathrm{d}K(x)}{\mathrm{d}x} - \frac{\mathrm{d}I(x)}{\mathrm{d}x}K(x) = \frac{1}{x}$ and similarly for the toroidal functions of equation (14): $P(x)\frac{\mathrm{d}Q(x)}{\mathrm{d}x} - \frac{\mathrm{d}P(x)}{\mathrm{d}x}Q(x) = \frac{1}{x}$. With these Wronskian determinants, the derivative $\partial\tilde{G}^{\mathrm{D}}(\vec{x}, \vec{x}')/\partial n'$ on the trap's surface is greatly simplified. Using the boundary conditions of figure 3, the electric potential $\Phi_0(\vec{x}) = \Phi_{\mathrm{cyc}}(\vec{x}) + \Phi_{\mathrm{tor}}(\vec{x})$ is obtained:

$$\begin{aligned}
\Phi_{\mathrm{cyl}}(r, z) &= -\frac{1}{4\pi}\int_0^{2\pi} R_0\,\mathrm{d}\varphi' \cdot 2\int_{z_1}^{L/2} \mathrm{d}z'\,\Phi(R_0, z') \cdot \left.\frac{\partial\, G_{\mathrm{cyl}}(r, z \mid r', z')}{\partial r'}\right|_{r'=R_0} \\
&= \frac{2}{L}\sum_{n=1,3,\ldots}^{\infty} \frac{1}{I_0(\kappa_n R_0)}\left[2\int_{z_1}^{L/2} \mathrm{d}z'\,\Phi(R_0, z')\cos(\kappa_n z')\right] I_0(\kappa_n r)\cdot\cos(\kappa_n z) \\
\Phi_{\mathrm{tor}}(u, v) &= -\frac{1}{4\pi}\int_0^{2\pi} h_{\varphi'}\cdot\mathrm{d}\varphi' \int_{\pi/2}^{3\pi/2} h_{u'}\cdot\mathrm{d}u'\,\Phi(v_0, u')\frac{1}{h_{v'}}\left.\frac{\partial\, G_{\mathrm{tor}}(u, v \mid u', v')}{\partial v'}\right|_{v'=v_0} \\
&= \frac{U_0}{2\pi}\sqrt{\cosh v - \cos u}\sum_{m=0,1,\ldots}^{\infty}\epsilon_m \frac{\left[\int_{\pi/2}^{3\pi/2}\mathrm{d}u' \dfrac{\cos(mu')}{\sqrt{\cosh v_0 - \cos u'}}\right]}{P_{m-(1/2)}(\cosh v_0)} P_{m-(1/2)}(\cosh v)\cdot\cos(m\,u).
\end{aligned} \tag{15}$$

The factor of 2 appearing in front of the integral $\int_{z_1}^{L/2}\mathrm{d}z'$ arises from the symmetry of the trap around the $z = 0$ plane. In the case where the voltages applied to lower correction electrode and/or end cap differ from those applied to the corresponding upper electrodes, a further integral $\int_{-L/2}^{-z_1}\mathrm{d}z'$ would have to be evaluated instead. The scale factors of the toroidal coordinates, $h_{u'}$

and $h_{v'}$, are equal [35] and in the expression for calculating Φ_{tor} they just simplify. On the other hand, the scale factor $h_{\varphi'} = \frac{a \sinh v_0}{\cos u' - \cosh v_0}$ has to be included in the integral. Furthermore, it has been assumed that the ring has a constant voltage $U_0 \rightarrow \Phi(u', v_0) = U_0\,, \forall\, u' \in [0, 2\pi]$. As mentioned before, the latter integral $\int_{P_1}^{P_1'} \mathrm{d}u'$ is delimited to the surface 'looking' inside the trap's volume. Finally, the toroidal coordinates (u, v) can be transformed into the cylindrical ones (r, z). The transformation is given by $v = 2\,\mathrm{Re}[\coth^{-1}(\frac{r+\mathrm{i}z}{a})]$ and $u = -2\,\mathrm{Im}[\coth^{-1}(\frac{r+\mathrm{i}z}{a})]$ [35].

3.3. *The electric potential of the toroidal hybrid trap*

Having obtained the zeroth-order approximation $\Phi_0(r, z)$, we are now in a position to solve the integral equation:

$$\Phi(r, z) = \Phi_0(r, z) + \int_0^{R_0} \mathrm{d}r'\, r'\, \Phi(r', z_1) \underbrace{\left[\frac{\partial F_{\text{cyl}}(r, z \mid r', z_1)}{\partial z'} - \frac{\partial F_{\text{tor}}(r, z \mid r', z_1)}{\partial z'}\right]}_{f_+(r,z|r',z_1)}. \tag{16}$$

The explicit forms of the functions $F_{\text{cyl}}(r, z|r', z')$ and $F_{\text{tor}}(r, z|r', z')$ result from the corresponding Green's functions from equations (13) and (14), as defined in equation (2):

$$F_{\text{cyl}}(r, z \mid r', z') = -\frac{4}{L} \sum_{n=1,3,\ldots}^{\infty} \frac{K_0(\kappa_n R_0)}{I_0(\kappa_n R_0)} \cos(\kappa_n z) \cos(\kappa_n z')\, I_0(\kappa_n r) I_0(\kappa_n r') \tag{17}$$

$$F_{\text{tor}}(u, v \mid u', v') = -\frac{1}{a\pi} \sqrt{\cosh v - \cos u}\, \sqrt{\cosh v' - \cos u'} \times \sum_{m=0}^{\infty} \epsilon_m \frac{Q_{m-(1/2)}(\cosh v_0)}{P_{m-(1/2)}(\cosh v_0)} \cdot \cos(mu) \cos(mu') \cdot P_{m-(1/2)}(\cosh v)\, P_{m-(1/2)}(\cosh v').$$

The structure of the integral equation (16) itself already suggests the solution: the zeroth-order approximation $\Phi_0(r, z)$ has to be substituted into the integral on the right-hand side of equation (16) to get the first-order correction: $\Delta\Phi_1(r, z) = \int_0^{R_0} \mathrm{d}r'\, r'\, \Phi_0(r', z_1)\, f_+(r, z \mid r', z_1)$, which leads to the first-order approximation $\Phi_1(r, z) = \Phi_0(r, z) + \Delta\Phi_1(r, z)$. The complete solution of the integral equation is obtained by iteration: $\Phi(r, z) = \lim_{j\rightarrow\infty} \Phi_j(r, z)$, where $\Phi_j(r, z)$ denotes the jth-order approximation to the potential given by:

$$\Phi_j(r, z) = \Phi_0(r, z) + \underbrace{\int_0^{R_0} \mathrm{d}r'\, r'\, \Phi_{j-1}(r', z_1)\, f_+(r, z \mid r', z_1)}_{\Delta\Phi_j(r,z)}. \tag{18}$$

The zeroth-order approximation of the potential $\Phi_0(r, z)$ consists of linear combinations of the sets of functions $\{I_0(\kappa_n r) \cdot \cos(\kappa_n z)\}$ and $\{P_{m-(12)}(\cosh v) \cdot \cos(m u)\}$ as can be seen from equation (15). These sets both form a basis of the linear space including the solutions to the Laplace equation in the appropriate coordinate systems. Additionally, the propagator $f_+(r, z|r', z_1)$ from equation (17) also consists of a linear combination of $\{I_0(\kappa_n r) \cdot \cos(\kappa_n z)\}$ and $\{P_{m-(12)}(\cosh v) \cdot \cos(m u)\}$. Hence, the corrections $\Delta\Phi_j(r, z)$ can be written as linear

combinations of these sets, and the electric potential can be expanded as follows:

$$\Phi(r,z) = U_0 \sum_{n=1,3\ldots}^{\infty} A_n\, I_0(\kappa_n r)\cdot\cos(\kappa_n z) + U_0\sqrt{\cosh v-\cos u}\sum_{m=0,1,2,\ldots}^{\infty} B_m\, P_{m-(1/2)}(\cosh v)\cdot\cos(mu). \tag{19}$$

In order to obtain an explicit form of the potential $\Phi(r,z)$, the coefficients A_n and B_m have to be determined iteratively following the scheme presented above. Therefore, the expansion coefficients of the jth iteration of the potential $\Phi_j(r,z)$ are given by $A_n^{(j)}$ and $B_m^{(j)}$. According to equation (19) their value is related to the coefficients of the zeroth-order approximation through the correction terms $\Delta A_n^{(j)}$ and $\Delta B_m^{(j)}$ such that: $A_n^{(j)} = A_n^{(0)} + \Delta A_n^{(j)}$ and $B_m^{(j)} = B_m^{(0)} + \Delta B_m^{(j)}$. The zeroth-order approximation of the expansion coefficients can be taken from equation (15). The correction terms of the jth order are obtained by substituting $\Phi_{j-1}(r,z)$ in equation (18). Resolving for the expansion coefficients yields, with the boundary conditions taken from figure 3,

$$A_n^{(0)} = \frac{8}{L\cdot d\cdot\kappa_n^2\, I_0(\kappa_n R_0)}\left[\sin\left(\frac{\kappa_n(d+2z_1)}{2}\right)\sin\left(\frac{\kappa_n d}{2}\right) - \frac{\kappa_n d}{2}\sin(\kappa_n z_1) + 2\,T\sin\left(\frac{\kappa_n(d+l_k)}{2}\right)\cos\left(\frac{\kappa_n(2d+2z_1+l_k)}{2}\right)\sin\left(\frac{\kappa_n d}{2}\right)\right];\quad n=1,3,5,\ldots,$$

$$B_m^{(0)} = \frac{1}{2\pi}\frac{\epsilon_m}{P_{m-(1/2)}(\cosh v_0)}\int_{\pi/2}^{3\pi/2} \mathrm{d}u\,\frac{\cos(mu)}{\sqrt{\cosh v_0-\cos u}};\quad m=0,1,2,\ldots, \tag{20}$$

In equation (20) the tuning ratio is defined as: $T = U_c/U_0$. The potential at the isolating gaps between neighboring electrodes has been approximated by a linear interpolation of the constant voltages applied at those electrodes. This approximation is valid whenever those gaps are small compared with the lengths of the trap's electrodes.

The jth-order correction terms of the expansion coefficients are given by

$$\Delta A_n^{(j)} = \frac{1}{U_0}\alpha_n\int_0^{R_0}\mathrm{d}r\, r\,\Phi_{j-1}(r,z_1)\,I_0(\kappa_n r);\quad \alpha_n = \frac{4\kappa_n}{L}\frac{K_0(\kappa_n R_0)}{I_0(\kappa_n R_0)}\sin(\kappa_n z_1),$$
$$\Delta B_m^{(j)} = \frac{1}{U_0}\beta_m\int_0^{R_0}\mathrm{d}r\, r\,\Phi_{j-1}(r,z_1)\,\mathrm{Y}_m(r,z_1);\quad \beta_m = \frac{\epsilon_m}{4\pi a^2}\frac{Q_{m-(1/2)}(\cosh v_0)}{P_{m-(1/2)}(\cosh v_0)}. \tag{21}$$

The iteration order j obviously starts at $j=1$ and should theoretically go up to infinity. The function $Y_m(r,z)$ is given by $Y_m(r,z) = \sqrt{\cosh v-\cos u}\,\{(4m-2)\cos(mu)P_{m-(3/2)}(\cosh v)\sin u + 4m\,P_{m-(1/2)}(\cosh v)\,[\sin(mu)-\cosh v\,\sin((m+1)u)]\}$, which results from the derivation of the Green's function of the torus $\partial F_{\mathrm{tor}}(r,z|r',z_1)/\partial z'$ as indicated in equation (16). In the expression for $Y_m(r,z)$ the toroidal coordinates (u,v) must be transformed into the cylindrical ones (r,z_1).

If for each new iteration the integrals in equation (21) had to be evaluated, the process of calculating the correction coefficients would be extremely cumbersome. Fortunately, this is not the case: equation (21) shows that the correction terms $\Delta A_n^{(j)}$, $\Delta B_m^{(j)}$ are related to the

expansion coefficients $A_n^{(j-1)}$, $B_m^{(j-1)}$ through a simple linear relation, enabling us to write in matrix notation:

$$\begin{pmatrix} \Delta A_p^{(j)} \\ \Delta B_q^{(j)} \end{pmatrix} = \begin{pmatrix} S_{p,n} & T_{p,m} \\ V_{q,n} & W_{q,m} \end{pmatrix} \cdot \begin{pmatrix} A_n^{(j-1)} \\ B_m^{(j-1)} \end{pmatrix}; \quad \mathcal{U} = \begin{pmatrix} S_{p,n} & T_{p,m} \\ V_{q,n} & W_{q,m} \end{pmatrix}. \tag{22}$$

The matrices for the correction terms and expansion coefficient are column vectors of dimension $(N+M)\times 1$, where N and M denote the number of terms used in the expansion of the cylindrical and toroidal part of $\Phi(r,z)$, respectively, as can be seen from equation (19). Theoretically, an exact solution demands $N, M \to +\infty$. Moreover, the $(N+M)\times(N+M)$ square matrix $\mathcal{U}$ depends only on the geometry of the hybrid trap: $\mathcal{U} = \mathcal{U}(L, R_0, z_1)$. It depends neither on the iteration order j nor on the applied voltages U_0, U_c. Its elements are integrals which need to be evaluated once. The explicit form of $\mathcal{U}$ is obtained after some tedious algebraic calculations; here we just present the result:

$$\begin{aligned}
S_{p,n} &= \alpha_p \cos(\kappa_n z_1) \cdot \begin{cases} n = p & \frac{1}{2} R_0^2 \left[I_0 (\kappa_n R_0)^2 - I_1 (\kappa_n R_0)^2 \right], \\ n \neq p & \dfrac{R_0}{\kappa_p^2 - \kappa_n^2} \left[\kappa_p I_0(\kappa_n R_0) I_1(\kappa_p R_0) - \kappa_n I_0(\kappa_p R_0) I_1(\kappa_n R_0) \right] \end{cases} \\
T_{p,m} &= \alpha_p \cdot \int_0^{R_0} \mathrm{d}r\, r\, I_0(\kappa_p r) \sqrt{\cosh v - \cos u}\, P_{m-(1/2)}(\cosh v) \cos(mu), \\
V_{q,n} &= \beta_q \cos(\kappa_n z_1) \cdot \int_0^{R_0} \mathrm{d}r\, r\, Y_q(r, z_1) I_0(\kappa_n r), \\
W_{q,m} &= \beta_q \cdot \int_0^{R_0} \mathrm{d}r\, r\, Y_q(r, z_1) \sqrt{\cosh v - \cos u}\, P_{m-(1/2)}(\cosh v) \cos(mu).
\end{aligned} \tag{23}$$

In general, the sub-matrices of $\mathcal{U}$ each have a different dimension: $S \equiv N \times N$, $T \equiv N \times M$, $V \equiv M \times N$ and $W \equiv M \times M$. The expansion coefficients A_n, B_n of the potential are thus given by

$$\begin{pmatrix} A_n \\ B_m \end{pmatrix} = \sum_{j=0}^{\infty} \mathcal{U}^j \cdot \begin{pmatrix} A_n^{(0)} \\ B_m^{(0)} \end{pmatrix}. \tag{24}$$

Now, the iteration coefficient j starts from $j = 0$ since the zeroth-order coefficients $A_n^{(0)}$, $B_m^{(0)}$ have to be included in the above summation. Technically, the matrix $\mathcal{U}$ together with the initial zeroth-order coefficients $A_n^{(0)}$, $B_m^{(0)}$ delivers the solution of the potential $\Phi(r,z)$ inside the toroidal hybrid trap.

3.4. Comments on the solution

The main features of the solution for the hybrid trap obtained in the preceding section are the following:

1. The solution is analytical; the function $\Phi(r,z)$ is obtained as given in equation (19). However, the coefficients A_n, B_m will be in general numerical, with no closed symbolic expression. The analyticity of $\Phi(r,z)$ has decisive advantages over a pure numerical approach when designing the trap. This will become clear in section 4.

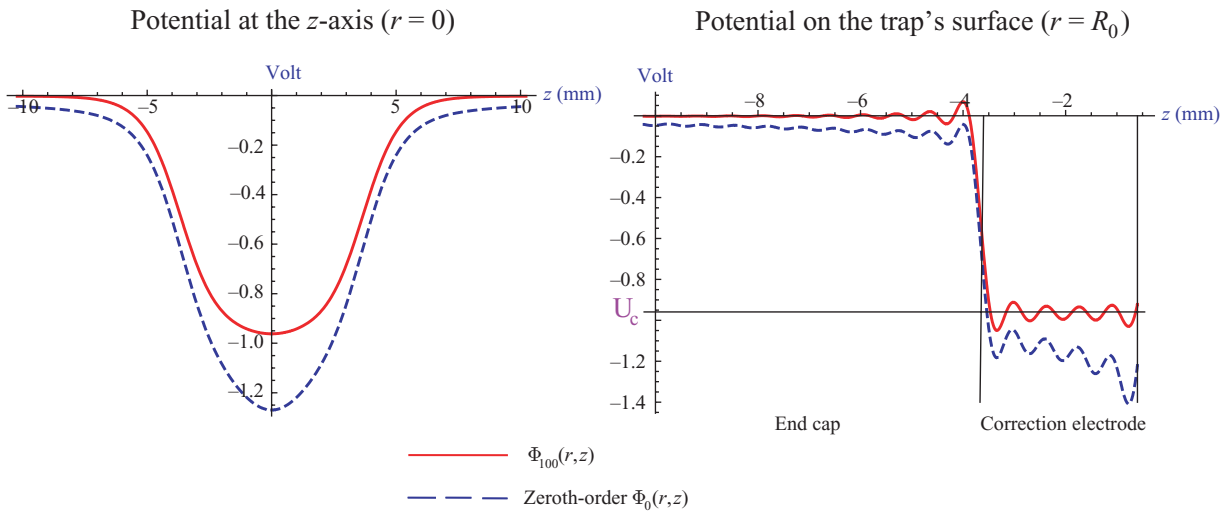

Figure 5. Example of the potential of a toroidal hybrid trap. The ring voltage is set to $U_0 = -1\,\mathrm{V}$ with a tuning ratio of $T = 0.96$ and grounded end caps. The roughness of the zeroth-order approximation $\Phi_0(r, z)$ is visible: the boundary conditions are not fulfilled, neither at the correction electrode nor at the end cap. On the contrary, the 'exact solution' $\Phi_{100}(r, z)$ fulfills them. All graphs are calculated with $R_0 = 2\,\mathrm{mm}$, $z_1 = 0.46\,\mathrm{mm}$, $L = 20.44\,\mathrm{mm}$ and $N = M = 40$.

2. $\Phi(r, z)$ is a linear combination of functions obeying the Laplace equation; therefore it itself satisfies $\nabla^2\Phi(r, z) = 0$ inside the trapping volume. A plot of $\Phi(r, z)$ on the surface of the trap showing that it also satisfies the boundary conditions confirms *ex post* its validity. This is demonstrated in figures 5 and 6.
3. An exact calculation of the potential would theoretically require infinite terms and summands. In practice though, we observe that setting $N = M = 20$ suffices for calculating the potential close to the $\hat{u}_z$-axis, which is usually the region of interest.
4. The main difficulty in the calculation is the computation of $\mathcal{U}$, which requires $(N + M)^2$ numerical integrations. The complexity of the problem increases quadratically with the number of terms N, M.

3.5. *Convergence of the iterative solution*

The convergence of equation (24) is guaranteed by the fact that $\lim_{j\to\infty} \mathcal{U}^j = 0$. This can be proved for any geometrical parameters L, R_0, z_1 and exploiting that $\lim_{j\to\infty} \alpha_n^j = \lim_{j\to\infty} \beta_m^j = 0\,\forall\, n, m$. Convergence is provided by the fact that $K_0^j(\kappa_n R_0)$ and $Q_{m-1/2}^j(\cosh v_0)$ tend very rapidly to zero for increasing j and n, m, respectively. Upon exponentiating, any element of the matrix $\mathcal{U}_{n,m}^j$ contains products of the form $\alpha_n^k \cdot \beta_m^l$ with $k + l \leqslant j$ which tend to zero while $k, l \to \infty$; therefore $\lim_{j\to\infty} \mathcal{U}_{n,m}^j = 0$ holds. In figure 7, the convergence of the particular $\mathcal{U}^j$ for the example considered in figures 5 and 6 is shown.

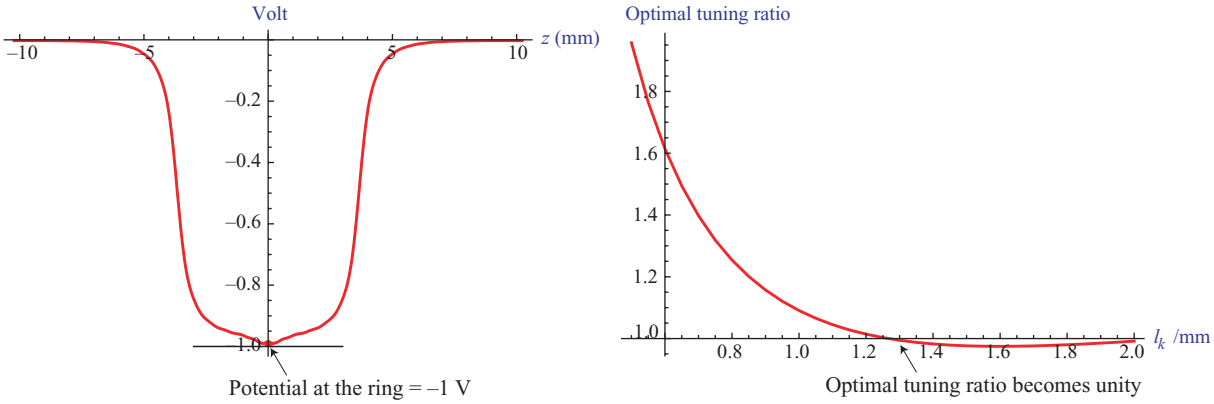

Figure 6. Left: the curve shows that the boundary conditions are fulfilled at the ring. Right: optimal tuning ratio as a function of the length of the correction electrode. For one specific length, $l_k = 1.25$, the optimal tuning ratio can even be set to 1.

3.6. The electric potential of the cylindrical Penning trap

As a corollary of the calculation of $\Phi_0(r, z)$ in the previous section, the potential of the cylindrical Penning trap is obtained by adding a further integral of the form $\int_{-z_1}^{z_1} \mathrm{d}z'\, U_0 \cos(\kappa_n z')$ to $\Phi_{\mathrm{cyl}}(r, z)$ from equation (13), where U_0 is the applied voltage to the (cylindrical) ring. With the boundary conditions shown in figure 3, the potential of the cylindrical Penning trap is given by:

$$\Phi_{\mathrm{cylinder}}(r, z) = U_0 \sum_{n=1,3,\ldots}^{\infty} \left\{ \frac{8}{L \cdot d \cdot {\kappa_n}^2 \cdot I_0(\kappa_n R_0)} \sin\left(\frac{\kappa_n d}{2}\right) \left[\sin\left(\frac{\kappa_n (d + l_r)}{2}\right) + 2\, T \sin\left(\frac{\kappa_n (d + l_k)}{2}\right) \cos\left(\frac{\kappa_n (2d + l_r + l_k)}{2}\right) \right] I_0(\kappa_n r) \cdot \cos(\kappa_n z) \right\}. \tag{25}$$

Here, $l_r = 2\, z_1$ is now the length of the cylindrical ring. All electrostatic properties of the cylindrical five-electrode Penning trap can be deduced from equation (25). Of special relevance for precision experiments are *compensation* and *orthogonality*, which will be investigated for the toroidal hybrid trap in section 4.

3.7. The electric potential of a toroidal ring

As in the case of the cylindrical trap, the electric potential created by a ring of circular cross section at a constant voltage is obtained as a corollary of the calculation of $\Phi_0(r, z)$ for the toroidal hybrid trap. Taking into account that $\int_0^{2\pi} \mathrm{d}u' \frac{\cos(mu')}{\sqrt{\cosh v_0 - \cos u'}} = 2\sqrt{2}\, Q_{m-(1/2)}(\cosh v_0)$ [29, 37], we have

$$\Phi_{\mathrm{torus}}(u, v) = U_0 \frac{\sqrt{2}}{\pi} \sqrt{\cosh v - \cos u} \sum_{m=0,1,\ldots}^{\infty} \epsilon_m \frac{Q_{m-(1/2)}(\cosh v_0)}{P_{m-(1/2)}(\cosh v_0)} P_{m-(1/2)}(\cosh v) \cdot \cos(mu). \tag{26}$$

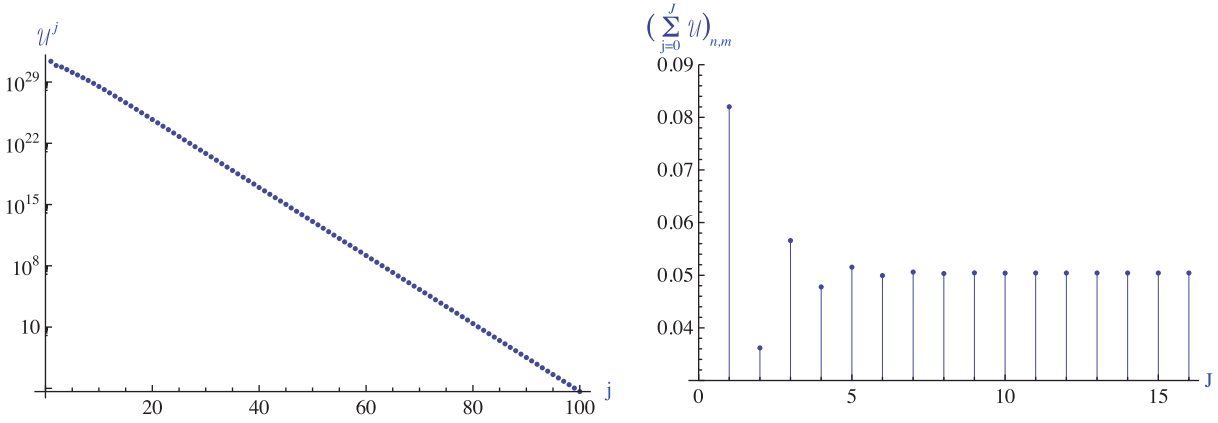

Figure 7. Example of the convergence of $\sum_{j=0}^{\infty}\mathcal{U}^j$. The semilogarithmic plot on the left shows how the norm of the $\mathcal{U}$ vanishes with increasing exponent: $|\,\mathcal{U}^j\,| \to 0$. The graph on the right shows the convergence of an arbitrary element of $\sum_{j=0}^{\infty}\mathcal{U}^j$ after having added a few summands to the series. All elements of that matrix satisfy this behavior.

This expression is valid for points outside the torus. It can be converted to Cartesian (x, y, z) or cylindrical coordinates (r, φ, z) with the transformations given in sections 3.1 and 3.2, respectively.

4. Anharmonicity compensation and orthogonality of the toroidal hybrid trap

Precision experiments with ion traps depend critically on the electrostatic performance of the trap. For example, the compensation of electrostatic anharmonicities of a Penning trap was first achieved by *Dehmelt* [38] in the context of his famous $g-2$ experiment [4]. The so-called c_j- and d_j-*coefficients* determine systematically the electrostatic properties of any Penning trap and are essential for its accurate design. These coefficients have been extensively investigated for both truncated hyperbolic [39] and cylindrical traps [3]. Their meaning and relevance for high-precision Penning trap experiments is also described in [40]. In this section, we will derive analytic expressions for c_j- and d_j-coefficients for the toroidal hybrid trap. This will clearly illustrate the power of the method developed in section 3. The task of designing a suitable toroidal hybrid trap for high-precision experiments, like the planned measurement of the g-factor of the (anti)proton, is enormously simplified having analytic expressions for the fundamental coefficients c_2, c_4, c_6 and d_2. Higher-order coefficients can also be calculated without any additional numerical effort.

4.1. Determination of c_2, c_4 and c_6 for the toroidal hybrid trap

Close to the center of the trap ($r = z = 0$) the electrostatic potential of equation (19) can be expressed as a Taylor expansion of the form:

$$\Phi(r,z) = \Phi_0 + r\,\frac{\partial\Phi}{\partial r} + z\,\frac{\partial\Phi}{\partial z} + \frac{r^2}{2!}\,\frac{\partial^2\Phi}{\partial r^2} + \frac{z^2}{2!}\,\frac{\partial^2\Phi}{\partial z^2} + \cdots = \sum_{j=0}^{\infty}\sum_{i=0}^{j}\binom{j}{i}\,\frac{\partial^j\Phi}{\partial r^i\,\partial z^{j-i}}\,r^i z^{j-i}, \qquad (27)$$

where all derivatives are evaluated at $r = z = 0$. We define the c_j-coefficients as

$$c_j = \frac{1}{U_0} \cdot \frac{1}{j!} \cdot \frac{\partial^j \Phi(r, z)}{\partial z^j}\bigg|_{(0,0)}. \tag{28}$$

These coefficients are solely functions of the trap geometry and the applied tuning ratio: $c_j = c_j(l_e, l_k, l_r, d, R_0, T)$. From equation (19) the determination of c_j is straightforward through direct derivation. The first most relevant ones are given by

$$\begin{aligned}
c_2 &= -\frac{1}{2}\left(\sum_{n=1,3,\ldots}^{\infty} A_n \kappa_n^2 + \frac{\sqrt{2}}{a^2}\sum_{m=0,1,\ldots}^{\infty} B_m(-1)^m(4m^2+1)\right),\\
c_4 &= \frac{1}{24}\left(\sum_{n=1,3,\ldots}^{\infty} A_n \kappa_n^4 + \frac{\sqrt{2}}{a^4}\sum_{m=0,1,\ldots}^{\infty} B_m(-1)^m(16m^4+56m^2+9)\right),\\
c_6 &= \frac{1}{720}\left(\sum_{n=1,3,\ldots}^{\infty} A_n \kappa_n^6 + \frac{\sqrt{2}}{a^6}\sum_{m=0,1,\ldots}^{\infty} B_m(-1)^m(64m^6+512m^4+1756m^2+225)\right).
\end{aligned} \tag{29}$$

Note that due to the symmetry of the potential across $z = 0$, all odd coefficients vanish. Thus, with the coefficients A_n and B_m of equation (24) already computed, the c_j-coefficients can be found without loss of accuracy.

4.2. Optimal tuning ratio and orthogonality

The c_j-coefficients can be written as the sum of two terms: $c_j = e_j(l_e, l_k, l_r, d, a) + T \cdot d_j(l_e, l_k, l_r, d, a)$, which can be seen from equation (20). If the applied tuning ratio $T = U_c/U_0$ is chosen such that $T = -e_4/d_4$, then c_4 is automatically canceled. The biggest electric anharmonicity is normally represented by that coefficient. With $c_4 = 0$ the trap is said to be *compensated* and $T = -e_4/d_4$ is the *optimal tuning ratio*. Compensation is absolutely necessary for many high-precision experiments since, as a result, the frequency of the trapped particle does not depend on its oscillation amplitude. Thus, uncontrolled or systematic errors are substantially reduced and the frequency can be treated as a constant for many applications. The specific optimal tuning ratio for the toroidal hybrid trap in the example of figure 5 can be taken from figure 8 after having computed c_4 with equation (29) for different values of T.

An additional property usually desired in precision Penning traps is the *orthogonality* [3]. A trap is said to be *orthogonal* when the curvature of the trapping potential is independent of the applied tuning ratio: $c_2 \neq c_2(T)$ or $d_2 = \frac{\partial c_2}{\partial T} = 0$. As before, the d_2-coefficient is received from equation (29) through derivation:

$$d_2 = -\frac{1}{2}\left(\sum_{n=1,3,\ldots}^{\infty} \frac{\partial A_n}{\partial T}\kappa_n^2 + \frac{\sqrt{2}}{a^2}\sum_{m=0,1,\ldots}^{\infty} \frac{\partial B_m}{\partial T}(-1)^m(4m^2+1)\right). \tag{30}$$

To compute $\frac{\partial A_n}{\partial T}$, $\frac{\partial B_m}{\partial T}$, the zeroth-order coefficients $A_n^{(0)}$, $B_m^{(0)}$ from equation (20) first have to be derived and, subsequently, equation (24) is used to achieve the desired level of precision.

In figure 8, d_2 has been calculated as a function of the length of the correction electrode l_k, while keeping all other geometric parameters constant. It can be seen that for one specific l_k the d_2-coefficient is equal to zero and the trap of the example becomes orthogonal.

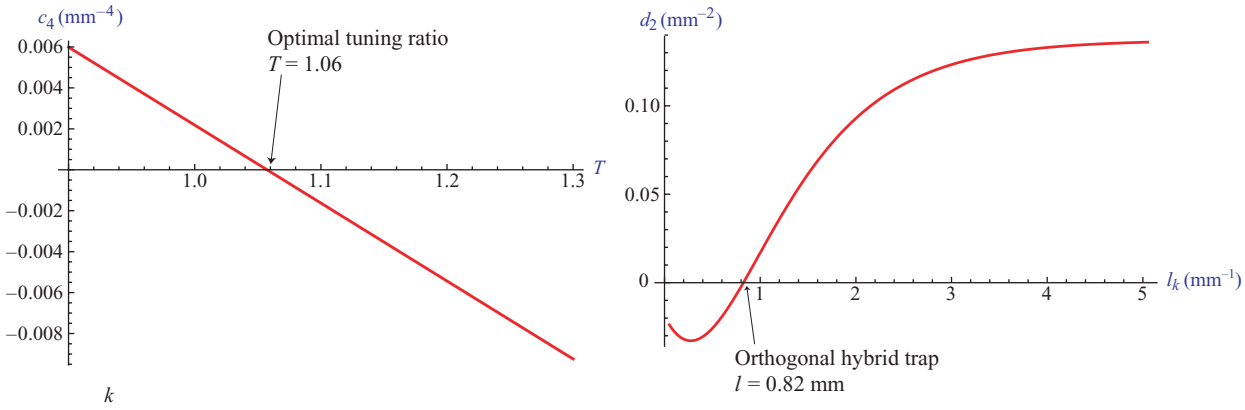

Figure 8. Left: the c_4 term can be canceled by applying the optimal tuning ratio. Right: a specific l_k makes $d_2 = 0$ and the trap becomes orthogonal.

Table 1. Parameters of an orthogonalized and compensated *toroidal hybrid trap*.

Geometric and electrical properties			
R_0	3.600 mm	d_2	4.02797×10^{-5} mm^{-2}
z_1	0.200 mm	T_{c_4}	0.913088
l_k	1.279 mm	$c_4(T_{c_4})$	-2.51735×10^{-8} mm^{-4}
l_e	8.741 mm	$c_6(T_{c_4})$	-3.43197×10^{-5} mm^{-6}

4.3. Numerical example for an orthogonal and compensated toroidal hybrid trap

Table 1 shows a numerical example for an orthogonal and compensated toroidal hybrid trap. To achieve this, the trap is first made orthogonal for a specific thickness of the ring l_r via the corresponding length of the correction electrode l_k. Subsequently, the coefficient c_4 is tuned to zero with the appropriate tuning ratio. Finally, the value of the coefficient c_6 is determined. Since machining of the parts sets a limit of some micrometres to the accuracy achievable, the coefficients will never be identical to zero. As a measure of how well the trap is orthogonalized, it is therefore convenient to examine the change of axial frequency ν_z as a function of the tuning ratio. With the calculated d_2-coefficient of $d_2 = 4.02797 \times 10^{-5}\,\mathrm{mm}^{-2}$, a micro-unit change in the tuning ratio shifts ν_z by 0.1 mHz at an axial frequency in the case of a singly trapped proton of roughly 700 kHz, which is negligible.

Thus, we have demonstrated that the parameters of the toroidal hybrid trap can be tuned in such a way as to yield a harmonic potential and an orthogonal trap, where the axial frequency depends neither on the axial energy nor the voltage applied to the correction electrode. Finally, the hybrid traps offer all the tuning possibilities for which cylindrical Penning traps are exploited.

5. Further applications

The calculation of the toroidal hybrid trap for the measurement of the g-factor of the (anti)proton [24, 25] has been the main motivation for the general method developed in

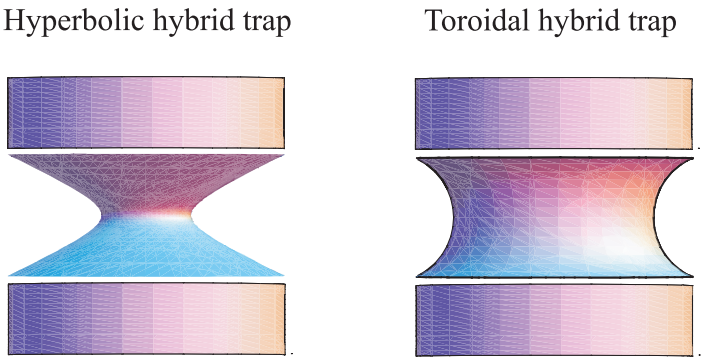

Figure 9. The hyperbolic hybrid trap is an interesting possibility which can be calculated analytically with the 'quasi'-Green's function method of section 3.

section 2. Beyond that, the method can solve the Laplace equation analytically in many other situations. Here, we want to comment briefly on some possibilities.

5.1. Other possible hybrid traps

Different hybrid traps can be thought of just by replacing the toroidal ring by other electrodes with more convenient shapes depending on the goal of the experiments. For example, in high-precision mass measurements with experimental setups at room temperature, like those of [15, 41], traditional hyperbolic Penning traps are commonly used. This is due to the larger volume in which the potential is harmonic as compared with cylindrical traps. However, no analytic formulae have been known for these traps until now. A hyperbolic hybrid trap with a (truncated) hyperbolic ring and cylindrical correction electrodes and end caps would have a very similar harmonicity volume plus the advantages of being open, and therefore easily accessible for beam-lines. Moreover, it would be much easier to design with the method of section 2 and easier to machine. The basic Green's function $\frac{1}{|\vec{x}-\vec{x}'|}$ is well known in oblate spheroidal coordinates [29, 30, 32], with which the 'quasi'-Green's function for the hyperbolic hybrid trap can be constructed, and hence application of equation (12) becomes straightforward. A comparison between the hyperbolic and toroidal hybrid trap is shown in figure 9.

Additionally, with the method employed for the toroidal trap, an appropriate 'quasi'-Green's function for the classical hyperbolic trap (hyperbolic ring and end caps) might be constructed using oblate spheroidal coordinates; with it an analytical solution to that trap might be obtained.

5.2. Applications to planar traps

Another interesting problem that can immediately be solved with the 'quasi'-Green's function method of section 2 is the propagation of microwaves in quasi-TEM modes [42] in planar structures like micro strips, coplanar waveguides and slot lines. For instance, coplanar waveguides (short CPW) have been used recently for building planar cavities in circuit-QED experiments [43]. Experiments where the electromagnetic field of a CPW cavity is coupled to ions, neutral atoms [44] or even polar molecules [45, 46] have been proposed or are under construction. The problem of calculating the propagating quasi-TEM modes arises through the

different dielectric constant (ϵ) of the substrate and the 'air side' of the transmission line [47]. This can be easily overcome just by partitioning the space into two regions with different Green's functions, each with the corresponding ϵ and again applying equation (12). With the Green's function in rectangular Cartesian coordinates, the problem can in principle be solved easily. It must be mentioned that analytical solutions for the micro strip, CPW and slot lines have been found already [47]–[49]. However, extensions to situations with multiple substrates, partial filling with other dielectrica, etc can be handled conveniently with the 'quasi'-Green's function method of section 2 while being inaccessible by other means.

6. Conclusion

Within this article, we have presented an analytically solvable extension of Dirichlet's problem. The analytical calculation of the electric potential distribution of a novel kind of Penning trap, *the hybrid trap*, has been performed. The hybrid Penning trap introduced represents a new powerful tool in high-precision experiments. Intricate mass and g-factor measurements, such as our planned measurement of the (anti)proton's magnetic moment, appear feasible by using this novel type of trap. As mentioned before, in order to make use of the continuous Stern–Gerlach effect, a strong magnetic bottle with a high curvature B_2 is required. The magnetic bottle is superimposed onto the homogeneous magnetic field B_0 needed for radial confinement yielding a net magnetic field along $\vec{u}_z$ of the form: $B_z = B_0 + B_2 z^2$. For our measurement of the (anti)proton's magnetic moment, we have manufactured a toroidal hybrid trap with $B_2 \sim 400\,\mathrm{mT\,mm^{-2}}$, resulting in a frequency shift of about 200 mHz for a single (anti)proton at ~ 700 kHz axial frequency, thus enabling the non-destructive detection of the (anti)proton's spin state [28]. This has been our main motivation for developing the hybrid Penning trap. A complete discussion on all the advantages of this toroidal trap over other conventional designs with hyperbolic or cylindrical traps for the measurement of the (anti)proton's magnetic moment goes beyond the scope of this paper and will be reviewed in future publications.

Another type of hybrid trap can be realized by replacing the center ring by a hyperboloid, as seen in figure 9. The hyperbolic hybrid Penning trap is an attractive alternative to classical hyperbolic traps with truncated electrodes. Avoiding the difficult manufacturing process of the hyperbolic end caps and correction electrodes used in pure hyperbolic Penning traps is only one of the advantages of the hybrid hyperbolic trap worth mentioning. Additional advantages are the open access for particle injection and the good anharmonicity behavior. Furthermore, other shapes can be thought of, with which hybrid traps could increase the range of applications of Penning traps in experimental physics.

Finally, the 'quasi'-Green's function formalism developed can be extended to other problems of interest in physics and engineering. Future experiments with planar traps using microwave guides might profit from this technique.

Acknowledgments

We acknowledge funding from the Helmholtz Foundation under contract number VH-NG-037 as well as the German Science Foundation under contract number QU 122/3-1. JV acknowledges support from the Marie Curie fellowship MIEDFAM. We thank S Stahl and M Kretzschmar for fruitful discussions.

References

[1] Dehmelt H G and Walls F L 1968 Bolometric technique for the rf spectroscopy of stored ions *Phys. Rev. Lett.* **21** 127–31

[2] Hanneke D, Fogwell S and Gabrielse G 2008 New measurement of the electron magnetic moment and the fine structure constant *Phys. Rev. Lett.* **100** 120801

[3] Gabrielse G and MacKintosh F C 1984 Cylindrical Penning traps with orthogonalized anharmonicity compensation *Int. J. Mass Spectrom. Ion Process.* **57** 1

[4] Dehmelt H G 1990 Experiments with an isolated subatomic particle at rest *Rev. Mod. Phys.* **62** 525

[5] Blaum K 2006 High-accuracy mass spectrometry with stored ions *Phys. Rep.* **425** 1–78

[6] Häffner H, Beier T, Hermanspahn N, Kluge H-J, Quint W, Stahl S, Verdú J and Werth G 2000 High-accuracy measurement of the magnetic moment anomaly of the electron bound in hydrogenlike carbon *Phys. Rev. Lett.* **85** 5308–11

[7] Verdú J, Djekić S, Stahl S, Valenzuela T, Vogel M, Werth G, Beier T, Kluge H-J and Quint W 2004 Electronic g factor of hydrogenlike oxygen $^{16}O^{7+}$ *Phys. Rev. Lett.* **92** 093002

[8] Gabrielse G, Hanneke D, Kinoshita T, Nio M and Odom B 2006 New value of the fine structure constant from the electron g-value and QED *Phys. Rev. Lett.* **97** 030802

[9] Gabrielse G, Khabbaz A, Hall D S, Heimann C, Kalinowsky H and Jhe W 1999 Precision mass spectroscopy of the antiproton and proton using simultaneously trapped particles *Phys. Rev. Lett.* **82** 3198–201

[10] Pinegar D B, Zafonte S L and Van Dyck R S 2007 The UW-PTMS: recent measurements and technological progress *Hyperfine Interact.* **174** 47–53

[11] Rainville S, Thompson J K and Pritchard D E 2004 An ion balance for ultra-high-precision atomic mass measurements *Science* **303** 334–8

[12] Nagy S, Fritioff T, Suhonen M, Schuch R, Blaum K, Björkhage M and Bergström I 2006 New mass value for ^{7}Li *Phys. Rev. Lett.* **96** 163004

[13] Blaum K, Audi G, Beck D, Bollen G, Herfurth F, Kellerbauer A, Kluge H-J, Sauvan E and Schwarz S 2003 Masses of ^{32}Ar and ^{33}Ar for fundamental tests *Phys. Rev. Lett.* **91** 260801

[14] Rodríguez D *et al* 2004 Mass measurement on the rp-process waiting point ^{72}Kr *Phys. Rev. Lett.* **93** 161104

[15] Bollen G *et al* 2006 Experiments with thermalized rare isotope beams from projectile fragmentation: a precision mass measurement of the superallowed β emitter ^{38}Ca *Phys. Rev. Lett.* **96** 152501

[16] George S *et al* 2007 Ramsey method of separated oscillatory fields for high-precision Penning trap mass spectrometry *Phys. Rev. Lett.* **98** 162501

[17] Thompson J K, Rainville S and Pritchard D E 2004 Cyclotron frequency shifts arising from polarization forces *Nature* **430** 58

[18] Amoretti M *et al* 2002 Production and detection of cold antihydrogen atoms *Nature* **419** 439

[19] Gabrielse G *et al* 2002 Background-free observation of cold antihydrogen with field-ionization analysis of its states *Phys. Rev. Lett.* **89** 213401

[20] Van Dyck R S, Schwinberg P B and Dehmelt H G 1987 New high-precision comparison of electron and positron g factors *Phys. Rev. Lett.* **59** 26–9

[21] Stahl S, Galve F, Alonso J, Djekić S, Quint W, Valenzuela T, Verdú J, Vogel M and Werth G 2005 A planar Penning trap *Eur. Phys. J.* E **32** 139–46

[22] Galve F, Fernández P and Werth G 2006 Operation of a planar Penning trap *Eur. Phys. J.* D **40** 201–4

[23] Castrejón-Pita J R and Thompson R C 2005 Proposal for a planar Penning ion trap *Phys. Rev.* A **72** 013405

[24] Quint W, Alonso J, Djekić S, Kluge H-J, Stahl S, Valenzuela T, Verdú J, Vogel M and Werth G 2004 Continuous Stern–Gerlach effect and the magnetic moment of the antiproton *Nucl. Instrum. Methods* B **214** 207–10

[25] Verdú J L *et al* 2005 Penning trap measurement of the magnetic moment of the antiproton *AIP Conf. Proc.* **796** 260

[26] Hermanspahn N, Häffner H, Kluge H-J, Quint W, Stahl S, Verdú J and Werth G 2000 Observation of the continuous Stern–Gerlach effect on an electron bound in an atomic ion *Phys. Rev. Lett.* **84** 427–30
[27] Dehmelt H G 1986 Continuous Stern–Gerlach effect: principle and idealized apparatus *Proc. Natl Acad. Sci. USA* **83** 2291–4
[28] Stahl S, Alonso J, Djekić S, Kluge H-J, Quint W, Verdú J and Vogel M 2005 Phase-sensitive measurement of trapped particle motions *J. Phys. B: At. Mol. Opt. Phys.* **38** 297–304
[29] Morse P M and Feshbach H 1953 *Methods of Theoretical Physics* (New York: McGraw-Hill)
[30] Moon P and Spencer D E 1971 *Field Theory Handbook: Including Coordinate Systems, Differential Equations and Their Solutions* (Berlin: Springer)
[31] Jackson J D 2005 *Classical Electrodynamics* (New York: Wiley)
[32] Cohl H C, Tohline J E, Rau A R P and Srivastava H M 2000 Developments in determining the gravitational potential using toroidal functions *Astron. Nachr.* **321** 363–73
[33] Gabrielse G, Haarsma L and Rolston S L 1989 Open-endcap Penning traps for high precision experiments *Int. J. Mass Spectrom. Ion Process.* **88** 319–32
[34] Verdú J 2004 *PhD Thesis* Johannes Gutenberg Universität, Mainz, Germany
[35] Arfken G B and Weber H J 2005 *Mathematical Methods for Physicists* (San Diego, CA: Academic)
[36] Abramowitz M and Stegun I A 1965 *Handbook of Mathematical Functions with Formulas, Graphs, and Mathematical Tables* (New York: Dover)
[37] Cohl H C and Tohline J E 1999 A compact cylindrical green's function expansion for the solution of potential problems *Astrophys. J.* **527** 86–101
[38] Van Dyck R S, Wineland D J, Ekstrom P A and Dehmelt H G 1976 High mass resolution with a new variable anharmonicity Penning trap *Appl. Phys. Lett.* **28** 446
[39] Gabrielse G 1983 Relaxation calculation of the electrostatic properties of compensated Penning traps with hyperbolic electrodes *Phys. Rev.* A **27** 2277–90
[40] Brown L S and Gabrielse G 1986 Geonium theory: physics of a single electron or ion in a Penning trap *Rev. Mod. Phys.* **58** 233–311
[41] Blaum K *et al* 2005 Isoltrap mass measurements of exotic nuclides at $\delta m/m = 10^{-8}$ *Nucl. Phys.* A **752** 317c–20c
[42] Lindell I V 1981 On the 'quasi'-TEM modes in inhomogeneous multiconductor transmission lines *IEEE Trans. Microw. Theory Tech.* **29** 812
[43] Wallraff A, Schuster D I, Blais A, Frunzio L, Huang R-S, Majer J, Kumar S, Girvin S M and Schoelkopf R J 2004 Strong coupling of a single photon to a superconducting qubit using circuit quantum electrodynamics *Nature* **431** 162
[44] Verdú J *et al* 2008 Strong magnetic coupling of an ultracold gas to a superconducting waveguide cavity arXiv:0809.2552v1 [cond-mat.mes-hall]
[45] André A, DeMille D, Doyle J M, Lukin M D, Rabl P, Schoelkopf R J and Zoller P 2006 A coherent all-electrical interface between polar molecules and mesoscopic superconducting resonators *Nat. Phys.* **2** 636
[46] Rabl P, DeMille D, Doyle J M, Lukin M D, Schoelkopf R J and Zoller P 2006 Hybrid quantum processors: molecular ensembles as quantum memory for solid state circuits *Phys. Rev. Lett.* **97** 033003
[47] Pozar D M 2004 *Microwave Engineering* (New York: Wiley)
[48] Simons R N and Arora R K 1982 Coupled slot line field components *IEEE Trans. Microw. Theory Tech.* **30** 1094
[49] Cohn S B 1972 Slot line field components *IEEE Trans. Microw. Theory Tech.* **20** 172

REVIEW ARTICLE

g-factor experiments on simple systems in Penning traps‡

K Blaum[1,2], H Kracke[3], S Kreim[3], A Mooser[3], C Mrozik[3], W Quint[4], CC Rodegheri[3], B Schabinger[3], S Sturm[3], S Ulmer[1,2], A Wagner[1,2], J Walz[3] and G Werth[3]

[1] Max-Planck-Institut für Kernphysik, D-69117 Heidelberg, Germany
[2] Fakultät für Physik und Astronomie, Ruprecht-Karls-Universität Heidelberg, D-69120 Heidelberg
[3] Institut für Physik, Johannes Gutenberg-Universität, D-55099 Mainz, Germany
[4] GSI Helmholtzzentrum für Schwerionenforschung Darmstadt, D-64291 Darmstadt, Germany

E-mail: klaus.blaum@mpi-hd.mpg.de

Abstract. Penning traps serve for the precise measurement of magnetic moments of simple atomic systems and fundamental particles. Here we present attempts to measure the magnetic moment of the electron bound in hydrogen-like or lithium-like heavy ions as well as of the proton and antiproton. While the first experiment aims for a more stringent test of bound-state quantum-electrodynamic calculations the second experiment provides a new high-precision test of the CPT theorem on the baryonic sector.

PACS numbers: 06.20Jr, 31.30.Jv, 32.10.Dk

Submitted to: *J. Phys. B: At. Mol. Opt. Phys.*

‡ The results which are presented here are part of the ongoing PhD theses work of H Kracke, S Kreim, CC Rodegheri, B Schabinger, S Sturm, S Ulmer, and A Wagner.

1. Introduction

The magnetic moment is one of the basic quantities of any atomic system. For multi-electron atoms or ions it provides information on the wave function and represents an important quantity to test atomic physics calculations. This is particularly true for systems with few electrons where the magnetic moment can be calculated with high precision.

Penning traps have in recent years contributed substantially to our knowledge of magnetic moments in charged systems. In fact the most precise measurements to date arise from Penning trap experiments using different techniques. The magnetic moment of the electron bound in singly charged alkali-like ions has been determined in various experiments with typical fractional uncertainty of 10^{-8} using optical-microwave double resonance technique [1, 2, 3]. With similar techniques nuclear magnetic moments of those systems have been derived with uncertainties in the range of 10^{-6} [2, 4, 5].

For fundamental particles the most notable result has been obtained for the free electron. Based on the pioneering experiments of Dehmelt and coworkers [6] Gabrielse and coworkers have recently determined the magnetic moment of the electron with extreme precision [7]. Usually it is expressed in units of the Bohr magneton $\mu_{\mathrm{B}} = (e/m)\hbar$ using the dimensionless g-factor:

$$\vec{\mu} = g\mu_{\mathrm{B}}\vec{s} \tag{1}$$

where s is the electron spin. Presently the most precise value for g is [7]

$$g = 2.002\,319\,304\,361\,46\,(56).$$

This value can be compared with quantum electrodynamics (QED) calculations which are expressed in a perturbation series using the fine structure constant α as expansion parameter:

$$g = 2 + C_1(\alpha/\pi) + C_2(\alpha/\pi)^2 + C_3(\alpha/\pi)^3 + C_4(\alpha/\pi)^4 + \ldots \quad . \tag{2}$$

While the coefficients C_n have been calculated with sufficient accuracy up to the forth order and also additional correction from hadronic contributions have been included [8, 9], the value for α is not known accurately enough to match the experimental precision. However, the problem can be inverted: If one assumes that QED is correct, the combination of the experimental and theoretical value for the electrons g-factor results in the most precise value for α [9, 10].

When the electron is bound to a nucleus forming a hydrogen-like system, the g-factor is changed by binding corrections, additional bound-state quantum electrodynamics (BS-QED) contributions, and by nuclear structure effects. In recent years these contributions have been calculated to high accuracy [11, 12]. Measurements to test these calculations have been performed on C^{5+} [13] and O^{7+} [14]. In these experiments single ions have been confined in a double Penning trap [15, 16]. The spin-precession frequency of the bound electron $\omega_{\mathrm{L}} = g(e/m)sB$ is measured simultaneously

with the ion's cyclotron frequency $\omega_c = (qe/M)B$. Here, q is the charge state of the ion and M its mass, and the g-factor follows from the ratio of the frequencies

$$g = 2\frac{\omega_L}{\omega_c}\frac{m}{M}\frac{q}{e}, \tag{3}$$

provided that the electron/ion mass ratio m/M is known. Within the uncertainty of about 10^{-9} the results agree with BS-QED calculations and represent a stringent test of the theory [13, 14].

The BS-QED contributions scale approximately with the square of the nuclear charge Z of the H-like ion. Thus measuring the g-factor of systems with higher Z would represent a more stringent test of the BS-QED calculations [17]. In the experiments on C^{5+} and O^{7+} the ions were produced by consecutive electro-ionization within the trap system. Going to higher-Z systems requires higher electron energies to account for the increasing electron binding energies of the ions. Technical reasons limit the energies in a closed system to a few keV. New experiments have been started at the University of Mainz with the aim of measuring the g-factor of the electron bound in Si^{13+} and Ca^{19+}. Also the electron g-factor of of Li-like Si^{11+} and Ca^{17+} will be measured [18]. A comparison of H- and Li-like ions of the same element will eliminate partly the uncertainties from nuclear structure contributions [19]. Ca^{19+} is the highest-Z ion which is accessible with a setup similar to the one used in the experiments on C^{5+} and O^{7+}. The present experiments are based on the same principles as in the preceding experiments. Details will be given below.

Similarly, attempts are under way to determine the g-factor of the proton with high accuracy [20]. This is considered a feasibility test for planned experiments on the anti-proton using the same technique. The comparison of the magnetic moments of proton and anti-proton would represent a test of the CPT invariance for baryonic systems.

The purpose of this contribution is to present the status of both experiments. As it will be outlined below, they have reached a status which allows expecting first results in the near future.

2. Experimental method

The dynamic of a single particle stored in a Penning trap has been described extensively in literature [21, 22]. In such a trap we have three different oscillation frequencies. The axial frequency in the direction of the magnetic field is given by $\omega_z = (qU/Md^2)^{1/2}$ with the potential difference U applied between the trap electrodes and the trap's characteristic dimension d. In the radial plane we have the so-called perturbed cyclotron frequency $\omega_+ = \omega_c/2 + (\omega_c^2/4 - \omega_z^2/2)^{1/2}$ and the magnetron frequency $\omega_- = \omega_c/2 - (\omega_c^2/4 - \omega_z^2/2)^{1/2}$. The square sum of these three frequencies gives the cyclotron frequency of the free particle as required for the calibration of the magnetic field:

$$\omega_+^2 + \omega_-^2 + \omega_z^2 = \omega_c^2. \tag{4}$$

This relation ("invariance theorem") is in first order independent of perturbations arising from trap imperfections which may shift the frequencies [21]. The axial- and the perturbed cyclotron frequency are measured by detection of image currents induced in the traps electrodes due to the particles oscillation. The detection systems consist of high-quality resonance circuits followed by GaAs field effect transistor amplifiers. The resonance frequencies are chosen at the ion's oscillation frequencies in axial and radial direction, respectively. In order to keep the noise of the detection circuits small the trap as well as the attached amplifiers are kept at liquid helium temperature. A Fourier transform of the induced noise spectrum reveals the respective ion oscillation frequency. The magnetron frequency is measured via sideband coupling to the axial motion [21].

The spin-precession frequency ω_{L} of the bound electron is determined by a measurement of the energy difference ΔE between the two spin directions

$$\omega_{\mathrm{L}} = \Delta E/\hbar = g\frac{e}{2m}B. \tag{5}$$

Spin flips are induced by microwaves radiated into the trap. They are detected by the "continuous Stern-Gerlach effect" [22, 23, 24]: The central ring electrode of the Penning trap is made out of ferromagnetic material. This deforms the magnetic field $\vec{B}$ in a bottle-like manner:

$$\Delta\vec{B}(r,z) = B_2\left[-z\cdot r\cdot\hat{u}_r + \left(z^2 - \frac{r^2}{2}\right)\cdot\hat{u}_z\right], \tag{6}$$

where for cylindrical traps

$$B_2 \approx \frac{\mu_0 M}{2}\left[\frac{a}{\sqrt{R^2+a^2}}\right]. \tag{7}$$

Here M is the saturation magnetization of the material, a is the hight and R the inner radius of the ring electrode. In the inhomogeneous magnetic field the force acting on the electron's magnetic moment adds or subtracts, depending on the spin orientation, to the electric binding force of the Penning trap. This causes a slight difference in the ion's axial oscillation frequency

$$\omega_z^{'} \cong \omega_z \pm \frac{\mu_z B_2}{m\omega_z} = \omega_z \pm \delta_{\omega_z}. \tag{8}$$

When a spin flip is induced the change in axial frequency serves as a monitor. For typical operating parameters in our experiments this frequency change is rather small: It amounts to about 200 mHz in case of Si^{13+} and Ca^{19+} but only about 10 mHz for the proton due to the 658 times smaller magnetic moment of the proton compared to that of the electron, while the axial oscillation frequency is in the few hundred kHz range. The detection of these small frequency changes represents an experimental challenge, requiring extremely stable trap operating conditions. The previous experiments on C^{5+} and O^{7+} demonstrate that induced spin flips can be detected without ambiguity. Feasibility tests have shown that the sensitivity of spin flip detection can be improved by measuring phase differences of the axial oscillation frequencies [25].

Since the inhomogeneous magnetic field of the trap required for analysis of the spin direction would lead to a broadening and asymmetry of the spin and motional

frequencies, we separate the region where spin flips are induced from the one where the spin direction is determined using a double trap technique. The spin direction is first determined in an "analysis" trap with superimposed inhomogeneous B-field. Then the ion is transferred to a second trap ("precision trap") located a few cm apart where the magnetic field is kept homogeneous. The geometry of this trap is identical with the analysis trap. Here, attempts to induce spin transitions take place. The ion is then transferred back to the analysis trap where the spin direction is probed. The spin flip probability as function of the microwave frequency shows a maximum at the Larmor precession frequency. While the ion is in the precision trap its motional frequencies are determined as described above. The simultaneous measurement of cyclotron and Larmor frequency eliminates to a large degree uncertainties caused by unavoidable temporal instabilities of the magnetic field. From the ratio of both frequencies the g-factor is determined according to equation (3) provided that the electron/ion mass ratio is known.

3. g-factor of Si^{13+} and Ca^{19+}

We are in the process to determine the g-factor of the electron bound in hydrogen-like Si^{13+} and Ca^{19+}. For this purpose we have extended the double Penning trap as used in the experiments on C^{5+} and O^{7+} by a third trap ("creation trap") which is used to produce highly charged ions by charge breeding similar as in EBIT ion sources [26]. Because the cross section for electron exchange with restgas atoms is larger for higher charge states extreme vacuum conditions are required. Therefore the traps are located inside a sealed vacuum chamber at liquid helium temperature. Figure 1 shows an outline and a photograph of the triple trap. The electrodes of 7 mm inner diameter are made our of oxygen-free copper and the surfaces are gold plated. The precision and the analysis trap consist of a ring and two endcap electrodes with correction electrodes placed between them. In contrast, the creation trap has only three electrodes. Singly charged ions are produced by electrons emitted from a field emission point at a few hundred eV energy and reflected at hyperbolical shaped electrodes a few cm apart. They hit a target surface from which the required atomic species ions as well as impurities are detached. They are first ionized and stored in the creation trap before by consecutive ionization higher charged states are produced. After creation the ion cloud is transported to the precision trap. Here, a mass spectrum of the stored ions can be obtained when the voltage applied to the trap electrodes is scanned. Since the ion's axial oscillation frequency depends on the charge-to-mass ratio and the square root of the applied voltage, the trapped ions are consecutively brought into resonance with a tank circuit attached to the electrode. In the case of resonance the noise power across the tank circuit increases by the induced noise from the axial oscillation. The noise is amplified and displayed as shown for the preparation trap in figure 2. Strong radio-frequency excitation of the axial oscillation at their respective frequencies eliminates all ion species from the trap except those under investigation. Then the trap potential depth is carefully reduced and ions

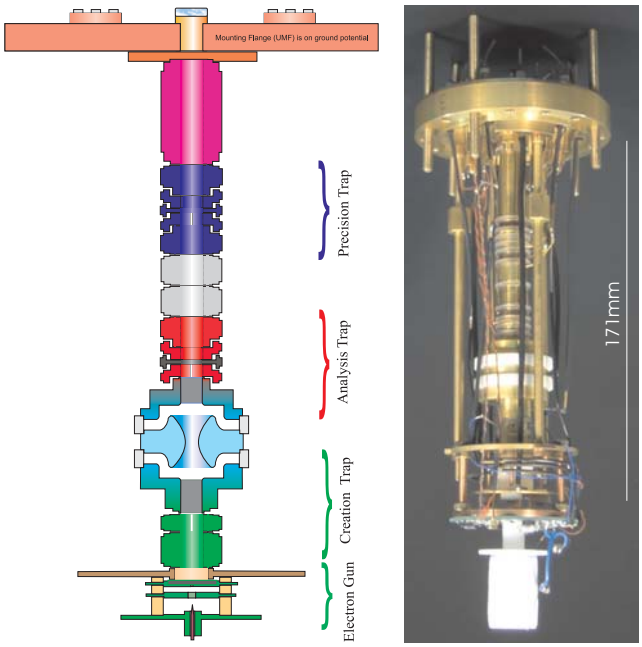

Figure 1. Outline (left) and photograph (right) of the triple Penning trap. The total length is about 17 cm.

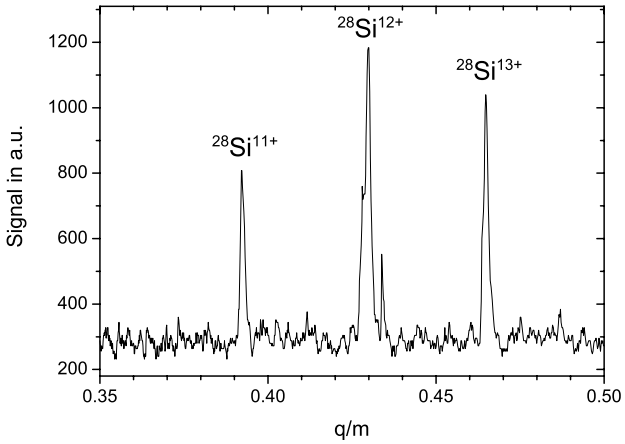

Figure 2. Induced noise in the axial detection circuit from oscillating ^{28}Si ions in different charge states when the trap voltage is scanned.

of large oscillation amplitude will leave the trap until a single particle is left. The ion is kept continuously in resonance with the circuits and its oscillation amplitude is damped by the induced currents until it reaches temperature equilibrium with the environment. The presence of the ion in thermal equilibrium with the environment manifests itself by a minimum in the noise spectrum of the axial tank circuit (figure 3a). This can be understood when we consider the oscillating ion as an equivalent series resonance circuit. Its quality factor is very high since there is little damping of the axial oscillation. At

its resonance frequency the noise voltage across the attached parallel circuit is shortcut leading to the observed minimum in the spectral density. After averaging for about 90 seconds the axial frequency can be determined with uncertainties below 100 mHz. As stated above this is a necessary requirement to detect induced spin flips by a change in axial frequency. When we couple the axial to the cyclotron motion by an additional r.f.

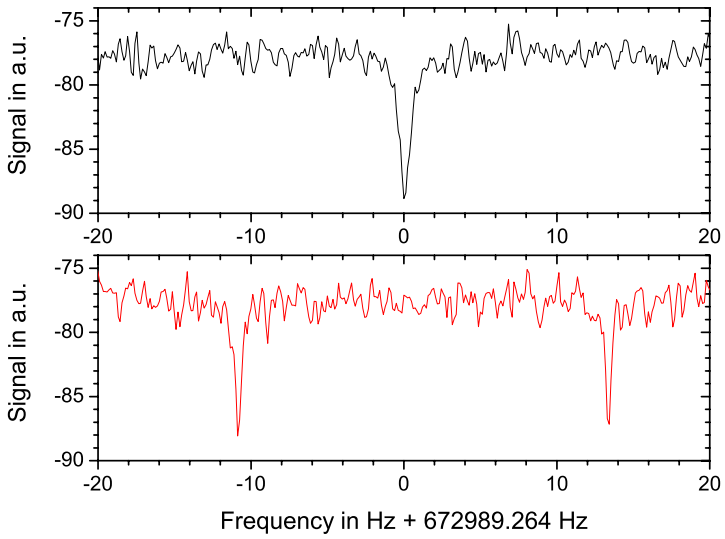

Figure 3. a(upper trace): Axial signal from a single Si^{12+} ion resistively cooled to 4K. b(lower trace): Split of the axial resonance into two components when axial and cyclotron oscillations are coupled by an additional rf field at their frequency difference.

quadrupole field at the frequency $\omega_{\mathrm{couple}} = \omega_+ - \omega_\mathrm{z} + \delta$, where δ is a detuning from the frequency difference, the axial dip splits into two components [15] (see figure 3b). The perturbed cyclotron frequency can be obtained from the splitting through

$$\omega_+ = \omega_{\mathrm{couple}} + \omega_\mathrm{z} + 2\left(\frac{\omega_\mathrm{r} + \omega_\mathrm{l}}{2} - \omega_\mathrm{z}\right). \tag{9}$$

The components $\omega_{\mathrm{r,l}}$ are given by

$$\omega_{\mathrm{r,l}} = \omega_\mathrm{z} - \frac{\delta}{2} \pm \sqrt{\delta^2 + |A|^2} \tag{10}$$

where $|A|$ is a proportion for the measure of the coupling in units of frequency and δ is a measure for the detuning of the coupling frequency to the sideband frequency $\omega_+ - \omega_z$. The uncertainty of the observed minima in figure 3 allows determining the cyclotron frequency of (nominally 26.9 MHz in a B-field of 3.77 T in case of Si^{13+}) to a few parts in 10^{-9}.

Presently, the detection of the spin direction is being prepared and we expect to observe induced spin flips in the near future.

On the theoretical side calculations of the different contributions to the g-factor of

Table 1. Theoretical contributions to the electron g-factor in hydrogen-like $^{40}Ca^{19+}$ and $^{28}Si^{13+}$. The values are taken from [11] for Ca and from [27] for Si. The largest uncertainty comes from an estimate of uncalculated higher order terms.

Ion	Dirac value	BS-QED	Nuclear effects	Total
$^{40}Ca^{19+}$	1.985 723 203 7(1)	0.002 336 871 3(2)	0.000 000 410 0(1)	1.988 056 946 6(100)
$^{28}Si^{13+}$	1.993 023 570 6(1)	0.002 328 682(2)	0.000 000 224 74	1.995 348 962

hydrogen-like Si^{13+} and Ca^{19+} are available. They are listed in table 1. To evaluate the g-factor from the measured ω_L/ω_c frequency ratio the mass ratio m/M of the electron to the ion has to be known accurately. The electron mass (in atomic units) is known to $5.3 \cdot 10^{-10}$ [28]. The masses of ^{40}Ca and ^{28}Si have been determined by the SMILETRAP group in Stockholm to $7 \cdot 10^{-10}$ [29] and $4 \cdot 10^{-11}$ [30], respectively.

4. *g*-factor of the (anti)proton

The magnetic moment of the proton is known to 8 significant digits from measurements of the hydrogen hyperfine structure [31]. An improvement of this number is of utmost importance in itself since it is a fundamental constant but also because it used in many applications like NMR spectroscopy. However, it cannot be calculated to the aimed accuracy from strong interaction models. On the other hand the magnetic moment of the antiproton is currently known from measurements of the fine structure splitting of X-ray transitions in antiprotonic lead atoms to a precision of only 10^{-3} [32]. A proposal to determine the g-factor of the antiproton by means of spectroscopy of antiprotonic helium [33] aims for an uncertainty of 10^{-5}. An accuracy of the same order of magnitude as for the proton would allow to compare both numbers as test of the CPT invariance for baryonic systems [34].

Penning traps offer the opportunity to measure the g-factor of the antiproton with high accuracy using the same method as described above for H-like ions. As a first step towards this goal we have set up an experiment to determine the g-factor of the proton, potentially improving the existing value. The advantage of performing the measurement on a single isolated particle is that the result is free of any corrections from the environment and the precision is only limited by technical limitations such as stability of the traps electric and magnetic fields. If successful we plan to use the setup for antiprotons when a source of low energy antiprotons will be available at the FLAIR facility of GSI/Darmstadt [35].

The main challenge for the g-factor determination of the proton arises from its smaller magnetic moment compared to the case of the electron. According to equation (8) this leads to a smaller change in the axial oscillation frequency due to an induced spin flip. In order to increase this shift a novel kind of Penning trap as shown in figure 4 was developed. The analysis trap consists of a CoFe ring electrode of toroidal shape. Due to that design, the strength of the magnetic bottle is increased by a factor of 40

compared to the Si/Ca analysis trap. A detailed theoretical description of this trap is given in [36]. The B_2 term of about $400\,\mathrm{mT/mm^2}$ will lead to an axial frequency change of 220 mHz at a total frequency of about 690 kHz. The trap is placed in a closed vacuum

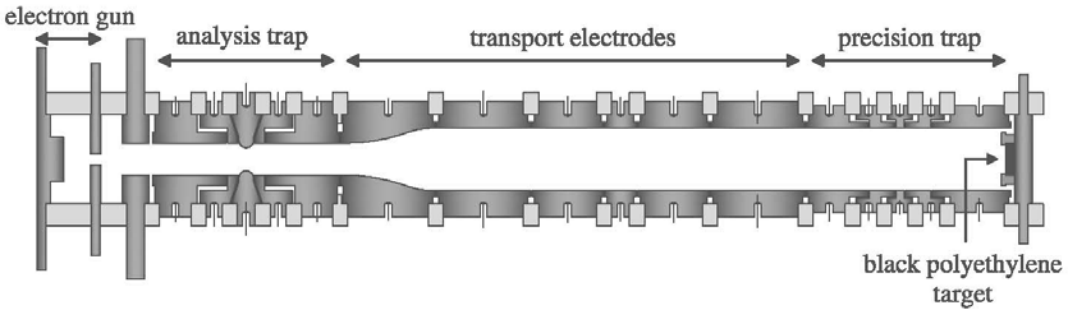

Figure 4. Sketch of the double trap for (anti)proton g-factor determination. Both traps are compensated Penning traps consisting of five electrodes. In order to maximize the inhomogeneity of the magnetic field in the center of the analysis trap, it has a smaller diameter and the inner surface of the ring electrode has toroidal geometry. The particle is transported between the traps via adiabatic ramping of the transport electrodes.

system and is held at cryogenic temperatures of about 4 K by a pulse tube cooler. This ensures ultrahigh vacuum by cryo-pumping and long storage times of the proton.

The protons are created inside the trap by electron impact from a black polyethylene target, using a field emission point as electron source. The single proton preparation is similar to the cleaning process described in the Si/Ca experiment. For the axial frequency measurement a superconducting NbTi resonator with a quality (Q) factor of ≈ 5000 was developed, the cyclotron frequency is measured with a detection system based on a copper resonator, showing a Q-factor of ≈ 1100. The voltage noise of the cryogenic amplifiers lies below $1.1\,\mathrm{nV/Hz^{1/2}}$.

In order to measure the perturbed cyclotron frequency directly the proton has to be excited to a few eV. Energy dissipation through the resonant impedance yields a sharp peak in the noise spectrum of the circuit due to the particles oscillation at $\approx 29\,\mathrm{MHz}$. Such a signal is shown in figure 5a. For high excitation energies, the perturbed cyclotron frequency is modified by higher order corrections in the trapping potentials. Thus, the frequency depends on the particles oscillation amplitude. Since the energy is damped exponentially a cooling curve as shown in figure 5b is obtained from which the perturbed cyclotron frequency for the particle at rest can be extracted. Another possibility would be the cyclotron frequency measurement via equation (9). A detailed comparison between both methods is given in [37].

The axial frequency is measured as previously described for H-like ions. In figure 6 the axial resonance after averaging for 90 s is shown. High resolution scans of the signal show that the axial frequency can be determined with uncertainties below 100 mHz, sufficient to detect changes due to an induced spin flip.

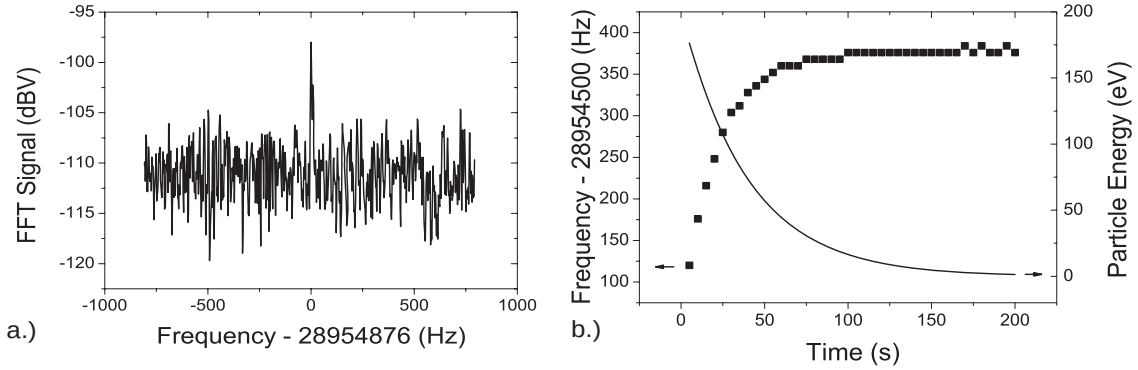

Figure 5. a.) Fourier-transform of the noise in the radial detection circuit showing a maximum at the perturbed cyclotron frequency induced by a single trapped proton. b.) Change of the cyclotron frequency of a single proton in the precision trap by resistive cooling. The squares show the measured cyclotron frequency. The solid line gives the equivalent particle energy. The drift results from the anharmonic potential seen by the initially highly excited particle.

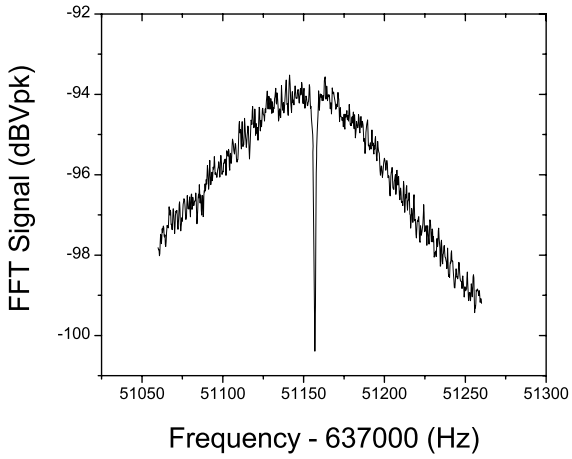

Figure 6. Axial resonance of a single proton in thermal equilibrium with the detection circuit. At its resonance frequency the proton shorts the noise of the axial detector, resulting in a dip in the noise resonance.

5. Conclusion

The experimental setups for precise g-factor measurements on medium-heavy hydrogen- or lithium-like ions as well as on bare protons have been completed. Single particles have been stored for several weeks and have been lost only due to technical reasons. Their energy has been reduced in all degrees of freedom to the ambient temperature by resistive cooling using high-Q circuits held at liquid helium temperature. Presently measurements are under progress to determine the motional frequencies with high accuracy in order to calibrate the magnetic fields of the Penning traps. Transport of the particles between the two potential minima of the double Penning trap has been

successfully performed. We expect the detection of induced spin flips in the near future. The prospects are that the g-factors derived from the ratio of the Larmor- and the cyclotron frequencies will have uncertainties of 10^{-9} or below. This will represent a significant contribution to tests of bound state quantum electrodynamic calculations and to a future test of CPT invariance for protons and antiprotons.

Acknowledgments

Financial support by the Programme Alβan, the European Union Programme of High Level Scholarships for Latin America, scholarship no. (E06D101305BR), by the Deutsche Forschungsgemeinschaft DFG under contract QU122/3, by the German Ministry for Education and Research BMBF (06MZ227I), and by the Helmholtz Association for National Research Centers HGF (VH-NG-037) is acknowledged.

References

[1] Itano W *et al* 1985 *J. Opt. Soc. Am.* B **2** 1352
[2] Marx G *et al* 1998 *Eur. Phys. J.* D **4** 279
[3] Tommaseo G *et al* 2003 *Eur. Phys. J.* D **25** 113
[4] Bollinger J J *et al* 1983 *Laser Spectroscopy VI* ed Weber H P and Luthy W (Heidelberg: Springer)
[5] Trapp S *et al* 2003 *Eur. Phys. J.* D **26** 237
[6] Van Dyck R S *et al* 1987 *Phys. Rev. Lett.* **59** 26
[7] Hannecke D *et al* 2008 *Phys. Rev.Lett.* **100** 120801
[8] Kinoshita T and Nio M 2006 *Phys. Rev.* D **73** 013003
[9] Aoyama T *et al* 2007 *Phys. Rev. Lett.* **99** 110406
[10] Gabrielse G *et al* 2006 *Phys. Rev Lett.* **97** 030802
[11] Pachucki K *et al* 2005 *Phys. Rev.* A **72** 022108
[12] Jentschura U *et al* 2006 *Int. J. Mass Spectr.* **51** 102
[13] Häffner H *et al* 2000 *Phys. Rev. Lett.* **85** 5308
[14] Verdú J *et al* 2004 *Phys. Rev. Lett.* **92** 093002
[15] Häffner H *et al* 2003 *Eur. Phys. J.* D **22** 163
[16] Werth G *et al* 2006 *Int. J. Mass Spectrom.* **251** 152
[17] Vogel M *et al* 2008 *Eur. Phys. J. Special Topics* **163** 113
[18] Schabinger B *et al* 2007 *J. Phys. Conf. Ser.* **58** 121
[19] Shabaev V M *et al* 2003 *Nucl. Instrum. Meth.* B **205** 30
[20] Verdu J *et al* 2005 *Proc. of the LEAP Conference AIP* **796** 260
[21] Brown L S and Gabrielse G 1986 *Rev. Mod. Phys.* **58** 233
[22] Major F G *et al* 2005 *Charged Particle Traps* (Heidelberg: Springer)
[23] Dehmelt H and Eckstrom P 1973 *Bull. Am. Phys. Soc.* **18** 727
[24] Werth G *et al* 2002 Adv. At. Mol. Opt. Phys. **48** 191
[25] Stahl S *et al* 2005 *J. Phys.* B **38** 297
[26] Alonso J *et al* 2006 *Rev. Sci. Instr.* **77** 03A901
[27] Beier Th *et al* 2000 *Phys. Rev.* A **62** 032510
[28] Mohr P J and Taylor B N 2005 *Rev. Mod. Phys.* **77** 1
[29] Bergström I *et al* 2003 *Eur. Phys. J.* D **22** 41
[30] Bergström I *et al* 2002 *Phys. Scr.* **66** 201
[31] Winkler P F *et al* 1972 *Phys. Rev.* A **5** 83
[32] Kreissl A *et al* 1988 *Z. Phys.* C **37** 557

[33] Bakalov D and Widmann E 2007 *Phys. Rev.* A **76** 012512
[34] Quint W *et al* 2004 *Nucl. Instr. Meth. Phys. Res.* B **214** 207
[35] http://www.gsi.de/flair/
[36] Verdú J *et al* 2008 *New J. Phys.* **10** 103009
[37] Verdú J *et al* 2003 *PhD Thesis* University of Mainz.